I. SHOCK METAMORPHISM OF THE COCONINO SANDSTONE AT METEOR CRATER, ARIZONA

II. THE SPECIFIC HEAT OF SOLIDS OF GEOPHYSICAL INTEREST

Thesis by

Susan Werner Kieffer

In Partial Fulfillment of the Requirements

for the Degree of

Doctor of Philosophy

California Institute of Technology

Pasadena, California

1971

(Submitted December 14, 1970)

ACKNOWLEDGMENTS

The ever-optimistic encouragement of Dr. E. M. Shoemaker, whose belief that the story of shocked rocks is "in the field map of a thin section", was equaled only by the much appreciated freedom he allowed in unravelling the story. Dr. Barclay Kamb provided many hours of enthusiastic discussion of both parts of this thesis in the midst of hectic times in his schedule; these were much appreciated. Dr. Pol Duwez most courteously extended the use of X-ray diffraction equipment, lent a kind ear and hearty spirit to many questions and discussions. Dr. Thomas Ahrens was always willing to answer questions about shock wave properties and techniques.

I thank the following people for help given, laboratory space loaned and ideas profferred: Dr. Samuel Epstein, Dr. Ronald Scott, Dr. Leon Silver, Paul Knauth, Donald Gault and Dr. Henry Moore.

I thank my father, Glenn Werner, for an early introduction to science, and my mother, Helen Werner, for providing the musical background that has so often enlightened the evenings.

Above all, the patience and 15, 000 miles of commuting by my husband, Hugh, have made possible the completion of this thesis.

Support for this thesis work was obtained from the following sources: Phelps Dodge Corporation Grant to CIT; NASA PO A-8209-A to Dr. R. P. Sharp, Dr. E. M. Shoemaker and S. W. Kieffer; Geology General Budget; NASA NGL 05 002 105 to Dr. T. J. Ahrens; NASA NGL 05 002 03G; NASA and NSF graduate traineeships.

ABSTRACT

PART I: SHOCK METAMORPHISM OF THE COCONINO SANDSTONE AT METEOR CRATER, ARIZONA

A study of the shocked Coconino sandstone from Meteor Crater, Arizona, was undertaken to examine the role of porosity in the compression of rocks and in the formation of high-pressure phases. A suite of shocked Coconino specimens collected at the crater is divided into five classes, arranged in order of decreasing quartz content. The amounts of coesite, stishovite (measured by quantitative x-ray diffraction) and glass vary systematically with decreasing quartz content. Coesite may comprise one-third by weight of some rocks, whereas the stishovite content does not exceed 1%. The five classes of rocks have distinct petrographic properties, correlated with the presence of regions containing coesite, stishovite or fused silica. Very few occurrences of diaplectic glass are observed, in striking contrast to its abundant occurrence in the non-porous rocks from the Ries Crater.

In the lowest stages of shock metamorphism (Class I), the quartz grains are fractured and the voids in the rock are filled with myriads of small chips derived from neighboring grains. The fracture patterns in the individual quartz grains are controlled by the details of the initial morphology of the colliding grains. In one weakly shocked rock, it was possible to map the general direction of shock passage by recording the apparent direction of collision of individual grains. The principal mechanism of energy deposition by a shock wave in a porous material is the reverberation of shock and rarefaction waves through

grains due to collisions with other grains. A one-dimensional model of the impact process can predict the average pressure, volume and temperature of the rock if no phase changes occur, but cannot predict the observed nonuniformity of energy deposition.

In all rocks shocked to higher pressure than was necessary to close the voids, high-pressure and/or high-temperature phases are present. Locally high pressures enduring for microseconds and high temperatures enduring for milliseconds controlled the phases of SiO_2 which formed in the rock. Collapsing pore walls became local hot spots into which initial deposition of energy was focused. Microcrystalline coesite in Class II rocks occurs in symplektic regions on quartz grain boundaries which were regions of initial stress and energy concentration, or in sheared zones within the grains. The occurrence and morphology of the coesite-rich regions can be explained only if the transformation from quartz to coesite proceeds slowly in the shock wave. In Class III rocks, microcrystalline coesite occurs in opaque regions which surround nearly isotropic cores of cryptocrystalline coesite. The cores are interpreted to be the products of the inversion of stishovite (or a glass with Si in six-fold coordination) which initially formed in the shock front in regions of grains shocked to pressures near 300 kb. Stishovite is preserved only in the opaque regions, which are believed to have been cooler than the cores.

In Class IV rocks, vesicular glass occurs in core regions surrounded by opaque regions containing coesite. The relation of the glass to the coesite and quartz suggests that the glass was formed by inversion

of stishovite formed above 350 kb upon release to lower pressure.

Class V rocks are composed almost entirely of glass with vesicles uniformly distributed in the glass. These vesicles were probably formed by exsolution of water that had been dissolved in melted SiO_2 during passage of the shock.

PART II: THE SPECIFIC HEAT OF SOLIDS OF GEOPHYSICAL INTEREST

The use of Debye temperatures as parameters for material properties of silicate minerals is becoming common in geophysical studies. The elastic Debye temperature, θ_{el}, alone is, in general, insufficient to specify properties which depend on lattice vibrations. Two effects ignored by the Debye model are shown to be important: high frequency lattice vibrations and the dispersion relation. As an alternative to the Debye model, a somewhat more complicated model is proposed that is still reasonably convenient and is able to account much better than the Debye model does for the variation of specific heat of complex substances over a wide range of temperature. This model is designated the acoustic-optic model. The parameters required for this model are the maximum lattice vibrational frequency, the elastic Debye temperature, and the specific heat at a single (say, room) temperature. Adequate approximations to these parameters are generally available.

To consider heat capacity data and compare the data with either the Debye or acoustic-optic model, the calorimetric Debye temperature, $\theta_{CAL}(T)$, is considered. $\theta_{CAL}(t)$ is the value of Debye temperature

that will reproduce the specific heat at constant volume at the temperature T. For silicates, a large increase at high temperatures in $\theta_{CAL}(T)$ above the elastic Debye temperature is due to the presence of oscillators between the elastic Debye frequency and a maximum vibrational frequency which exceeds the Debye frequency. Vibrations of these oscillators cause the spectral lines observed at infrared frequencies. The proposed model takes these oscillators into account by adding a constant-valued continuum to an assumed low-frequency Debye spectrum.

In all substances considered, $\theta_{CAL}(T)$ at low temperatures initially decreases to values below θ_{el}. This decrease is believed due to the dispersion relation, i.e., the nonlinear relation between the wave vector and the frequency.

In two substances of geophysical interest, NaCl and MgO, the maximum observed vibrational frequency is depressed below the observed elastic Debye frequency as a consequence of the dispersion relation. The acoustic-optic model is capable of predicting the specific heat of these two substances and the acoustic-optic spectra which result from application of the model to these substances describe qualitatively the spectra that result from the dispersion relation.

The nonlinearity of the dispersion relation dominates the specific heat behavior of NaCl and MgO and influences the low temperature behavior of all silicates with varying degrees of severity. The effect of the dispersion relation can be ignored for some silicates if specific heats only at high temperatures ($T > 100°K$) are considered. The effect cannot be ignored in the case of rutile or stishovite.

TABLE OF CONTENTS

PART I: SHOCK METAMORPHISM OF THE COCONINO SANDSTONE AT METEOR CRATER, ARIZONA

	Page
I. INTRODUCTION	2
II. METEOR CRATER AND THE COCONINO SANDSTONE	
GENERAL FEATURES OF METEOR CRATER	5
THE COCONINO SANDSTONE	7
Mineralogy	10
Shape of grains	14
Grain size distribution	16
Fabric	16
Pores	18
III. SHOCKED COCONINO SANDSTONE	25
THE OCCURRENCE OF SHOCKED COCONINO	29
CLASSIFICATION OF THE SHOCKED ROCKS	30
DESCRIPTION OF THE SHOCKED ROCKS	34
Type Ia rocks	35
Type Ib rocks	35
Type II rocks	45
Type III rocks	56
Type IV rocks	71
Type V rocks	82
IV. INTERPRETATION: PROPAGATION OF A SHOCK WAVE THROUGH GRANULAR QUARTZ	86
THE SHOCK WAVE AT METEOR CRATER	88
STRUCTURE OF THE SHOCK FRONT IN GRANULAR QUARTZ	91
ELASTIC MODEL FOR STRESS IN SAND GRAINS DURING IMPACT	111
GENERAL MODEL OF PORE CLOSURE, TRANSIENT STRESS AND TEMPERATURE DISTRIBUTIONS	118
EXPERIMENTAL DATA ON SHOCKED COCONINO SANDSTONE	120

TABLE OF CONTENTS (cont.) Page

SHOCK METAMORPHISM OF THE COCONINO SANDSTONE

Interpretation of Type I rocks 126

A missing rock? 127

Interpretation of Type II rocks 128

Type III rocks 130

Type IV and V rocks 137

V. CONCLUSIONS 141

Appendices

A. THE PROCEDURE FOR EXTRACTION OF STISHOVITE AND COESITE FROM SHOCKED SANDSTONE 146

B. QUANTITATIVE X-RAY DIFFRACTION 148

C. WAVE PROPAGATION IN A ONE-DIMENSIONAL MEDIUM: A DESCRIPTION OF THE COMPUTER CODE FOR SHOCK CALCULATIONS 168

D. EQUATIONS OF STATE OF QUARTZ AND STISHOVITE 172

E. CALCULATION OF SHOCK TEMPERATURES 176

F. RADIATION AND CONDUCTION FROM A LOCALIZED HEAT SOURCE 181

References 186

PART II: THE SPECIFIC HEATS OF SOLIDS OF GEOPHYSICAL INTEREST 192

I. INTRODUCTION 193

II. TEMPERATURE DEPENDENCE OF THE SPECIFIC HEAT OF COMPLEX SUBSTANCES

DEBYE MODEL 195

ACTUAL HEAT CAPACITIES IN RELATION TO THE DEBYE MODEL 197

ELASTIC DEBYE TEMPERATURE 200

TABLE OF CONTENTS (cont.)

	Page
CAUSES OF THE NON-DEBYE BEHAVIOR OF SILICATES	203
THE DISCRETE-FREQUENCY SPECTROSCOPIC MODEL	205
III. THE ACOUSTIC-OPTIC MODEL	207
ASYMPTOTIC BEHAVIOR	210
IV. APPLICATION TO MINERALS OF GEOPHYSICAL INTEREST	211
GENERAL FEATURES OF THE RESULTS	214
MINERALS WITH TAILED SPECTRA	216
Quartz	216
Coesite	217
Microcline, Albite	218
Jadeite, Diopside	218
Forsterite	219
Spinel	219
MINERALS WITH COMPRESSED SPECTRA	220
Halite	220
Periclase	221
CAUSE OF THE LOW-TEMPERATURE THERMAL BEHAVIOR	222
MINERALS WITH HYBRID SPECTRA	224
Rutile	225
Stishovite	226
V. SUMMARY	228
Tables	230
Figure Captions	234
Figures	238
References	249

PART I

SHOCK METAMORPHISM OF THE COCONINO SANDSTONE AT METEOR CRATER, ARIZONA

I. INTRODUCTION

This study of the shocked Coconino sandstone from Meteor Crater, Arizona, was undertaken to investigate the processes of shock wave propagation through a porous, granular medium. Previous studies of shock effects in single crystals or of shock effects in individual minerals in rocks have led to recognition of distinctive mineralogic criteria diagnostic of the passage of a shock wave. The role of porosity in the compression of the rock and in the formation of high-pressure phases, however, has not been previously considered.

The study of shock processes in porous media is important because nearly all known terrestrial and suspected planetary erosion processes act to fragment and disintegrate planetary surfaces, and, for this reason, a large proportion of impact events produce shock waves that traverse porous, granular materials. In order to interpret the record of impact on a planetary surface and to clearly differentiate the record of impact from the record of volcanism, it is necessary to be able to relate the observed shock-produced changes to the initial state of the surface material and to the pressure, temperature, and duration of the shocks to which it has been subjected.

On the earth, the thick atmosphere partly shields the surface against cosmic intruders, and active tectonic and erosion processes tend to erase the surface record of impact. Thus, a few fairly recent, well-preserved terrestrial craters, such as Meteor Crater, Arizona, provide the primary basis for the interpretation of ancient impact features on this and other planets.

Meteor Crater, Arizona, has been an important locality for the study of impact crater structure and high-pressure phases of SiO_2. Shoemaker (1960) described in detail the structure and stratigraphy of the crater; these field studies led to a description of the sequence of events that occurred during the formation of the crater. Coesite (Chao, Shoemaker and Madsen, 1960) and stishovite (Chao, Fahey, Littler and Milton, 1962) were first identified as naturally occurring minerals at Meteor Crater. It serves as the world's most convenient known source of these minerals. Naturally occurring shocked samples of the Coconino sandstone are readily available at Meteor Crater. These samples, which have been subjected to a range of shock pressure and temperature histories and to variable conditions of cooling, represent a broad range of final states that result from a meteorite impact.

The Coconino sandstone from Meteor Crater was selected for this study because it is composed almost entirely of quartz, the only mineral for which sufficient data exist to allow an interpretation of the complex behavior which results from shock loading. At low pressures and temperatures, the primary effect of the shock is to close up pore spaces; the rock is comminuted and the fractured grains are rearranged into a close-packed texture. At higher pressures and temperatures, the primary effect of the shock is to transform the quartz into the high-pressure phases, stishovite and coesite, and to amorphous silica. This thesis examines the process of void closure, the effect of the voids on the shock wave, and the formation of the high-pressure phases.

Samples of unshocked Coconino sandstone collected at Meteor Crater are described in Chapter II. Shocked sandstone collected at the crater was studied in thin section, by quantitative X-ray diffraction and by Debye-Scherrer photography (Chapter III). These observations are interpreted in terms of a model for the propagation of a shock wave through granular quartz in Chapter IV.

II. METEOR CRATER AND THE COCONINO SANDSTONE

GENERAL FEATURES OF METEOR CRATER

Meteor Crater, Arizona, lies in the Canyon Diablo region of the southern part of the Colorado Plateau (Fig. 1). The crater was formed in sedimentary rocks ranging from Permian to Triassic age. The lowest unit in the crater is the Coconino sandstone of Permian age, which is a light colored, cross-bedded quartzose sandstone. Overlying the Coconino is the Toroweap Formation, a 9-foot thick unit of medium- to coarse-grained dolomitic sandstone and sandy dolomite. The Kaibab Formation of Permian age consists of 270 feet of dolomite and dolomitic sandstone overlying the Toroweap Formation. About 30 to 50 feet of buff to reddish-brown sandstone and dark reddish-brown siltstone of the Triassic Moenkopi Formation unconformably overlie the Kaibab.

The rim of Meteor Crater is blanketed by ejecta thrown out from the crater and by Pleistocene and Recent alluvium (Shoemaker, 1960 and 1963). The stratigraphy of the units associated with the crater is shown in Figure 1. The ejecta (the throwout) consist of angular fragments ranging in size from microns to more than 100 feet in diameter. Bedrock stratigraphy is preserved, inverted, in the ejecta.

The lower walls and floor of the crater are covered by Pleistocene and Recent deposits. Talus along the crater walls grades into alluvium on the floor of the crater, which, in turn, interfingers with a series of lake beds about 100 feet thick. These deposits overlie a layer of thoroughly mixed debris (the fallout) composed of fragments

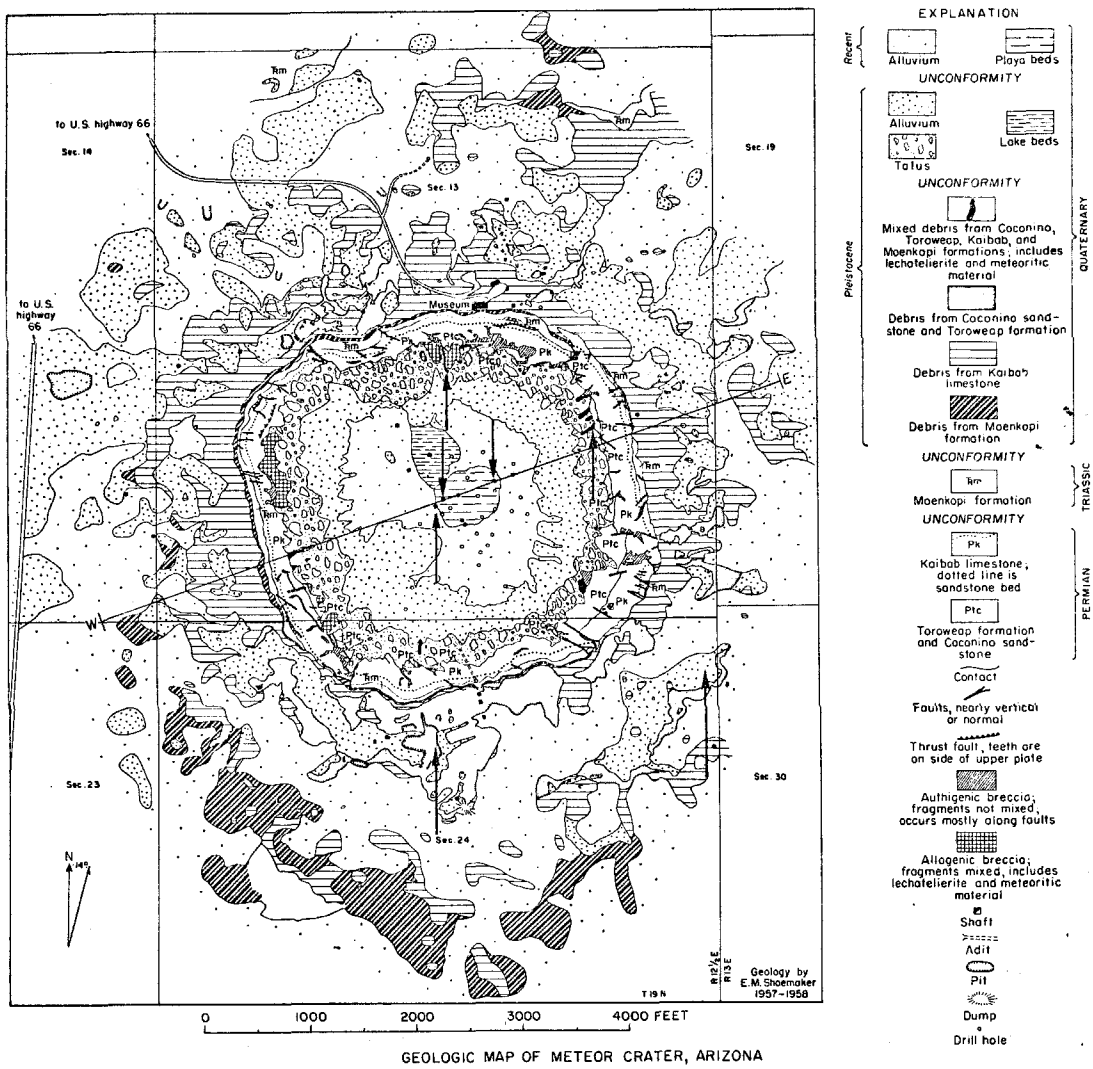

GEOLOGIC MAP OF METEOR CRATER, ARIZONA

Fig. 1. Geologic map of Meteor Crater, Arizona (courtesy of E. M. Shoemaker) showing structure of the crater and the location of sample collecting areas (arrows).

of Coconino sandstone, Toroweap Formation, Kaibab Formation, Moenkopi Formation and meteoritic fragments. The mixed debris unit is exposed in the walls of the crater and has been penetrated by several shafts in the bottom of the crater. This unit is slightly graded from coarse at the base to fine at the top and was attributed by Shoemaker to fallout of debris thrown to great height. The mixed debris on the floor of the crater is underlain by a breccia composed of fragments of Coconino sandstone. Along the walls the mixed debris is underlain by a breccia composed of Kaibab fragments.

THE COCONINO SANDSTONE

The Coconino sandstone (named by Darton, 1910) underlies 32, 000 square miles of the Colorado Plateau province in northern Arizona, extending south to the Mogollon cliffs and west to the Grand Wash cliffs. It is exposed as far east as Holbrook, Arizona, and thins to apparent extinction near the Utah border, but probably grades laterally into the DeChelly Formation in the north (Baker and Reeside, 1929). At Meteor Crater, outcrops of Coconino are best seen on the southeast wall, but small outcrops also occur on the north, east and south walls. The nearest exposures outside of the crater are 15 miles to the south. The Coconino sandstone attains a maximum thickness of 1000 feet at its southern extent and is estimated to be 700-800 feet thick in the vicinity of Meteor Crater (Shoemaker, 1963). Only the uppermost 300 feet are exposed at the crater.

The first good description of the Coconino, as exposed in the Grand Canyon, was given by Noble (1914). He described wedge-shaped units of pale buff, fine-grained, cross-bedded sandstone whose distinctive features are the huge scale of the cross-bedding, the massive appearance and the uniform fineness of the component grains of sand. The wedge-shaped units often exceed 40 feet in length and 100 feet in height. The dip of the bedding planes in a southern direction is commonly 15° to 25°, or exceptionally 30°.

The origin and mode of transport of the Coconino sands has long been and still is a subject of controversy. There is general agreement that the beds dip to the south (Reiche, 1938) implying that the direction of transport was from the north. Schuchert (1918), on the basis of ripple marks found in the Coconino in one place at the Hermit Trail, Grand Canyon, postulated that the sands comprised a large delta of continental deposits laid down under constant, but probably local, sheets of fresh water. Read (1950, 1961) interpreted the Coconino sands as beach and nearshore deposits. Reiche (1938), McKee (1934), Matthes (quoted by McKee, 1934) and Opdyke and Runcorn (1960) cite the preservation of vertebrate tracks on the cross-bedded surfaces, wind ripples and the great extent of the homogeneous quartz sand as evidence that the sand was transported and deposited by wind.

The upper part of the Coconino as exposed at Meteor Crater is a pale-buff, white or pink (Fig. 2a) cross-bedded sandstone. The coarseness of the cross-bedding causes a massive appearance in outcrop. Occasional fragments of Coconino show red stains on weathered surfaces. Small amounts of hematite in some hand specimens give the rock a

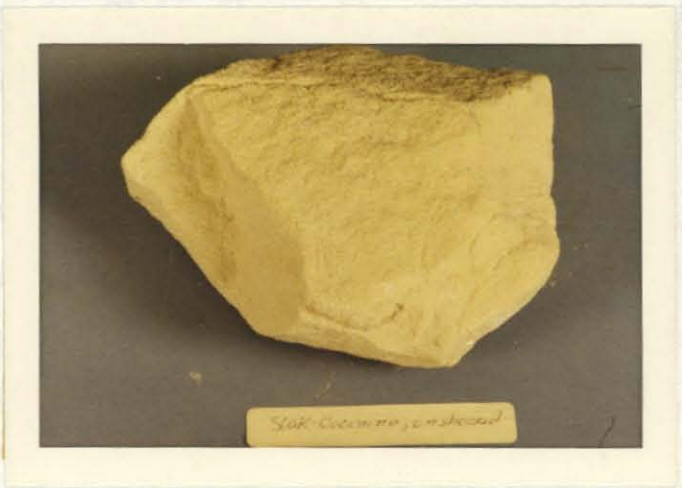

Fig. 2a. Typical massive unshocked Coconino sandstone (from the silica pits on the rim of Meteor Crater). Scale is same as shown in (b).

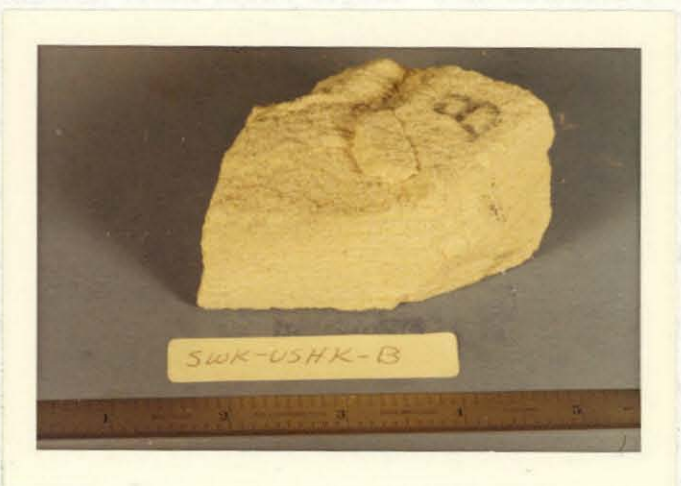

Fig. 2b. Typical laminated sandstone. Thin parallel laminations show on the vertical surface.

uniform pink color; concretions of goethite have been found up to several centimeters in diameter (E.M. Shoemaker, personal communication).

It is convenient to recognize two types of sandstone in hand specimen and thin section: (1) massive sandstone, in which laminations if they exist, are several centimeters thick, and (2) laminated sandstone, containing parallel laminations which are 0.5 to 2.0 mm thick (Figs. 2b, 3b). The widest variations of mineralogy, porosity and grain size are associated with these laminations. In places, hematite is concentrated in some laminations, giving the rock a slightly striped appearance. Many hand specimens part easily along the laminations.

Mineralogy. The Coconino sandstone at Meteor Crater is composed of over 95% quartz. Eight thin sections were examined of rocks selected to represent the range in type of sandstone which occurs at Meteor Crater, and the following analysis is based on four rocks selected for detailed examination from these eight. The detrital constituents of the Coconino observed in these thin sections include quartz, feldspars, heavy minerals and rock fragments. Chlorite, sericite and clay minerals, recrystallized quartz, hematite and goethite occur as secondary minerals.

The detrital quartz grains, which constitute the bulk of the Coconino sandstone, are rather well-rounded, and generally slightly elliptical (Figs. 3, 4). The boundaries of the detrital grains against secondary overgrowths of quartz (discussed below) are revealed by a layer of dust and vesicles (Fig. 4). A number of quartz grains contain linear or curvilinear chains of fluid inclusions resembling Boehm lamellae. A few quartz grains contain long needle-like crystals (which may be rutile) or euhedral red-brown crystals less than 10 microns

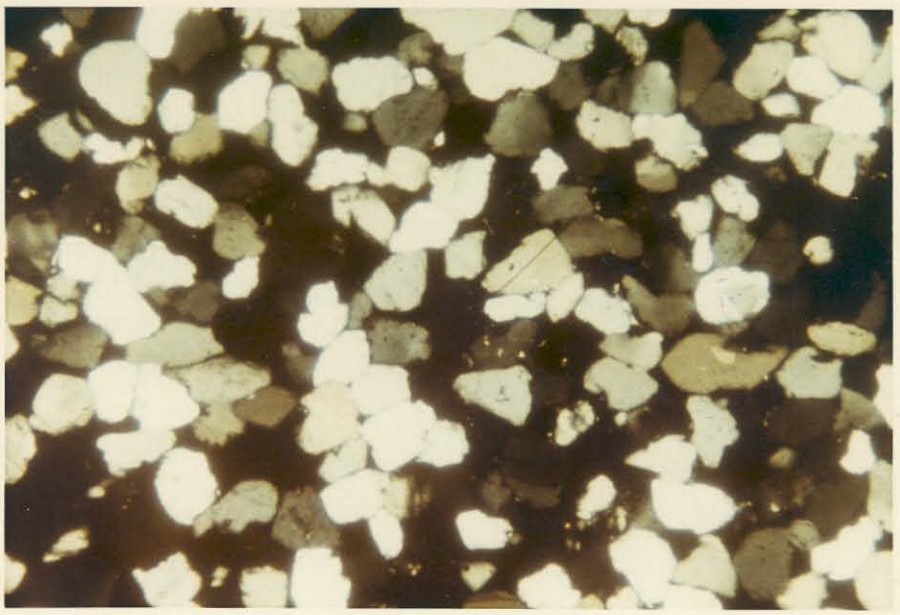

(a)

Fig. 3a. Massive Coconino sandstone (x 65, crossed nicols) showing mosaic-like texture. The grains have a shape parameter of 1.6 and are approximately 0.2 mm in longest dimension. Grains are free of wavy extinction.

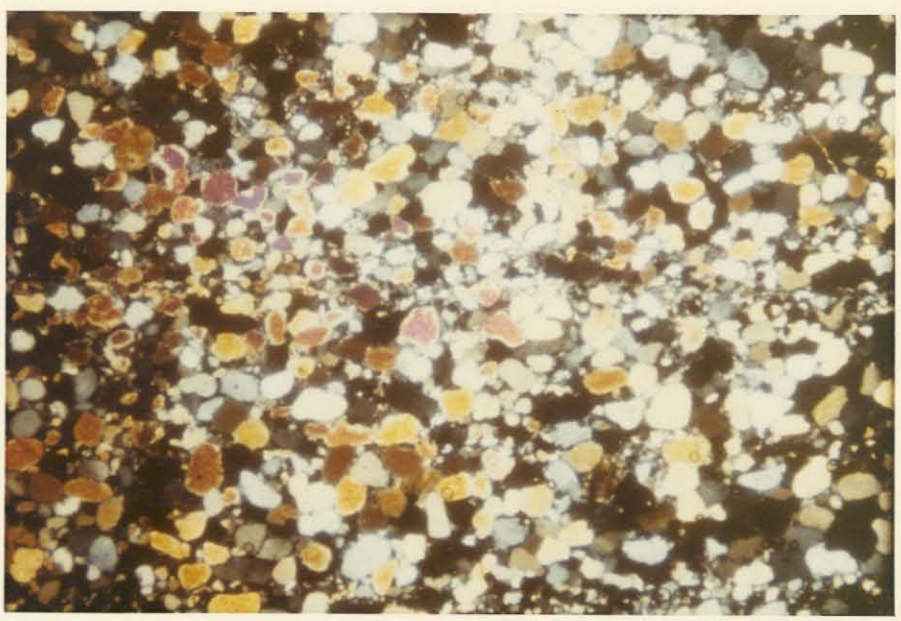

(b)

Fig. 3b. Bimodal size distribution in laminated sandstone (x 65, crossed nicols). Four thin (~3 mm) laminations traverse from left to right, and contain smaller grains of quartz than the thicker laminations.

Fig. 4. Quartz grains in unshocked Coconino. The boundaries between detrital grains and secondary quartz are marked by lines of inclusions, e.g., on the large white grain in the center right. The boundary between the two white grains at the lower left is typical of the irregular boundary formed by solution of the original detrital quartz (x 400, crossed nicols).

across, which were not identified. The quartz grains are free of irregular or wavy extinction under crossed nicols.

Rock fragments and feldspars constitute the second most-abundant detrital material in the Coconino. The rock fragments are quartzites, siltstones and some crystalline fragments which are composed of many minerals of differing indices and colors. These crystalline fragments are assumed to be igneous or metamorphic. The feldspars, microcline, adularia, perthite, are relatively unaltered. The unaltered condition led McKee (1934) to suggest a short distance of travel from the source area to the area of deposition and/or an arid climate during deposition.

The heavy detrital minerals in the Meteor Crater Coconino were not studied in detail; McKee (1934) reported zircon, green tourmaline, blue tourmaline, leucoxene, monazite, rutile, magnetite, anatase, in total amount less than 0.2% in the Coconino in northern Arizona.

The most prominent secondary mineral is recrystallized quartz. The recrystallized quartz is the primary cement in the Coconino at Meteor Crater. This is in agreement with the observations of McKee (1934) on Coconino samples from a much larger area of the Colorado Plateau.

Chlorite (nonpleochroic, colorless) is a minor cementing material and appears in different occurrences to have been deposited both before and after the recrystallized quartz. It is most easily recognized by its radiating crystal habit and very faint yellow color.

In some specimens, the boundaries of a few quartz grains (and, occasionally, thin planar regions within a grain) have been replaced by sericite. Sericite and clays occur as fine-grained aggregates.

Hematite and goethite occur as opaque flakes interspersed between the quartz grains or as sub-millimeter concretions.

The results of point count analyses of four representative rocks are shown in Table 1. Detrital and recrystallized quartz were not differentiated in these analyses. These counts are believed to be typical of the mineralogy, even of the highly laminated specimens, since the laminations are due primarily to grain size differences; small amounts of hematite may be concentrated in some of the laminations. The quartz content exceeds 95%, except in the laminated rock. Although chlorite, feldspars and the detrital rock fragments occur in such minor amounts that they can have little influence on the general nature of a shock wave traversing the material, it is important to be able to recognize the minor constituents when they occur in shocked rocks so that they are not misinterpreted as shock features. In particular, the detrital quartzite fragments are strikingly like fractured quartz grains in the weakly shocked rocks.

Shape of grains. The detrital grains of the Coconino are well rounded (about 0.7 - 0.8 on the scale of W.C. Krumbein, 1941, for estimating visual roundness). Including the secondary overgrowths, the grains are generally slightly elliptical in shape and may have angular boundaries. The shape of the grains was characterized by the ratio of two perpendicular diameters, one of which was the longest grain

TABLE 1

Mineralogy of the Coconino Sandstone

Sample:	EMS-Coco (massive)		Rock 15 (massive)		Rock D (massive)		Rock A (laminated)	
Mineral	% of area in thin sect.	% of area of solids	% of area in thin sect.	% of area of solids	% of area in thin sect.	% of area of solids	% of area in thin sect.	% of area of solids
Quartz	81.0*	98.2	81.1	96.8	87.0	95.6	84.5	91.0
Rock Fragments	0.3	0.4	0.8	0.9	0.7	0.8	1.5	1.6
Feldspars	0.1	0.1	0.3	0.3	0.7	0.8	---	---
Heavy Minerals	minor**	minor	---	---	0.3	0.3	2.0	2.1
Chlorite	0.5	0.6	1.6	1.9	1.3	1.4	1.0	1.1
Sericite; Clay	0.6	0.7	---	---	1.0	1.1	4.0	4.2
Hematite; Geothite	minor	minor	---	---	minor	minor	minor	minor
Voids	17.5		16.2		9.0		7.0	
TOTAL	100.0	100.0	100.0	100.0	100.0	100.0	100.0	100.0
Total no. of counts:	1010		319		308		200	

*Estimated error on quartz content is less than 2%, on all others less than 1%.

**Mineral was detectable in thin section but did not fall under cross hairs for point counting.

dimension. Measurements of this ratio $d_{MAX}/d_{\perp}$ (Fig. 5a) obtained in traverses of a typical massive specimen yield a mean value, $\bar{x}$, of 1.5 with a standard deviation, s, of 0.5. The mode of the shape parameter curve in Fig. 5a is between 1.0 and 1.4. A somewhat wider variation of grain shapes is observed in the laminated rocks.

Grain size distribution. In a typical specimen of "massive" sandstone, the longest dimension of the grains in thin section was found to range from 0.088 mm to 3.90 mm with a mean value of 0.19 mm (Fig. 5b). The size-frequency distribution is unimodal with the mode between 0.250 and 0.177 mm (2.0 and 2.5 φ units).

Laminated sandstones typically show a bimodal size distribution with modes at longest grain diameters of about 0.1 mm and 0.2 mm.

Texture. Solution and recrystallization of original detrital grains have generally altered original grain boundaries. The recrystallized grains are subhedral to euhedral in outline. Secondary quartz is in optical continuity with detrital grains (Fig. 4). Planar crystal faces are present on the secondary quartz along the walls of voids. Occasionally, intersecting crystal faces form a staircase structure with as many as five "steps" visible. In other places, secondary quartz completely fills the space between two grains. The cement joins smoothly with the rounded surfaces of detrital grains, giving contacts which, in thin section, are slightly curved to linear. In places, the secondary quartz overgrowth is more than 0.15 mm thick, occasionally

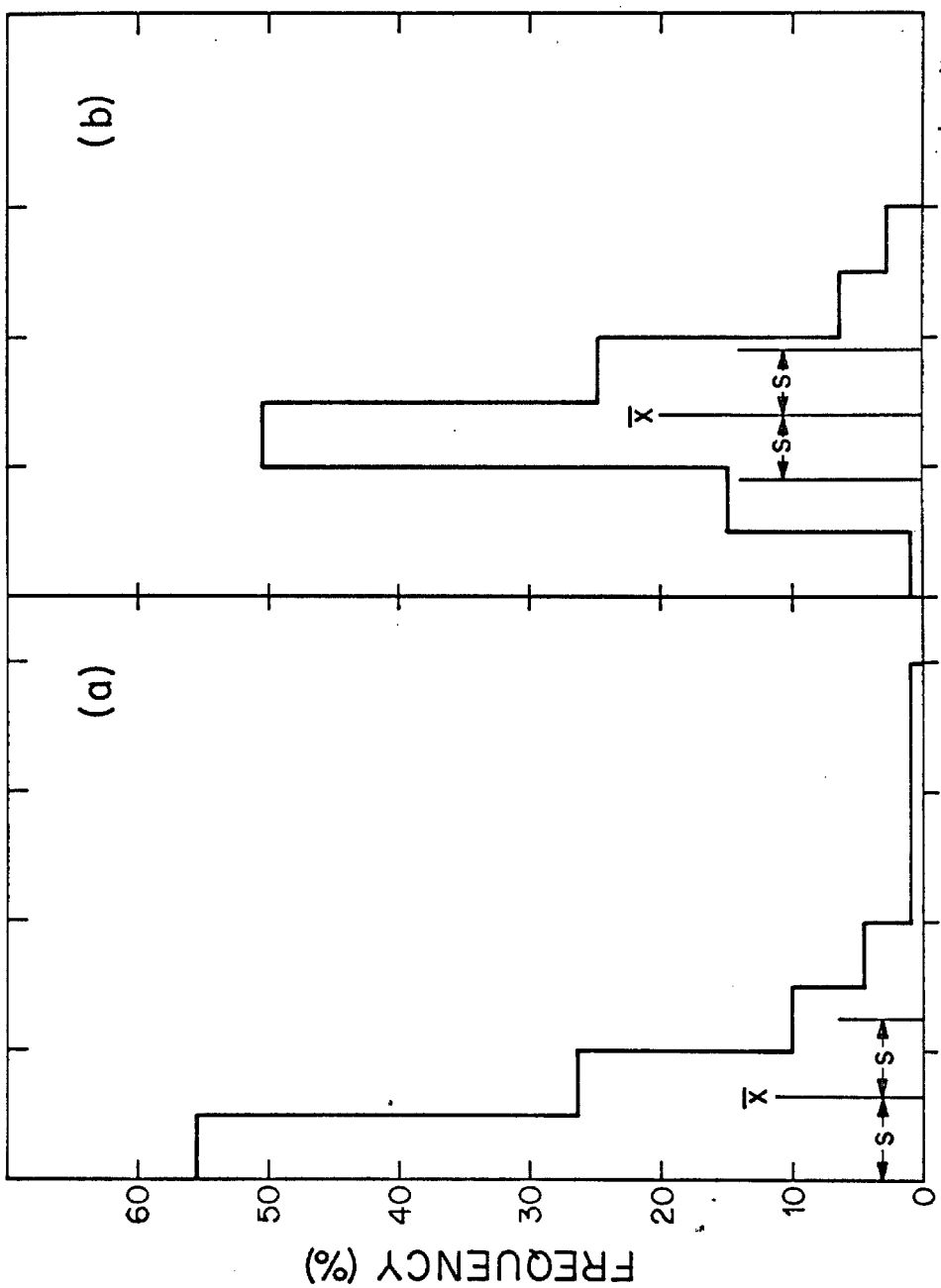

Fig. 5. Frequency distribution of (a) the grain shape parameter $d_{MAX}/d_{\perp}$ and (b) longest grain dimension in massive unshocked Coconino.

exceeding the thickness of the overgrown detrital grain. In one case, an overgrowth was observed to be partially replaced by sericite.

Grains from which some detrital quartz was dissolved show microstylolitic penetration of the sand grains in regions where the solution of the quartz occurred (Fig. 4). Undissolved parts of the detrital grains have irregular shapes and irregular, interpenetrating contacts with other grains. These features are illustrated in Fig. 4. Solution contacts are the most irregular of the quartz grain boundaries and are not common.

In massive specimens, no orientation of the overgrown grains was observed. In bedded specimens, slight alignment of the long axes of detrital grains parallel to the bedding is preserved in the overgrown grains. In general, the overgrowth is thin compared to the grain dimensions.

Pores. The ratio of pore space to grain space in thin sections of three typical massive rocks taken from the rim is 0.18, 0.16, and 0.09. The porosity of the laminated rocks is considerably less, generally less than 10%. Variation in porosity on both a large scale and small scale (locally within a hand specimen or thin section) has a significant effect on the nature of the shock wave passing through the material (see Chapter IV). The porosity varies over distances on the order of millimeters as seen in Fig. 6 in which the pores vary in size from a fraction of a millimeter to nearly 3 millimeters across. To measure the distribution of distances of closure under shock compression, traverses

Fig. 6. Nonuniform pore distribution and irregular structure in massive, unshocked sandstone (x 65, plane polarized light). Pores are darker areas with small bubbles in the impregnating fluid.

were made across a typical thin section of massive sandstone, and the diameter of each pore encountered was measured in the direction of the traverse. The pore closure distances, as measured in this way, range from the limit of resolution (0.005 mm) to nearly 0.4 mm (Fig. 7a). The mean closure distance is 0.04 mm (φ = 4.44) with a standard deviation of 1.36 φ units.

The distance across grains to the edges of pores was measured in traverses of a thin section of typical massive sandstone. The mean distance of separation of the pores is equal to the mean grain diameter of the quartz grains, 0.19 mm (Fig. 7b). Separations up to one millimeter are common; occasionally larger separations are observed. Separations of less than 0.044 mm were observed but not counted.

One way to characterize a pore that is applicable both before and after it has been collapsed by shock is by the number of grain junctions on its wall (Fig. 8). Pore walls are defined as boundaries between quartz grains and void space in the rock. A grain junction is defined as any place on the pore wall where two or more grains are in contact or are within a few hundredths of a millimeter of each other. For example, there are ten junctions associated with the pore in the sketch. Traverses of a thin section of massive Coconino showed that on the average 48 pores (greater than 40 μ) exist per centimeter. As shown in the histogram in Fig. 9b, most of these pores have 3-9 junctions on their walls. Pores were observed which had as many as 18 junctions. The number of junctions is related, to a first approximation, to the length of the longest pore dimension (Figure 9a). The considerable

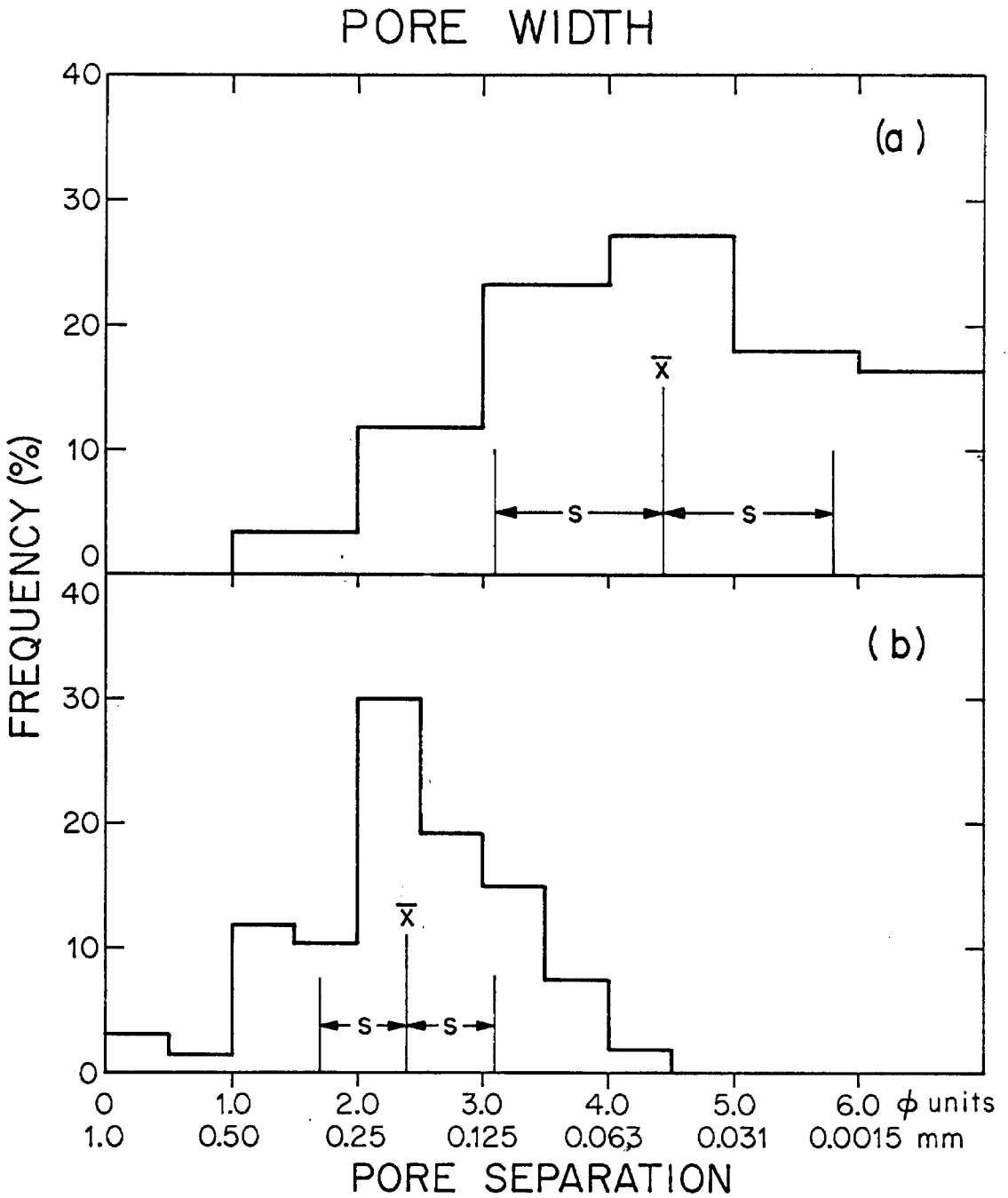

Fig. 7. Frequency distribution of (a) pore closure distances (width) in traverses of a thin section, and (b) distances across grains between pore walls in massive sandstone.

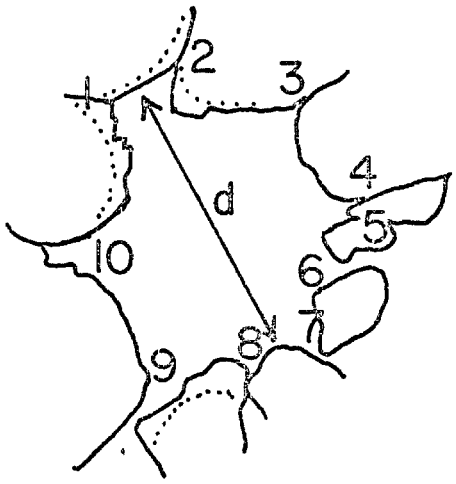

Fig. 8. Sketch of typical equant pore showing effect of grain packing and shapes on pore structure. Small dots represent vesicles between detrital quartz grains and secondary overgrowths.

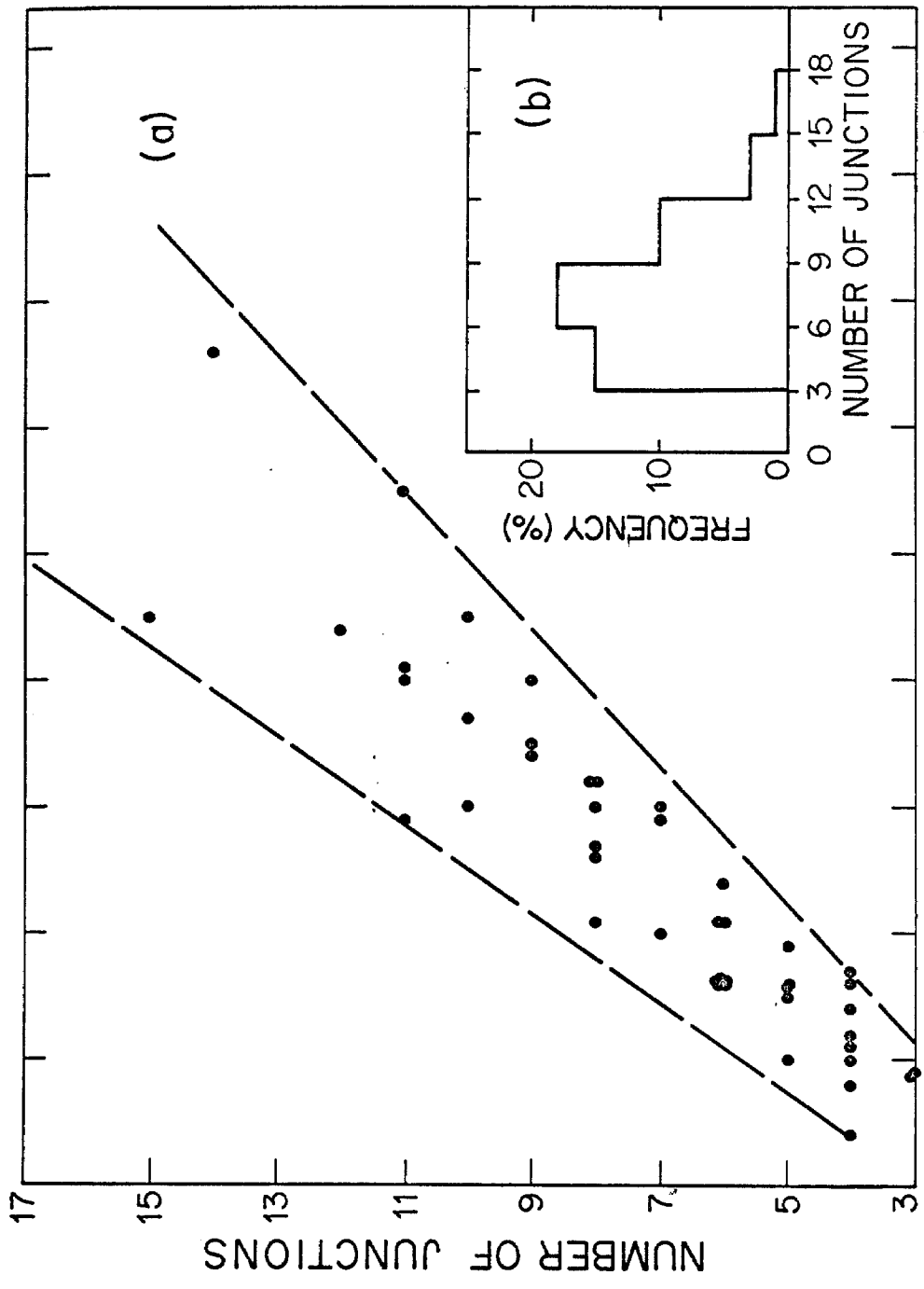

Fig. 9. (a) Relation between longest dimension of a pore and number of junctions on its wall. (b) Frequency distribution of number of junctions on encountered pores per cm in traverses of thin section.

scatter of the data in this figure reflects the fact that the pores -- especially the larger pores -- are very irregular in shape, allowing the fitting of different numbers of grains around the walls.

In detail, the pore shapes are extremely complex and irregular (Figs. 6, 8); in some places, small channels connect the major pores. For purposes of discussion of shock propagation, it is probably adequate to consider only the major pores and to characterize pore shapes without consideration of channels less than a few hundredths of a millimeter in width.

The pores are generally elongate, but the smaller pores may be equant. The shape of the pores is controlled by (1) the packing of the grains, and (2) irregularities on the surfaces of the grains themselves. The latter effect is minor, except for the sets of intersecting crystal faces on the secondary quartz, which form sharp corners in the pore wall. Thus, the three most frequent shapes of grain surfaces observed on a pore wall are (1) rounded (parts of approximately spherical or elliptical grains), (2) planar (recrystallized quartz faces), and (3) angular (intersecting crystal faces). Rounded surfaces are the most commonly occurring type.

III. SHOCKED COCONINO SANDSTONE

Shock metamorphosed Coconino sandstone was first recognized at Meteor Crater by Barringer (1905), Tilghman (1905) and Fairchild (1906). These early investigators recognized three types of shocked sandstone. One variety consists of crushed and pulverized sandstone; the most extreme example of crushing is a fine quartz powder, "white as snow", consisting of minute fragments of sharp, angular quartz.

"Variety A" of the shock metamorphosed sandstone was described by Barringer (1905, 1909) as having a higher density than the original sandstone and a slaty structure at varying angles to the original rock lamination. Merrill (1907, 1908) in a microscopic study of these rocks recognized an extinction pattern in the quartz grains, which he suggested resulted from pressure on the grains while in a plastic condition. He also observed "small, colorless, interstitial areas showing by ordinary light a fibrous structure, but which are, for the most part completely isotropic between crossed nicols, and which the chemical analysis suggests may be opal" (Merrill, 1908, p. 475). He recognized a "marked rhombohedral cleavage" of quartz in these rocks; later studies by Bunch and Cohen (1964) suggested that the texture of these cleavages was sufficiently different from the texture of quartz deformed by other geologic processes to serve as an indicator of an impact event.

"Variety B" of the shock metamorphosed sandstone, as defined by the early explorers at Meteor Crater, has a very cellular, pumiceous structure. The density is so low that it will float on water. Under the

microscope it was recognized to be composed mostly of amorphous silica, lechatelierite, with scattered particles of crystalline quartz. Fairchild (1906) suggested that there was sufficient water, perhaps in the joints of the strata, to effect aqueo-igneous fusion. Rogers (1928) observed numerous minute bubbles in thin sections of the Variety B glass, and suggested that moisture originally present was converted to steam and was in part responsible for the vesicles.

Rogers (1928) recognized in the Variety B rocks silica glass which retained the structure of the sandstone from which it was formed and which he called "paramorphs of lechatelierite after quartz". Chao (1967) and von Engelhardt and Stöffer (1968) have recognized glass with the same property and refer to it as diaplectic or thetamorphic glass.

Coesite (Chao, Shoemaker and Madsen, 1960) and stishovite (Chao, Fahey and Littler, 1962) were first discovered as naturally occurring minerals at Meteor Crater in the Type A rocks and as a minor constituent in the Type B rocks. The coesite was found in the interstitial areas suggested by Merrill (1908) to be opal. Determinations of the phase boundaries (summarized in Fig. 10) between the phases of SiO_2 revealed that coesite is the stable phase between pressures of approximately 30 kb and 75 kb and stishovite is the stable phase above these pressures.

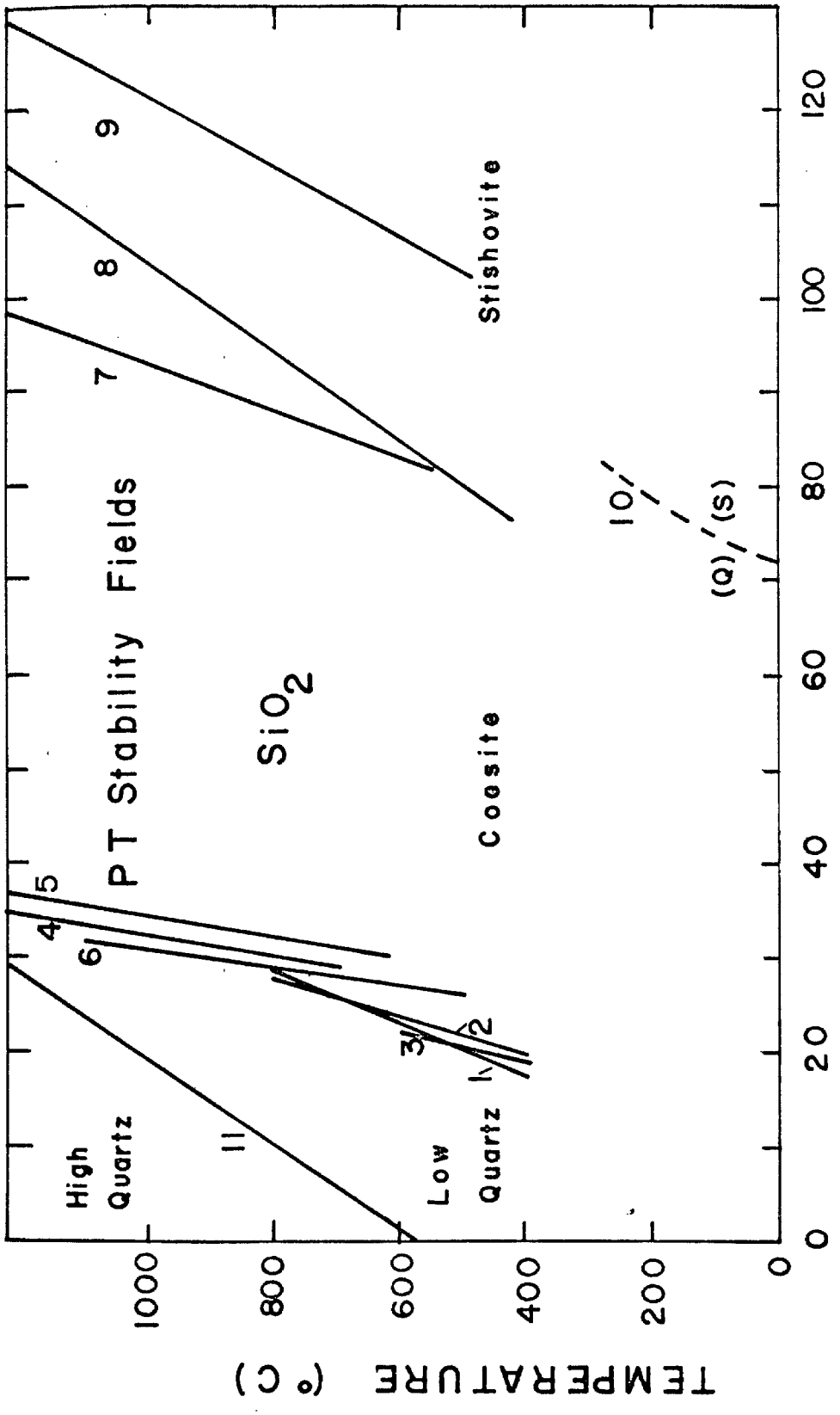

Fig. 10. Pressure-temperature stability fields of SiO_2. References from which the numbered curves were obtained are given in Table 2.

Table 2

Sources of data for SiO_2 stability fields.

Numbers correspond to numbers on curves in Fig. 10.

Number	Transition	Investigators	Reference
1	Quartz to Coesite	Griggs & Kennedy	Am. Jour. Sci., 254, 722, 1956
2	Quartz to Coesite	MacDonald	Am. Jour. Sci., 254, 713, 1956
3	Quartz to Coesite	Dachille & Roy	Z. Krist., 111, 451, 1959
4	Quartz to Coesite	Boyd & England Boyd, Bell, England & Gilbert	J. Geophys. Res., 65, 749, 1960 Carnegie Inst. Wash. Yr. Book, 65, 410, 1966
5	Quartz to Coesite	Takahashi	in High-Pressure Measurement, A. A. Giardini & E. C. Lloyd, eds., p. 240, 1963
6	Quartz to Coesite	Kithara & Kennedy	J. Geophys. Res., 69, 5395, 1964
7	Coesite to Stishovite	Akimoto & Syono	J. Geophys. Res., 74, 1653, 1969
8	Coesite to Stishovite (estimated)	Stishov	Dokl. Akad. Sci. USSR, 148(5) 1186, 1963
9	Coesite to Stishovite	Ostrovsky	Izv. Akad. Sci. USSR, Ser. Geol., #10, 132, 1965 Geol. J., 5, 321, 1967
10	Quartz-to-Stishovite (calculated)	Holm, Kleppa, Westrum	Geochim. et Cosmochim. Acta, 31, 2289, 1967
11	High to low quartz	Cohen & Klement	J. Geophys. Res., 72, 4245, 1967

THE OCCURRENCE OF SHOCKED COCONINO

The distribution of ejecta and shocked Coconino sandstone at Meteor Crater was first described and mapped by Shoemaker (1960). Fragments of shocked Coconino sandstone are found in the Coconino sandstone debris unit, the breccia under the crater floor, the mixed debris unit (fallout), alluvium and lake beds. The walls of the crater mark the approximate boundary at which shocks and rarefactions no longer exceeded the compressive strength of the material. Therefore, bedrock samples of the Coconino show only minor shock effects.

Shocked material from the breccia, mixed debris and lake beds underlying the crater floor is presently accessible in the dumps adjacent to the shafts on the floor of the crater (Fig. 1, center of crater). As the shafts were sunk, material from each of the units was brought up relatively undisturbed and free of mixing with other units and dumped in such a way that material in the dumps may be identified with source units. From these dumps, shocked Coconino was obtained from the breccia, mixed debris and lake beds in the center of the crater.

Each of the units mentioned above has particular types of shocked material in it. The breccia underlying the crater bottom is composed of fractured and crushed Coconino sandstone and includes dispersed fragments containing coesite. Overlying the breccia is the mixed debris unit, which extends sufficiently high on the crater walls to overlie Kaibab breccia and to be exposed by erosion. Samples of shocked Coconino were taken from two exposures of mixed debris (shown in

Fig. 1) on the (approximately) north and east walls of the crater, as well as from the dumps. The mixed debris unit is an especially rich source of shocked sandstone containing coesite and stishovite. Overlying the mixed debris are Pleistocene lake beds. The lowermost Pleistocene lake beds contain abundant fragments of pumiceous shock melted sandstone.

Shocked sandstone may also be obtained outside of the crater. Abundant fragments of shocked sandstone containing coesite and stishovite and pumiceous shock-melted material are found in the alluvium surrounding the crater. They are particularly abundant on the southeast side of the crater (Fig. 1). This alluvium was derived from mixed debris and also from the stratified debris units of the crater rim. The silica pits on the south side of the crater (Fig. 1) are a source of very weakly shocked sandstone from the Coconino sandstone debris unit.

Two trips were made to Meteor Crater to collect samples for these thesis studies. Material was collected from three shaft dumps in the center of the crater, two exposures of mixed debris on the crater walls, the silica pits and an alluvial terrace on the south side of the crater. These locations are shown by arrows in Fig. 1.

CLASSIFICATION OF THE SHOCKED ROCKS

From several hundred pounds of shocked Coconino, forty-eight rocks were selected for thin section examination. From these, sixteen rocks representative of varying degrees of shock metamorphism were

selected for measurement of silica polymorph abundances by X-ray diffraction.

Some of the rocks collected from Pleistocene alluvium contain abundant calcite in fractures and vesicles. This calcite was deposited in the rocks by soil-forming processes during late Pleistocene time (E.M. Shoemaker, personal communication). The calcite is not relevant to the shock history of the rocks and was extracted before measurements of SiO_2 polymorph abundances were made.

The abundances of quartz, coesite and stishovite were determined by techniques of quantitative X-ray diffraction described in Appendix B. Abundances of quartz and coesite were determined with a relative error of less than 10%. The glass content was obtained by subtracting the sum of the quartz, coesite, and stishovite content from 100%. As a 10% relative error in rocks with large quartz content would lead to a very large relative error in the estimate of glass content, quartz abundance in shocked rocks with more than 80% quartz was checked by point count analyses of thin sections of the rocks. The point count abundances agreed within 2% of the values measured by X-ray diffraction. A further indication that the errors are not as large as 10% is that the weight fraction of quartz measured by the X-ray diffraction technique in five unshocked rocks was 95, 97, 99, 101 and 102%. The lower values are within the range of values measured by point counts of unshocked rocks; the higher values suggest that the experimental error is a few per cent.

Calibration curves were established so that stishovite content could be measured. However, stishovite was found to occur in

quantities less than 1% and excessive X-ray diffraction time would have been required to establish variations in the stishovite content at these levels. Stishovite is therefore treated as a minor mineral; efforts were directed only toward detetting its presence in the rocks.

The results of the X-ray diffraction measurements, shown in Fig. 11, provide a convenient basis for classifying the specimens of shocked Coconino. The suite of shocked rocks is divided into five types, arranged in order of decreasing quartz content. Boundaries between the types are chosen approximately halfway between adjacent data points in Fig. 11. The five types are denoted by Roman numerals I, II, III, IV, V and subcategories are denoted by small Arabic letters a and b. These categories are:

Type I Weakly shocked rocks containing no high-pressure phases and 95% or more quartz.

a. With petrographically observable remnant porosity

b. Without petrographically observable remnant porosity

Type II Moderately shocked rocks containing 80 to 95% quartz. These rocks typically have 2 to 5% coesite, 3 to 10% glass, and do not have detectable stishovite.

Type III Moderately shocked rocks containing 45 to 80% quartz. These rocks typically have 18 to 32% coesite, trace amounts of stishovite and 0 to 20% glass.

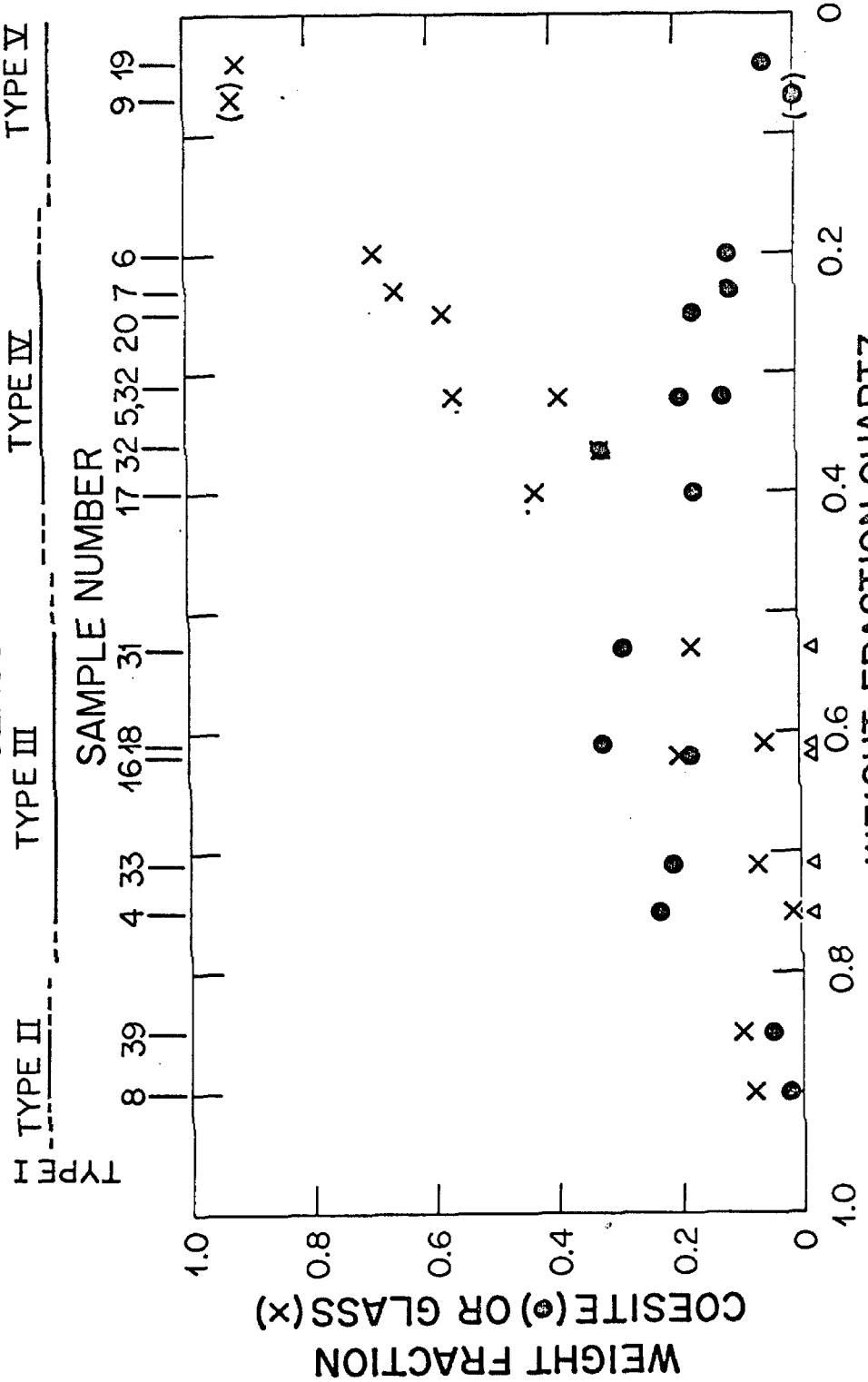

Fig. 11. Abundance of coesite (●) and glass (x) in shocked Coconino sandstone as a function of quartz content. Rocks in which stishovite was detected and estimated to be less that 1% by weight are indicated by a triangle. Limiting quartz contents of 5 classes of rocks are shown on top line. Sample numbers of rocks are shown at top of graph.

Type IV Strongly shocked rocks containing 15 to 45% quartz. These rocks have 10 to 30% coesite, 20 to 75% glass, and no detectable stishovite.

Type V Very strongly shocked rocks which contain 0 to 15% quartz. These rocks may have 0 to 5% coesite, 80 to 100% glass, and have no detectable stishovite.

DESCRIPTION OF THE SHOCKED ROCKS

Thin sections of forty-eight rocks were examined. All rocks required impregnation to render them sufficiently firm to be cut. Thirty-eight rocks were impregnated with epoxy and the thin sections of twenty-eight of these were covered with a cover glass. The remaining ten were left uncovered. Ten rocks were impregnated with Lakeside, and uncovered thin sections were made. The Lakeside impregnation makes grinding of the section more difficult, because the Lakeside softens during grinding, but it provides sections from which small pieces of material can be removed with tweezers for examination by X-ray. All thin sections were nominally 30 μ thick; thin edges frequently occurred and were often convenient places to study the fine structures in the rock. The limit of microscopic resolution was 2 μ.

Type Ia rocks. Samples of Type Ia rocks were collected from the dumps at the shafts in the center of the crater and from the silica pit on the south side of the crater. Four thin sections of these rocks were examined. In general, specimens of weakly shocked rocks with remnant porosity do not differ in macroscopic appearance from unshocked Coconino sandstone (Fig. 12a). They are granular (0.1-0.2 mm average grain size), weakly to moderately cemented, and may be either massive or laminated.

In thin section, these rocks characteristically show less porosity than massive unshocked Coconino (Fig. 12b). The apparent porosity in thin section of one massive Type Ia rock was measured to be 8%, the other 3 were estimated to have less than 5% porosity. The recrystallization features of the quartz and linear chains of vesicles are undisturbed, except in a few places where a grain or bit of cement is fractured (Fig. 12b). The reduction of porosity in Type Ia rocks apparently occurred by slight translation and rotation of individual grains or small groups of grains. Fractures may exist in up to 5% of the grains. Wavy extinction under crossed nicols occurs in less than 5% of the grains.

Type Ib rocks. Type Ib rocks were collected from the mixed debris or breccia in the shaft dumps in the center of the crater. When moist, some of these rocks are nearly indistinguishable from the fines which comprise part of the dumps and can be easily overlooked. When allowed to dry, they become coherent though fragile, fine-grained and friable (Fig. 13a). Other Type Ib rocks, although powdery in texture,

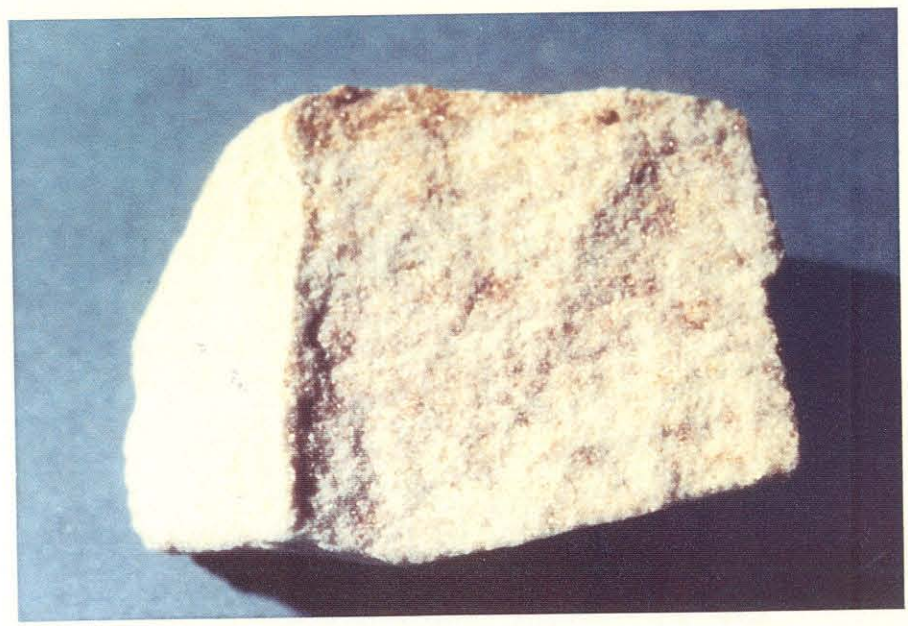

Fig. 12a. Type Ia hand specimen which resembles an unshocked rock. The rock is 5 cm in longest dimension. Undeformed laminations are seen on the front surface; reflections are visible from individual grains.

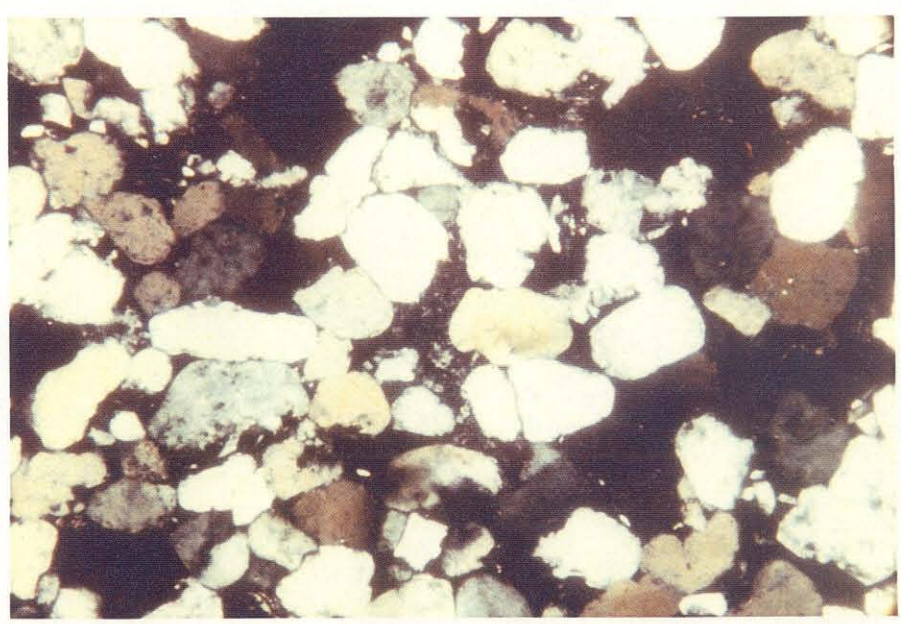

Fig. 12b. Thin section of laminated Type Ia rock (x65, crossed nicols) showing patchy extinction in some of the grains. The grain boundaries are slightly chipped.

Fig. 13a. Typical friable, fine-grained Type Ib hand specimen. The rock is 1-1/2" in longest dimension.

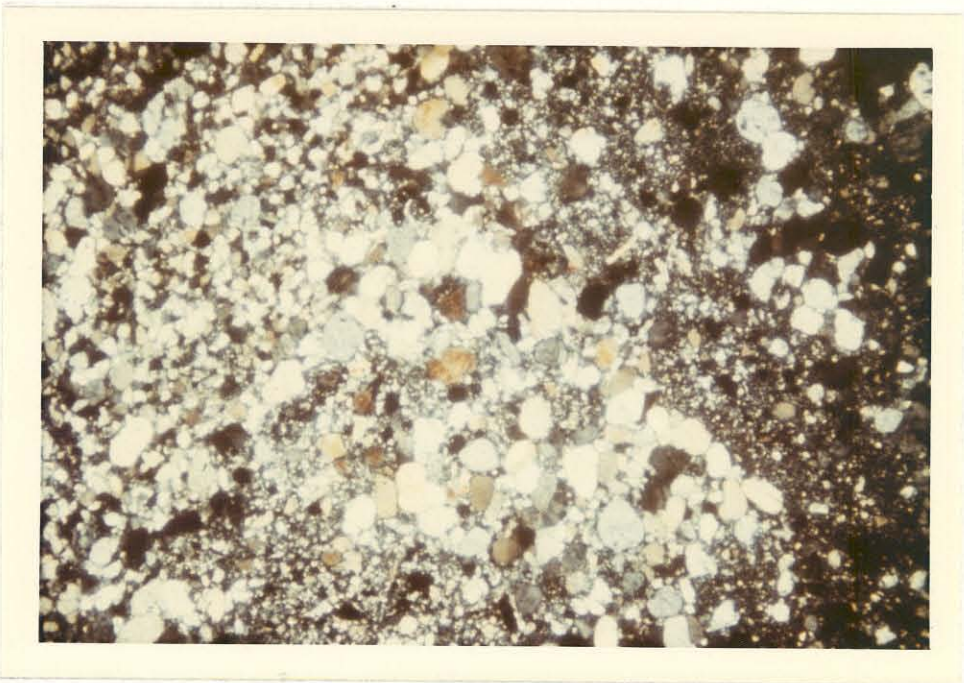

Fig. 13b. Comminution in typical Type Ib rock (x 65, crossed nicols). Comparison of this photomicrograph with Fig. 3 shows reduction of average grain size due to fractures.

retain their coherence when wet. These rocks are snow white in hand specimen. They are generally small; the largest found was $2\frac{1}{2}$" in longest dimension. Undistorted laminations may be seen on some specimens. Individual grains are easily resolved with a hand lens. The rock powder is gritty between the teeth.

Thin sections of five of these rocks were examined. A wide range of grain sizes is observed in all cases (Fig. 13b). In laminated rocks, remnant bedding (with the bimodal size distribution characteristic of the original rock) and fracture within the grains both contribute to the observed wide variation in sizes. In massive rocks, the size of the grains is reduced by fracturing.

Fracturing of grains occurs irregularly throughout the rock. Groups of quartz grains which are relatively unfractured may be set in a large area of tiny quartz shards, many of which are smaller than 5 microns; small nests or pockets of chips may exist between large, relatively unfractured quartz grains. The resolvable chips are tabular in shape; some retain a rounded surface from the original detrital grain. Disoriented shards frequently form nests or pockets between large quartz grains.

In each of the five thin sections examined, over 40% of the fractured quartz grains retain their continuity. In the massive Type Ib rock shown in Fig. 14, in which nearly every quartz grain is fractured, over 75% of the quartz grains retain their continuity, even though most of these grains have 5-10 fractures within the grain outline. Examples of

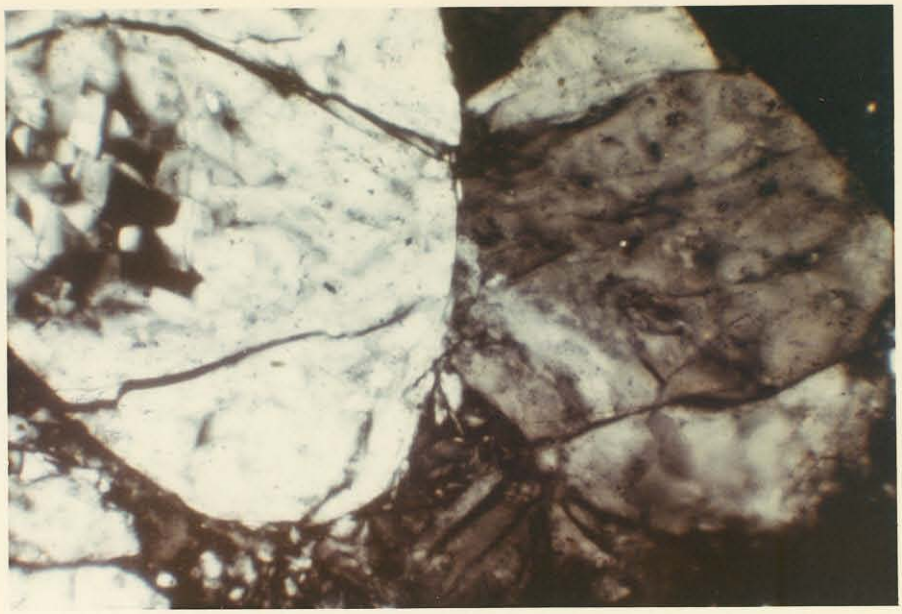

Fig. 14a. Concussion fractures in Type Ib rock in which the fractures and surface of contact are free of fine-grained material. The apparent concussion axis trends from left to right (x265, crossed nicols).

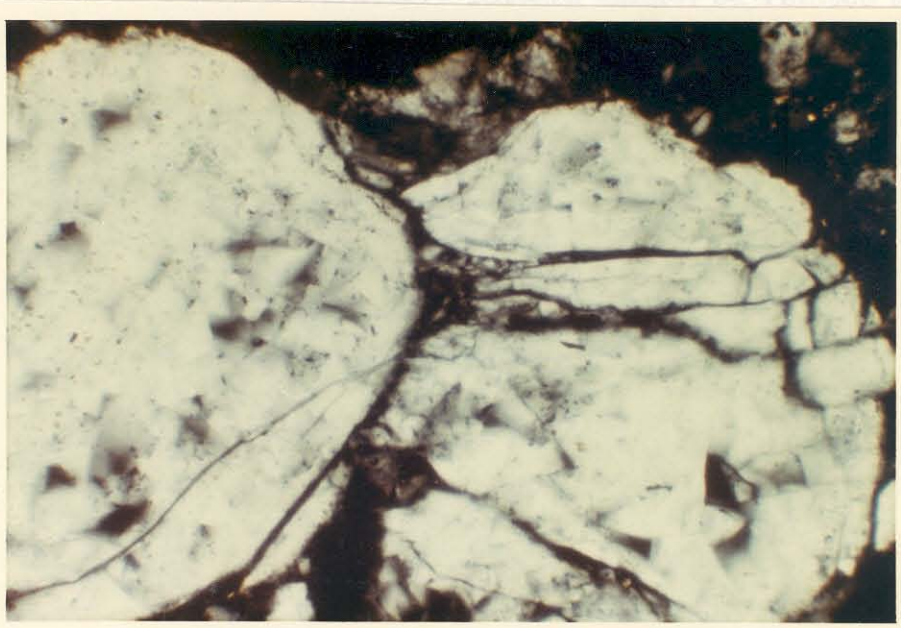

Fig. 14b. Concussion fractures in which small amounts of fine-grained material were forced into the fractures. The apparent concussion axis trends from left to right (x265, crossed nicols).

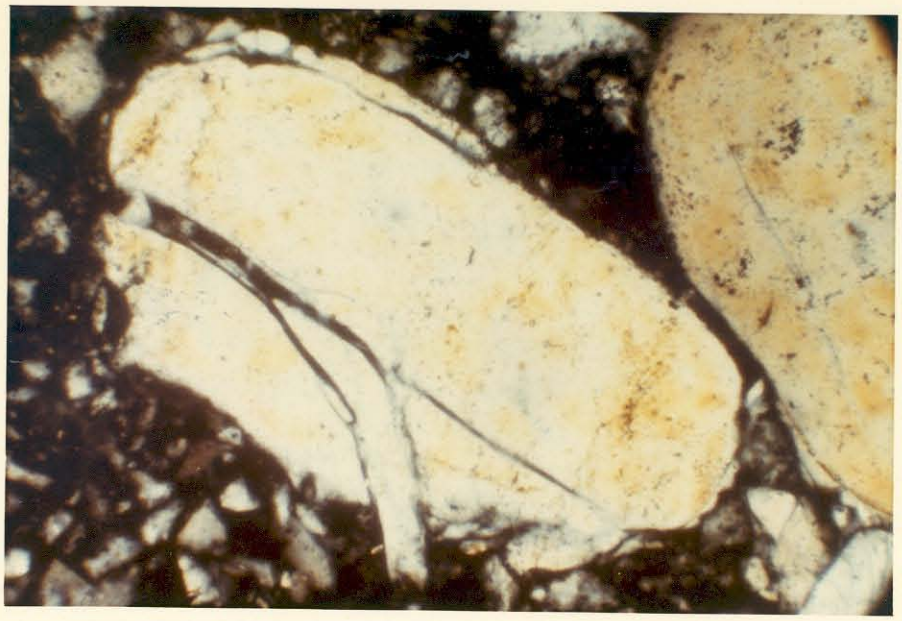

Fig. 14c. A grain in which the fracture pattern cannot be related to an apparent impact direction (x265, crossed nicols).

recognizable grains are shown in Fig. 14a, b, c. The rest of the quartz grains in this rock have been fractured, and the chips have been displaced so that the original grain is no longer recognizable.

Remnant lines of vesicles associated with the boundary between detrital grains and quartz overgrowths are commonly visible, on grains that have been undamaged, on grains which have been fractured, and on rotated chips.

Fractures in the grains which have retained their continuity can generally be related to surfaces of contact with other grains. Extensive networks of radial fractures (Fig. 14a, b) emanate from the contact surface of up to 20% of the grains. Because of their resemblance to fracture systems produced by hypervelocity impact in solid rock, these fracture systems are herein called concussion fractures. The radial fractures and contact surface between the grains may be free of fine-grained shards (Fig. 14a) or may be lined with small amounts of fine-grained material (Fig. 14b). Frequently the regions adjacent to the contact surface are nests of fine-grained chips (Fig. 14b). The fractures in the concussion patterns are partly controlled by the cryst cleavage directions.

Let the line joining the centers of pairs of grains which show concussion fractures be called the apparent concussion axis of these grains. A set of three mutually perpendicular thin sections was made from a moderately laminated Type Ib rock which showed concussion fractures. The orientation of the three thin sections is shown

schematically on the cube in Fig. 15. The directions of the apparent concussion axes were measured in each of the thin sections. The results are shown on the foldout of the cube OABCGDE in Fig. 15, and in the polar plots adjacent to the foldout. Seventy-two apparent concussion axes were measured in thin section 1, thirty-three in section 2 and twenty-seven in section 3. As shown by the polar plots, the axes of sections 1 and 2 are aligned to within ±15° and ±20°, respectively, of the median value.

A concentration of about 10 axes/mm^2 appears desirable to obtain a representative median value of the axial direction in thin section; the assignment of a median direction for sections 3 and 2 may not be statistically significant.

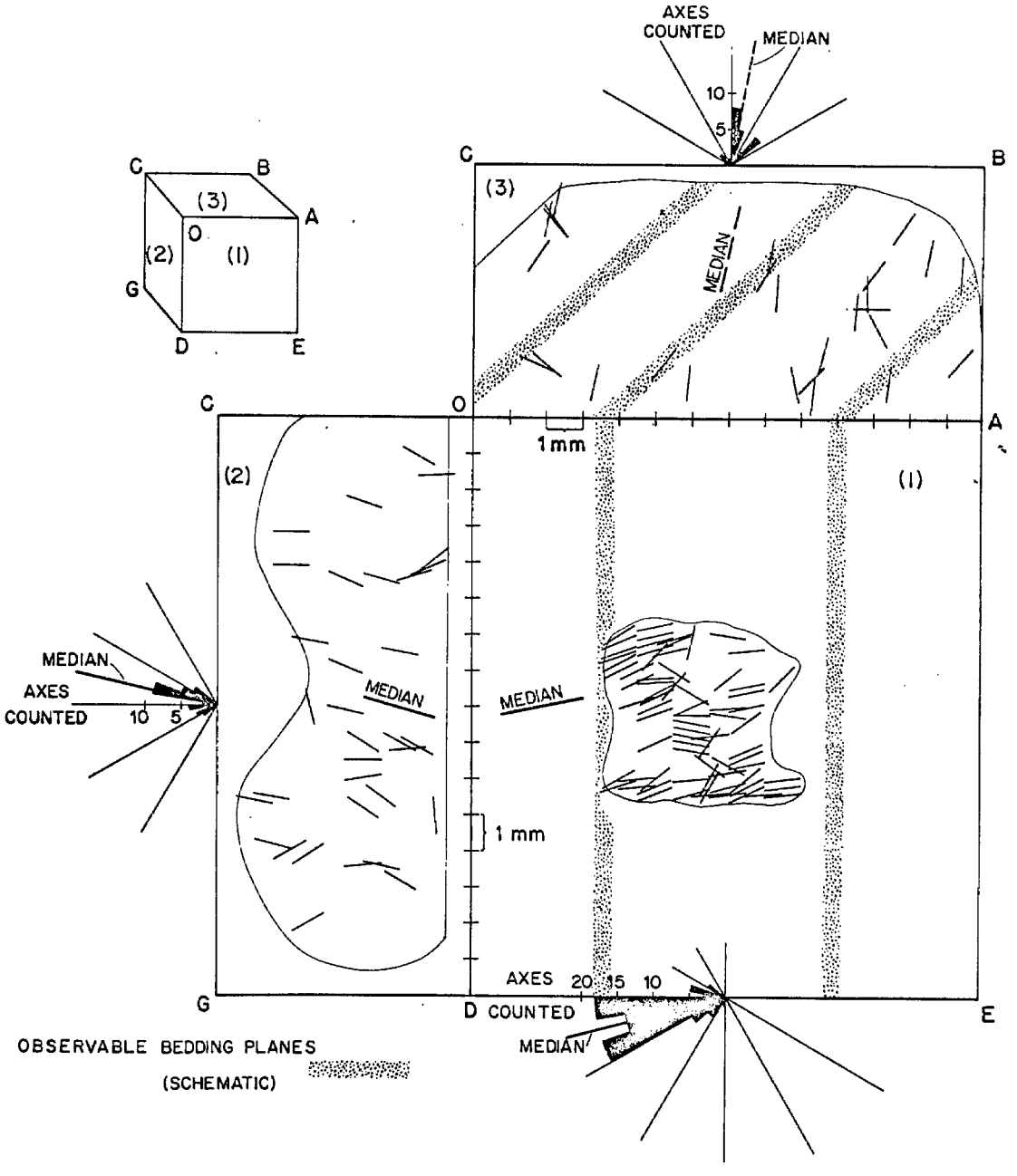

Fig. 15. Cube AODEGCB shows orientation of three orthogonal thin sections from rock #37. Foldout shows orientation of apparent concussion axes in the three thin sections; outlines and relative sizes of thin sections are shown to scale. Polar plots show distribution of axial directions and median direction.

The radial concussion patterns are believed to be tensile fractures formed by the impact of neighboring grains as the shock front initially traversed the material and closed the pore spaces (see p. 111 for further discussion). The median value of the axial direction is believed to be nearly the direction of shock passage through the material. The concussion axes do not provide a vector direction, so the shock may have propagated in either direction along the median.

Type II rocks. The specimens of Type II rocks examined in thin section and by X-ray diffraction were collected from the shaft dumps in the center of the crater and probably came from the mixed debris unit. Similar, but much smaller, fragments are found in the exposures of mixed debris on the crater walls.

In hand specimen, Type II rocks are white. Generally, they are smaller than 2" in longest dimension. They are well-indurated, dense and fine-grained; some grains can be seen with a hand lens. Most Type II rocks are traversed by small parallel partings whose separation does not exceed 0.1 mm (see Fig. 16a). Undeformed laminations are observable on a freshly-sawed surface of one specimen.

In thin section, two different types of areas are observed. Quartz grains, which are approximately the same size as the original grains, cover 80 to 95% of the area of the thin sections. There is no petrographically observable porosity in these rocks, and the quartz grains interlock with one another like pieces of a jigsaw puzzle (Fig. 16b). Lining parts of the boundaries of most of the grains are areas which appear yellow to gold in transmitted light and which scatter obliquely incident light. These regions (5 to about 50 microns wide and up to 0.2 mm in length) are composed of submicron to micron-sized, high-index crystallites of coesite, areas of glass, and quartz, which are generally visible in optical continuity through the regions. A large region such as this is shown in Fig. 17. The minerals, intermixed within microns, appear in a vermicular habit; this suggests the name symplektic regions for these areas. A sketch of a typical large symplektic region is shown in Fig. 19c.

Fig. 16a. Type II hand specimen, 2" in longest dimension. Parallel cleavages are visible on the vertical surface; separation along the cleavages does not exceed 0.1 mm.

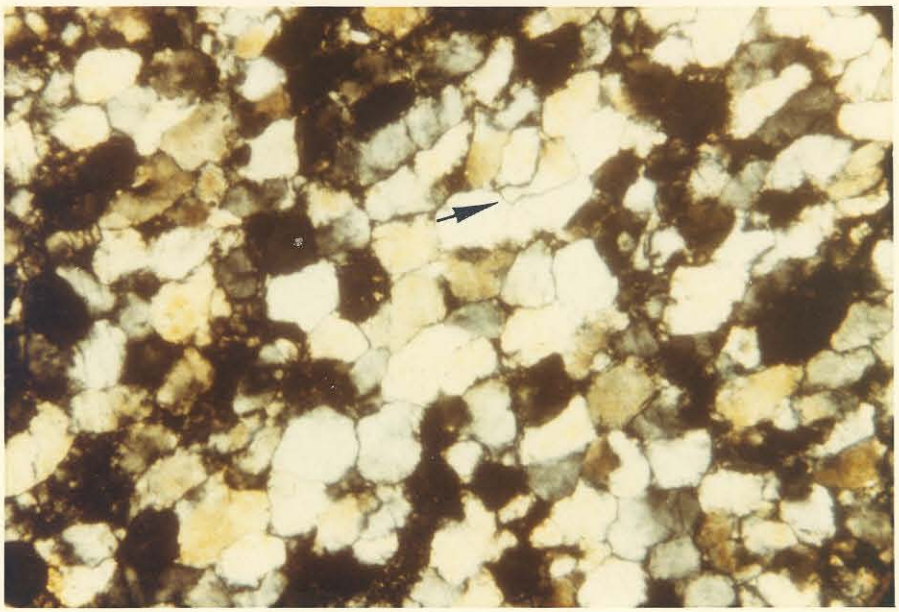

Fig. 16b. Quartz grains in a Type II rock are deformed into interlocking shapes and resemble pieces of a jigsaw puzzle (x 65, crossed nicols). Comparison of this photomicrograph with Fig. 3 shows that the size of the quartz grains is not appreciably reduced.

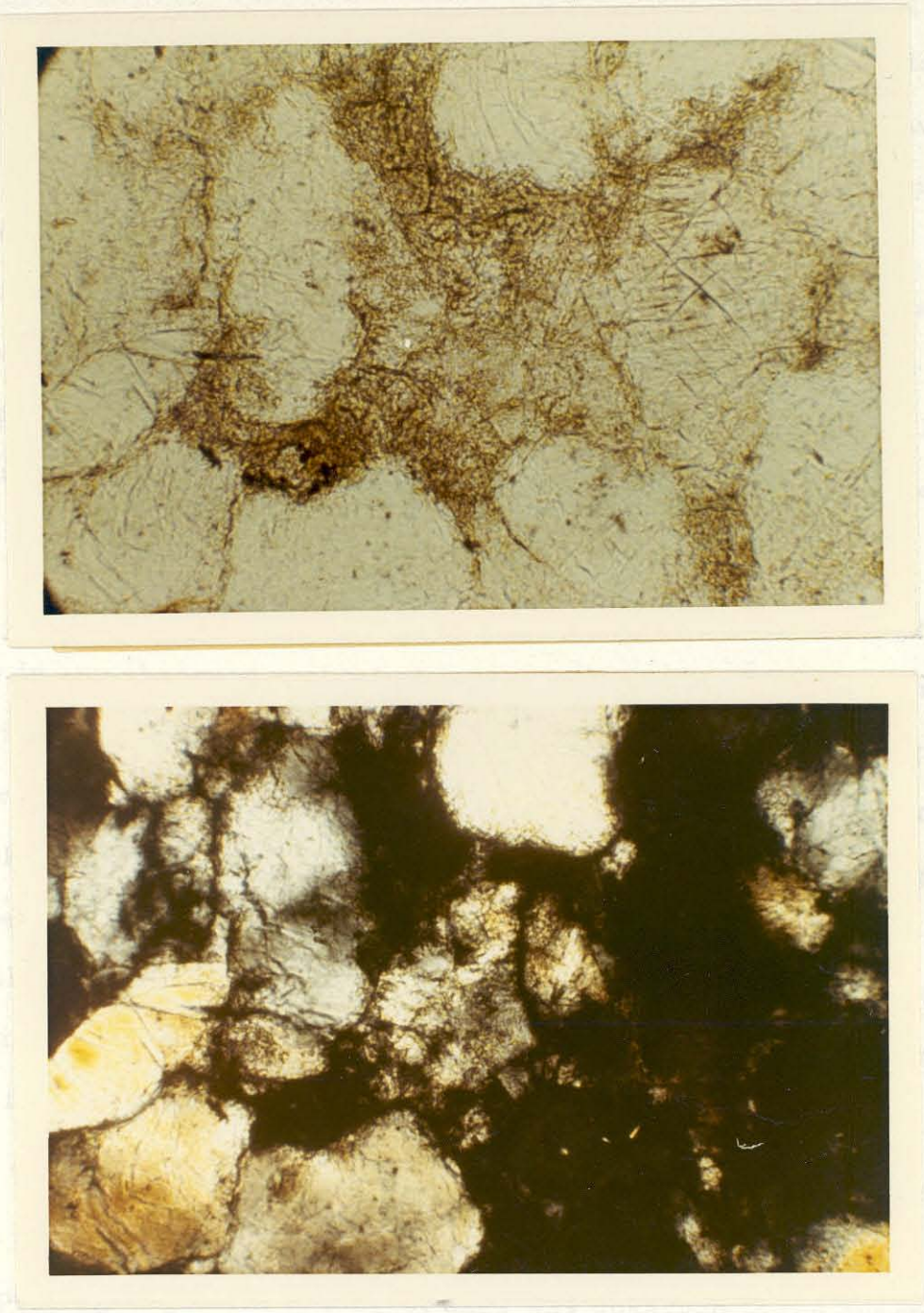

(a)

(b)

Fig. 17. A large symplektic region in the center of photomicrograph (x265) contains quartz (large grains), coesite (small, high-index crystallites visible on edges of quartz grains and giving quartz boundaries diffuse appearance) and some glass. A quartz grain in the center of the symplektic region is not visible in plane polarized light (a), but is visible under crossed nicols (b). Cleavages are visible in the quartz grains.

In contrast to the Type Ib rocks, in which the grain size is reduced from that of the unshocked Coconino by fracturing, the average grain size of the quartz in Type II rocks is similar to the grain size in unshocked rocks (compare Fig. 16b and Fig. 3). In Type II rock #39, for example, the average longest grain dimension is 0.18 mm, as compared to 0.19 mm in a typical, massive unshocked rock; the average area of a grain is 2.2×10^{-2} cm^2, as compared to 2.7×10^{-2} cm^2 in an unshocked rock. The difference is probably within the range of initial grain sizes in the Coconino.

Quartz grain shapes in Type II rocks are different from grain shapes in any observed unshocked rock. Adjacent quartz grains interlock with each other like pieces of a jigsaw puzzle. Many of the grains are irregular, containing gentle reentrants, which are observed in the unshocked rock only on the solution boundaries of detrital quartz grains. An especially irregular grain is indicated in Fig. 16b by an arrow. The grain shape parameter (the ratio of longest to shortest axes) is 1.8, indicating that the grains are somewhat more elongated than the original grains for which the grain shape parameter was 1.5.

The direction of elongation of the quartz axes appears to be aligned in four of the five thin sections of Type II rocks examined. No corresponding alignment of longest axes was observed in the quartz grains in unshocked massive rocks (Fig. 18a). The direction of elongation of quartz grains was measured in rock #39 and was found to be aligned to within ±25° of the median direction (Fig. 18b). The direction of elongation may be tangential to the shock front and might provide

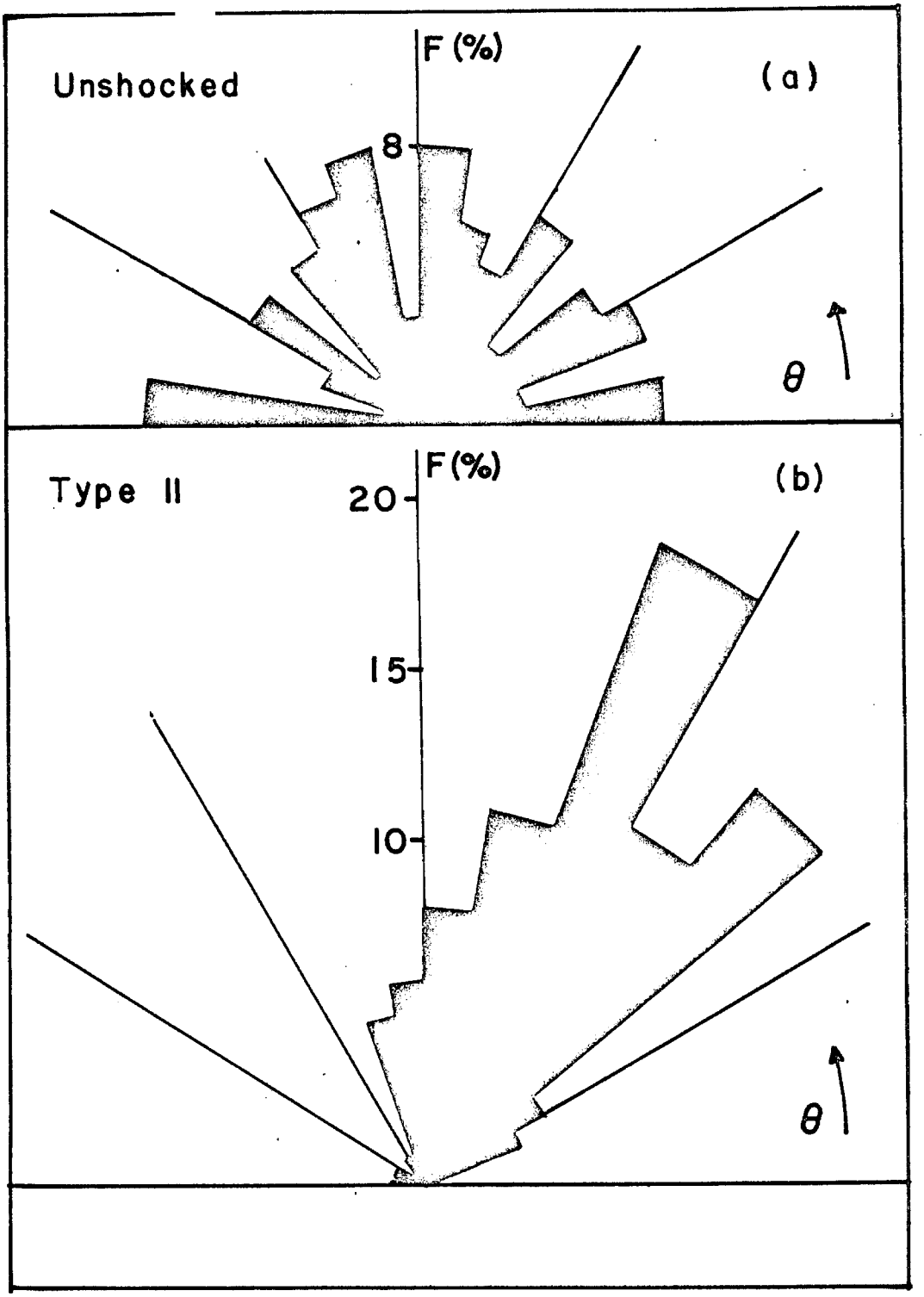

Fig. 18. Direction of alignment of longest axes in unshocked Coconino (a) and in massive Type II rock (b). Directions relative to arbitrary axis.

a useful criterion for determining the direction of shock passage.

Nearly all quartz grains show cataclastic damage. Cleavages and planar features are both observed in Type II rocks. Cleavage is defined as "a separation normal to one or more planes of low crystal indices" (Carter, 1968, p. 454). Planar features are thin planar structures (1-2 μ or less in width), are very closely spaced (2-5 μ apart), occur exclusively in sets of more than five individuals, and occur in multiple sets (Hörz, 1968, p. 247). Over 90% of the grains are permeated with sets of cleavages. Planar features are observed on less than 5% of the grains; some planar features are undoubtedly missed because of lack of resolution of the microscope used in this thesis. The parallel partings, visible in hand specimen, are seen in thin section to fracture quartz grains and separate the two parts by as much as 0.05 mm; the grains are not laterally offset by these partings. The concussion fractures, which were present in the Type Ib rocks, are absent in the quartz grains of moderately shocked rocks. Thus, the alignment of concussion axes, which provides a criterion for detecting direction of shock passage in the Type Ib rocks, cannot be used as an indicator of shock direction in Type II rocks.

The change in shape of the quartz grains without fracturing suggests that extensive plastic deformation of the grains occurred as they were compressed and squeezed into pore spaces. Strain within the grains is indicated by wavy extinction under crossed nicols; most grains show a variation of 10° to 20° in extinction position across the grain. Small (0.01-0.04 mm), local, isotropic areas may be seen

along about 1% of the grain boundaries. The small vesicles marking the boundary between detrital sand grains and crystalline overgrowths are preserved on less than 5% of the grains; plastic deformation at the grain boundaries appears to have eliminated these features.

The symplektic regions are yellow to light brown in transmitted light and scatter obliquely incident light. They are regions containing material of mixed indices and very fine grain size (< 5 microns), intermixed in a vermicular habit with the quartz at the boundaries of the quartz grains. In plain light, the symplektic regions appear to lie between regions of undeformed quartz (Fig. 17a), but when viewed under crossed nicols, the quartz grains are generally visible in optical continuity, through the symplektic regions (Fig. 17a, b, grain in center).

Small pieces of the symplektic regions containing high-index crystallites were selected from crushed Type II rocks placed in an immersion oil. These pieces, when examined by methods of Debye-Scherrer photography, were found to contain coesite and quartz. From this it is inferred that the high-index crystallites are coesite.

Coesite, in the 1 to 2 micron resolvable crystallites (Fig. 17a) seen in the symplektic regions will be referred to as <u>microcrystalline coesite.</u> It was measured in two Type II rocks to be 2 to 5% by weight.

The glass content of two Type II rocks analyzed (#8, #39) is estimated by difference to be 8 and 10% respectively. Since appreciable error in the quartz content could greatly affect this estimated amount of glass, point count analyses were done to verify the quartz content. In these analyses, quartz and symplektic regions were counted, for in general, the coesite cannot be resolved from the glass. Comparison between the point count analyses and X-ray measurements are given below:

	ROCK #8		ROCK #39	
	Point Count	X-Ray	Point Count	X-Ray
Quartz	90%	90%	87%	85%
Symplektic	10%	2% coesite 8% glass	13%	5% coesite 10% glass

The only place in these rocks where small amounts of glass could occur, other than the symplektic regions, are the few small isotropic areas on the boundaries of less than 1% of the quartz grains. These areas could at most account for 1% glass by weight. Therefore, it is inferred that the symplektic regions contain four or five times as much glass as they do coesite. In most of the large symplektic regions, it is possible to identify regions of isotropy 10 to 30 microns in diameter. In a very few instances, it is possible to identify isotropic regions of low index in the symplektic region if they occur adjacent to the quartz grains. In general, though, the glass must occur in unresolved domains to account for the estimated amount of glass.

The symplektic regions vary in shape from 5 micron wide regions which line the contact surface between adjacent quartz grains to 0.1 to 0.2 mm regions that surround and encompass parts of several quartz grains. They are generally elongated tangential to quartz grain boundaries for distances up to 0.2 mm but are only 5 to 50 microns in width perpendicular to the boundary.

The resemblance of the distribution of distances between symplektic regions to pores in unshocked rocks is shown in Fig. 19a. The smaller regions occur at nearly every grain boundary; the larger regions are frequently separated by 10 to 20 grains. The distance between centers of symplektic regions was counted in traverses of a thin section. The smallest regions are difficult to identify with certainty; however, the resemblance between the distribution of pores and symplektic regions, when considered with the occurrence of the symplektic regions only at grain boundaries and the elongation of the regions tangential to the grain boundaries, suggests that the symplektic regions line the walls of collapsed pores.

The symplektic regions in Type II rocks tend to be irregularly oriented, but in rock #8 are aligned and elongated to within ±20° of the mean direction. The quartz grains in this rock do not show a preferential direction of elongation but are of complex shapes and highly strained. No type II rock was found that had both aligned grains and aligned symplektic regions.

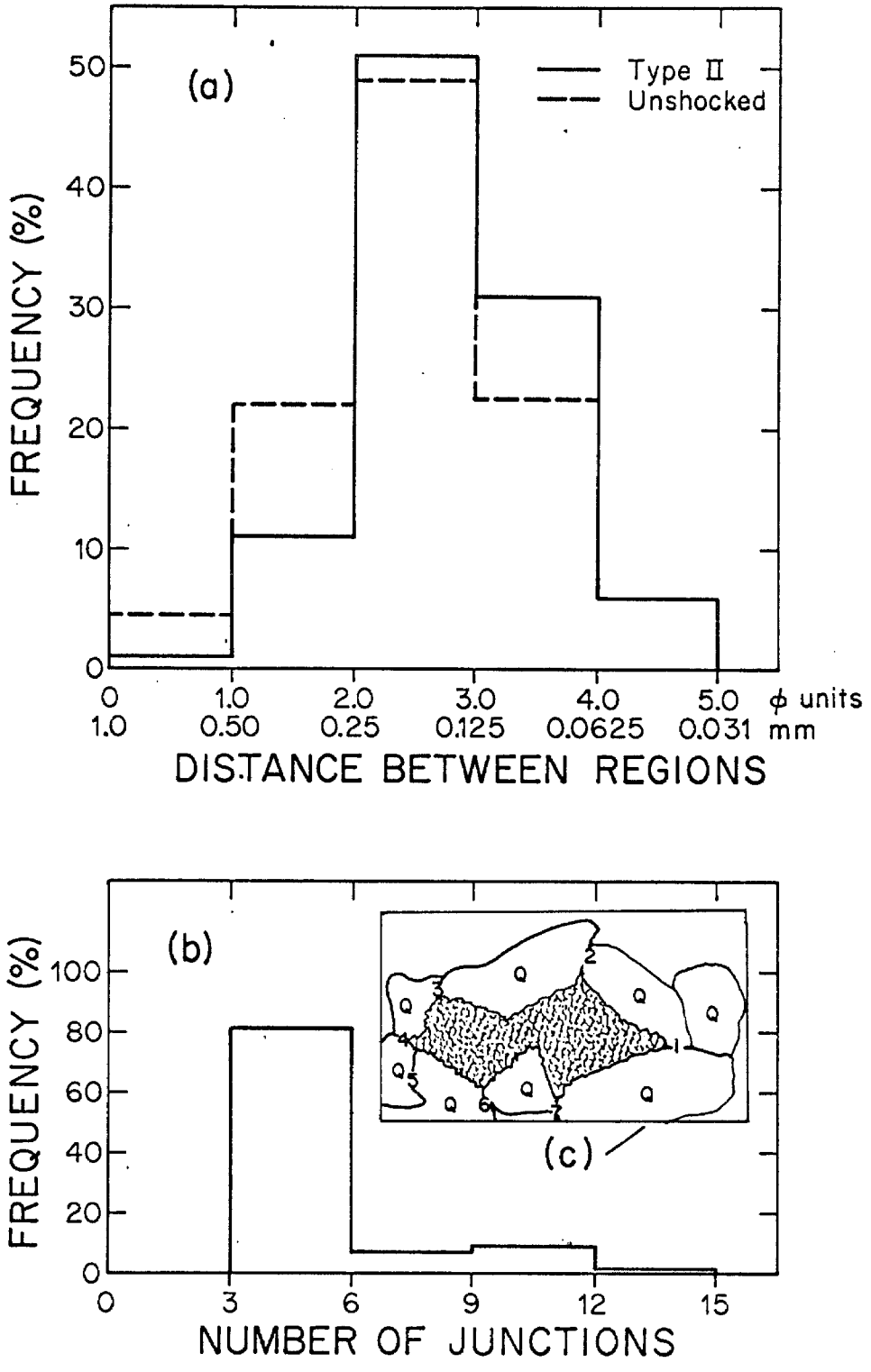

Fig. 19. (a) Frequency distribution of distance between pores in typical massive unshocked rock (dashed line) and between symplektic regions in Type II rock (solid line). (b) Frequency distribution of number of junctions around symplektic regions in Type II rocks. (c) Sketch of symplektic region with seven junctions of quartz grains on its perimeter.

To further compare the symplektic regions with the original pores, the number of junctions between quartz grains surrounding a symplektic region was counted. A sketch of a typical configuration for a large symplektic region is shown in Fig. 19c. The dotted area represents a symplektic region lining parts of the boundaries of the adjacent quartz grains; seven junctions between quartz grains surround this region. Counts on rock #39, shown in Fig. 19b, show that there are fewer symplektic regions than pores with between 6 and 15 junctions. If the symplektic regions are collapsed pores, a possible interpretation of this is that the number of grains along a large pore wall is not conserved during shock.

Type III rocks. Five specimens of Type III rocks examined by X-ray diffraction were collected on the alluvial terrace on the south side of the crater. Two additional rocks, which in thin section had nearly identical petrographic properties, were collected from the shaft dumps and probably came from the mixed debris unit.

The largest sample of Type III rock collected was 5" in length, but larger hand specimens have been found. The surfaces of samples found on the south alluvial terrace are stained a yellow-orange to light brown color (Fig. 20a), but are very white in the interior. These rocks fizz weakly when HCl is applied to the surface; up to 5% $CaCO_3$ was measured. Samples collected from the shaft dumps have only a light tan surface stain and are indistinguishable in hand specimen from Type II rocks. All Type III rocks are well-indurated, dense, fine-grained and gritty between the teeth. Every specimen has a slaty structure, but in some rocks it is much better developed than in others. A Type III rock with a well-developed slaty structure is shown in Fig. 20a. The separation of the plates along parallel partings is less than 0.1 mm, except in rock #16, in which the separation is as great as 2 mm. Most of the $CaCO_3$ occurs in these partings.

Fig. 20a. Hand specimen of a typical Type III rock with well-developed slaty cleavage. Parallel partings which give the slaty appearance in this rock do not exceed 0.01 mm in open width. The rock is light brown on the surface but white in the interior. Longest dimension is 5.5 cm.

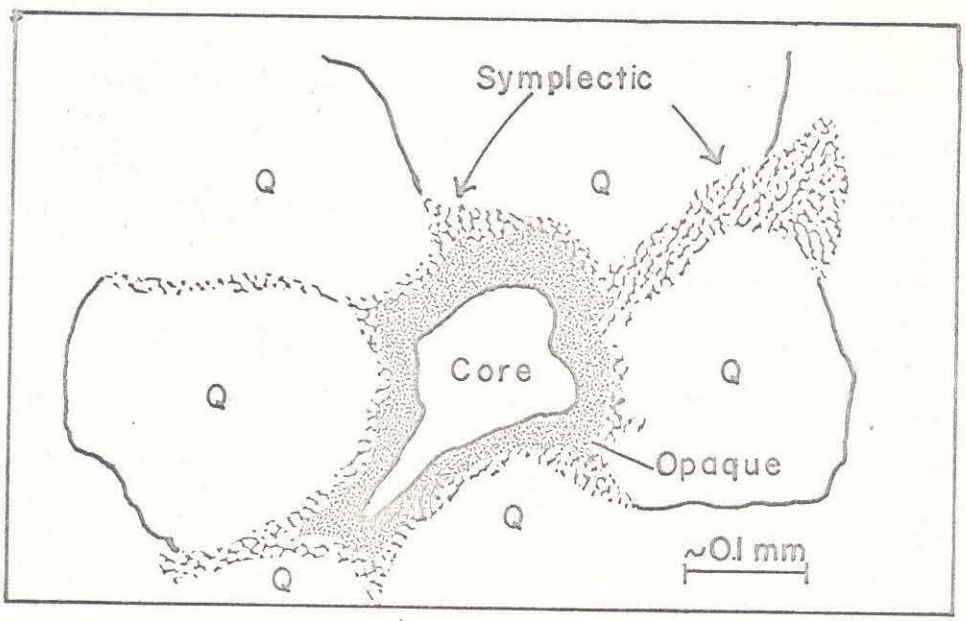

Fig. 20b. The typical occurrence of the four regions seen in Type III rocks: (1) quartz grains, (2) symplektic region on the borders of the grains grading over a distance of 10 microns into (3) an opaque region. This opaque region may have (4) a transparent, high-index core.

In thin section, the following regions of SiO_2 with different properties can be identified:

(1) quartz grains,

(2) symplektic regions on quartz boundaries,

(3) opaque regions grading into the symplektic region over a distance not exceeding 10 microns,

(4) high-index cores within some opaque regions.

The typical occurrence of these four types of regions is shown in the sketch in Fig. 20b.

Quartz comprises 45 to 80% of the area of the thin sections and occurs as remnant grains. The boundary of nearly every quartz grain is rimmed with a 10 to 40 micron symplektic region, containing material of varying indices of refraction intermixed with the quartz in 1 to 5 micron domains. The smaller symplektic regions cause the boundaries of the quartz grains to have a diffuse appearance. The larger symplektic regions grade over a distance of about 10 microns into regions of total opacity. These regions appear dark brown or black in transmitted light. In four of the six thin sections of Type III rocks studied, over 50% of the opaque regions that were larger than 0.1 mm have transparent, high-index, round or oblate cores which may be up to 0.1 mm in longest dimension. In the other two thin sections (#16, #31) these cores were observed in about 10% of the large opaque regions.

Quartz grains are generally between 0.1 and 0.3 mm in diameter in these rocks. Less than 5% of the thin section area is covered by regions of quartz chips smaller than 0.05 mm. The integrity of the original grains is generally preserved, and the individual grains remain in optical continuity. The similarity in grain size of a Type III rock and an unshocked rock can be seen by comparing Fig. 21 and Fig. 3.

On the order of 10 to 20% of the quartz grains cannot be distinguished from their neighbors under crossed nicols because wavy extinction prevents definition of the boundaries. Quartz grains commonly extinguish through an angle of 45°.

Nearly every quartz grain can be seen to have bent and deformed around its neighbors (Fig. 21). The grains are interlocked like pieces of a jigsaw puzzle, as were the grains in Type II rocks. The deformation of the quartz grains in Type III rocks suggests that the grains were plastically deformed around each other to fill in the void space as the rock was compressed.

All quartz grains are permeated with cleavages; most grains have intersecting sets of cleavages (visible on the grains in Fig. 21). Faults, defined as offsets parallel to a plane of discontinuity (after Carter, 1968, p. 457), are observed in about 5% of the grains and account for a small amount of deformation. Offset along faults is usually less than 0.03 mm. Planar features were seen in about 5% of the grains; an extensive search for planar features was not conducted.

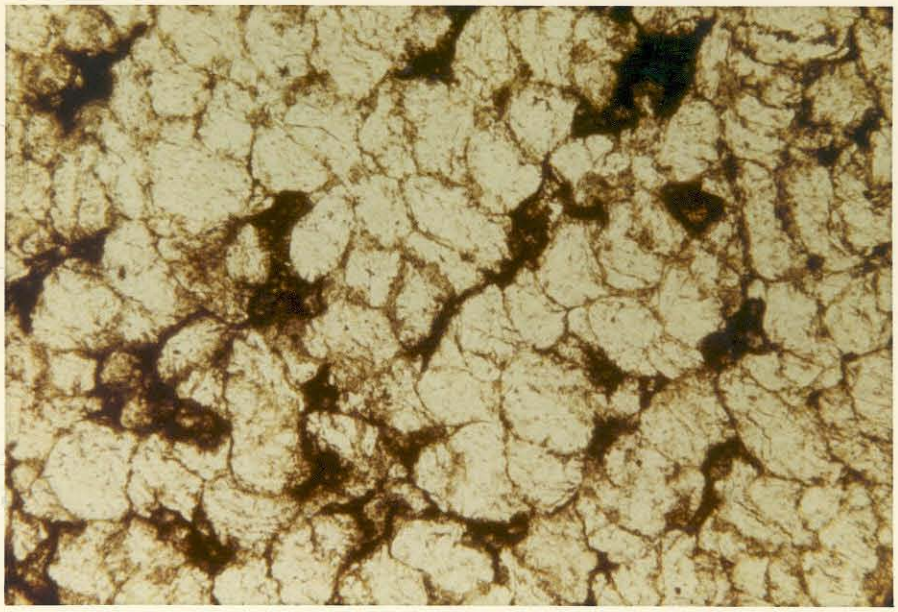

Fig. 21. Quartz grains (white) in Type III rock are generally the same size as grains in unshocked rocks, as can be seen by comparing this photomicrograph with Fig. 3. The grains are deformed into interlocking shapes. All boundaries are rimmed with symplektic regions. Large opaque areas are generally aligned from lower left to upper right. The distribution of the large opaque areas resembles the distribution of the large pores (compare with Fig. 3). (plane polarized light, x 65).

The amount of high-pressure phases in the rocks is shown in Table 3.

Table 3

Sample #	Quartz (%)	Coesite (%)	Glass (%)	Stishovite (%)
4	75	23	1*	trace ($\leq$1%)
33	71	21	7*	trace ($\leq$1%)
18	61	32	6*	trace ($\leq$1%)
16	62	18	20	trace ($\leq$1%)
31	53	29	18	trace ($<<$1%)

*Since non-silica minerals may comprise up to 5% of the original rock, and since measurement errors may be on the order of 5%, it is possible that there is no glass in these rocks.

Coesite content was measured to have values between 18 and 32%. Stishovite is detected only in Type III rocks and does not exceed 1% by weight. The glass content is estimated to be very low for the Type III rocks in which the quartz content is greater than 70% and higher for the rocks with less than 60% quartz.

Coesite and stishovite are located in identifiable regions adjacent to some of the quartz grains; these regions are here called high-pressure phase regions and include symplektic regions in which some quartz is identifiable, opaque regions, and high-index, transparent cores (Fig. 20b, 21). Since quartz and glass occur in these regions, the name

"high-pressure phase region" is not totally descriptive; it is used because the high-pressure phases are apparently restricted to these regions.

The distribution of high-pressure phase regions in Type III rocks resembles the initial pore distribution in the unshocked material. To demonstrate this, the spacing between high-pressure phase regions was measured in the thin section of rock #4. The distribution of spacings between high-pressure phase regions is very similar to the spacing between pores in the unshocked rocks, with slightly more high-pressure phase regions at smaller spacings (Fig. 22). The totally opaque parts of the high-pressure phase regions are more sparsely distributed than the symplektic parts which are found to rim nearly every quartz grain (Fig. 22).

The high-pressure phase regions in these rocks may show strong local alignment, as shown in Fig. 21 where the opaque regions are elongated from lower left to upper right. The local alignment of high-pressure phase regions does not appear to be correlated with the more general alignment of long axes of grains. With increasing degree of shock metamorphism, the size of the high-pressure phase regions increases. The high-pressure phase regions in rock #31 (53% quartz), the most transformed member of the stishovite-bearing rocks, are frequently 0.5 mm in longest dimension. In rocks of this degree of shock metamorphism, the high-pressure phase regions are not recognizably elongated.

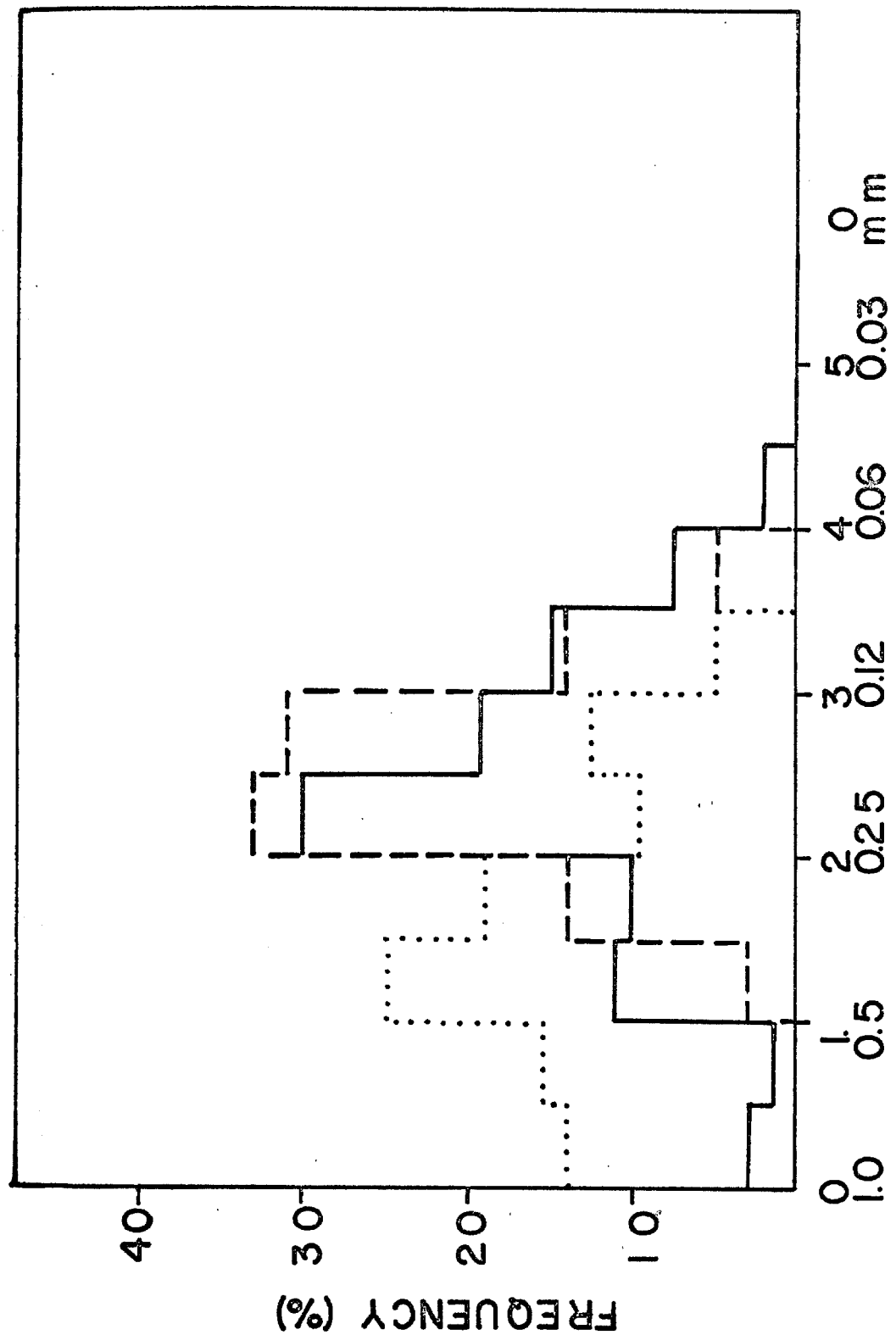

Fig. 22. Frequency distribution of separation distance of pores (---), high-pressure phase regions (opaque regions plus symplektic regions, ——), and opaque regions only (·····) in typical Type III rock.

Nearly every quartz grain in Type III rocks is surrounded by a 10 to 40 micron wide symplektic region (Fig. 21). These regions are generally wider than the 5 to 10 micron symplektic regions that bordered most grains in Type II rocks, but are elongated tangential to the quartz grain boundaries in the same way. The large symplektic regions penetrate deeply into quartz grains (Fig. 23a, b), usually following cleavage directions into the grain. The symplektic regions are composed of quartz in optical continuity with the rest of the grain and vermicular intergrowths which are about 5 microns in diameter and appear to contain high-index microcrystalline coesite. The coesite crystals may be up to 2 microns in diameter. Some of the wider veins of this material are isotropic and are assumed to contain glass.

The symplektic regions grade into regions which are entirely opaque to transmitted light. In the Type III rocks, the opaque regions assume two characteristic shapes (Fig. 24a, b). Smaller regions are generally elongated and entirely opaque. Larger regions frequently consist of an elliptical border (adjacent to the symplektic regions of the quartz grains) surrounding a core of high-index and extremely faint birefringence. The opaque regions, either in thin section or in crushed grains in immersion oil, scatter reflected light diffusely and can be easily identified by this property. They differ from the symplektic regions in that quartz is not visible within the region. The borders of the opaque region grade into the symplektic region (Fig. 24) and appear to have a similar vermicular habit.

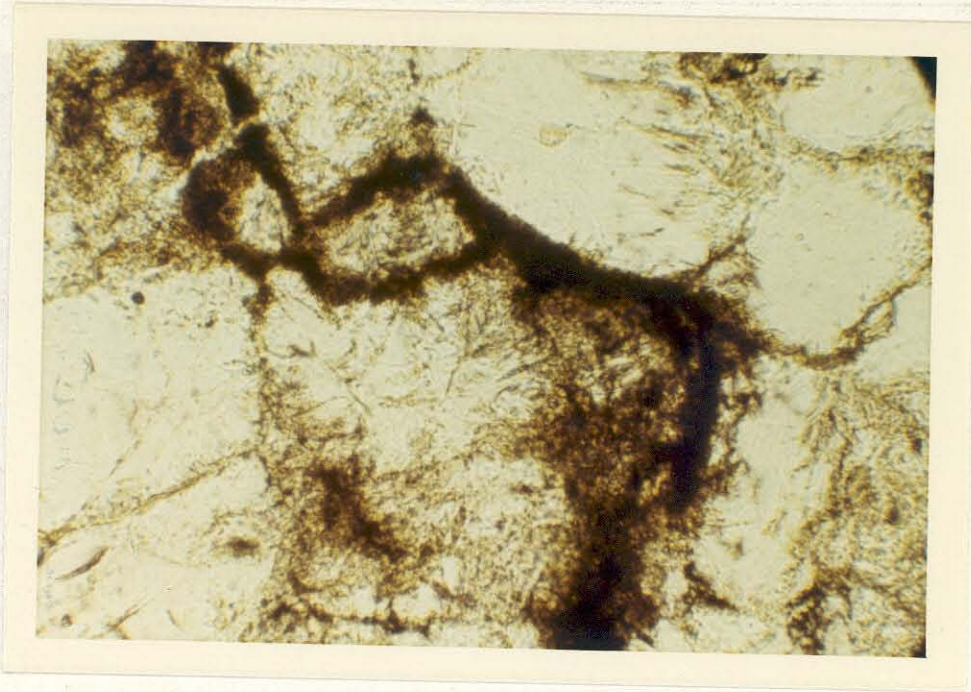

Fig. 23a. Quartz grains (white) in Type III rock with yellowish to black high-pressure phase regions deeply penetrating into center and upper grains (plane polarized light, x 265). Two cores are visible within the opaque region in the upper left.

Fig. 23b. Same (crossed nicols, x 265).

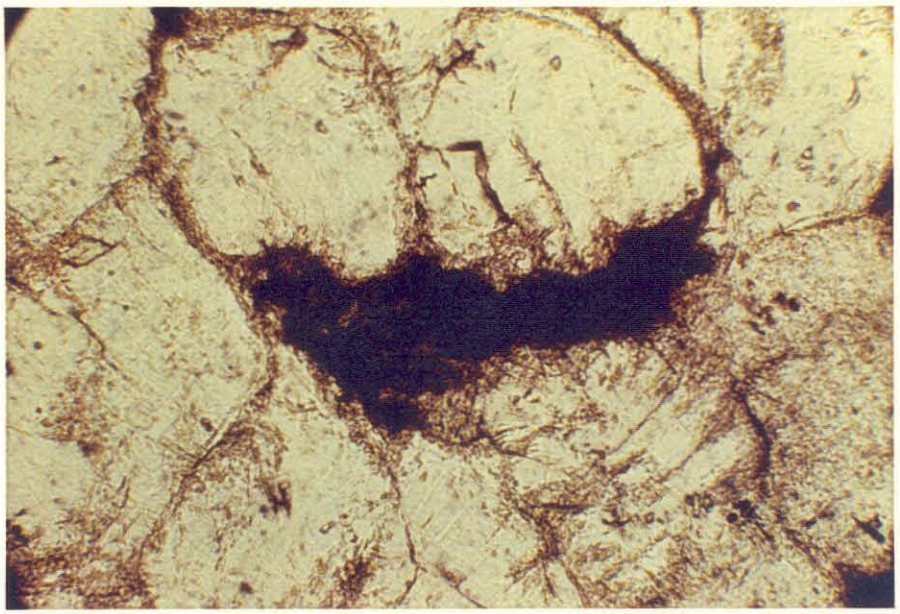

(a)

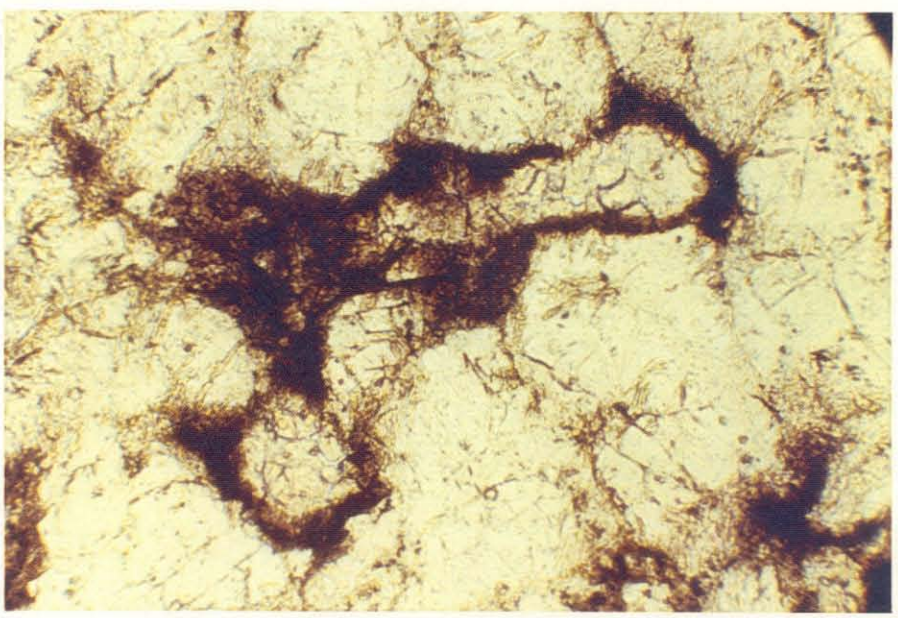

(b)

Fig. 24. Two characteristic shapes of opaque regions in Type III rocks (x 265, plane polarized light). (a) Elongated opaque region. (b) Opaque border with cryptocrystalline coesite core. Large white grains are quartz; coesite crystallites are visible in light brown symplektic regions on borders of quartz grains.

To examine the properties and occurrence of coesite and stishovite in the high-pressure phase regions in these rocks, coesite and stishovite were extracted from Type III and IV rocks by the procedure described in Appendix A. The recovered coesite consists of fine-grained aggregates in which the particle size is generally less than 1 micron. The index was measured to be 1.595 ± 0.003.* Larger aggregates may be up to 1 mm in diameter, have a light gold or brown color, and scatter obliquely incident light. Stishovite occurs in aggregates in which the particle size is less than 1 micron. The smallest aggregates (diameter less than 10 microns) are transparent; the larger aggregates are gold to light brown and scatter obliquely incident light. It is likely that the color of both the coesite and stishovite aggregates is an effect due to partial opacity of the aggregates. The reported index for pure stishovite is 1.80. The average index of the recovered stishovite aggregates varies; some aggregates were found with indices less than 1.74. The low index of the stishovite aggregates may be caused by an intermixing of two phases--stishovite plus trace amounts of a phase of lower index. Skinner and Fahey (1963) have suggested that low indices in material recovered from shocked sandstone may be due to glass that was protected from HF attack by an "armor" of stishovite. Glass in the aggregate may cause the lowered index, but does not seem to be present in sufficient amounts to cause the opacity of the large aggregates. Void spaces within the aggregate may cause the opacity.

---

* The refractive indices of coesite reported by Coes (1953) are $\alpha = 1.599$, $\gamma = 1.604$, $\alpha - \gamma = 0.005$.

Debye-Scherrer X-ray analysis of material from the high-pressure phase regions was also done to determine the phases that existed in these regions. Opaque parts of the high-pressure phase regions were obtained from uncovered thin sections and from samples of crushed rock placed in immersion oil. The symplektic region between the opaque region and the quartz grains is not mechanically separable from the opaque region and was probably included in most of these analyses. Adjacent quartz grains also were difficult to remove from the opaque regions taken from thin sections. In the 20 regions examined, coesite was always present. Quartz was generally present; it was impossible to determine if the quartz was within the opaque region or was part of a grain attached to the region. Stishovite was detected in about one-third of the opaque regions and could not be found elsewhere. The stishovite lines were weak on the Debye-Scherrer photographs. This is perhaps anomalous because a factor of about 4 to 8 in concentration of the stishovite should be attained if it were restricted to the opaque regions and were uniformly distributed in the cores. It is thus possible that stishovite may exist elsewhere within the rocks.

The partial opacity of the symplektic regions and total opacity of most of the high-pressure phase regions is probably related to the mixing of two or more substances of varying indices. To investigate this, a heavy liquid separation of a crushed Type III rock with an estimated glass content near zero (rock #4) was performed. Crushed rock powder was placed in a liquid of density 2.61 g/cm^3, a density less than

quartz. After centrifuging, 20-30% of the material floated on the liquid. This fraction consisted of quartz grains, nearly all of which showed vermicular symplektic regions on some part of the grain. The average density of these grains must be less than 2.61 g/cm^3, and, since the density of quartz is 2.648g/cm^3, a considerable amount of glass (density 2.2 g/cm^3) would be required on these grains. Glass was not observed on the grains and is not estimated to be present in this rock. It is possible that the grains in this low density fraction are quartz or quartz plus a small amount of high-pressure phases and some unresolved vesicles of vapor or void space.

Cores located within the opaque regions are usually 60 to 100 microns in longest dimension, but occasionally are as large as 200 microns (Fig. 21, 24b). Small crystallites of microcrystalline coesite penetrate the outer regions of the core with the same vermicular texture that they penetrate the quartz region on the other side of the opaque region. This relationship indicates that the cores were formed before the microcrystalline coesite which occurs in them. The cores are seldom structureless; rather, they are pervaded by a network of fractures which subdivide them into smaller "cells" which are generally less than 20 microns in diameter (Fig. 24b). These cells are usually round to oblate in shape. The whole texture of the isotropic core may be said to resemble a small area of mudcracks. The fractures in the cores may extend into the opaque rim and occasionally into the symplektic region of the quartz grain, but do not appear to extend into the untransformed quartz grain.

Three high-index cores were extracted from a thin section and X-rayed. Coesite and some quartz were present; the quartz was probably attached to the core because it was impossible to isolate a core from surrounding material. To isolate the cores, a finely-ground Type III rock (#33) was crushed and centrifuged in heavy liquid of density 2.7 g/cm^3. About 20% of the material which sank in this heavy liquid was composed of these cores. They were either free of any adjacent opaque material or occurred in their typical relationship to the surrounding opaque region, symplektic region and quartz grain (see the sketch in Fig. 20b). Individual cores were easily selected from this fraction and used for index of refraction and X-ray measurements. The index of the cores is 1.590 ± 0.002, and the X-ray pattern confirmed that they are pure coesite. The cores are nearly isotropic; a faint birefringence can be detected in parts of cores or in an occasional whole core. The low birefringence and nonuniform distribution of the birefringence suggests that these cores are cryptocrystalline coesite. The grain size is substantially less than 1 micron; this habit of coesite is distinctly different from the microcrystalline coesite seen in the symplektic regions.

Type IV rocks. Seven samples of Type IV rocks examined by X-ray diffraction were collected on the south terrace and from the shaft dumps, where they were probably obtained from dumps of the mixed debris unit. Three additional Type IV rocks were studied in thin section. Rocks obtained on the south alluvial terrace are surface stained yellow-orange to light brown. The rocks react with HCl and were measured to have between 4 and 30% $CaCO_3$. Rocks obtained from the shaft dumps are white and do not react with HCl. The rocks are extremely coherent and withstand weathering on the alluvial slopes. The largest Type IV rock examined is 5" in longest dimension.

Type IV rocks are usually distinguishable by their elongated, aligned fractures or vesicles (Fig. 25a). The sets of megascopic fractures were described by Chao (1967, p. 206) as "parallel, discontinuous, sinuous tension fractures." Generally only one set is visible. The fractures are lenticular, ranging from a few tenths of a millimeter to millimeters in width and up to centimeters in length. Chao (1967) noted that on some cases, the development of the openings in laminated rocks is concentrated in particular beds, perhaps reflecting grain size or porosity control. The cavities, though frequently lined with calcite, are not coated by any particular forms of SiO_2 and, in thin section, frequently bisect quartz grains or high-pressure phase regions. They were therefore formed after the shock had transformed material to high-pressure phases.

Of the ten rocks examined, seven have these sets of parallel fractures. The other three (all obtained from the shaft dumps) do not

Fig. 25a. Hand specimen of typical Type IV rock showing aligned fractures and vesicles. Label is 1-1/2" in length.

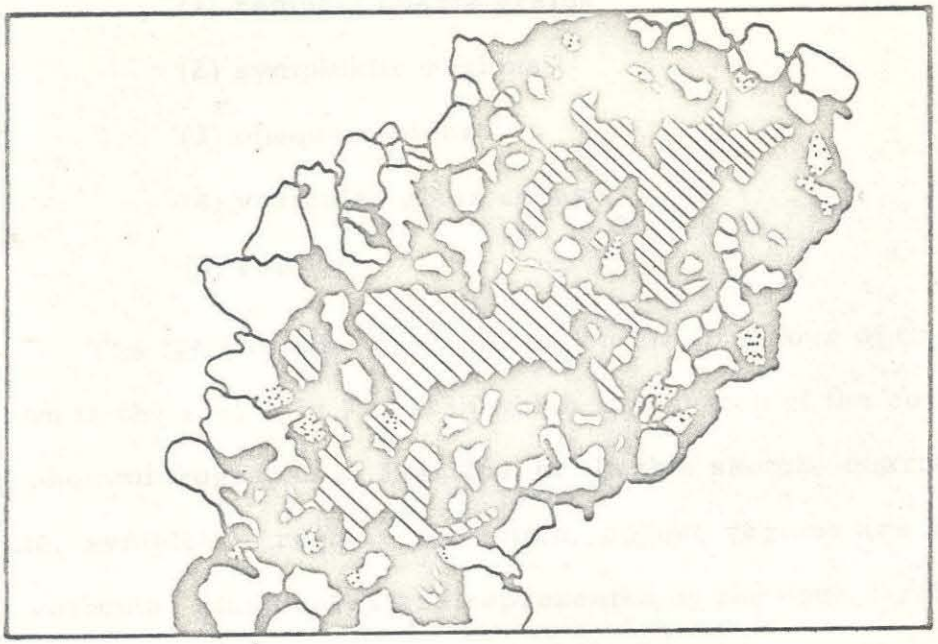

Fig. 25b. The typical occurrence of the four different SiO_2 regions in a Type IV rock: quartz grains (white), opaque rims (black) on many of the quartz grains and a vesicular glass core (striped) surrounded by the opaque rim. A few symplektic regions (dotted pattern) are shown on the quartz grains. This is a sketch of the central region of Fig. 26a and b and can be used to locate these regions in the photos. Largest quartz grains are 0.2 mm in diameter.

have any visible vesicles or fractures in hand specimen, but in thin section are observed to have small parallel fractures which are about 0.2 mm in width and up to several millimeters in length.

Remnant laminations are visible on hand specimens of two of the rocks. The laminations are warped through an angle of 5° to 10° and appear to be inflated, that is, they appear to have expanded in a direction perpendicular to the bedding.

In thin section, five regions with differing optical properties in these rocks are observed:

(1) remnant quartz grains

(2) symplektic regions

(3) opaque regions

(4) vesicular glass cores

(5) calcite

The typical relationship between the first four of these regions is shown in the sketch in Fig. 25b which is a sketch of the central region in the photomicrographs in Fig. 26a, b. In this sketch, quartz grains are white, symplektic regions are dotted, opaque regions are black, and the vesicular glass cores are represented by the open circle pattern. Remnant quartz grains and fragments of grains are observed to cover 20 to 40% of the area of the thin sections. The grains appear to be floating in a sea of opaque material and vesicular glass; only 20 to 30% of the grains are in contact with other quartz grains. Nearly every grain is rimmed with a thin symplektic region and a border of opaque

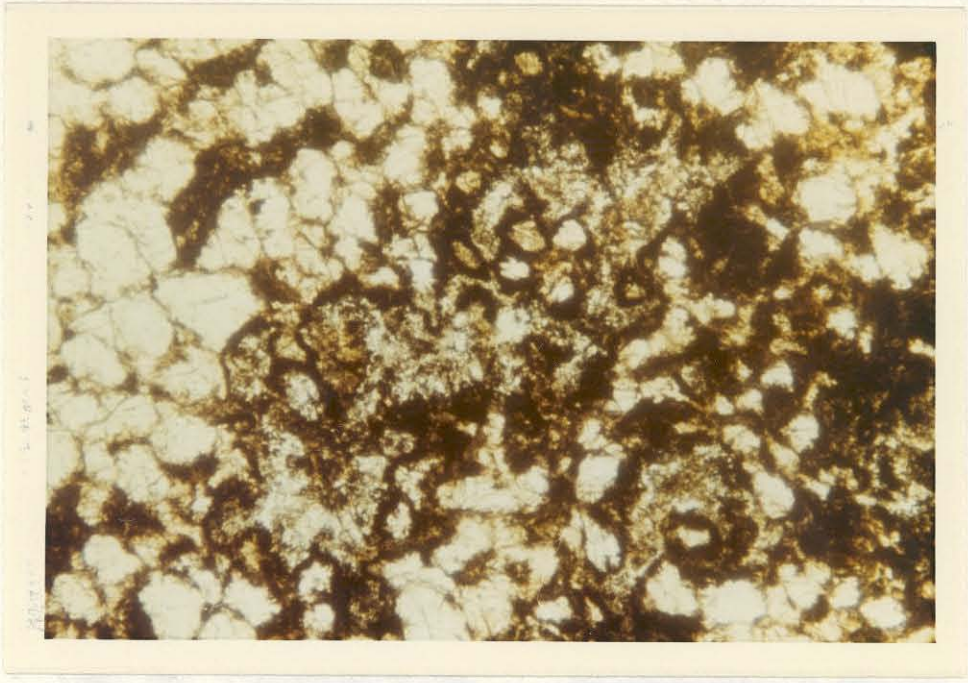

Fig. 26a. Photomicrograph (x 65, plane polarized light) of typical Type IV rock in thin section. The quartz, opaque regions and vesicular glass in the center of the photo are shown in the sketch of Fig. 25b.

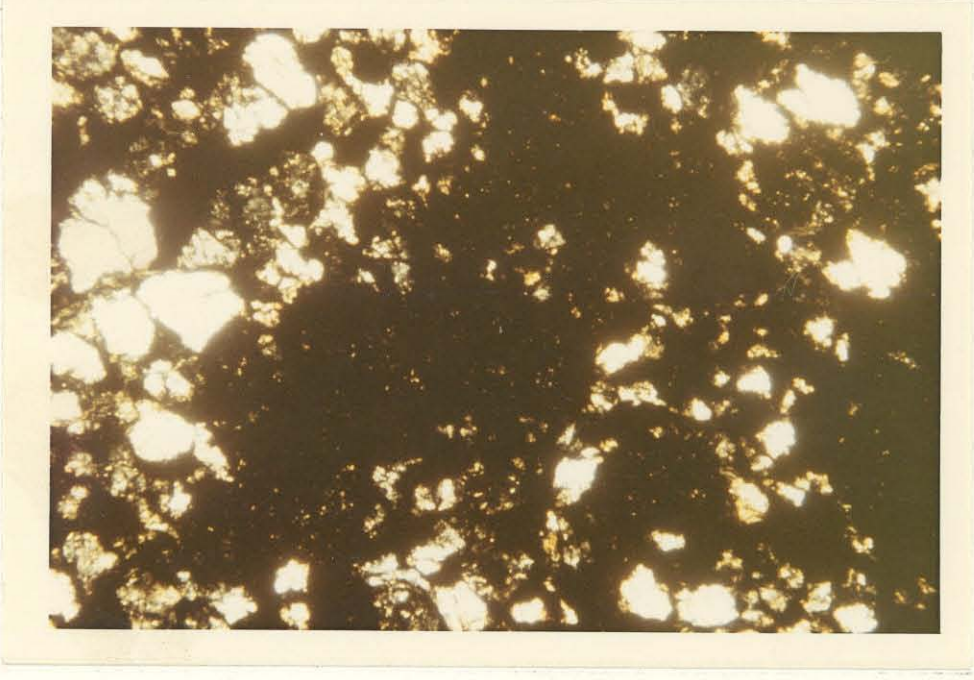

Fig. 26b. Same, crossed nicols. Several "islands" of quartz are visible in the center part of the isotropic (black) glass region.

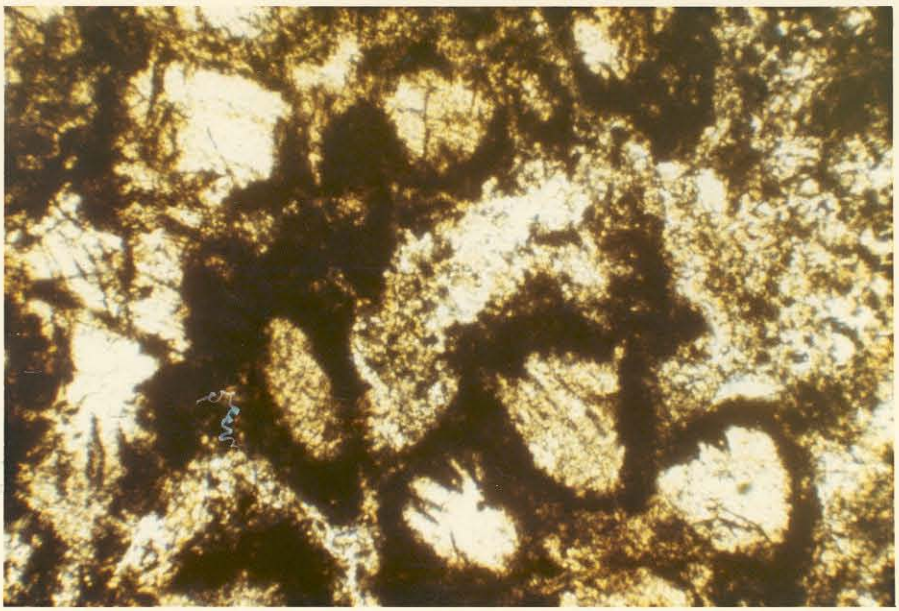

Fig. 26c. Four quartz grains located in the center of the vesicular glass core in Fig. 26a, b are visible in the lower half of this photomicrograph (x265, plane polarized light). Two of the grains appear yellowish and are comprised primarily of symplektic regions. The four grains are rimmed with opaque material and are surrounded by vesicular glass.

material. The opaque material frequently forms a continuous border up to 50 microns in width around 10 to 20 quartz grains and resembles a black ribbon tying together the grains (Fig. 26a, c). Adjacent to this black ribbon and frequently interior to it are found large areas of vesicular glass, forming cores within the opaque rims. Calcite pervades the rock in fractures and vesicles; it was deposited in the rocks as they weathered on the alluvial slopes. It is fine-grained, highly birefringent, and is often finely laminated in contorted shapes in its occurrence within fractures.

Quartz grains in Type IV rocks show a wider variation of sizes than in Types II and III. About half of the remnant grains are 0.15 to 0.25 mm in longest dimension, similar to the unshocked rock. The remaining grains are smaller and a few per cent of the observable quartz is in the form of particles smaller than 20 microns. Quartz grains which are smaller than 0.15 mm and are enveloped by symplektic and opaque rims appear to have been partially converted to high-pressure phase regions. Over 95% of the quartz grains in Type IV rocks are permeated by sets of cleavages. Planar features were observed in up to 25% of the grains.

The distribution of phases in these rocks is given in Table 4. Although the trend in this part of the shock metamorphosed sequence is decreasing coesite and quartz content, and increasing glass content, some irregularities do occur, e.g., rock #32 and rock #30 which are rich in coesite.

Table 4

Sample #	Quartz %	Coesite %	Glass %
17	40	20	40
32	36	32	32
5	32	12	56
30	32	25	43
20	25	17	58
7	23	11	66
6	20	11	69

Symplektic regions are found on the edges of all quartz grains and frequently extend into the interior of the grains along cleavage directions. Symplektic regions which lie between quartz and opaque regions are usually 10 to 20 microns in width. Symplektic regions not bordered by opaque regions may be up to 0.1 mm in width. (A large symplektic region is visible as a light gold area in the upper right corner of Fig. 26a.) Small, high-index crystallites are frequently visible in the symplektic regions and are assumed to be coesite.

Opaque regions in Type IV rocks occur as rims of 10 to 100 micron width on the quartz grains. Less frequently (20 to 50% of the occurrences) opaque regions may be up to 0.2 mm in width. The relationship between quartz grains and opaque rims is shown in Fig. 25b and 26. Many of the quartz grains in Fig. 26 are completely rimmed with black or brown borders which are, on the average, 50 microns in width. Four quartz islands preserved in the middle of the isotropic region in the center of the photo are also rimmed by opaque material. Debye-Scherrer X-ray photography of the opaque regions in Type IV rocks showed them to be rich in coesite. The opaque and symplektic regions are the only occurrences of coesite in Type IV rocks; cryptocrystalline coesite was not found in these rocks.

Naturally occurring silica glass was first recognized in 1915 by Lacroix and given the name lechatelierite. Melted silica glass in the shocked Coconino sandstone occurs only in Type IV and V rocks. Glass in Type IV rocks occurs in vesicular isotropic regions within the opaque rims. These regions may be up to 3 mm in longest dimension. Glass cores were found associated with more than 50% of the opaque regions in all Type IV rocks except in #32, which has an anomalously high coesite content for a Type IV rock. About 10% of the opaque regions in this rock have vesicular cores.

The glass is filled with spherical inclusions which are observed from 2 μ to 0.1 mm in longest dimension. No direct index measurement is possible on the smallest vesicles, but the larger ones are observed to be filled with impregnating fluid when the thin sections are

prepared and are therefore vesicles in the rock. Most vesicles are less than 10 microns in diameter and occur so profusely as to cause an opacity in parts of the core similar to the coesite-rich opaque areas. Some vesicles are flattened and appear to have been sheared. Thin fibrous "bridges" of glass extend across some vesicles greater than 0.05 mm. The glass in the cores contains schlieren.

The presence of vesicles in the glass regions indicates that a gas was present as the pressure on the rock was released. Three possible vapors have been considered:

(a) SiO_2 vapor

(b) air

(c) water vapor.

It is unlikely that sufficient energy was available to vaporize SiO_2 in these rocks (the heat of sublimation of SiO_2 is $\Delta H_{s_{298}} = 143$ kcal·mole^{-1}; the heat of fusion ΔH_m is 2 kcal/mole (Janaf, 1965)). Had vaporized SiO_2 formed, low-pressure phases of SiO_2 would probably have formed in the vesicles as the rock cooled. No such phases are observed. It is therefore improbable that SiO_2 vapor formed the vesicles. Air is extremely compressible compared to SiO_2 and would probably be eliminated from the rocks as the pores were closed; furthermore, a plausible mechanism for trapping shocked air cannot be proposed to account for the interspersing of the vesicles within the silica glass. It thus seems likely that water vapor caused the vesicles in Type IV rocks. Further consideration of the role of water in the shock compression of these rocks is given in Chapter IV.

The presence of sheared vesicles and fibrous bridges across vesicles indicates that this glass was fluid at relatively low pressures. This implies that if the rock were dry, temperatures of approximately 1700°C existed in these regions upon release of the rock to low pressures. If the rock were wet, the temperature may have been as low as 1100°C (Kennedy, et al., 1962). Since the quartz grains within 0.1 mm of the isotropic regions did not melt, they must have been below 1700°C, and perhaps below 1100°C.

Observations on the existence of vesicles and on the proximity of fused SiO_2 to quartz suggest that water in the pores of the rock initially may have played an important role in allowing parts of the rock to melt at relatively low temperatures because they were wet, while other (dry) parts of the rock were not exposed to melting temperatures.

A preliminary effort has been directed toward detecting trapped water in these rocks, assuming that it was either tied up as OH in the glass or as trapped water in the smallest vesicles. A Type IV rock (#17) with 40% glass was finely ground and placed in a heavy liquid of density less than 2.20 g/cc. (The density of this liquid was not measured, but a piece of solid glass sank immediately in it.) The crushed rock in heavy liquid was centrifuged and the residue which floated was collected. From X-ray spectra and petrographic analysis, the composition of this residue was estimated to be 40% coesite, 40% glass and 20% quartz. The coesite and quartz were frequently attached to vesicular glass, but some opaque fragments were found which must be coesite-rich and were not apparently attached to glass. To account for their net

density being lower than 2.2 g/cc, these fragments may have a significant amount of void space within them. (Opaque fragments also sank in a heavy liquid of density 2.70 g/cc; these heavy liquid separations are by no means definitive tests of the nature of these particles.)

Paul Knauth (CIT, Geology Division) analyzed the amount of water which was given off by 24.4 mg of this low-density fraction at 200°C and 1000°C. 0.50% of the weight of the sample was released at 200°C and 0.85% by weight was released at 1000°C. These values are above average values for sandstone and even above average values for cherts. Until standards are run on unshocked Coconino and on whole-rock samples of shocked rock, these results are at best indicative of high water content in local regions. They do resemble strongly the results which Merrill (1908, p. 475) obtained when he heated Variety A of the sandstone to ignition and obtained 1% by weight of water. This lead Merrill to suggest that part of the silica is in the condition of opal.

Type V rocks. Type V rocks consist primarily of glass and are, in hand specimen, low-density, vesicular, nearly pumiceous in texture (Fig. 27). The lechatelierite-rich rocks vary from "clear colorless to subtranslucent white" (Rogers, 1928). Type V rocks found on the south alluvial terrace are light brown; rocks found in the shaft dumps are white and sometimes covered with a tan or cream fine-grained powder. Six rocks were examined in thin section, two by X-ray diffraction. One rock had planar laminations which are about 1 mm thick.

Thin sections of these rocks show a flowed, stretched glass (lechatelierite) in which vesicles of all sizes exist. Remnant fragments of quartz grains are embedded in a matrix of vesicular SiO_2. Rogers (1928) observed cristobalite in Variety B rocks, which are probably the same as these Type V rocks, but none was recognized in these studies.

The remnant quartz in these rocks ($< 10\%$) consists of irregular chips and fragments less than 0.1 mm in average dimension. The quartz content of rock #9 was measured to be 15%; later thin section studies showed that some of this quartz was in the form of a fine-grained coating on the surface of the rock. The quartz content in the rock is estimated to be 8%, and is shown in parentheses in Fig. 11 to indicate that a correction to the measured value has been applied.

Wavy extinction in quartz grains which are about 0.1 mm in diameter under crossed nicols indicates that they are strained. The grains extinguish through an angle of about 20°. Cleavages and planar features were seen on a few of the larger quartz grains.

Fig. 27. Vesicular, pumiceous Type V hand specimen. The largest fragment is 2" in longest dimension.

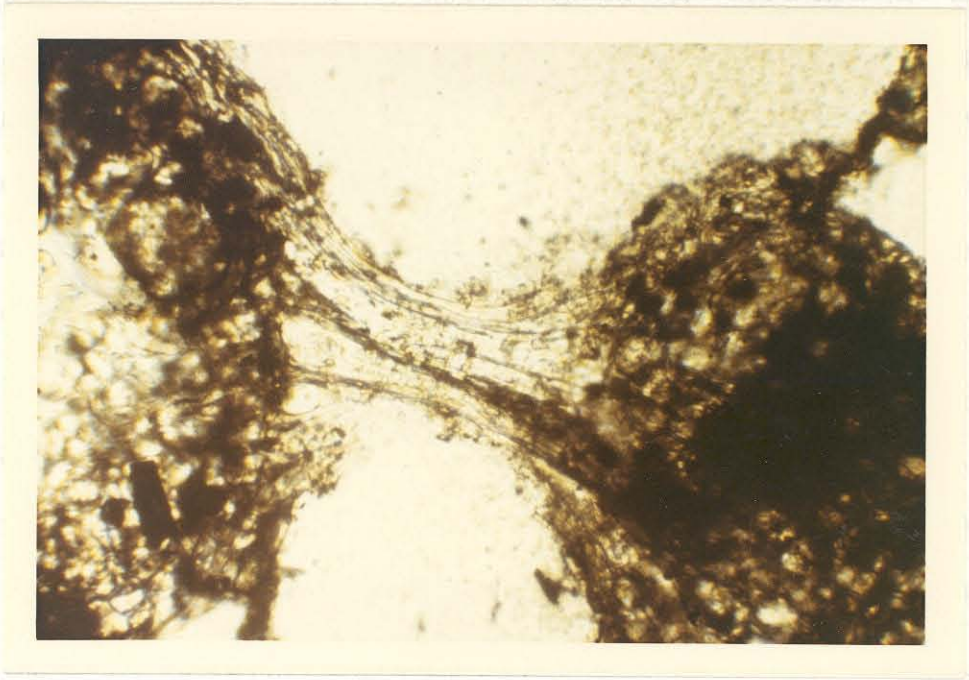

Fig. 28. Vesicular fibrous glass in Type V rock showing schlieren (plane polarized light, x 1525).

The glass in the rocks is of index 1.46 ± 0.005. An extensive study of glass indices was not undertaken. Extensive networks of glass fibers and schlieren are found in the glass (Fig. 28). It is frequently opaque due to the presence of numerous vesicles smaller than 2 microns.

Coesite was measured to comprise 5% of one Type V rock (#19); no coesite was detected in rock #9. The coesite could not be identified in the thin section of rock #19. It may occur in opaque or symplektic regions or in isolated crystals, although symplektic regions were not observed on the quartz grains, and opaque coesite-rich regions cannot be distinguished from the opaque glass. By analogy with the occurrence of coesite in Type III and IV rocks, it is expected that the coesite is located in close proximity to the quartz grains rather than interspersed as crystallites within the glass.

Chao (1968, p. 149) reported that coesite is not found in rocks in the Ries Basin in which lechatelierite is observed. Coesite in close proximity to the lechatelierite in Type IV and Type V rocks from Meteor Crater is apparently associated with the presence of pores in the unshocked rocks.

Vesicles in Type V rocks were observed from 1 micron to several millimeters in length. A fibrous glass "bridge" across a large vesicle is shown in Fig. 28. Smaller vesicles can be seen in the glass in the photo. In some rocks, the vesicles are nearly round or slightly oblate (shape parameter: 1 to 2). In other rocks in which extensive flow of the glass is observed, the vesicles are elongated and aligned, and

the shape parameter frequently is 20 to 25. In rock #35 in which planar laminations are observed in hand specimen, the larger vesicles (greater than 0.1 mm) have a shape parameter of about 5 and are concentrated in some of the laminations. They are elongated parallel to the laminations. Vesicles smaller than 0.1 mm in this rock have a shape parameter of 1 to 2 and are not aligned.

It is probable that the vesicles in Type V rocks were caused by conversion of water in the unshocked rocks to steam under shock compression. This hypothesis was advanced in 1906 by Fairchild and in 1928 by Rogers.

IV. INTERPRETATION: PROPAGATION OF A SHOCK WAVE THROUGH GRANULAR QUARTZ

Shock metamorphism of the Coconino sandstone involved closing of pores and local deposition of internal energy around collapsed pores. At low pressures, brittle fracture of the grains occurred. At higher pressures, the quartz grains flowed plastically around one another and into the pores. Microcrystalline coesite formed at the boundaries of quartz grains. Cryptocrystalline coesite cores were formed in the stishovite-bearing rocks. In rocks shocked to higher pressures, cryptocrystalline cores are not observed, but vesicular glass cores are observed in the same relationship to the other SiO_2 phases. Vesicular glass is observed in some rocks; opaque coesite regions may owe their opacity to minute unresolved vesicles. The shock metamorphosed SiO_2 rocks are, in summary, extremely heterogeneous.

The following problems have been posed by observations of the shocked Coconino sandstone:

(1) How are pores in a granular material closed?

(2) How was the energy deposited preferentially around the closed pores?

(3) Under what rèğimes of pressure and temperature did the phases of SiO_2 form and in what sequence?

(4) What was the role of interstitial water?

In the beginning of this chapter, a model of the shock structure at Meteor Crater is presented. Before considering in detail the very complex history of the shock metamorphosed rocks, a simple one-dimensional model of shock wave propagation through a granular material is examined. This model was proposed by Hoffman, Andrews and Maxwell (1968) to account for the measured properties of the equation of state of porous aluminum. It shall be shown that this model gives the correct average volume and internal energy of states on the porous quartz Hugoniot in which phase changes have not occurred. The model fails, however, to give the observed microscopic features noted above to occur in the shocked rocks, but serves as a conceptually useful approach to the more complicated problem of nonplanar impacts.

Following the discussion of one-dimensional impact, the problem of the impact of sand grains is treated by obtaining an approximate solution for the impact of two quartz spheres. This model predicts the existence of the observed concussion fracture patterns. Normal and shear stresses generated by the impact of two spheres are considered.

Finally, the details of shock compression of each type of shocked rock are examined. No adequate theoretical model of shock-induced phase changes exists. The detailed observations on the shocked Coconino permit construction of a model of shock compression of granular quartz.

THE SHOCK WAVE AT METEOR CRATER

The shock wave generated by the impact event at Meteor Crater consisted of a relatively sharp rise to peak pressure, the shock front, and a slower decay to ambient pressure, the rarefaction (Shoemaker, 1963; Bjork, 1961). The shock structure is shown schematically in Fig. 29. The work done in increasing the internal energy of the rock mass by compression of the material is accomplished in the shock front. The release of shocked material to zero pressure occurs when the tail of release waves from the ground surface and edges of the meteorite reach the shocked material. Pressures high enough to transform SiO_2 into high-pressure phases are maintained until the shock decays below approximately 30 kb in the rarefaction wave.

The time available for the formation of high-pressure phases may be estimated by considering separately the rise time to peak pressure and the decay time to pressures of approximately 30 kb. The rise time is shown in the next section of this chapter to be on the order of several microseconds. The decay time may be estimated by using the one-dimensional model of penetration mechanics developed by Shoemaker (1963). At the time that rarefaction waves reach the meteorite-rock interface, the shock front in the rock will have reached a distance of approximately three times the meteorite diameter, L (L is assumed to be about 30 m, E.M. Shoemaker, personal communication), and the particle velocity of the shocked rock will be about 10 km/sec at this distance (corresponding to pressures of several megabars in porous quartz). At this time, the rarefaction

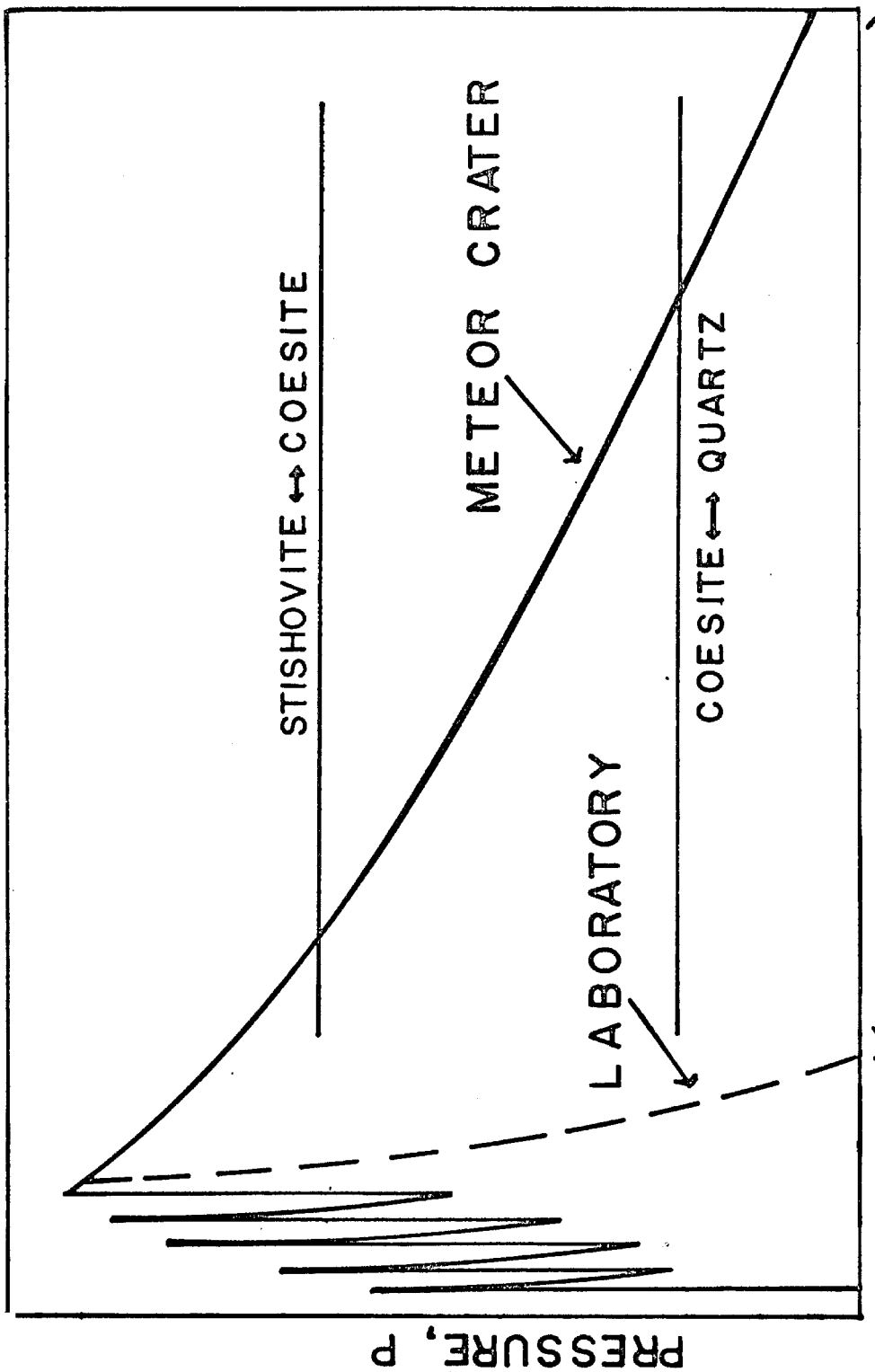

Fig. 29. Schematic diagram of shock structure at a point several hundred feet from the center of impact and of a laboratory shock event.

which originated at the back surface of the meteorite will begin to penetrate the rocks. The rarefaction wave will travel at the sound speed appropriate to the local pressure. Assuming a sound speed of 7.5 km/sec (calculated by the methods described in Chapter IV and Appendix C) for quartz at 30 kb to be appropriate to the shocked SiO_2 phases, 10 milliseconds will elapse before the material at distance 3L is released to 30 kb. This may be considered a lower limit for the duration of the strong shocks. To obtain an upper limit on the duration of the shock, we consider that the Supai Formation at a depth of 1000' has been only weakly shocked, as revealed by drill holes in the center of the crater (Shoemaker, 1963). Rarefaction waves must have overtaken the shock front by this distance and reduced shock pressures to several tens of kilobars. Assuming a shock speed of 10 km/sec, and a zero pressure sound speed of 3 km/sec, the duration of the shock could not have exceeded 45 msec. In contrast to this calculated duration of tens of milliseconds, a laboratory shock wave will last for only several microseconds.

STRUCTURE OF THE SHOCK FRONT IN GRANULAR QUARTZ

A theoretical one-dimensional model was used to attempt to explain the fundamental mechanisms of energy deposition that occur as a shock passes through a granular material and to examine the effect of the porosity on these processes. Basically, as a shock propagates through a granular material the shock is transmitted grain by grain, and each grain is shocked and released due to collisions of other grains. Because of the thermodynamics of the shock process, energy is deposited irreversibly in a grain each time it is shocked, and it becomes hotter and hotter.

The geometry of the theoretical model is shown in Fig. 30. An infinitely long quartz driver impacts one-dimensional grains separated by gaps. The Coconino sandstone shocked in the laboratory (Ahrens and Gregson, 1964; Shipman and Gregson, 1970) had a reported porosity of 25%, so detailed calculations were done with this porosity in order that the computed results could be compared with laboratory equation of state data. The case of 25% porosity, 0.2 mm thick grains is shown in Fig. 30.

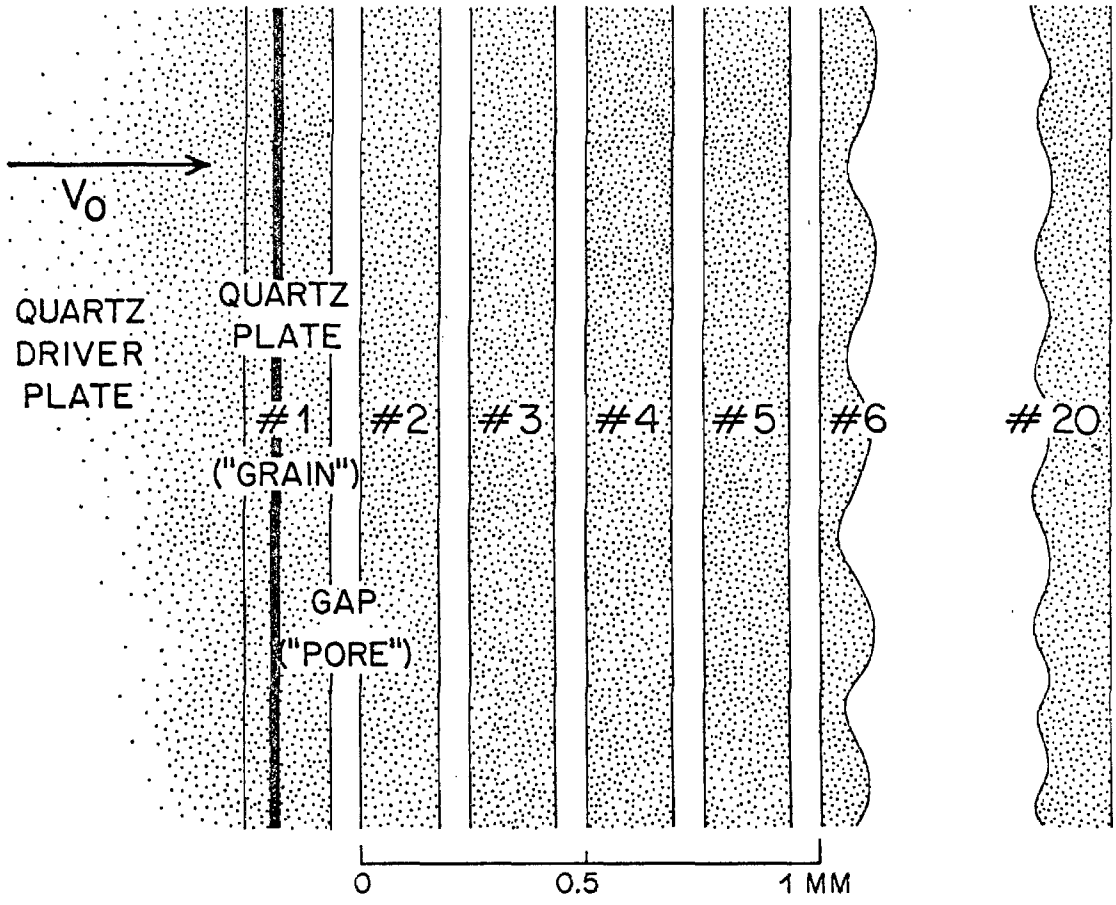

Fig. 30. Geometry of one-dimensional impact, showing plates separated by pores, and driver plate, which is assumed to be infinitely long. Shock history of unit mass of material in grain #1 is considered in detail in text.

Finite difference analogs to the one-dimensional Lagrangian equations of conservation of mass, momentum and energy (Appendix C) are solved in conjunction with an appropriate equation of state for quartz. For this purpose, a computer program purchased through COSMIC (Computer Software Management and Information Center) and originally developed by Herrman, Holzhauser and Thompson (1967) at Sandia Corporation, was modified from a CDC 3600 computer to the IBM 360.

In this calculation, the one-dimensional material continuum is divided into a mesh by lines drawn on the material at the initial instant of time. Real viscosities of quartz are too small to provide numerical stability unless an exceedingly small mesh size is used; therefore an artificial viscosity consisting of terms linear and quadratic in the volumetric strain rate is necessary for numerical stability across the shock front. In the discussion which follows, the effects of this viscosity are negligible. Quartz was assumed to obey the hydrostatic linear shock-velocity particle-velocity relation measured by Wackerle, and no phase changes have been considered in this model. (See Appendix D for a description of the thermodynamic parameters of quartz used in all parts of this thesis.) A similar study was done by Hoffman, Andrews and Maxwell (1968) for aluminum of 50% porosity.

Consider the sequence of events illustrated in Fig. 30. As the driver, which is given an initial velocity v_o, hits the first plate, a shock is sent to the right in that plate and to the left in the driver.

The right-travelling wave in the first grain reflects from the right free surface at the first pore as a rarefaction, or release, wave. This accelerates the free surface across the pore, and the rarefaction travels back through the first grain reducing the pressure gradually to zero. After the grain has traversed the pore, it impacts the second grain. This again sends waves to the right and to the left from the interface. Because of the increase of wave velocity with pressure, a trailing wave will overtake a leading wave. Hence, the left-travelling shock generated by the second impact will travel back through the first grain, overtaking the first rarefaction, which was, in turn, overtaking the first left-travelling shock. This process is repeated over and over as successive grains impact and waves are sent back into previously shocked material. It is this process of reverberation of shock and rarefaction waves through the grain that results in the deposition of energy in a porous material in excess of that deposited in a solid material of the same mineral composition.

Figure 31 is a pressure-specific volume diagram of the thermodynamic paths which a unit mass of material (shown in Fig. 30 in grain number 1) follows to a final steady state for cases of three different porosities. The initial conditions appropriate to this graph are an impacting driver velocity of 1.5 km/sec, porosities of 5%, 25%, and 35%, and 0.20 mm quartz grains. Consider the middle figure for the case of 25% porosity. The upper dots represent shock states (numbered in succession), and the lower x's are the corresponding release states as the respective shocks are reflected from free surfaces adjacent to pores. The material is initially shocked from state x_o to state S_1 at 105 kb by the first right-travelling shock, along the Rayleigh line 1. It is then released to -2 kb along the left (outer) release adiabat, reshocked to state S_2 at 106 kb by the first left-travelling shock, released to the second rarefaction state at 0.5 kb, and so on. Owing to the unusually low Grüneisen's ratio for quartz, successive release adiabats are not much separated and only the first two have been shown in Fig. 31. Final equilibration occurs to a pressure of 63 kb, specific volume 0.3407 g/cm^3. The equilibration pressure is taken as the average of the last computed shock and rarefaction pressure.

This model may be expected to give a reasonable approximation to the shock history of real Coconino sandstone grains only at those pressures where pore space is totally collapsed, but significant amounts of phase transitions have not occurred. Data published by Shipman and Gregson (1970) and Ahrens and Gregson (1964) suggest that this range is between 50 and 130 kb. The equilibrium point calculated at 63 kb by

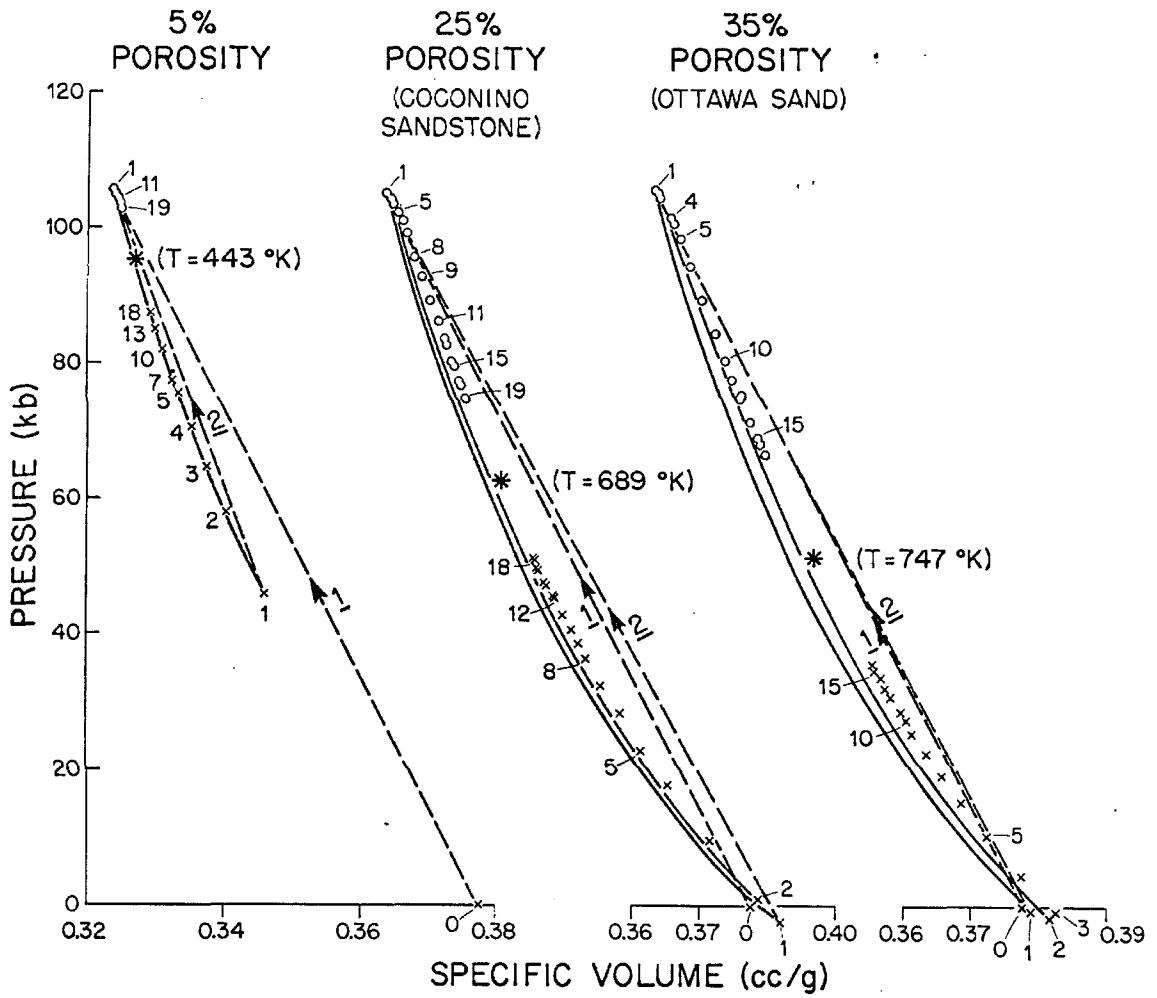

Fig. 31. Pressure-specific volume diagram of thermodynamic paths of unit mass of material in grain #1. The history of a grain within media of three different porosities is shown. Successive shock states are indicated by circles, successive release states by x's and are numbered according to the number of shocks which have passed through the material. Two successive Rayleigh lines are indicated by dashed lines; successive release adiabats are solid curves. Final equilibration states are indicated by an asterisk and are taken to be the average pressure and volume of the last computed shock states and rarefaction states.

this one-dimensional model falls within the scatter of measured sandstone Hugoniot data and very close to (P, V) points at 67 kb, 0.330 cc/gm measured by Ahrens and Gregson (1964), and 66 ± 1 kb, 0.341 ± .003 cc/gm measured by Shipman and Gregson (1970). This point is shown by an arrow in Fig. 39.

For purposes of comparison, Fig. 31 illustrates the difference in final state in material of three porosities produced by the same driver impacting velocity. Porosities of 5% (a slightly porous polycrystalline target), 25% (Coconino sandstone) and 35% (Ottawa sand) were examined because of their previous use in laboratory shock experiments. In a sample of 5% porosity, shocks are generated after a relatively small time interval because of the small average size of the pores. Rapid attenuation of the rarefactions occurs and the material is quickly brought to equilibrium at pressures near the peak pressure. In the case of 35% porosity, successive shocks are generated so long after the rarefactions begin that attenuation does not occur rapidly; many more impacts are required before the approach to equilibrium begins, and equilibration occurs to a lower pressure than for the less porous material.

For a given grain size, the length of time until equilibration occurs is governed by the porosity. The rate of approach of these samples to a steady state is shown in Fig. 32, which is a graph of time vs. the magnitude of pressure oscillation $\Delta P = S_n - X_n$, $n = 1, 2, 3, \ldots$, where S and X represent shock and rarefaction

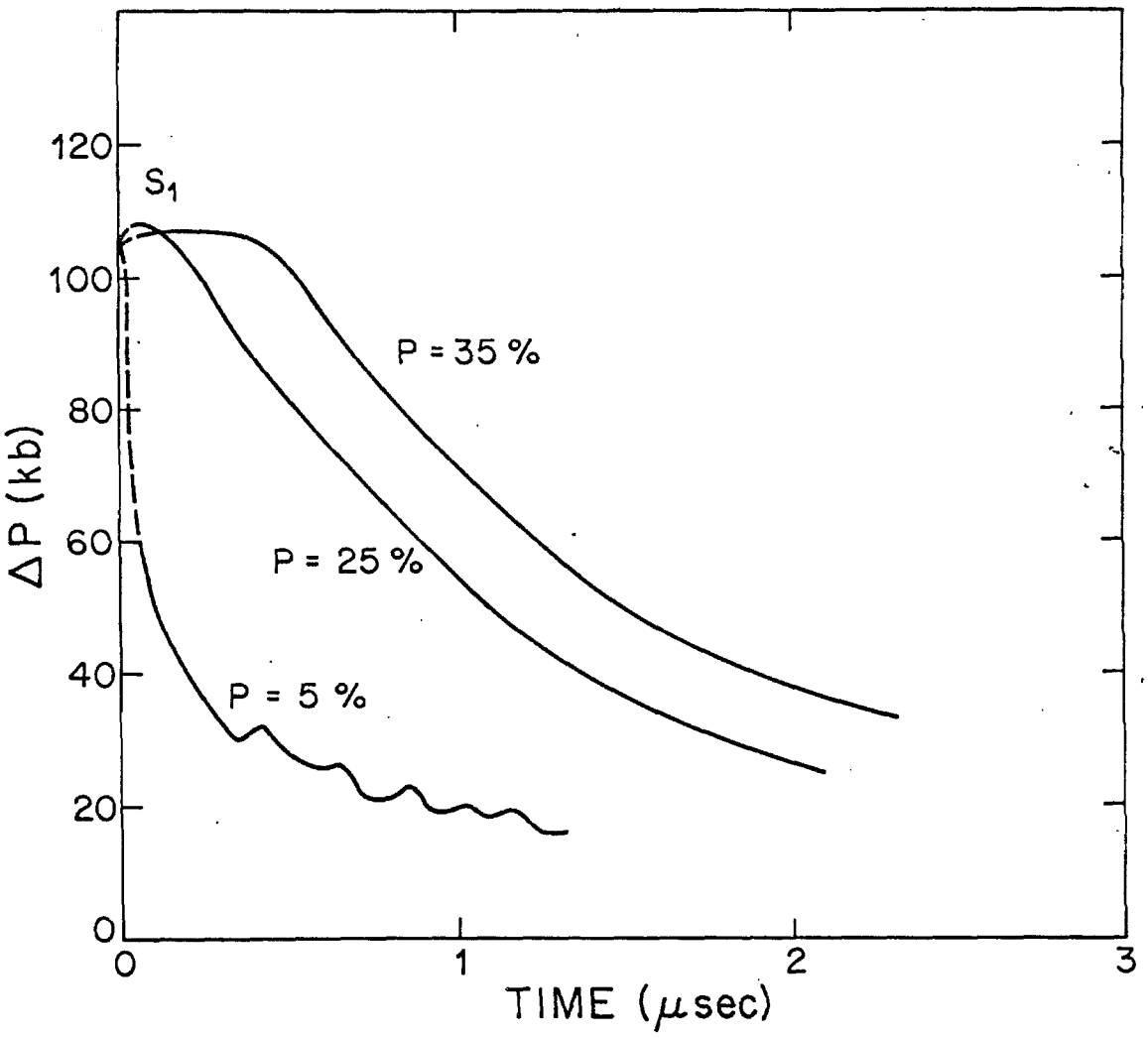

Fig. 32. Magnitude of pressure oscillation, P, versus time for model impacts in material of three different porosities, p.

states. For constant grain size, the length of time that it takes a sample to come to its steady state increases as the porosity increases. The length of time to reach an oscillation of 1/e of the peak pressure varies from a few tenths of a microsecond for the case of 5% porosity to several microseconds for 35% porosity. This corresponds to the passage of the shock through four grains in a 5% porosity material and through more than 15 grains of 35% porosity. These equilibration times are appropriate to the one-dimensional model and can only describe qualitatively the rate of approach to equilibrium. Extra free surfaces associated with real grains would probably act to attenuate the oscillations more quickly, and the figures quoted above may be indicative of maximum times for equilibration. It seems likely, however, that the equilibration time cannot be less than the time required for the shock to pass through several grains and rise times of arriving waves in laboratory shock experiments on the order of several tenths of a microsecond should be observed.

It is not directly predictable from a macroscopic model of the shock process that the peak pressure (105 kb in the sample case of 25% porosity shown in Fig. 31) seen by individual grains in a porous material is much greater than the final equilibration pressure (63 kb). It has been hypothesized (Shipman and Gregson, 1970) that phase transitions in porous media proceed at lower (equilibration) pressures than in solid material because the porous material is hotter. This model suggests an additional reason why the phase changes appear to proceed at lower final equilibration pressures: peak shock pressures in

the grains may be comparable to the single-crystal transition pressures, even though the final equilibration pressure is less, and significant residence time may be spent at the higher pressures. As discussed later in this chapter, the "points" and irregularities in geometry in real sand grains may create spots of even locally greater pressure than predicted by the one-dimensional model.

Each time the material is shocked and released, an amount of energy equal to the area between the Rayleigh line and the release adiabat is irreversibly deposited, and the material becomes hotter and hotter. Each shock raises the internal energy above that of the previous shock, and each release also attenuates at a higher level until a steady value of internal energy is attained. For the case of 25% porosity and v_o = 1.5 km/sec, $e = 0.49 \times 10^{10}$ ergs/gram, in close agreement with the value $e = 0.504 \times 10^{10}$ ergs/gram obtained by application of the Rankine-Hugoniot energy equation

$$\Delta E = \frac{1}{2} P \Delta v \qquad (1)$$

to a sandstone of 25% porosity shocked to 63 kb and compressed to volume $v = 0.3407$ g/cm^3. This serves as a check on the finite difference scheme used in the computer program.

Temperatures have been calculated from internal energies by the method described in Appendix E, using for the values of the specific heat of quartz the continuum model developed in Part II of this thesis.

Figure 33 shows the temperature of a unit mass of material in examples of the three porosities 5%, 25%, and 35% in various shock (S_n) and rarefaction (X_n) states. The abscissa is equivalent to a time axis, but in consideration of the previous discussion of the effects of the one-dimensional geometry on the equilibration time, it is more appropriate to describe the increase of energy of temperature associated with various numbers of shocks rather than with time. Each successive shock ($S_1, S_2, S_3 \ldots S_n$) raises the internal energy and, hence, the temperature, above the previous state, and each rarefaction is also at higher temperature until small oscillations about a final steady value occur. The number of shocks required for approach to equilibrium increases as the porosity increases, and the final equilibration temperature also increases as the porosity increases, even though the final equilibration pressure is less for the more porous materials (Fig. 31).

The possible effect of this process on shock metamorphism is best described by examining the pressure-temperature excursions in relation to the SiO_2 stability fields. The quartz, coesite and stishovite stability fields, as well as the calculated metastable quartz-stishovite transition, are shown in Fig. 34. Superimposed on these stability fields are the traverses of a unit mass of material in the shock calculation described for material of 25% porosity, $v_o = 1.5$ km/sec. The thermodynamic paths of this grain traverse all of the stability fields and have a significant residence time in the stishovite field. Thus, if the metastable quartz-stishovite phase transformation occurs in the shock front and has a characteristic time of hundredths of

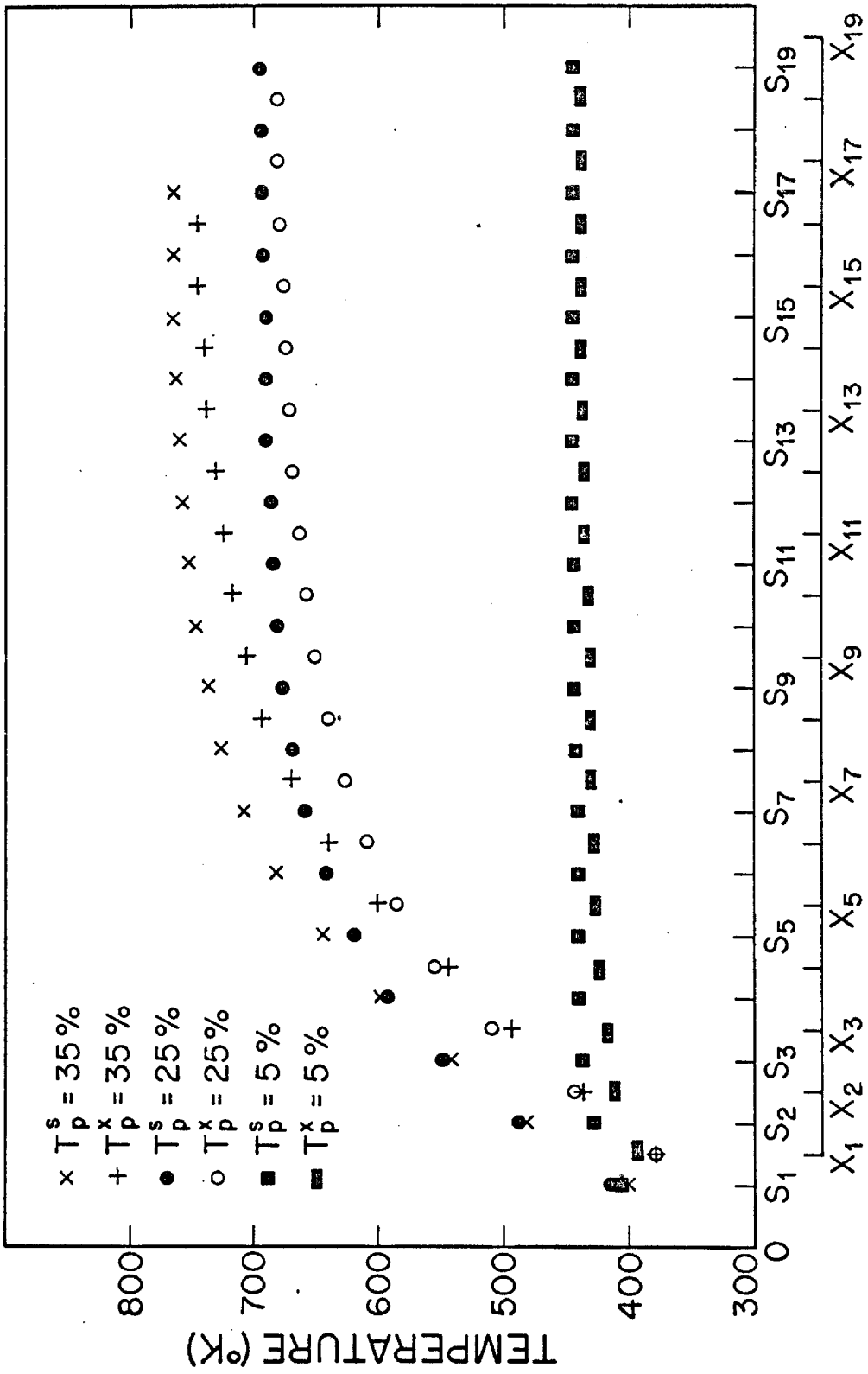

Fig. 33. Temperature of a unit mass of material in succcsive, shock states, S_n, and rarefaction states, X_n. The symbols (x, o, ■) represent shock states for porosities of 35%, 25% and 5% respectively. The symbols +, o and ■ denote corresponding rarefaction states.

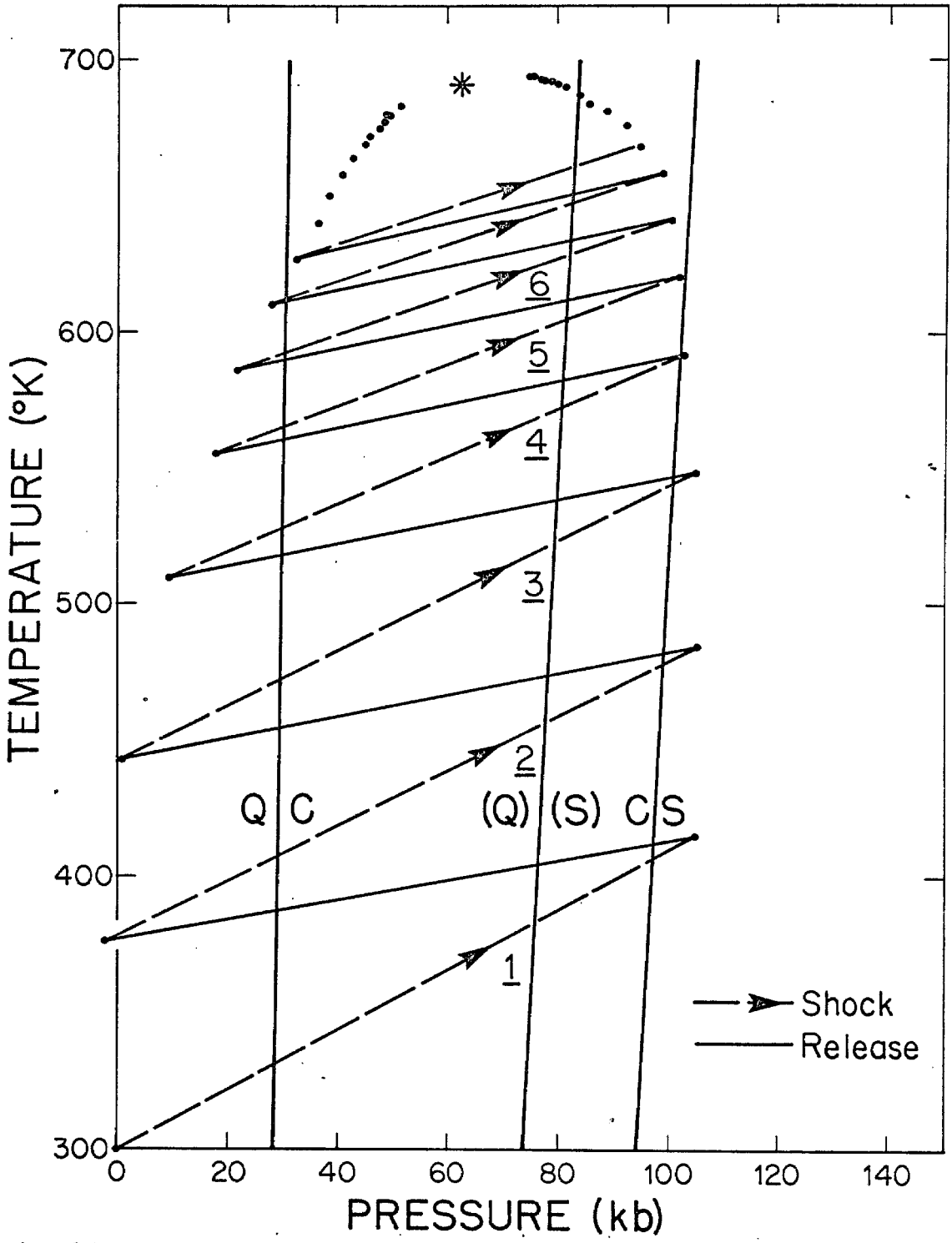

Fig. 34. Pressure-temperature traverses of a unit mass of material. Shock "paths" are shown by dashed lines, but the temperature is actually discontinuous. Final equilibration temperature (*) is obtained by interpolating between the last calculated points.

microseconds, the transition can proceed while the material is temporarily in the high-pressure regime, even though the final equilibration pressure is not in the high-pressure stability field. No consideration has been given to how the process of phase change would affect the equilibration pressure or the equilibration phases.

With the use of this model, the effect of nonuniform porosity, due to either bedding or to local variations in porosity, can be examined. Regions of locally varying porosity in the original material affect the shock and cause relatively hotter and colder spots to form as the shock wave passes. The "hot spots" are the focus of energy deposition and might be expected to contain areas of more highly metamorphosed grains.

To simulate the nonuniform porosity of the Coconino sandstone, gaps of 0.2 mm were placed between grains number 1, 2, 3, 4, 5, and 6 and gaps of 0.0667 mm between the remaining 0.2 mm grains, thus creating an area of 50% porosity within a medium of 25% porosity. The resulting P-V traverses of a unit mass of material in grain number 1 are shown in Fig. 35. The first five reflections from the 0.2 mm pores allow grain number 1 to be released into states of tension. Most of the heating of the grain occurs during the first five shocks and releases because the energy deposited irreversibly (the sum of the areas between successive Rayleigh lines and release adiabats) is large. The increase in temperature associated with the shocks is shown in Fig. 36 and compared to the temperature increase due to a similar number of shocks in a material of uniform 25% porosity. The shock equilibration

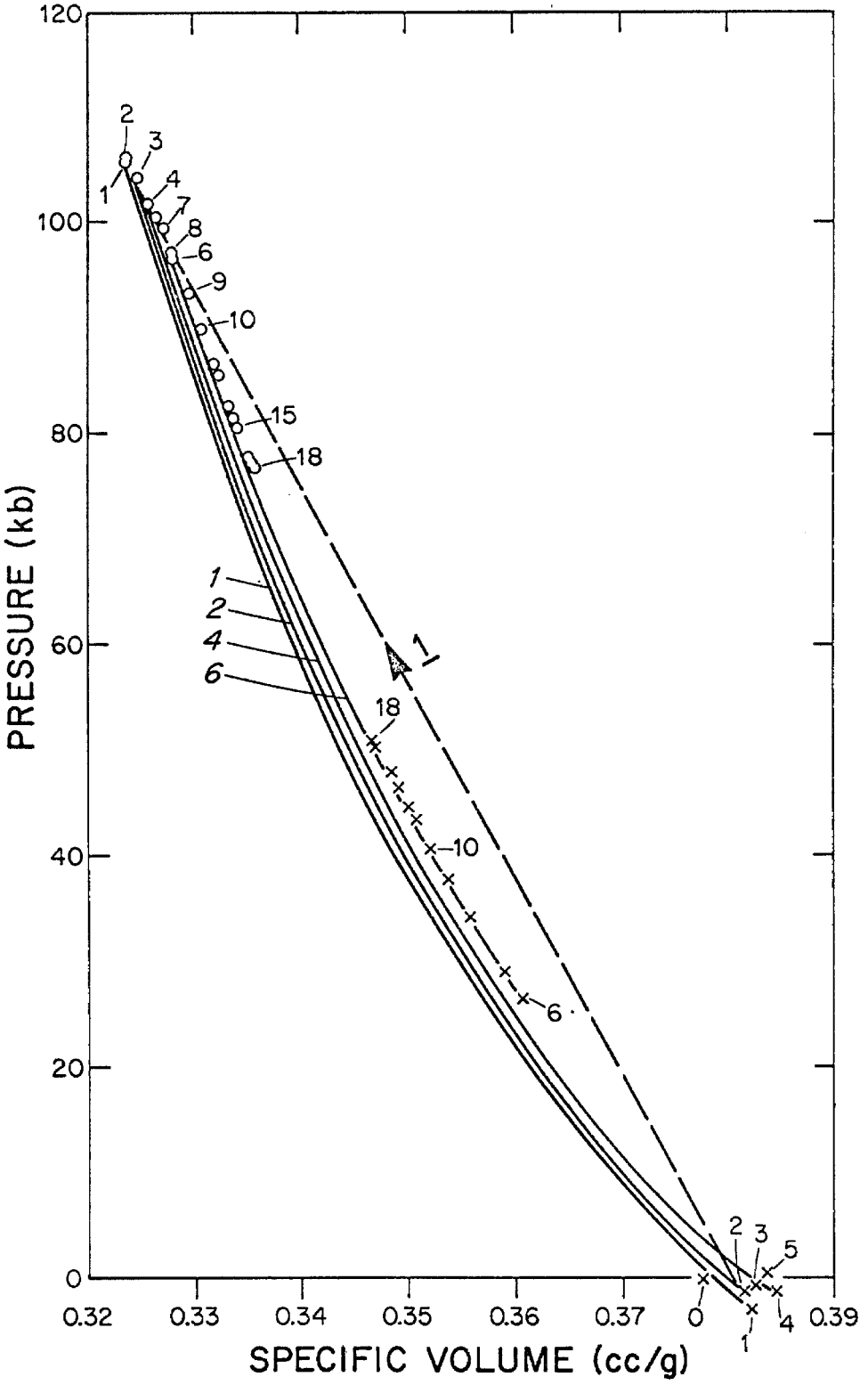

Fig. 35. Pressure-specific volume traverses of a unit mass of material in a locally porous area. Notation is same as for Fig. 31.

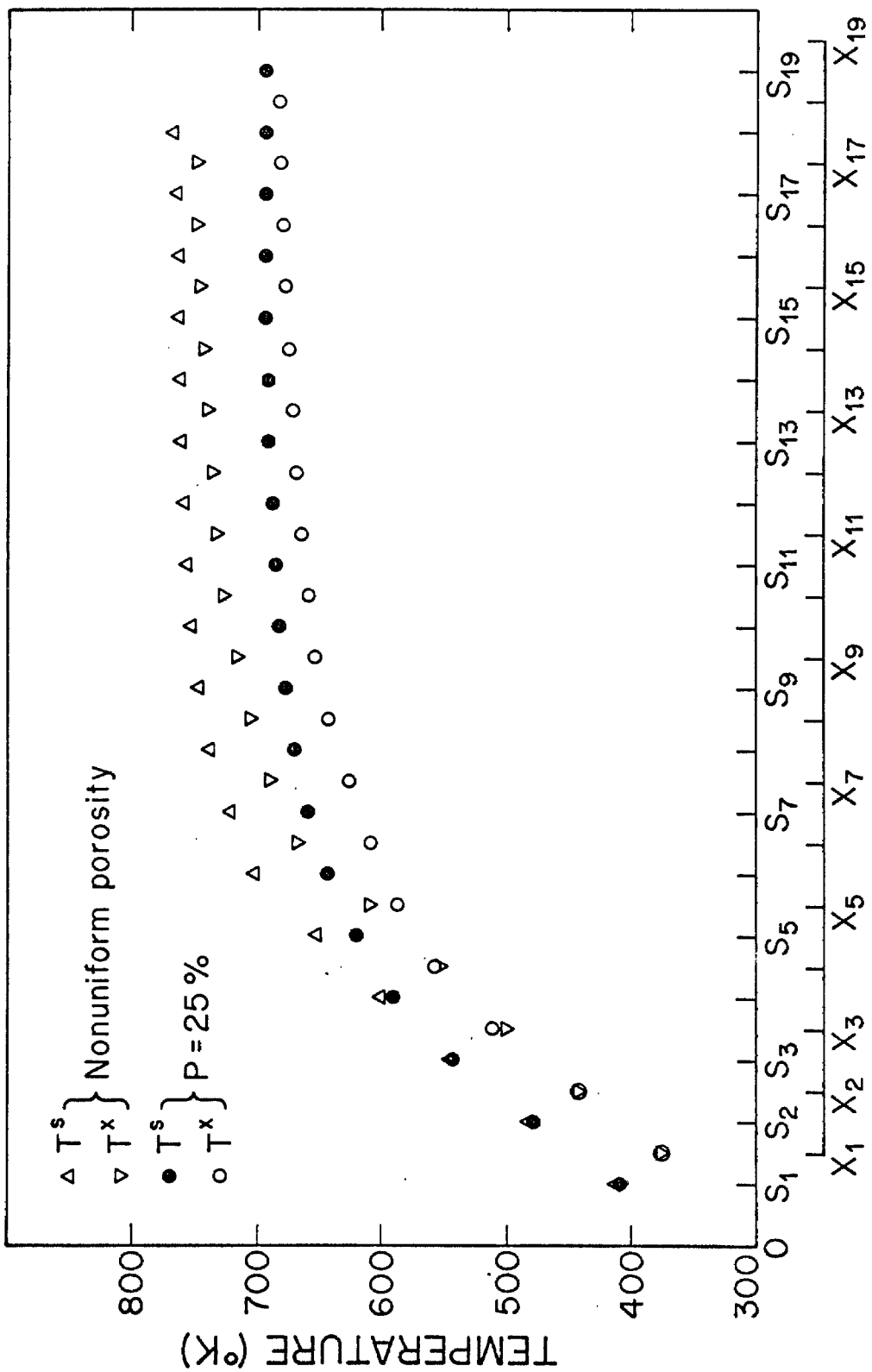

Fig. 36. Temperature of a unit mass of material in successive shock states, S_n, and rarefaction states, X_n. The history of a grain in a medium of 25% porosity is shown by circles and in an area of 50% within a medium which otherwise has 25% porosity by triangles.

temperature is 80° higher in the "hot spot". Because of the multitude of variations in porosity that could exist in a sandstone, local temperature increases of 100° seem plausible due to this mechanism.

Variations of initial porosity may cause variations of deposition of energy over a distance of several grain widths. To explain the observed relationships of fracturing and phases in the shocked Coconino, however, a mechanism is required which will allow deposition of energy locally at the grain boundary. The computer model used to simulate the one-dimensional shock problem is not adequate for considering details of the behavior at grain interfaces because of the artificially large viscosity used to control the stability of the equations. This artificially large viscosity acts to increase the internal energy at impacting grain interfaces by nearly a factor of 1.5 over the mean energy for the grains. The calculations do suggest that large viscosities could be a cause of local energy deposition at grain boundaries but cannot be investigated quantitatively.

Another possible cause of nonlocal energy deposition is the overtaking of leading shocks by trailing rarefactions, resulting in multiple shocks in some parts of the material but not in others. Consider the case of a single pore in an otherwise infinite one-dimensional medium in which a shock is travelling to the right (Fig. 37). The material to the left of the pore is initially shocked to a peak pressure. As the shock reflects from the pore, material adjacent to the pore is released to zero pressure by the left-travelling rarefaction wave. As the pore collapses and the left side impacts the right side, a left-travelling shock is generated. This left-travelling shock will eventually

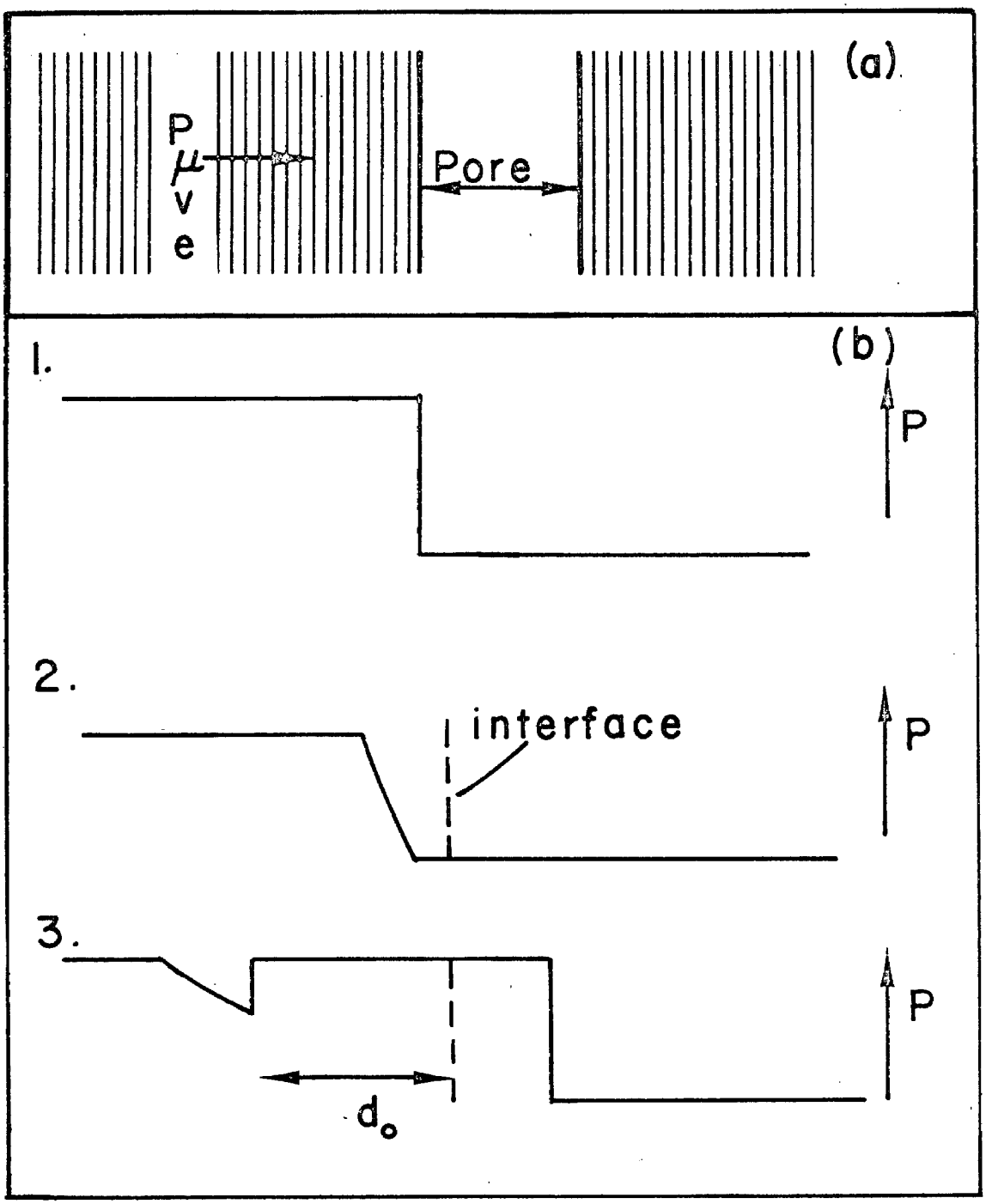

Fig. 37. (a) A single pore between two plates at the instant that the shock in the left plate reaches the free surface. (b) The pressure in these two grains at three times: (1) at t = 0, the instant that the right-travelling shock reaches the free surface of the left grain, (2) just prior to collision of the left and right grains, and (3) at some later time when the shock has overtaken most of the rarefaction wave. Coordinate system is centered on left grain.

overtake the left-travelling rarefaction at some distance d_o into the shocked material. All material between the collapsed pore and this point will have been shocked once, released once and shocked again. This leads to an excess energy deposition by the mechanism discussed previously. All material to the left of d_o would be affected by the collision of the left- and right-travelling shocks; this collision would presumably result in different energy deposition from the multiple shock process. (The collision of a left- and right-travelling shock was not investigated in this thesis.) If d_o were a fraction of the grain diameter, this process could account for local deposition of energy at grain boundaries. In all calculations, however, d_o was on the order of three or more grain diameters.

The conclusions from this one-dimensional consideration of energy deposition in a porous material may be summarized as follows: (1) The mechanism of equilibration to a final thermodynamic state in a granular material is the reverberation of shock and rarefaction waves created by multiple grain impacts. (2) This reverberation results in the deposition of energy in a porous material in excess of that deposited in a similar solid material because there are differences in the thermodynamic paths for each successive wave. (3) Peak shock pressures in individual grains may be as much as twice the final steady-state pressure. In the case of quartz, the grain may have significant residence time in a stability field other than that to which it finally

equilibrates. (4) Local variations of porosity within a material before it is shocked may account for nonuniform deposition of energy in grains. (5) The reverberation of shock and rarefaction waves can account for the average shock properties of a granular material (P, V, T), but cannot account for the microscopically observed nonuniformity of energy deposition. (6) Large dynamic viscosity at grain boundaries may be a cause of local energy deposition, but cannot be investigated quantitatively with models with mesh sizes necessary for the investigation of multiple-plate impacts.

ELASTIC MODEL FOR STRESS IN SAND GRAINS DURING IMPACT

To obtain a qualitative idea of stress concentrations in impacting sand grains, consider the impact of two perfectly elastic spheres of identical size and properties. This problem was considered by Hertz (1896) and, more recently, summarized by Timoshenko and Goodier (1970). We wish to consider the state of deformation and stresses which initially occur in the region very near the point of contact. Let the spheres touch at time $t = 0$ and compress elastically until some time t_1 when maximum deformation of the surfaces in contact is attained. The surface which is common to the two bodies when in closest contact shall be called the surface of contact. If the time taken for the spheres to reach closest contact is short compared to the time taken by shock waves to traverse the length of the spheres, the elastic state of the two bodies near the point of impact may be approximately the same as the state of equilibrium which is produced by a total pressure assumed to be acting between the two bodies for a long time (after Hertz, 1896; Timoshenko and Goodier, 1970). The total pressure will change rapidly from the time of initial contact to the time of closest approach, but the general form of the stress field may be expected to remain unchanged during the initial instants of collision. It should be emphasized that the solution to the problem approximated in this way, at best, will give a model of the deformation of spheres during the first instants of impact, before rarefaction waves, which arise when the shocks reflect from the surfaces of the spheres, reach the region in the vicinity of the contact surface. Thus, the solution can be extended no further in time

than the instant, t_1, at which closest approach of the spheres takes place.

Let α be the distance the centers of the two spheres approach each other due to local compression at the point of contact. The compressive force F is obtained by considering the deceleration of the two spheres and, for spheres of identical mass, m, F is (Timoshenko and Goodier, 1970)

$$\ddot{\alpha} = -F\,(2m) \tag{2}$$

The solution for α from the differential equation of motion is

$$\alpha = \left(\frac{5\sqrt{2}\pi}{4}\,\rho\,\frac{(1-\nu^2)}{E}\,v^2\right)^{2/5} R \tag{3}$$

where ρ is the density of the spheres, ν is Poisson's ratio, E is Young's modulus, R is the radius and v is the impact velocity.

The compressive force F at the moment of closest contact is

$$F = \left(\frac{\alpha^3\, R \cdot 16}{9\pi^2\, 8k^2}\right)^{1/2} \tag{4}$$

where $k = \frac{1-\nu^2}{\pi E}$. The maximum radius of the surface of contact is

$$a = \sqrt[3]{\frac{3\pi}{4}\,F\,k\,R} \tag{5}$$

The maximum pressure, q_o, at the center of the surface of contact is

$$q_o = \frac{3F}{2\pi a^2} \tag{6}$$

Hence, given an impact velocity, v, and material properties ρ, ν, and E, the maximum pressure in the center of the region contact can be calculated at the time of closest approach. These equations are summarized

below in Table 5 in a manner that emphasizes the role of the radius of curvature of the impinging bodies and the velocity of impact.

For two 0.1 mm quartz spheres approaching each other at relative velocity 0.05 km/sec, the maximum pressure at the instant of closest approach is q_o = 93 kb. Observed values of elastic limits in quartz under shock depend on driving pressure and sample thickness. The highest observed values are for z-cut quartz, 65 to 130 kb (Wackerle, 1962). Therefore, impact velocities of greater than 0.05 km/sec to 0.08 km/sec will cause the maximum pressure in impacting spheres to exceed the maximum estimated elastic limits of quartz. The maximum pressure obtained by two infinite flat plates impacting each other with velocity v = 0.05 km/sec is less than 5 kb (estimated from Wackerle's (1964) pressure-particle-velocity relationship for elastic waves in quartz). Hence, at low impact velocities, maximum pressures in impacting spheres are approximately 20 times as great as would be attained by impact of flat plates!

Since the one-dimensional model, which gives correct average properties of porous materials, predicts that final equilibration pressures will be approximately half the peak pressures generated by plate impacts, peak pressures in spherical grains may be as much as 40 times the final equilibration pressure. This ratio will be a function of impact velocity and will be highest for impacts at low velocity.

The distance the centers of the spheres approach each other due to compression is α = 0.04 mm, i.e., each grain compresses 0.02 mm or about 1/5 of a grain radius.

Table 5

Formulae for the Impact of Two Elastic Quartz Spheres

For $*\nu = 0.077$ R in cm

$E = 0.95 \times 10^{12}$ dynes/cm^2 v in cm/sec

$\rho = 2.65$ g/cc

$k = (1 - \nu^2)/\pi E = 0.3 \times 10^{-12}$ cm^2/dyne

The distance the two spheres approach each other: $\alpha = 4.5 \times 10^{-5} v^{4/5} R$ cm

The compressive force: $F = 1.5 \times 10^{5} R^2 v^{6/5}$ dynes

The radius of the circle of contact: $a = 4.8 \times 10^{-3} R v^{2/5}$ cm

The maximum pressure at the center: $q_o = 3.1 \times 10^{9} v^{2/5}$ dynes/cm^2

$= 3.1 v^{2/5}$ kb

* Parameters obtained from O. L. Anderson, et al., 1968;
E calculated from bulk modulus and Poisson's ratio, $E = 3K(1 - 2\nu)$.

The maximum pressure q_o is obtained at the center of the surface of contact. The variation of compressive stress, σ_z, with depth along an axis, z, connecting the centers of the two spheres is shown in Fig. 38. The z-axis, in analogy with features defined in Type Ib rocks, may also be called the concussion axis. The radius of the surface of contact is taken as the unit of distance; the magnitude of q_o is taken as the unit of stress. The compressive stress, σ_z, decays rapidly with depth; as a rough measure, σ_z decays approximately as the square of the distance from the point of contact. The other two principal stresses σ_r and σ_θ at the center of the surface of contact are equal to $1/2\,(1 + 2\nu)\,\sigma_z = 0.3\sigma_z$ for quartz.

In the case of brittle materials such as quartz under low stresses, failure is produced by tensile stress because the tensile strength is low compared to the compressive strength. The maximum tensile stress occurs at the circular boundary of the surface of contact. It is radial to the center of the surface of contact in the plane of the surface of contact and has the magnitude

$$\sigma_r = \frac{(1 - 2\nu)}{3}\, q_o \sim 0.3\, q_o \qquad (7)$$

for quartz. Tensile fractures will tend to form normal to the maximum tensile stresses and would therefore form concentric to the boundary of the contact surface. Divergence of the tensile stress field with distance away from the contact surface would probably cause the tensile fractures to have the appearance of cones, truncated at the contact surface and diverging into the grains. A cross section of this pattern would give fractures which diverge radially from the contact surface into the grain;

this is the pattern of fractures seen in the grains with concussion fractures in Type Ib rocks.

The maximum shearing stress is small at the center of the surface of contact. The point with maximum shearing stress is on the z-axis at a depth equal to about half of the radius of the surface of contact. Along the boundary of the surface of contact, where normal pressure on the surface becomes equal to zero, shear stresses exist of magnitude $q_o(1 - 2\nu)/z \sim 0.3\ q_o$ for quartz. This stress is smaller than the maximum shearing stress at depth $z \sim 1/2$ a, but it is larger than the shearing stress at the center of the surface of contact where the compressive stress is the largest.

In summary, the Hertzian model for the elastic impact of two spheres suggests the following model which will be used in interpretation of the observations on the shocked Coconino:

(1) Maximum compressive stress in early stages of the impact of irregular quartz grains occurs at the center of the surface of contact and may be up to 20 times the compressive stress computed for impacting plates at low velocities and may be up to 40 times the final equilibration pressure in a sandstone of 25% porosity.

(2) The compressive stress decays rapidly with distance into the center of the grain.

(3) Brittle fracturing occurs along radials which emanate from the edges of the surface of contact and extend into the grains.

(4) The maximum shear stress occurs on the z-axis some distance below the center of the surface of contact; appreciable shear stresses also exist circumferential to the boundary of the surface of contact.

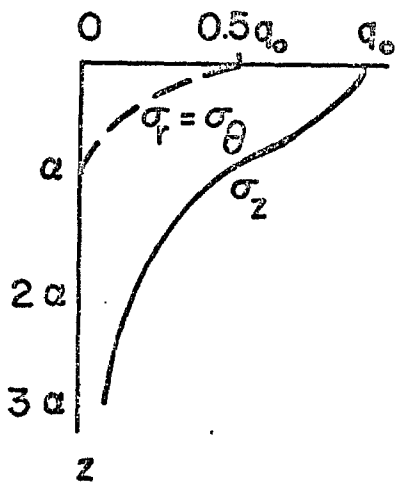

Fig. 38. Variation of stress with depth along concussion axis (z) in two impacting elastic spheres. Variation of σ_z with depth after Timoshenko and Goodier, 1970. Variation of $\sigma_r = \sigma_\theta$ for Poisson's ratio $\nu = 0.077$ is estimated.

GENERAL MODEL OF PORE CLOSURE, TRANSIENT STRESS AND TEMPERATURE DISTRIBUTION

Although it would be desirable to have theoretical models for the impact of nonplanar materials at all pressures and temperatures, such models do not exist. A model of pore closure and grain impact must therefore be constructed on the basis of the considerations presented for planar and spherical impacts.

Pore closure in granular materials must be nearly one-dimensional strain to conserve momentum in the shock front. Grains impact each other across pores with very little shearing of the pore walls. As the grains impact, locally high stresses are generated because of the nonplanar geometry of the grains. The stress field of grains near the pores decays toward the interior of the grains. Locally high shear and tensile stresses are generated near the contact surface of impacting grains. A large increase of internal energy and temperature in the grain boundary regions shocked to locally high pressures will occur. These regions will be quickly released to lower pressures by acoustic release waves, but reverberating waves from nearby impacts will reshock all material several times, depositing energy irreversibly with each shock and release. After the shock front has travelled several grain diameters from the pore, equilibration pressures that are lower than the peak pressures generated in the grains will be attained.

If a transition to a high-pressure phase proceeds in times less than a few microseconds, high-pressure phases may form at the grain

boundaries even when the final equilibration pressures are less than those required to transform to the high-pressure phase under hydrostatic conditions. Times on the order of tens of milliseconds are available before the shock pressure finally decays to lower pressures than required to form the SiO_2 high-pressure phases. If the transition rate to a high-pressure phase is temperature dependent or is accelerated by shear stresses, the phase will most likely form fastest at grain boundaries near pores.

EXPERIMENTAL DATA ON SHOCKED COCONINO SANDSTONE

One of the goals of this study of the Coconino sandstone is to correlate petrographic properties of a naturally shocked rock with shock pressures measured in laboratory experiments on specimens of the same rock. Previous studies of shocked rocks have relied on experimental Hugoniot data for single crystals (e.g., quartz, feldspar, biotite) to estimate pressures and temperatures in the rocks (Chao, 1968; v. Engelhardt and Stöffler, 1966). These previous studies and the observations on naturally shocked Coconino demonstrate that nonuniform conditions of pressure and temperature occur at least temporarily in the rocks. However, pressure equilibration, if not thermal equilibrium, is probably attained in the rock within the first few microseconds after the passage of the leading edge of the shock, and it is desirable to have some estimate of this equilibration pressure. With a careful interpretation of the Coconino sandstone equation of state data and the observations on the shocked sandstone, estimates of this pressure can be made for the Meteor Crater rocks.

The most important effects of shock metamorphism, the transitions to high-pressure phases, may be time dependent. These reactions would then appear to a very much greater extent in the naturally shocked rocks than in laboratory shocked material. The quartz-coesite transition is sluggish even under conditions of static compression experiments and requires temperatures of 400-500°C to proceed at an appreciable rate (Boyd and England, 1960; MacDonald, 1956; Griggs and Kennedy, 1956;

Kitihara and Kennedy, 1964). The reaction rate is accelerated by the presence of shearing stresses (Bell, et al., 1965; Bell and Boyd, 1968). Coesite has generally not been found in laboratory shock experiments (Chao, Shoemaker and Madsen, 1960; DeCarli and Jameson, 1959). A single finding of coesite in a shock experiment is mentioned by Shipman and Gregson (1970).

Further indication that coesite forms only in shock waves of longer duration than are attainable in a laboratory shock event is that very small amounts of coesite are found only at nuclear explosion craters and meteorite impact craters in granular soils, which are greater than 200 m in diameter (Meteor Crater, Wabar Crater, Scooter and Teapot nuclear explosion craters, E. M. Shoemaker, personal communication). Shoemaker also reports that Chao, in an extensive search of the ejecta from Henbury Crater (diameter 200 m) did not find coesite. It thus appears that the duration of a shock wave associated with the formation of a crater approximately 200 m in diameter is required for the formation of coesite. This is a shock of several milliseconds duration.

Two reported experiments indicate that stishovite or a short-range order form of SiO_2 with Si in six-fold coordination, can form in shock waves of the duration of laboratory shock events (microseconds). Stishovite has been synthesized in material shocked to 150 kb (DeCarli and Milton, 1965) and was recovered intermixed with large amounts of glass from the shock experiments. Release adiabats from shock states for quartz (Ahrens and Rosenberg, 1968) approach the zero-pressure

volume of stishovite and indicate that over 75% of the material formed at high shock pressures greater than 400 kb stishovite.

Shock equation of state data (the Hugoniot) for single-crystal quartz may be divided into three regimes.

In Regime I, material is compressed by elastic waves. Pressures in this regime range from 35 to 50 kb for x-cut quartz to 80 to 130 kb for z-cut quartz (Wackerle, 1962; Ahrens and Rosenberg, 1968; Fowles, 1961).

At higher pressures, Regime III, quartz appears to be completely converted to a high-pressure phase. McQueen, et al. (1963) and Ahrens and Rosenberg (1968) have suggested that this phase is stishovite on the basis of the release density of shock states between 300 and 350 kb. The lower limit of Regime III is 300 kb (Ahrens and Rosenberg, 1968; Wackerle, 1962).

Between Regime I and Regime III is a regime (II) in which the shock compressed volume of quartz is less than the volume of quartz compressed isothermally (Bridgman, 1948, 1949). This suggests that in this regime a mixture of phases is formed -- quartz and stishovite or possibly quartz, coesite and stishovite. Pressures appropriate to this regime are 130 to 300 kb.

The Coconino Hugoniot is shown in Fig. 39 in coordinates of pressure versus volume; the data of Shipman and Gregson (1970) and Ahrens and Gregson (1964) for Coconino sandstone, as well as the second wave data of Wackerle (1962) (which assumes hydrostatic compression) for single-crystal quartz are shown. Considerable scatter exists in the

data. This scatter increases the difficulty in interpreting the behavior of the sandstone under shock compression. The following interpretation is primarily after Ahrens and Gregson (1964) with consideration being given to the more recent data of Shipman and Gregson (1970) in those pressure regions where their data supplement the earlier data.

A system of pressure regimes in which certain phenomena occur may also be set up for Coconino sandstone Hugoniot data. These regimes (Fig. 39), which shall be denoted here as A, B, C, D, E, F to avoid confusion with the numbered regimes of the single-crystal quartz Hugoniot, are modified from those proposed by Ahrens and Gregson (1964).

In Regime A the sandstone deforms elastically, that is, grains are not permanently deformed, and pores are not permanently compressed. This regime extends to 2 to 9 kb (Ahrens and Gregson, 1964).

In Regime B the volume of the compressed sandstone is greater than the original volume of unshocked single-crystal quartz. This means that remnant porosity exists in the rocks under shock compression. The upper limit of pressure in this regime is between 22 kb (Ahrens and Gregson, 1964) and 45 kb (Shipman and Gregson, 1970). 30 kb will be assumed as an average value of the maximum pressure of Regime B.

In Regime C, the volume of the compressed sandstone is less than the initial volume of quartz and approaches the volume of shocked single-crystal quartz (Wackerle, 1962) at higher pressures. States in this pressure regime are interpreted to represent final states in which the porosity is reduced to zero and compression of the quartz grains

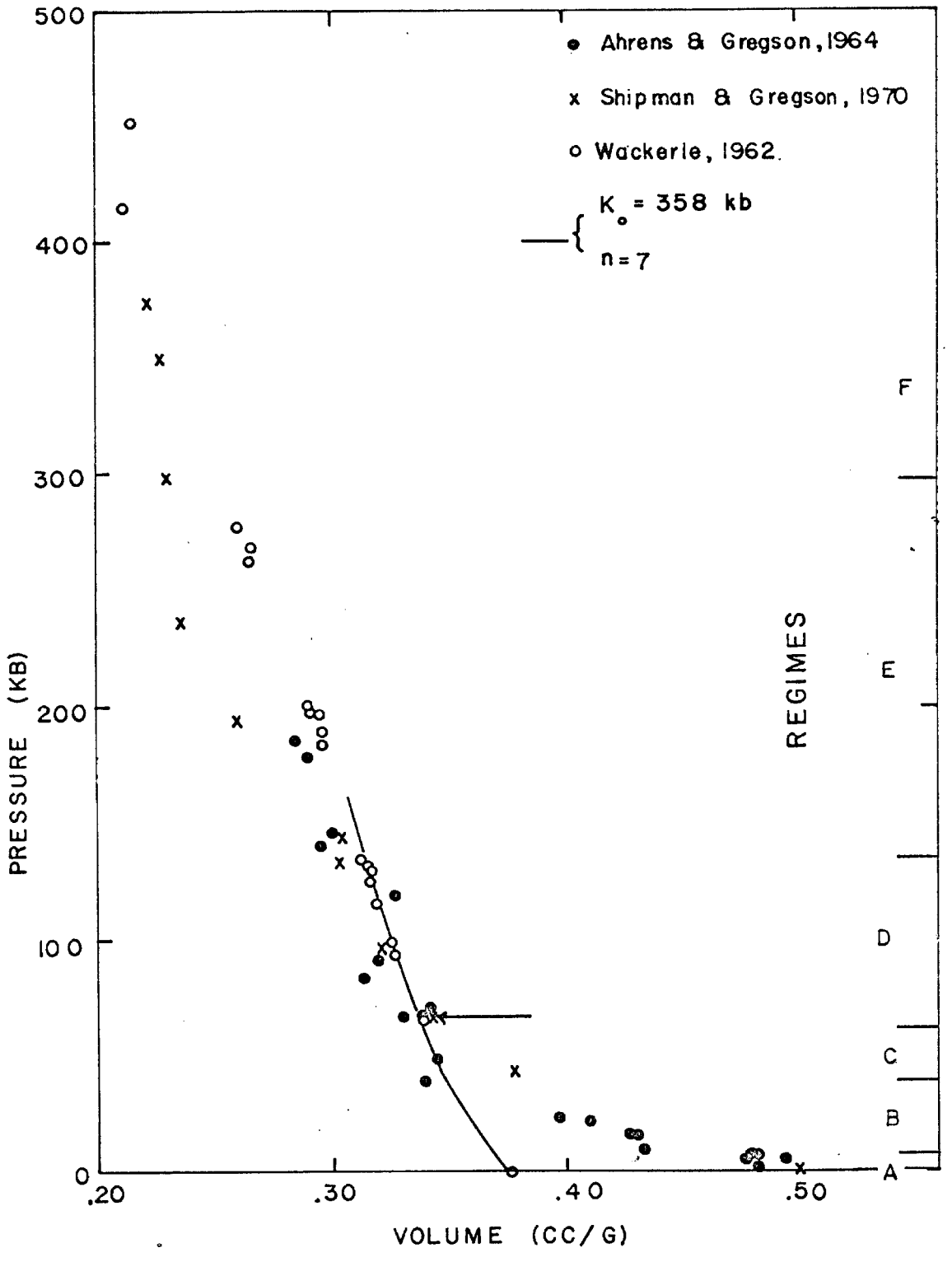

Fig. 39. Measured Hugoniot data points for Coconino sandstone (x, •) and single crystal quartz (o). The solid line is the Murnaghan equation for single-crystal quartz used in the one-dimensional model. The tip of the arrow represents a shock state computed by the one-dimensional model described in Chapter IV.

also occurs. Regime C extends from 30 kb to approximately 55 kb; the latter number is representative of the combined data of Ahrens and Gregson (1964) and Shipman and Gregson (1970). The upper limit obtained by considering the two data sets separately is 36 kb and 130 kb respectively.

From 55 kb to approximately 130 kb, the sandstone data follow closely the single-crystal Hugoniot of Wackerle. Small amounts of a high-pressure phase may be formed in this regime (D), and Shipman and Gregson have suggested coesite. However, release adiabats of Ahrens and Gregson (1964) in this pressure regime follow paths that would be expected if the material were solid quartz. It seems plausible, however, that if an impact event were of sufficient duration, coesite would be formed in this pressure regime.

At pressures above 300 kb, the sandstone is compressed to densities appropriate to shocked stishovite. The part of the Hugoniot above 300 kb shall be called Regime F. The release adiabat data of Ahrens and Rosenberg (1968) indicate that stishovite formed at pressures greater than 350 kb will melt to glass upon release to ambient pressure.

At pressures between 130 kb and 300 kb, the specific volume of the sandstone Hugoniot must be interpreted to imply that a mixture of phases is present, Regime E. At this time the phases of SiO_2 in this mixed phase regime are unknown, but it is conceivable that any combination of high-pressure phases, quartz and glass that accounts correctly for the specific volume could be present.

SHOCK COMPRESSION OF THE COCONINO SANDSTONE

Interpretation of Type I rocks. The lowest observed degree of shock metamorphism of the Coconino is found in Type Ia rocks in which a few grains are broken or strained, but which, in hand specimen, are practically unaltered from the original condition. The porosity was slightly reduced by rotation of individual grains or groups of grains into the pores. Sufficient stresses passed through these rocks to break them loose from the bedrock and eject them from the crater. Because these rocks contain only slight permanent deformation, they were probably formed in Regime A of the Hugoniot and have been shocked to equilibration pressures less than the 2-9 kb elastic limit measured by Ahrens and Gregson (1964). Since almost no fracturing of grains occurred, peak pressures were probably less than 10 kb.

At slightly higher pressures, characteristic of Type Ib rocks, grains are deformed by fracture. Small permanent strains have been induced in a few of the quartz grains, indicating that small amounts of plastic deformation occurred. Concussion fractures in impacted grains are observed radiating into the grains from the contact surface. Experimental work of Borg, et al. (1960) has shown that the deformation of dry quartz at room temperature is purely elastic to the point of rupture. A model of the impact of two spherical elastic quartz grains was therefore constructed to approximate the impact of two irregularly shaped quartz grains. The solution obtained for this model predicts a pattern of fractures, such as the observed concussion fractures, which

are due to tensile stresses in the initial moments of impact. In a sandstone, the problem of impact is complicated by the lateral support which each "sphere" receives from the neighbors in contact. This lateral support may inhibit tensile fracturing and support failure by shear. That the radial patterns of tensile fracturing predicted by theory to exist in the initial instants of compression are observed suggests that these fractures were formed before the mean pressure in the sandstone became large, i.e., in the impact of the sand grains caused by the first shock. Thus the observed alignment of concussion axis directions may be interpreted to give the direction of shock passage. Successive reflected shocks would quickly erase the initial pressure gradients in the grains. Nests of chips beside the contact surface and chips within the radial fractures and on the contact surface may be derived from the region of first contact.

The tensile strength of quartz is on the order of 1 kb (Borg, et al., 1960). Therefore, from Eq. 7, maximum compressive stresses, q_o, of 3 to 4 kb are sufficient to produce these fracture patterns if the grains are unconfined. The Hugoniot data indicate that pressures up to 55 kb (Regime B) may be required to eliminate porosity during shock compression. Equilibration pressures up to 70 kb (Regime C) appear to produce no phase changes in laboratory shock experiments and may have existed in the Type Ib rocks if the quartz-coesite transformation were sufficiently slow.

A missing rock? It is possible that some members of Type I rocks were not included in this study. Small fragments (less than 1 cm in diameter) of very white shocked material can be seen in exposures of

fallout; these fragments are too friable to be removed from their location without falling apart. They may be a more highly crushed member of the Type Ib series than was collected for this thesis. Field investigations and grain size analyses of these fragments should be done to identify their position in the sequence of shocked rocks.

Interpretation of Type II rocks. Plastic deformation, lack of brittle fracturing and the formation of small amounts of coesite and glass on grain boundaries are the distinctive characteristics of Type II rocks. Pore closure and elimination of porosity in Type II rocks was accomplished by a very different process than occurred in Type I rocks. The grains appear to have flowed plastically around each other and into the pores, forming an intricate network of grains that resembles a jigsaw puzzle.

The shape and distribution of the elongated and aligned symplektic regions in Type II rocks suggests that they are associated with collapsed pores. Microcrystalline coesite formed in the symplektic regions and occurs only in rocks which have deformed plastically. Coesite occurs in Type II rocks in regions where high local mean stresses and high shear stresses are believed to have been generated, that is, at the contact surface between irregularly shaped grains. Initial shear in a region may be necessary for the formation of coesite by shock.

Microcystalline coesite is believed to form under nonequilibrium conditions and to grow slowly during the shock because:

(a) A time on the order of tens of milliseconds was available for the transformation to occur while the grains were at pressures appropriate to the stability field of coesite; yet very little coesite formed. The pressures required to produce the observed plastic yielding in quartz probably exceed the pressures required to produce coesite under hydrostatic conditions. Yielding in quartz is believed to occur between 35 kb (for x-cut quartz) and 130 kb (upper limit for z-cut quartz, Wackerle, 1962). If initial pressures and temperatures at the grain boundaries exceeded the coesite stability field (i.e., exceeded 100-120 kb), coesite would probably not have formed until the pressures and temperatures decayed to the stability field in the rarefaction wave. During the rarefaction, times up to 30 msec were available while the material was in the coesite stability field. Since only minor amounts of coesite formed in these rocks, the transition must not have proceeded rapidly at pressures and temperatures appropriate to Type II rocks.

(b) In the sequence of 48 shocked rocks studied, there is no rock which is composed entirely of coesite, which would be expected if coesite formed rapidly in the shock front.

The replacement of quartz by coesite in vermicular habit appears in thin section to have proceeded more completely at the centers of the symplektic regions than in the margins. The growth of coesite in regions away from the boundary regions of high stress and high initial

internal energy may have been controlled by the temperature gradient from the boundary of the grain, which was initially the focus of energy deposition, into the center of the grain. The occurrence of glass intermixed with the coesite in the symplektic regions cannot be satisfactorily explained at this time. It is unlikely that temperatures in these regions were as high as the melting point of quartz. This glass may be similar to the diaplectic glass described by Chao (1968) and may be caused by solid-state disordering of the quartz lattice in the shock wave. It is possible that a disordered SiO_2 phase such as this glass is formed as an intermediate phase in the quartz-coesite shock transition if the density of the glass at the pressures at which the transition took place is intermediate between the density of quartz and coesite at that pressure. Alternatively, the microcrystalline coesite may have formed directly from quartz, and the glass may have formed by inversion of small regions of coesite upon release to lower pressures.

Peak pressures must have been greater than required for plastic yielding; values of 35 kb to 130 kb are suggested for the yield point. Peak pressures were apparently less than 300 kb, the pressure at which quartz appears to be completely converted to a high-pressure phase in the shock front. Equilibration to an average shock pressure in the coesite-stability field may have occurred since small amounts of coesite were formed. Equilibration pressures in Regime C may be appropriate -- 30 to 70 kb.

Interpretation of Type III rocks. In thin section Type III rocks have some features in common with Type II rocks. Regions which are transformed to high-pressure phases are elongated and locally aligned, and

are distributed in a way that closely resembles the distribution of pores in the initial rock. The shape and size of the remnant quartz grains suggests that pore closure and grain deformation in these rocks were accomplished by plastic flow rather than by brittle fracture.

The observations on Type I and II rocks suggest that the highest pressure regions were those nearest the boundaries of the quartz grains, and, correspondingly, farthest from the centers of the grains. In Type III rocks, the regions containing high-pressure phases, in order of increasing distance from the centers of quartz grains, are the symplektic regions, the opaque regions and the cryptocrystalline cores. It follows by analogy with Type I and Type II rocks that the cryptocrystalline cores were the regions of highest transient pressure.

The peak pressure in the region of the cryptocrystalline coesite cores is thought to have been greater than in the adjacent stishovite-bearing regions. The minimum pressure at which stishovite can form is 70 kb (by a metastable transformation from quartz). Peak pressures in the cryptocrystalline cores may have been substantially higher.

The cryptocrystalline fabric of the coesite cores could be due to the sudden nucleation of coesite at numerous random sites or could be controlled by the grain size of another material initially formed in the region. In either case, since the cores were formed early in the shock process, the cryptocrystalline fabric of the coesite cores suggests that all quartz in the region was destroyed prior to nucleation of the cryptocrystalline coesite. Pressures in excess of 150 kb are required to shock SiO_2 to a state from which the release densities are greater

than the density of coesite (Ahrens and Rosenberg, 1968). Pressures near 250 to 300 kb are required to transform most of a quartz region to high-pressure phases by a single shock. At these pressures quartz is converted to stishovite or to a short-range order glass in six-fold coordination (Regime III of the single-crystal quartz Hugoniot). It is interpreted that the regions which presently contain cryptocrystalline coesite were temporarily shocked to pressures in Regime F and that all of the quartz in the region was converted to stishovite. Owing to the decrease of entropy in conversion of quartz to the high-pressure phase, the stishovite regions became hot. As the exact pressure of the transformation is unknown, minimum temperatures in these regions have been estimated assuming

(a) that the transformation proceeds to completion at a local pressure of 144 kb (Wackerle, 1962). This is the lowest pressure at which it appears that any stishovite is formed in a shocked state.

(b) that the transformation requires a higher pressure to proceed to completion.

A pressure of 256 kb was chosen for case (b) because the temperature of stishovite formed at this pressure had been previously calculated by Ahrens, Anderson and Ringwood (1969). This choice provided a check for the model used here. In both calculations it was assumed that stishovite was formed by a single shock wave, so that the shock energy is given by the Rankine-Hugoniot jump condition for a single-step process. To estimate the minimum temperature difference

between the stishovite region and an adjacent region composed of untransformed quartz, the temperature of metastable quartz at 144 kb and 256 kb was calculated by the one-dimensional plate model described earlier in this chapter. The methods are given in Appendix E and the results are summarized in Table 6. The specific heat model described in Part II of this thesis was used for c_v in these calculations.

Table 6. Calculated shock temperatures of stishovite and metastable quartz at 144 kb and 256 kb.

	STISHOVITE		METASTABLE QUARTZ	
Pressure	Volume*	Temperature	Volume	Temperature
144 kb	0.266 cc/g	575°K	0.314 cc/g	491°K
256 kb	0.222 cc/g	1270°K (1245°K)**	0.297 cc/g	763°K

* The volumes of stishovite at 144 kb and 256 kb are computed from Ahrens, Anderson and Ringwood's (1969) published fit to the Hugoniot data at high pressures.

** Value of Ahrens, Anderson and Ringwood (1969) under assumption that stishovite is a Debye solid.

From these calculations it is evident that the temperature gradient across the high-pressure phase region into the quartz grains (a distance not exceeding 50 μ) was dependent on the pressure at which the stishovite formed. Temperature gradients from 2°/micron to 10°/micron may have occurred. Local peak pressures sufficient to form stishovite were maintained for only a few microseconds, and during this time radiation

and conduction could not appreciably decrease the temperature gradient across the regions (Appendix F).

Release of locally high pressure occurred in a few microseconds (pressure disturbances are propagated with the local sound speed (3-10 mm/μsec) and therefore traverse a grain diameter in a fraction of a microsecond). As hot stishovite regions were released to pressures appropriate to coesite stability conditions, they inverted to form the coesite cores. The high-temperature of the stishovite regions may have allowed the transition from stishovite to coesite to proceed at the phase boundary, approximately 100-120 kb. If the inversion to coesite occurred at the phase boundary, the temperature decrease associated with the (endothermic) reaction may be estimated from the slope of the phase line and an assumed specific heat and is on the order of 100°. It is possible, then, that (a) the residual temperature of the cores may have been reduced to approximately the same temperature as the surrounding regions or (b) may have been up to several hundred degrees hotter, depending on the initial pressure at which stishovite was formed. If it were several hundred degrees hotter, heat would have been conducted from a hot core into the surroundings during the 25-30 msec before release occurred to pressures below 30 kb. Twenty-five microseconds is sufficient time for excess heat in the core to be dissipated into surrounding regions, even if they are composed of glass (see Appendix F) which may have been formed as an intermediate phase in the quartz to coesite transition in the opaque regions. It is possible then that heat flow from a residual hot core could have accelerated the

rate of formation of coesite in the adjacent opaque and symplektic regions by increasing the temperature of the region.

In those coesite-rich regions which do not contain cores, a temperature gradient from regions of initial stress concentrations into the grain interiors may have controlled the rate of growth of coesite from quartz.

Metastable stishovite was preserved as the rarefaction wave released material through the coesite and quartz stability fields only in those regions which were relatively cool, that is, exterior to the main region of stishovite formation in the opaque material; most of the stishovite which was formed inverted to cryptocrystalline coesite. Approximately half of the coesite in rocks #4 and #33 is in the cryptocrystalline cores and is assumed to have been formed by the inversion of stishovite. Large amounts of metastable coesite are preserved apparently because of slow reaction rates at the low temperatures in the material by the time it is released to 30 kb.

The sequence of events for characteristic Type III rocks is interpreted to have been as follows. Upon impact of grains across pores, stishovite was formed from metastable quartz at pressures estimated to have been in excess of 250 kb. The temperature of these cores depended upon the pressure at which they were formed, but a temperature difference of 500° appears likely for cores formed at pressures in excess of 250 kb. Upon release of the locally high pressure in the stishovite region, coesite nucleated at many random sites, forming cryptocrystalline cores and lowering the excess temperature of the core

region by about 100°C. Microcrystalline coesite formed adjacent to the core regions. Heat conducted outward from the hot core into the surroundings may have accelerated the transformation rate of the quartz-coesite reaction causing abundant coesite to form in these rocks during the release of the material through the coesite stability field. The occurrence of microcrystalline coesite in opaque and symplektic regions on the borders of quartz grains and in vermicular habit with the quartz in the symplektic regions can be explained only by a model in which the quartz-to-coesite transformation proceeds slowly and in which the reaction rate is dependent on temperature gradients and/or initial shear stresses. The formation of coesite may have stopped when transient high temperatures decreased below certain levels or may have continued, at a decreasing rate, until the pressure decayed below 30 kb. Small amounts of stishovite are preserved in opaque regions, which are interpreted to have been relatively cool regions. The phases were then preserved metastably by quenching as the temperature decreased.

Pressures greater than 250 kb at grain boundaries probably did not exist for more than a few microseconds. Final equilibration pressures must have been less than 250 kb to account for the amount of residual quartz in the rocks. Peak pressures at grain boundaries were probably less than 350 kb, the pressure at which stishovite inverts to fused silica upon release to low pressures.

Interpretation of Type IV and V rocks. Type IV rocks are characterized by large areas of vesicular glass adjacent to coesite-rimmed quartz grains. Type V rocks are, for the purpose of this discussion, considered to be products of the processes described below in the limit of very high pressures.

The occurrence of vesicular glass in cores similar to the cryptocrystalline coesite cores of Type III rocks, suggests that the glass was formed from the same initial material as the cryptocrystalline coesite. These regions were apparently composed of stishovite formed above ~ 350 kb. Upon release from pressures above this value, stishovite inverts to glass, which is the material presently seen in the cores.

Skinner and Fahey (1963) first suggested that all of the silica glass found in direct association with stishovite formed by the breakdown of stishovite. Although measurements of amounts of phases in the shocked Coconino show that there is little glass in rocks containing detectable stishovite (Type III), the spatial relationships between the quartz, coesite and glass in Type IV rocks suggests that the glass in these non-stishovite bearing rocks formed by inversion of stishovite upon release to low pressures. Coesite may have been formed as an intermediate phase and then inverted to the observed glass.

In Type IV and V rocks, coesite which was adjacent to the stishovite cores apparently inverted to glass because of high temperatures. It is preserved only as rims against quartz grains, which must have been the regions which remained at lowest temperature during

shock compression of the Type IV and V rocks. The abundance of coesite in Type IV rocks containing 30 to 40% quartz suggests that coesite may be more stable at high temperatures and low pressures than stishovite.

The role of interstitial water must be considered in explaining the process by which the glass was formed. Observations on the shocked Coconino showed that water vapor was the most likely cause of the vesicles observed in the glass in Type IV and V rocks. The vesicles are thoroughly interspersed in the SiO_2 glass, an observation which poses the problem of finding the mechanism by which water which was originally interstitial can get into the interior of melted grains. Kennedy, et al. (1962) demonstrated that a critical end point for the univariant equilibrium melting curve of the SiO_2- H_2O system exists at 9.7 kb and 1080°C (Fig. 40). The composition of the system at this end point is 75% by weight SiO_2 and 25% by weight H_2O. Thus at pressures greater than 10 kb and temperatures greater than 1100°C complete intermixing of the SiO_2- H_2O phases occurs. If water were incorporated into the SiO_2 at pressures above 10 kb, some water would exsolve and form vesicles upon release to zero pressure. Incorporation of the water into an SiO_2 melt above 10 kb with subsequent exsolution of water vapor to form vesicles is apparently the process by which H_2O was thoroughly interspersed with SiO_2 in the Type IV and V rocks.

The glass in Type V rocks is frequently opaque owing to the presence of minute vesicles. By analogy with the glass and in consideration of the solubility of H_2O in SiO_2 at high pressures and

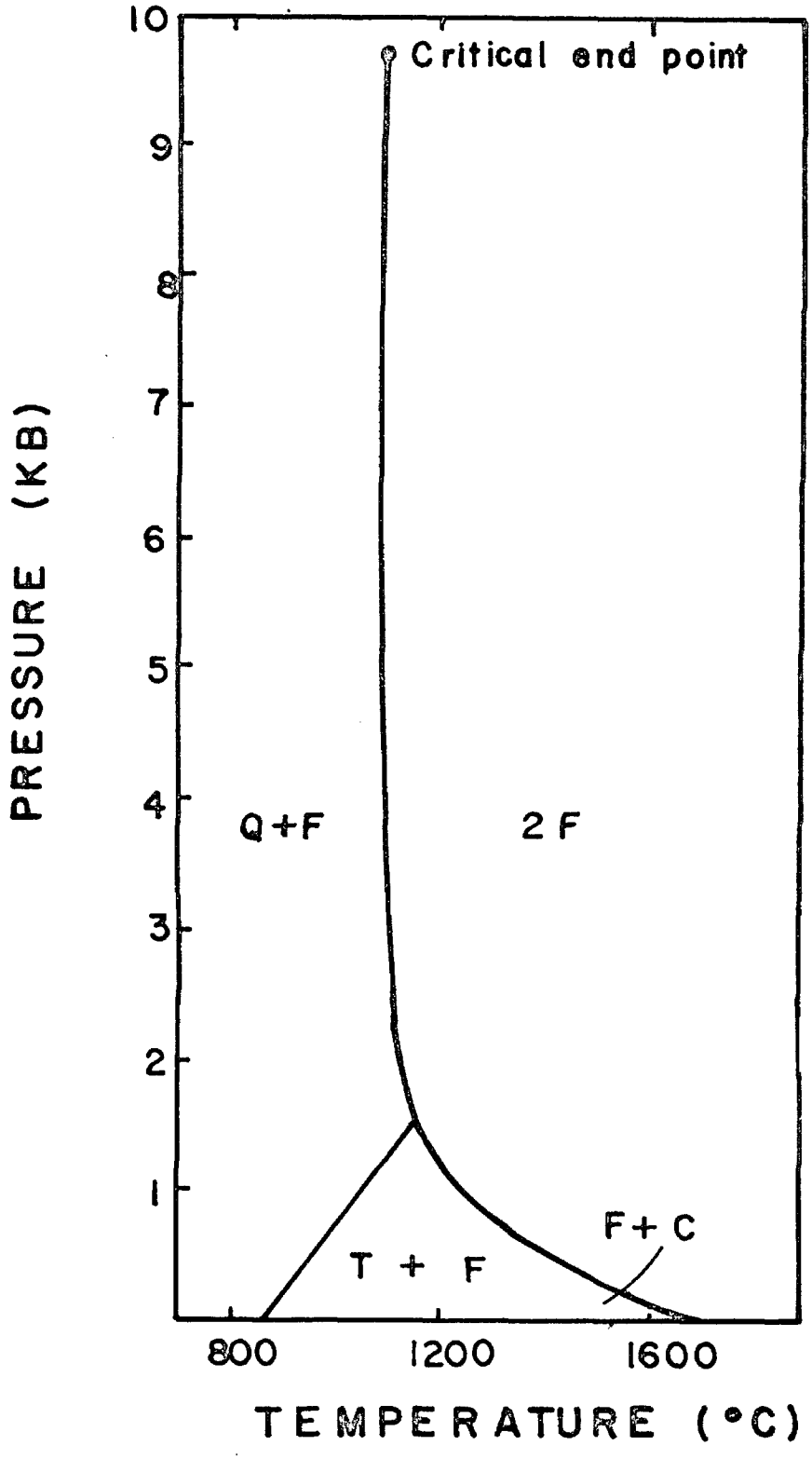

Fig. 40. Melting pressure of SiO_2 in equilibrium with H_2O on a P-T plane (after Kennedy, et al., 1962). Q = quartz, F = fluid, T = tridymite, C = cristobalite.

temperatures, it is hypothesized that the opacity of the coesite-rich regions is also due to the presence of minute vesicles which were formed by the solution of interstitial water into the boundaries of quartz grains. Study of the opaque regions by scanning electron microscopy may reveal the hypothesized vesicles.

The presence of interstitial water in the unshocked rock would lower the melting point of the adjacent SiO_2 to 1080°C at 9.7 kb (Kennedy, et al., 1962). Thus, if the vesicular glass had formed by melting of wet SiO_2 at the grain boundaries, the melting point of the wet material would have been much lower than that of quartz. Conduction and radiation of heat from the melted region would not melt dry SiO_2. Thus, the presence of slight amounts of water on the boundaries of grains may account for the existence of unaltered quartz within tens of microns of fused silica. The actual history of the regions may be more complex if the glass formed by inversion of stishovite, but it is expected that water would also depress the stishovite inversion temperature.

V. CONCLUSIONS

During shock metamorphism of the Coconino sandstone, locally high pressures enduring for microseconds and high temperatures enduring for milliseconds controlled the phases of SiO_2 which formed in the rock. The principal mechanism of energy deposition by a shock wave in a porous material is the reverberation of shock and rarefaction waves through grains due to collisions of other grains. A one-dimensional model of the impact process can predict the Hugoniot states of a porous material (if no phase changes occur) from the known properties of the single crystals and gives the correct average specific volume and mean temperature of the rock. This model cannot account for the microscopic nonuniformity of energy deposition observed in the shocked Coconino sandstone. Energy was concentrated in local regions of the grains, however, because of the nonplanar, irregular geometry of impacting grains, as shown by the fracture patterns and distribution of high-pressure phases. High transient pressures and shear stresses occurred in small regions because of nonplanar loading of the grains.

In rocks shocked to equilibration pressures less than 70 kb (Type I rocks), the grains are fractured and the pores are filled with myriads of small chips derived from neighboring grains. Concussion fracture patterns emanating from contact surfaces of grains are related to the direction of shock passage through the rock.

At higher pressures (Type II, III, IV, V rocks) grains are deformed plastically and pore closure is accomplished by flow of grains into and around each other and into the pores. Coesite is found in all rocks where plastic deformation is observed, and is found in those regions of the grains believed subjected to high shear stresses and high initial temperatures. The occurrence and morphology of the coesite-rich regions in the rocks can be explained only by assuming that the transformation from quartz to coesite proceeds slowly in the shock wave and is accelerated by high temperatures and/or high initial shear stresses.

In rocks in which the peak pressures were in the range of 200 to 350 kb, four types of SiO_2 regions are observed. They are, in order of increasing peak pressure which must have occurred in the region: quartz grains, symplektic coesite-bearing regions, opaque coesite-bearing regions, and cryptocrystalline coesite cores. Stishovite occurs in the opaque coesite-rich regions adjacent to cryptocrystalline coesite cores. Probably stishovite formed in the shock front in these regions and then inverted to cryptocrystalline coesite as the rarefaction wave released the material to lower pressures. Depending on the pressure at which the stishovite was initially formed and on the pressure at which it inverted to coesite, a residual high temperature in the cryptocrystalline coesite core may have existed; heat conduction from such a region may have accelerated the formation of coesite from quartz in the surrounding opaque and symplektic regions.

In rocks in which the peak pressures were above 350 kb, vesicular glass occurs in core regions, and the relations of the glass to the coesite

and quartz suggest that the glass was formed by inversion of stishovite upon release to lower pressure. Coesite may have formed as an intermediate phase and then inverted to the observed glass.

In all rocks containing core regions of glass, vesicles are abundant in the glass. These vesicles were probably formed by exsolution of water that had been dissolved in melted SiO_2 during passage of the shock. Intermixing of water with fused silica can occur at pressures near or above the critical point (9.7 kb, 1080°C; Kennedy, et al., 1962) of the SiO_2- H_2O melting curve because of increased solubility of H_2O in SiO_2.

Minute vesicles cause much of the glass to be opaque in thin section. The opacity of the coesite-rich regions is also thought to be due to minute (unresolved) vesicles formed by exsolution of water incorporated into the boundaries of quartz grains during the shock.

SUGGESTED FUTURE OBSERVATIONS

Several aspects of the problem of shock metamorphism of the Coconino remain unsolved because of the limits of optical microscopy. The details of intergrowth of the SiO_2 phases and the occurrence of the vesicles at a scale of less than 1 micron are important to the theory of processes by which these phases were formed, for equilibrium conditions may have been restricted to domains of less than 5 microns. A program of observations with a scanning electron microscope is being undertaken to investigate the following questions:

(1) What is the relationship between the SiO_2 crystalline phases and glass in the symplektic regions of Type II rocks? This question is critical to theories which postulate the existence of glass derived by solid-state transformation of SiO_2 and may reveal whether the glass in Type II rocks was formed as an intermediate phase in the quartz-coesite transition or as an inversion product of small domains of coesite.

(2) What causes the opacity of the coesite-bearing regions? This question must be answered before the growth of microcrystalline coesite and the role of water can be understood.

The observations on shocked Coconino also suggest that a laboratory investigation of the effect of the transition from brittle fracture to plastic flow in shocked rocks be undertaken to detect if this transition is measurable in the equation of state. It is necessary to know the pressure at which this phenomena takes place before a firm interpretation of the correlation between plastic flow and the formation of

coesite can be made. Laboratory shock experiments on Coconino sandstone from which samples are recovered might provide needed information on minimum pressures at which the stishovite regions formed.

It is also desirable to investigate the melting pressures and temperatures of coesite and stishovite as well as the phase boundary between these phases so that temperatures and pressures of inversion can be assigned to the cores in Type III, IV and V rocks.

APPENDIX A

THE PROCEDURE FOR EXTRACTION OF STISHOVITE AND COESITE FROM SHOCKED SANDSTONE

In order to extract pure coesite and stishovite, which were necessary for the calibration procedure in the X-ray diffraction analysis, a procedure somewhat modified from that briefly described by Fahey (1962) was used. Rocks assumed to contain coesite or coesite plus stishovite were ground by hand to particle sizes less than 0.5 mm. The crushed rock was then weighed and treated for twenty-four hours with HCl to eliminate $CaCO_3$ contaminants (which form insoluble fluorides in the extraction procedure. Should CaF form, it can be extracted by treatment with HCl and boric acid, a procedure suggested by George Rossman, CIT chemistry department.) The mixture of rock and acid was then centrifuged, dried and reweighed to obtain the weight per cent of $CaCO_3$ present. Small portions of the leached and ground sample were ground in a power alumina mortar for fifteen minutes; this grinding was repeated until the desired amount of sample was obtained. (A reliable estimate is that 10 g of rock will produce 0.5 to 1.0 g coesite or 0.1 g (or less) stishovite.) The grinding procedure produced a powder which generally passed through a #200 mesh.

Concentrated HF and HNO_3 (3 : 1) were then added slowly and in very small increments to this ground sample. The heat of reaction, large surface area associated with the fine grain size, and low thermal conductivity of Nalge beakers, require great caution in this procedure.

Plastic gloves, face mask, and lab coat were worn at all times. The HF was initially added to the rock in a 500 ml beaker which was placed in a large plastic tub to catch overflow should frothing have occurred. All HF procedures were conducted inside a hood with Nalge apparatus.

The HF-HNO_3-rock solution was stirred with a magnetic stirrer for six to eight hours. The residue was extracted by centrifuging, multiple washings and drying. It was found that placing the centrifuge extract and wash liquid in an ultrasonic bath prior to recentrifuging facilitated particle separation and helped clean the residual "clump" from the previous wash and centrifuging from the bottom. The sample was then X-rayed and if any quartz remained, the acid treatment was repeated. This procedure generally produced pure coesite (or coesite plus stishovite, although the latter combination can be avoided by judicious selection of hand specimen according to the results of this thesis).

Stishovite was recovered by an analogous procedure to this point, with due care taken to select a stishovite-bearing sample initially. The extract of coesite and stishovite obtained by the above method was treated on a steam bath with a solution of HF for eight to twenty-four hours in Nalge beakers. The Nalge beakers must be protected from overheating should the steam bath go dry because Nalge melts at quite low temperatures. During the heating, coesite is attacked by HF, but stishovite is not appreciably attacked. This solution plus extract was allowed to cool before centrifuging and washing to prevent etching of the centrifuge should caps blow off the centrifuge tubes due to hot HF vapor. No etching of the centrifuge or the magnetic stirring motor was observed during this project.

APPENDIX B

QUANTITATIVE X-RAY DIFFRACTION

Relative amounts of the SiO_2 polymorphs were measured by powder X-ray diffraction methods. Quantitative analysis of relative amounts of polymorphs is difficult or impossible by analytical chemical methods because of the similarity of chemical properties among the polymorphs. Progressive solution in hydrofluoric acid is the only feasible method of chemical analysis of SiO_2 phases. Because of the difficulty in obtaining the solubilities of the polymorphs in HF under controlled conditions (temperature, grain size) and the inherent unpleasantness of working with HF, X-ray diffraction methods were selected for this analysis.

Powder X-ray diffraction, in theory, is ideal for the quantitative analysis of polymorphs, because each polymorph produces its characteristic pattern independently of the others, and the intensities of the lines of each component are proportional to the amount present. Furthermore, the existence of high precision X-ray diffractometers and proportional counters allows accurate measurements to be made and small quantities (e.g., stishovite) to be detected.

Theoretical Aspects of the X-Ray Diffraction Procedure

The internal standard technique is the most accurate method of X-ray diffraction for obtaining relative amounts of components in a mixture. In this method, a known amount of standard (e.g., LiF was used in this study), x_s, is thoroughly mixed with a known amount of the

material to be analyzed, which consists of a number of components in unknown weight fractions, x_a, x_b, ... The mixture of unknown composition plus standard is then pressed into a flat cake, scanned with an X-ray beam, and the relative intensities of lines of the unknown are compared with intensities of lines of the standard.

The theory for the flat-cake geometry is presented in several texts, e.g., Klug and Alexander (1954), and will not be detailed here. The relative amount x_c of a component present is proportional to the intensity ratio I_n/I_s:

$$x_c = k_{n,s} \frac{I_n}{I_s} \qquad \text{(B1)}$$

where I_n is the intensity of a diffraction line of the unknown, I_s is the intensity of a diffraction line of the standard, and $k_{n,s}$ is a constant of proportionality, dependent on the lines used, the experimental conditions, and on the assumption that the weight fraction of standard added, x_s, is always the same. The subscripts n, s refer to the 2θ (θ = Bragg angle) of the lines being compared. The constant $k_{n,s}$ is determined by measurement of I_n/I_s for a series of standard powders for which x_c is known. Once the constants $k_{n,s}$ are determined, the concentration of a component in an unknown sample is obtained by measuring the ratio I_n/I_s for a composite sample containing the unknown and the same weight fraction of standard as was used in the calibration.

The largest deviations from the linear relation of Eq. B1 are caused by the effect of crystallite size. The number of crystallites contributing to each reflection must be sufficiently large to generate

signals of reproducible intensity. Materials of low symmetry, such as the phases of SiO_2, tend to be especially poor for reproducibility because of the low multiplicity factor associated with the crystal planes. Alexander, Klug and Kummer (1948) have shown, both experimentally and theoretically, that in order to obtain better than 2% accuracy in reproducibility, the maximum size of quartz crystallites must be less than 15 microns. If the sizes in the quartz fraction range from 5-50 microns (as is believed to be the size range attained in the experiments performed here), mean deviations in reproducibility are approximately 10%.

With the grinding equipment available and because of the reported inversion of stishovite to amorphous SiO_2 by prolonged mechanical grinding (Skinner and Fahey, 1963), 40 microns was chosen as the maximum allowed diameter of the quartz particles. It was believed that deviations of 10% of the actual values would still allow definition of systematics in the shocked rocks. As discussed later, the mean deviation of the quartz standards was found to be 10%.

In the theory from which Eq. B1 is derived, the "intensity" of a line is formally derived to be the integrated intensity of a peak (i.e., area). In previous quantitative diffraction work (see Klug and Alexander, 1954, p. 430 for a review of this work), primarily on quartz dust particles less than 5 microns in diameter, experimenters found that line shapes did not vary significantly. Measurement of relative peak heights* therefore provided an accurate measure of relative intensities. Peak heights, however, do not give an accurate measure of integrated

*A peak height is the area of a very narrow part of the peak at its angle (2θ) of maximum intensity.

intensity if the particle size distributions of the sample and standard are different, for example, because of pre-preparation history that cannot be controlled, or if plastic strain has deformed the lattice of the sample material. Comminution and plastic strain of the quartz grains in the Coconino sandstone by the shock wave provided a significant fraction of submicron particles which contribute to broadening the diffraction peaks; this condition and shock-induced lattice strain in the crystal were not reproducible by preparing standards from pure quartz crystals.

Hindsight suggests that standards prepared from quartz of closely related history might provide reproducible peak shapes and, hence, allow the use of peak heights as a measure of intensity. Because of the extensive plastic strain evident in the shocked grains, this would involve using quartz from weakly shocked rocks (Type II) which are also plastically strained, for the standard. The two effects of nonreproducible distribution of grain size and plastic strain made it necessary to use integrated peak area as the measure of relative intensity for quartz.

Integrated area was also used for the coesite peaks to assure that the change in size distribution caused by the extensive solution in HF during extraction of pure coesite from the rocks did not affect comparison of the standards with the rocks. The large amounts (up to 30%) of coesite measured in some rocks by this X-ray diffraction technique, when compared to the amount recovered by HF-solution techniques ($\leqq$10%), suggest that coesite is quite soluble in HF and that the small

crystallites are lost in the extraction procedure. This would change the size distribution of the standards relative to the rocks.

The average value of the quartz (10·1) area to height ratio in the shocked rocks was $12.7^{+0.9}_{-2.2}$ as compared to the value $11.2^{+1.0}_{-0.7}$ for the standards. This broadening of the peak, due to a combination of particle size changes and plastic strain in the quartz crystals would produce misleading results (values of x_q which were 10-20% low) if peak heights were used as the measure of intensity. Similarly, the average value of the coesite (002, 040) area to height ratio for the shocked rocks was $16.1^{+2.4}_{-2.9}$ as compared with the value $15.5^{+0.9}_{-0.9}$ for the standards. If the coesite peak height were used, the slight broadening would produce values of x_c that were 5-7% lower than the value obtained by using peak areas.

Such small amounts of stishovite were present in the rocks that prohibitive scanning time would have been required to obtain peak areas with any degree of statistical accuracy. Therefore, peak heights were used as a measure of stishovite content. That this procedure led to a very small deviation in the linear ratio of Eq. B1 for stishovite is due to (1) the very small (< 1 micron) crystallite size, and (2) the apparent insolubility of stishovite in HF, such that the size distribution was not affected by the extraction procedure.

The LiF internal standard was always obtained from the same source and treated identically in both standard and sample preparation, so peak height was used as a measure of LiF line intensity. The average deviation of the ratio of LiF area to LiF height for the (111) line was less than 5%.

Equation B1 is derived on the assumption of a randomly oriented sample. Except for the attainment of small crystallite size, this is the most difficult experimental condition to achieve because it is difficult to form a sample with the required flat surface without causing some preferential alignment of the grains on the surface. The depth of penetration of X-rays into an SiO_2- LiF sample is small, and, hence, the surface effects are important. The depth of sample at which the sample appears infinitely thick to X-ray penetration is given by

$$t_\infty = \frac{3.45 \text{ gm } \theta}{\mu} \qquad \text{(B2)}$$

where μ is the mass absorption coefficient (MAC) of the mixture (see, for example, Cullity, 1956, p. 189). For a typical sample, which would be two-thirds SiO_2 and one-third LiF by weight, the MAC is 27.33 and t_∞ is 230 microns at $2\theta = 20.74°$ (the (10·0) line of quartz).

To increase t_∞ of the sample and thereby minimize the contribution of the surface grains, one-third amorphous boron by weight was added. The effect of the boron addition was twofold:

(1) Boron has the lowest atomic weight, and hence, the lowest MAC of any substance practical for this use. The addition of one-third boron by weight reduces the MAC in Eq. B2 from 27.3 to 16.8 and thereby increases t_∞ to 375 μ. The SiO_2 and LiF grains, which the X-ray beam "sees" are distributed in a matrix of boron to this depth rather than to 230 microns as in the case of a SiO_2- LiF mixture.

(2) The noncrystalline boron fragments ($\ll$40 microns) are irregularly shaped and minimize preferred orientation of the crystalline

components by forming a matrix within which the crystalline components are "packed". Preferential alignment of the LiF cubes, in particular, is reduced by the boron.

LiF was chosen as the internal standard because it provides a small number of strong diffraction lines which do not seriously overlap any of the lines of the SiO_2 polymorphs, is readily available in good purity, and is of suitable crystallite size to give sharp diffraction lines.

Preparation of Standard and Sample Powders.

Standards were prepared containing mixtures of quartz, coesite, stishovite, and glass in proportions similar to those expected in the shocked rocks. Pure coesite and stishovite were obtained from shocked Coconino by procedures described in Appendix A. To the mixture of SiO_2 phases were added amorphous boron and LiF such that the SiO_2 phases, boron and LiF were each one-third by weight.

To prepare the mixture for analysis, quartz or the shocked Coconino and LiF were first ground individually. For the perfectly cubic LiF grains, which were already approximately 10 microns in size, the primary purpose of this grinding was to "knock off the corners" and create some (small) degree of irregularity in the grain shape and in the size distribution, so that preferred orientation of these cubes would be minimized. Pure quartz crystals were selected for the calibration work, crushed to less than 0.3 mm and then ground in a shatterbox for 3 minutes. Particles generally less than 30-40 microns were obtained by this procedure; this method proved more effective in reducing the particle size than grinding in a power mortar dry or in

methanol for more than two hours.

Coesite and stishovite, obtained by the recovery procedure described in Appendix A, were already sufficiently small for X-ray diffraction.

The standard series of mixtures (listed in Table B2) for use in preparing the calibration curves for quartz, coesite and stishovite were generally prepared from 0.7 gram portions of SiO_2 phases plus 0.7 gram boron, to which was added 0.7 gram LiF ($x_s = 0.33$). The components were carefully weighed, and shaken together in a Spex Mixer/Mill for seven minutes.

Mounting of Specimens.

The following method of sample mounting was adapted from the methods of McCreery (1949, as described by Klug and Alexander, 1954) to minimize preferred orientation while, at the same time, producing a plane surface.

The sample holder was a rectangular piece of bakelite, 5 x 2.5 x 0.2 mm in size with a 2.5 x 1.5 mm hole cut through the center. Other items necessary for the sample mounting were a glass slide, masking and scotch tape, small spatula, small pieces of index cards, and a brass tamper or tool that could serve to uniformly pack the powder into the cavity. The following procedure was always used for filling the sample holder:

(1) The sample holder was placed on the glass slide and held fast with masking tape at both ends.

(2) A small amount of the mixed sample (unknown or standard plus boron and LiF) was transferred from its container to the cavity of the sample holder and spread roughly across the glass with the spatula.

(3) The brass tamper was then used to apply uniform pressure on the powder and pack it into a coherent cake.

(4) Steps 2 and 3 were repeated until the cavity was filled.

(5) A small piece of index card was labeled with the specimen number and then taped across the back of the cavity.

(6) The glass slide was carefully untaped and removed, with great care being taken to avoid shearing the front surface of the specimen.

With practice, samples could be reliably prepared to avoid cracking and surface irregularities.

Operating Conditions.

At all times, the General Electric Model XRD-3 diffractometer was run under identical settings, given in Table B1.

Table B1

Operating Conditions
Copper anode
Tube current: 25 ma
Speed: Low-Low, $0.02°/100^{s}$
Angle: Increasing
Print Interval: 100^{s}

Peak area measurements were obtained by scanning at the rate of $0.02°/100^{s}$ across the peak; peaks are generally less than 1° in width.

Peak heights were obtained by scanning the top of the peak at the same rate and choosing the maximum peak value for a 0.02° interval. A typical scan showing the relative heights of the quartz, coesite and stishovite peaks and the background level is shown in Fig. B1.

Quartz, Coesite and Stishovite Standards.

The following mixtures of quartz, coesite, stishovite and glass were prepared to simulate rock compositions:

Table B2

Weight Fractions (x) of Components in Standard Mixtures

Standard	x_Q	x_C	x_S	x_G
I	1.00			
J'	0.80	0.04	0.08	0.08
F	0.70			0.30
D	0.60			0.40
K'	0.50	0.16	0.06	0.28**
E	0.40			0.60
L	0.30	0.12	0.04	0.54
H	0.20			0.80
(M_2	0.10	0.08	0.02	0.80)

**Amorphous boron replaced SiO_2 glass

The weight fractions x_Q, x_C, x_S, x_G refer to weight fraction in the SiO_2 part of one mixture. The SiO_2 part was one-third by weight of the total mixture, the remainder being one-third boron, one-third LiF.

The quartz calibrations involved scanning the (10·1) peak from $2\theta = 26°$ to approximately 27°, subtracting the total background, and

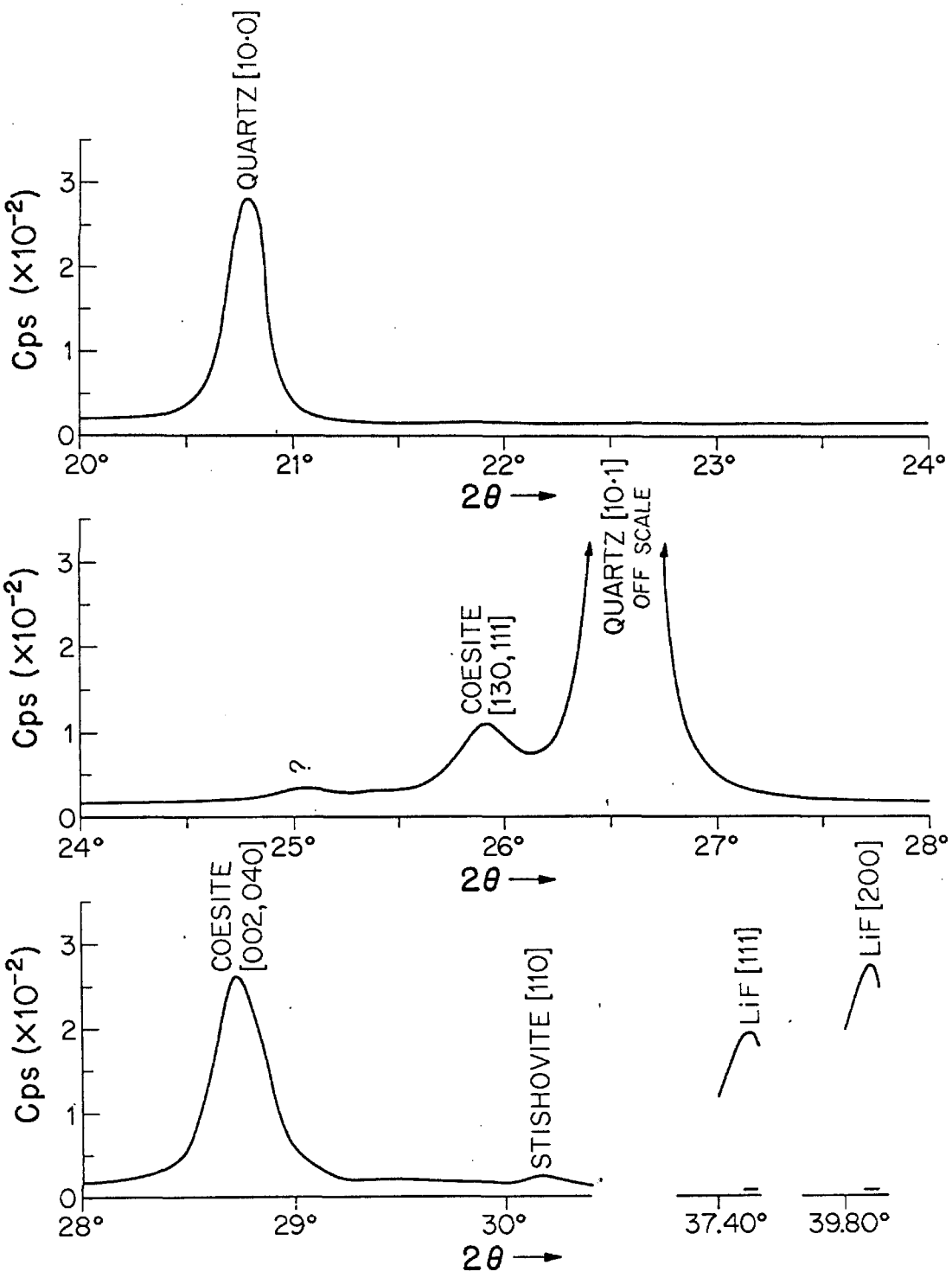

Fig. B1. Typical X-ray diffraction spectrum of a shocked Type III rock prepared for quantitative analysis. The peak heights and background are shown for LiF.

obtaining the height above background of the LiF (111) peak at $2\theta \cong 38.6°$.

The data from the quartz calibration runs are given in Table B3. In this and subsequent tables, the following notation is used:

$A_{n,i}$ Area of peak above background at $2\theta = n$ for substance i, where i = Q for quartz, C for coesite, S for stishovite and LiF for lithium fluoride.

$H_{n,i}$ Height of peak above background at $2\theta = n$ for substance i.

$k_{n,s}$ Defined in Eq. B1.

Some runs were made after the crystal monochromator shifted, causing uniformly reduced intensities. No effect on peak ratios was observed. Runs made after the monochromator shifted are denoted by an * in the tables.

Table B3

Data from Quartz Standards

Standard	x_Q	$A_{26,Q}$ (x10^{-1} counts)	$\frac{A_{26,Q}}{H_{26,Q}}$	$H_{38,LiF}$ (x10^{-1} counts per 100 sec.)	$\frac{A_{26,Q}}{H_{38,LiF}}$	$k_{26,38}$
I	1.00	90057	11.16	1708	52.73	0.019
J'	.80	76074	11.25	1598	47.60	0.017
F*	.70	50148	11.56	1431	35.04	0.020
D*	.60	41077	12.20	1365	30.09	0.020
K'*	.50	46130	11.09	1403	33.13	0.015
E	.40	40505	11.57	1693	23.92	0.017
L*	.30	22212	10.57	1249	17.78	0.017
H	.20	19567	10.67	1834	11.51	0.017

The data points determine the slope of the linear relation between x_Q and $A_{26,Q}/I_{38,LiF}$ to be 0.018 with a standard deviation of 0.0018. This linear relation is shown in Fig. B2. The reason for the relatively large scatter in these measurements was discussed in the introductory part of this appendix and is probably solely attributable to the relatively large size of some of the quartz particles.

The coesite calibration involved scanning the (002, 040) line from $2\theta = 28.0°$ to approximately 29.0°. The area to height ratio of the coesite peak in the standards was 15.5 ± 0.9. Because of the excellent linearity (Fig. B3) obtained with the first four coesite standards, no further coesite standards were run. This linearity is almost certainly due to the small particle size of the coesite crystallites.

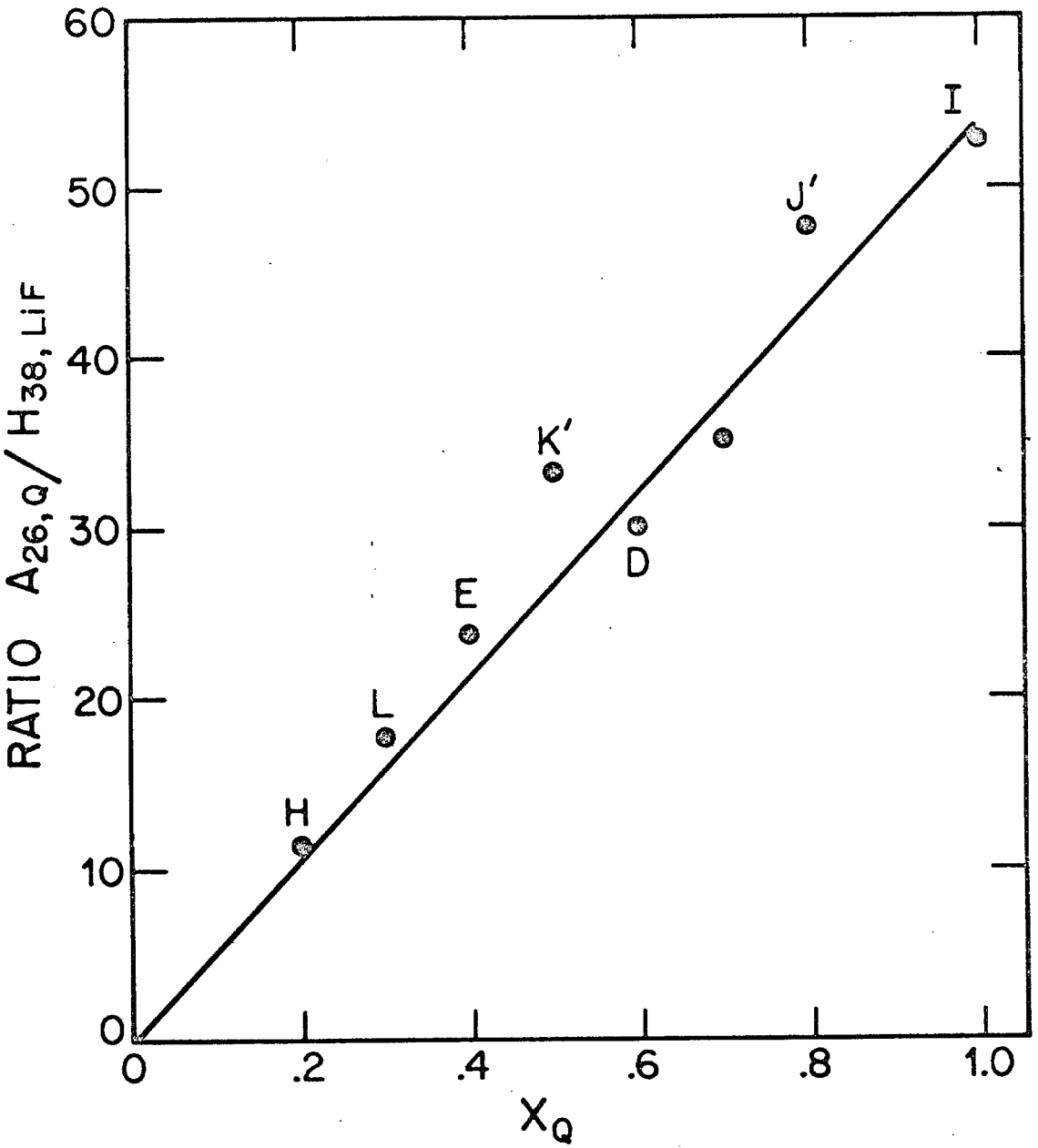

Fig. B2. Calibration curve for quantitative analysis of quartz content by measurement of area of quartz peak and height of LiF peak.

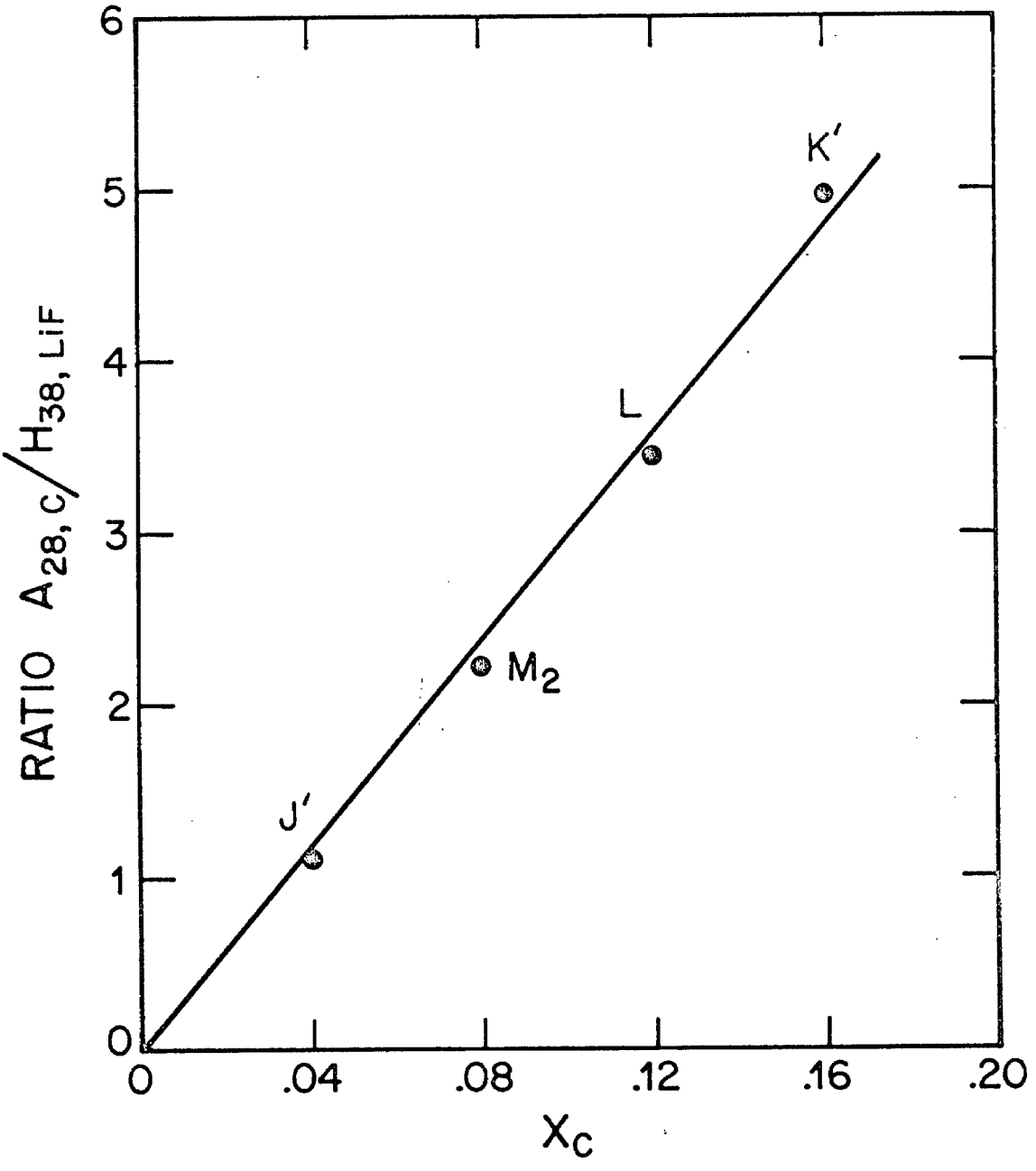

Fig. B3. Calibration curve for quantitative analysis of coesite content by measurement of area of coesite peak and height of LiF peak.

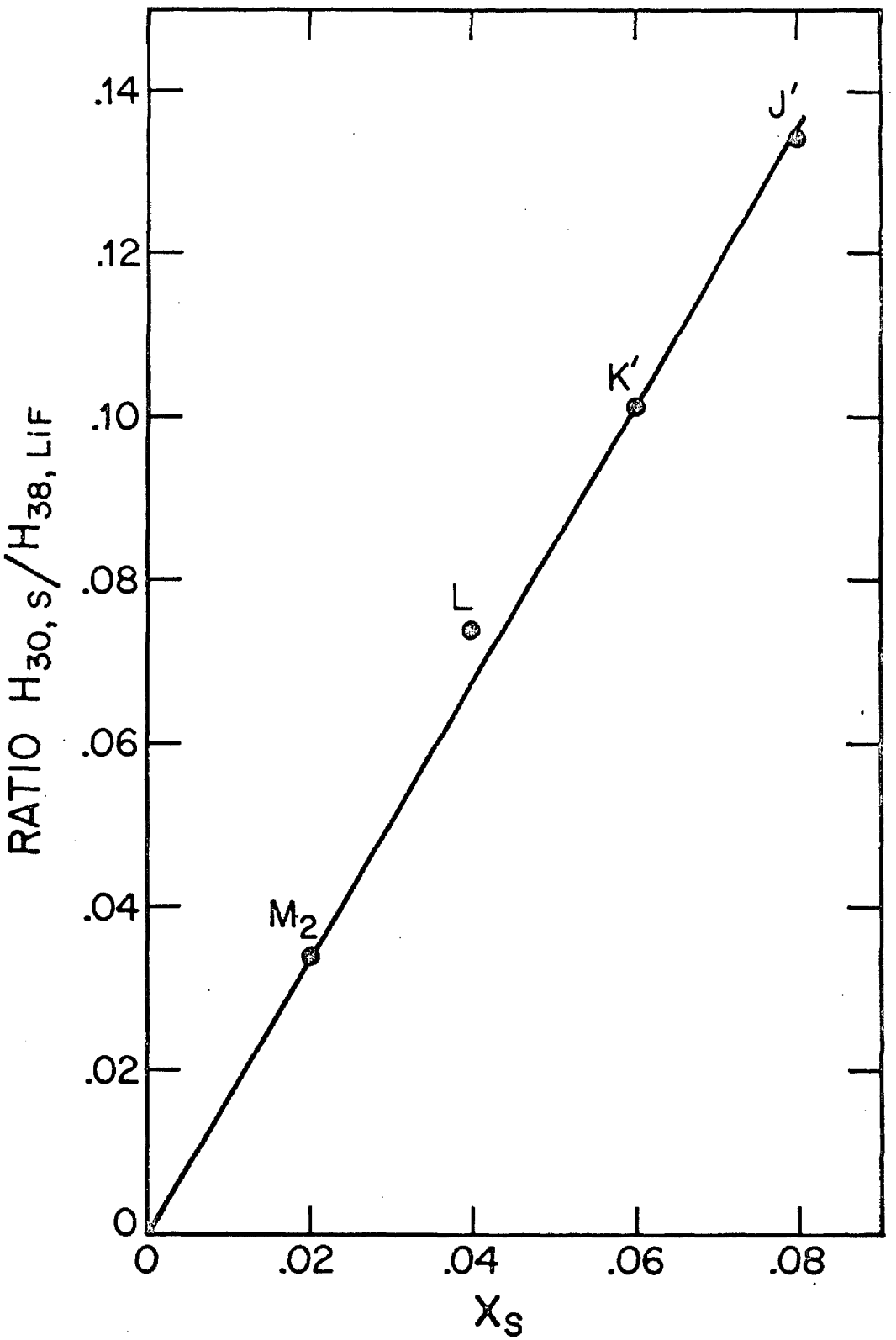

Fig. B4. Calibration curve for quantitative analysis of stishovite content by measurement of height of stishovite and LiF peaks.

$k_{28,38}$ was determined to be 0.034 with standard deviation 0.002. The data for the coesite standards are given in Table B4.

Table B4

Data for Coesite Standards

Standard	x_C	$A_{28,C}$ ($\times 10^{-1}$ counts)	$\frac{A_{28,C}}{H_{28,C}}$	$H_{38,LiF}$ ($\times 10^{-1}$ counts per 100 sec.)	$\frac{A_{28,C}}{H_{38,LiF}}$	$k_{28,38}$
K'	0.16	7886	16.4	1587	4.97	0.032
L	0.12	4954	15.1	1436	3.45	0.034
M_2	0.08	3457	14.7	1542	2.24	0.036
J'	0.04	1544	15.9	1388	1.11	0.036

Because of the small amount of stishovite present (<1%) in the shocked rocks, it was impractical to attempt to measure the integrated peak area of the (110) peak (see the strength of the stishovite peak in Fig. B1). Prohibitive diffraction time would have been required to reduce the counting errors. Peak heights were therefore measured for the stishovite calibration, and it was decided to treat stishovite as a trace mineral in the rocks, estimating only its maximum value. The linearity of the measured calibration curve suggests that the peak shape is nearly constant because of the small particle sizes of the stishovite crystallites. The slope of the calibration curve is 0.58 with standard deviation 0.05, as shown in Table B5 and Fig. B4.

Table B5

Data for Stishovite Calibration

Standard	X_S	$H_{30,S}$ ($\times 10^{-1}$ counts per 100 sec.)	$H_{38,LiF} \times 10^{-1}$ ($\times 10^{-1}$ counts per 100 sec.)	$\frac{H_{30,S}}{H_{38,LiF}}$	$k_{30/38}$
J'	0.08	211	1563	0.134	0.60
K'	0.06	171	1678	0.101	0.60
L	0.04	112	1511	0.074	0.54
M_2	0.02	51	1500	0.034	0.59

Finally, consideration must be given to the accuracy of the linear relation at low values of x, when the counting errors become significant. The per cent probable error in the net peak height (height above background) is given by (Klug and Alexander, 1954, p. 372):

$$100\ U_p = 67.5 \sqrt{(N_t + N_B)} / (N_t - N_B) \qquad (B3)$$

where U_p is the relative probable error, N_t is the total number of counts at the top of the peak, and N_B is the number of counts of background. Using the graphical exposition of Eq. B3 given in Klug and Alexander (1954, p. 372), the value of x at which counting errors equal the deviations determined for the calibration curves is less than 4% for all three SiO_2 crystalline polymorphs. For quartz, the counting errors are probably significant only at concentrations below 2% because the standard deviation is so large.

Quantitative analysis by techniques of X-ray diffraction has previously been restricted to crystalline phases. Several unsuccessful

attempts were made during the course of these experiments to measure the relative amounts of silica-glass present by measuring the height of the amorphous band characteristic of SiO_2. This band begins at $2\theta < 14°$, reaches a maximum at $2\theta \cong 21°$ and extends to approximately $2\theta \cong 40°$. These attempts were unsuccessful, primarily because amorphous boron also has a broad band at low angles, reaching a maximum near $2\theta = 20°$. The superposition of the two bands made quantitative glass analysis impossible. In general, however, the background at 20-22° does increase as the amount of glass in the sample increases. Glass content for the shocked rocks was obtained by subtracting the measured quartz, coesite and stishovite content from 100%.

Amounts of SiO_2 Polymorphs in the Shocked Rocks.

Sixteen rocks were selected from more than 65 specimens which had been examined in thin section. These sixteen rocks were chosen because they contained petrographic features typical of those which existed in the shocked sequence. All rocks were treated for 24 hours in HCl to remove the $CaCO_3$ deposits. All weight fractions of SiO_2 given are relative to the treated rock.

The data for these sixteen rocks are summarized in Table B6. Point count analyses verified the quartz content of rocks number 8 and 39 to within 2%. The estimated standard deviation for the rest of the quartz abundances is 10% of the measured value; for the coesite abundance the estimated standard deviation is 6% of the measured value. The data are discussed in the text.

Table B6. Summary of X-Ray Diffraction Data for Shocked Rocks

Sample No.	QUARTZ $A_{26,Q}$ (counts $\times 10^{-1}$)	A/H	$H_{38,LiF}$ (counts per 100 sec $\times 10^{-1}$)	x_Q	COESITE $A_{28,C}$ (counts $\times 10^{-1}$)	A/H	$H_{38,LiF}$ (counts per 100 sec $\times 10^{-1}$)	x_C	STISHOVITE $H_{30,S}$ (counts per 100 sec $\times 10^{-1}$)	x_S (approx.)	GLASS x_G
8	79140	13.5	1546	0.90	795*	13.2	1317	0.02			0.08
	76694	13.4	1510	0.89							
39*	63623	12.4	1305	0.85	2034	14.4	1305	0.05			0.10
4	64502	13.2	1511	0.75	9753	17.1	1511	0.23	30	~0.01	0.01
33*	55052	12.7	1350	0.71	8264	16.4	1350	0.21	35	~0.01	0.07
18	55663	12.4	1600	0.61	14410	17.3	1600	0.32	38	~0.01	0.06
16*	43072	13.2	1224	0.62	6211	17.2	1224	0.18	~10	$\ll$0.01	0.20
31*	40606	12.5	1342	0.53	11180	16.3	1342	0.29	~20	<0.01	0.18
17	36484	13.4	1590	0.40	7830	18.5	1590	0.17			0.43
32*	27609	12.8	1332	0.36	12311	17.3	1332	0.32			0.32
5*	23090	13.6	1244	0.32	4160	15.0	1244	0.12			0.56
30	28211	13.1	1567	0.32	12633	17.4	1564	0.29			0.39
20*	18386	12.4	1297	0.25	6306	16.3	1297	0.17			0.58
7*	15828	12.8	1223	0.23	4004	16.9	1223	0.11			0.66
6*	13198	13.1	1222	0.20	3930	15.4	1222	0.11			0.69
9*	10909	10.5	1276	0.15	not detectable						0.85
19*	2818	10.8	1227	0.04	1714	13.5	1227	0.05			0.91

* Runs made after monochromator shifted, causing uniform decrease in peak intensities.

APPENDIX C

WAVE PROPAGATION IN A ONE-DIMENSIONAL MEDIUM: A DESCRIPTION OF THE COMPUTER CODE FOR SHOCK CALCULATIONS

The propagation of shock and rarefaction waves through a one-dimensional continuum is solved by use of the Lagrangian form of the equations of conservation of mass, energy and momentum.

A computer code, WONDY, by W. Herrmann, P. Holzhauser and R. J. Thompson, Sandia Laboratory (1967), which solves the finite difference analogs to the Lagrangian equations of motion in rectangular coordinates was purchased through the Computer Software Management and Information Center. This program, written in CDC 3600 FORTRAN was modified, first to IBM 7090 FORTRAN and then to IBM 360 FORTRAN. Some alterations to this program were made to suit the specific requirements of this thesis, and a temperature calculation capability was added. The following summary of the routine is taken from the research report of Herrmann, Holzhauser and Thompson which accompanies the original version of the program.

Conservation of momentum, in rectangular coordinates is expressed by

$$\rho a = - \frac{\partial \sigma}{\partial x} - \frac{\partial q}{\partial x} \qquad (C1)$$

where x is the spatial coordinate, ρ the density, a the acceleration, σ the stress in the x-direction and q the viscous stress. The stresses

are taken to be positive in compression, negative in tension. The acceleration is given by

$$a = \frac{\partial u}{\partial t} \tag{C2}$$

where the velocity u is defined as

$$u = \frac{\partial x}{\partial t} \tag{C3}$$

Conservation of mass is expressed by

$$\frac{\rho}{\rho_o} = \frac{dV}{dv} \tag{C4}$$

where dV is an element of volume at time t = 0 when the density is ρ_o and dv is the volume of the same element at time t.

The equation expressing conservation of energy is

$$\rho \frac{\partial e}{\partial t} = (P + q) \frac{1}{\rho} \frac{\partial \rho}{\partial t} + P_d \tag{C5}$$

where P is the work done by the deviator stresses. This term is zero if the compression is assumed to be hydrostatic. Equation (C5) neglects conduction or addition of heat by chemical reaction or radiation. The constitutive relation chosen to accompany the conservation laws is the Mie-Grüneisen form:

$$p - p_H = \gamma_\rho (E - E_H) \tag{C6}$$

where $p_H(\rho)$ and $E_H(\rho)$ are the pressure and energy along the reference Hugoniot and are functions of density only. γ is the Grüneisen's ratio and is assumed to be a function of density only. The equation of state chosen for the Hugoniot was the linear shock-velocity-particle-velocity

form

$$U = c_o + su \tag{C7}$$

where U is the shock velocity and u is the particle velocity. c_o is the bulk sound speed. This leads to the form (Ruoff, 1967)

$$p_H = \frac{\rho_o c_o^2 \eta}{(1 - s\eta)^2} \tag{C8}$$

where $\eta = 1 - \rho_o / \rho$. The energy E_H is given by the Rankine-Hugoniot relation

$$E_H = \frac{p_H \eta}{2 \rho_o} \tag{C9}$$

where it is assumed that $E = 0$ at $p = 0$ at $\rho = \rho_o$. In all calculations it was assumed that

$$\gamma = \gamma_o (1 - \eta) \tag{C10}$$

Finally, this leads to the Mie-Grüneisen form

$$p = p_H \left\{1 - \frac{\gamma}{2} \left(\frac{\rho}{\rho_o} - 1 \right) \right\} + \gamma \rho E \tag{C11}$$

The one-dimensional continuum of material is considered to be subdivided by lines drawn on it at the initial instant of time into a material coordinate mesh. The mesh distorts with the material and the positions, velocities and accelerations of the lines defining the mesh boundaries are found at discrete times. Stresses, densities and energies, regarded as averages over each mesh between successive boundaries, are computed from the velocities and accelerations.

Since the finite difference analogs to these equations of motion are not stable when discontinuities or shock waves develop, it is

necessary to include an artificial viscosity in the solution which renders the shock waves as steep but finite gradients in the solution (see Rictmeyer and Morton, 1969). The shock waves occupy several mesh widths. Natural viscosity appears to be too small for this purpose, although dynamic viscosities for most substances are not known. An arbitrary form for q consisting of terms quadratic and linear in the volumetric strain rate was used:

$$q = \rho b_1^2 \left(\frac{1}{\rho}\frac{\partial \rho}{\partial t}\right)^2 + b_2 c \left(\frac{\partial \rho}{\partial t}\right) \qquad (C12)$$

The linear viscosity is effective in controlling small spurious oscillations in which gradients are insufficient to make the quadratic viscosity effective; the quadratic form is effective at controlling gradients at shocks while introducing minimal disturbances elsewhere.

The computer program solves finite difference analogs to the conservation equations and constitutive relation. In addition, error checks, output routines and a method for handling fractures are provided.

APPENDIX D

EQUATIONS OF STATE OF QUARTZ AND STISHOVITE

In this thesis, quartz and stishovite have been described by an equation of the Grüneisen form:

$$P(V, T) = P_{isotherm}(V, T_o) + \frac{\Gamma}{V} (E - E_{T_o}) \tag{D1}$$

where

$$E - E_{T_o} = \int_{T_o}^{T} c_v \, dT \tag{D2}$$

V is the specific volume and T is the temperature in °K of a state of the material, T_o is a reference isotherm, generally taken as 0°K, Γ is the Grüneisen's ratio, E and E_{T_o} are the internal energy of the final state and isothermal state at volume V respectively. The Murnaghan form for the isotherm $P(V, T_o)$ was chosen because it provides an equation which allows analytic integration and differentiation:

$$P = \frac{K_o}{n} \left[\left(\frac{V_o}{V} \right)^n - 1 \right] \tag{D3}$$

where K_o is the bulk modulus and n is the pressure derivative of the bulk modulus. As shown in Fig. 39 , this equation provides an adequate approximation to the behavior of quartz at the pressures of interest.

The bulk modulus, K_o, is given by

$$K_o = - V \frac{\partial P}{\partial V} \Big|_{V_o} \tag{D4}$$

and the pressure derivative of the bulk modulus, n, is given by

$$n = \frac{\partial}{\partial P}\left(-V\frac{\partial P}{\partial V}\right) \tag{D5}$$

To relate the Murnaghan equation of state to the shock velocity - particle velocity equation of state (U_s vs. u_p) directly obtained from shock experiments

$$U_s = c + su_p + s'u_p^2 \tag{D6}$$

it is assumed that s' is small. Ruoff (1967) has shown that under these conditions, the shock adiabat centered at P_o, V_o has the Murnaghan form (Eq. D3) where $K_{o_s} = c^2 \rho_o$ is the adiabatic bulk modulus and $n = 4s - 1$. The isothermal bulk modulus K_{o_T} can be derived from K_{o_s} by the relation

$$K_{o_T} = K_{o_s}(1 + T\alpha\gamma)^{-1} \tag{D7}$$

The correction is smaller and n is approximately the same for the isotherm as for the adiabat.

In those instances when the integral $\int_o^P V\,dP$ is needed along any isotherm $T > 0°K$, the Murnaghan equation is assumed to hold

$$P = \frac{K_T}{n}\left[\left(\frac{V_o}{V}\right)^n - 1\right] \tag{D8}$$

where K_T is given by

$$K_T = K_o + \left(\frac{\partial K}{\partial T}\right)_P (T - T_o) \tag{D9}$$

By inversion of Eq. (D8), V is given by

$$V = \frac{V_o K_T}{n\left(P + \frac{K_T}{n}\right)^{1/n}} \qquad \text{(D10)}$$

All values used in these equations and the references from which they were obtained are listed in Table D1.

Table D1

Physical Properties of Quartz and Stishovite used in this study. Superscripts refer to references below. Values in parentheses are assumed.

Property (at P=1 bar, T=298°K)	Units	Quartz	Stishovite
Density (theoretical bulk), ρ	g/cc	2.648 [1]	4.287 [7]
Poisson's ratio, σ_s		0.077 [1]	----
Thermal expansivity, α	/°K x 10^6	36.6 [1]	15 [3,2]
Specific heat, c_v	cal/mole °K	see part II of thesis	
Bulk modulus	kb		
K_{o_S}		377 [1]	3440 [4] *
K_{o_T}		374 [1]	3440 [4] *
K_{o_H}		356 [5]	----
Pressure derivatives			
$(\partial K_{o_S}/\partial P)_T = n$		7 [5]	6 [6] *
$(\partial K_{o_T}/\partial P)_T = n$		(7)	(6)
Temperature derivatives			
$(\partial K_{o_T}/\partial T)_{P=0}$	kb/°K	-0.10 [1]	(-0.5) *
$(\partial K_{o_S}/\partial T)_{P=0}$	kb/°K	(-0.10)	(-0.5) [2] *
Grüneisen's ratio, γ		0.703 [1]	1.6 [2] *

[1] Anderson, O. L., Schreiber, Liebermann, Soga, 1968.
[2] Ahrens, Takahashi, Davies, 1969.
[3] Weaver (personal communication to Ahrens, Takahashi and Davies, 1969).
[4] Liu, Takahashi and Bassett, 1969.
[5] Calculated from c_o, s in shock equation of state $U = c_o + su$ where U is shock velocity, u is particle velocity (Wackerle, 1964). $c_o = 3.68 \times 10^5$ cm/sec, $s = 2.12$. Assumes hydrostatic compression.
[6] Average value of shock data of Ahrens, et al., 1969 and Liu, et al., 1969.
[7] Chao, Fahey, Littler and Milton, 1962.

*For a review of the uncertainties associated with these values, see Ahrens, et al., 1969.

APPENDIX E

CALCULATION OF SHOCK TEMPERATURES

Temperatures of shocked quartz are computed by a variation of the method of Ahrens, Anderson and Ringwood (1969). This method, summarized below, was used to calculate temperatures in the one-dimensional model of a shock wave propagating through granular quartz (discussed in Chapter IV); a variation of this method is used to estimate the temperature in a region in which stishovite has formed.

Since internal energy is a state variable, the shock state P, V may be reached by a series of reversible paths, as shown in Fig. E1a. The increase in internal energy $(E_F - E_o)$ above that at the initial state E_o at any point (P_F, V_F) along the Hugoniot is given by the Rankine-Hugoniot conservation condition

$$E_F - E_o = \frac{1}{2} (P_F - P_o) (V_o - V_F) \qquad (E1)$$

($E_F - E_o$ may also be considered to be the difference between internal energy at time t in the computer code, and E_o and need not be given by a simple jump process, but may be computed from the conservation equations of fluid flow.) This increase in internal energy must be equal to that attained by the three successive paths, 1 (cooling from temperature T_o to 0°K and from volume V_o to volume V_{oo}), 2 (isothermal compression to volume V_f, pressure P_T) and 3 (isovolumetric heating to pressure P_F, temperature T_F). The internal energy change along path 1 was approximated as

$$\Delta E_1 = \int_{T_o}^{0°K} c_p \, dT \qquad (E2)$$

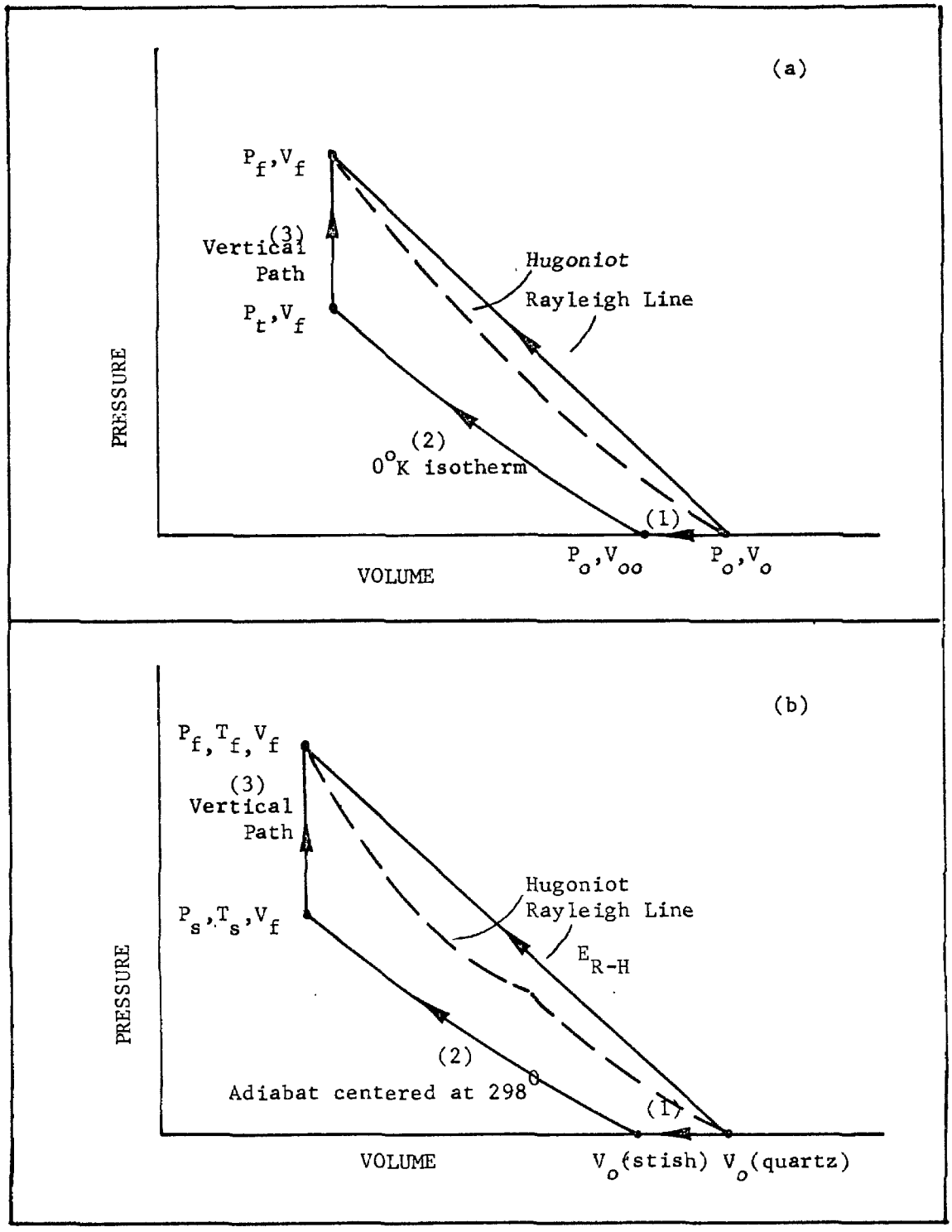

Fig. E1. Thermodynamic paths used in calculating shock temperatures in (a) quartz, and (b) stishovite.

It was assumed that c_p and c_v were equal for temperatures less than 298°K.

The energy increase during isothermal compression at 0°K is

$$\Delta E_2 = - \int_{V_{oo}}^{V_F} (P\,dV)_{T=0} \qquad (E3)$$

V_{oo}, the volume at P = 0, T = 0 was assumed equal to 0.3762 cc/g, which is the value given by McSkimmin, et al. (1965) at T = 77°K; since α decreases with decreasing temperature, the specific volume at this temperature is not expected to be very different from the 0°K volume.

The energy required to increase the pressure at constant volume from the isotherm to the Hugoniot is

$$\Delta E_3 = \int_{P_T}^{P_F} \left(\frac{V}{\gamma}\right) dP = \int_{0°K}^{T_F} c_v\,dT \qquad (E4)$$

in which c_v was taken as described in part II of this thesis. Equating Eq. (E1) with the sum of (E2), (E3), (E4) and solving for the temperature term:

$$\int_{0°}^{T_F} c_v\,dT = P_F(V_o - V_F)/2 - \int_{T_o}^{o} c_P\,dT + \int_{V_{oo}}^{V_F} (P\,dV)_{T=0} \qquad (E5)$$

T_F is given implicitly by the left-hand side of this equation and may be obtained in a variety of ways. In the one-dimensional model of shock wave propagation used in this thesis, a table of $\int_o^{T'} c_v\,dT$ was constructed at 10° intervals of T'. The right-hand side of Eq. (E5) was computed and, by searching and interpolating in the table, T_F was determined to within 1°. (It must be stressed that although an accurate model of specific heat has been provided, uncertainties still exist in γ, K_o, n and in the assumption that γ/V is constant. In view of these uncertainties, the estimated error on the temperature calculations may be

as large as 50°K.)

Results of temperature calculations for the porous quartz model are discussed in Chapter IV. Two calculated single-crystal quartz shock states are: P = 80 kb, V = 0.3319 cc/g, T = 372°K; P = 144 kb, V = 0.3143 cc/g and T = 491°K. The latter computed pressure and volume are identical to the pressure and volume given by Wackerle from second wave data (P = 144 kb, V = 0.314 cc/g); the temperature he computed (476°K) for this state under the assumption of constant specific heat is slightly lower.

As discussed in Chapter IV, it was also desired to compute the temperature in a region which had transformed to stishovite at 144 kb and 256 kb and to compare the temperature of this region with a region of metastable quartz at 144 kb and 256 kb, respectively. The method is similar to that used for calculating the temperature of shocked quartz, but a slightly different set of thermodynamic paths was used in order to make use of the published adiabats centered at 298°K for stishovite (Ahrens, Anderson and Ringwood, 1970) and to account for the change in internal energy due to the phase change.

It is assumed that stishovite is formed by a single shock at 144 kb and at 256 kb. As before, the energy change given by the Rankine-Hugoniot condition is equated to the sum of three separate, reversible processes, shown in Fig. E 1b: (1) transformation from quartz to stishovite at standard pressure and temperature, (2) adiabatic compression to volume V_F, temperature T_s and pressure P_s, and

(3) isovolumetric compression to final pressure P_F, temperature T_F. The energy of transformation was given by Holm, Kleppa and Westrum (1967) as $+0.80 \times 10^{10}$ ergs/g. The energy change upon adiabatic compression is

$$\Delta E_2 = - \int_{V_o}^{V_F} (P\,dV)_s \qquad (E6)$$

The adiabatic temperature increase is (Walsh and Christian, 1955)

$$T_s = T_o \exp (\gamma (V_o - V)/V) \qquad (E7)$$

The energy change along the vertical path 3 is

$$\Delta E_3 = \int_{T_s}^{T_F} c_v\,dT \qquad (E8)$$

Equating (E6), (E7) and (E8) to the Rankine-Hugoniot energy change and solving for the temperature terms gives:

$$\int_{T_s}^{T_F} c_v\,dT = \frac{1}{2}(P_F - P_o)(V_o - V_F) - E_{tr} + \int_{V_o}^{V_F} (P\,dV)_s \qquad (E9)$$

As discussed previously, T_F is obtained by solving the left-hand side of this equation for an assumed specific heat function. From equation (E9) the temperature of stishovite at two pressures was computed. These temperatures are compared with temperatures in metastable quartz in Table 6 in Chapter IV.

APPENDIX F

RADIATION AND CONDUCTION FROM A LOCALIZED HEAT SOURCE

Formation of stishovite in the shock front in local regions of grains due to high peak pressures produced a region which was 100° to 500° hotter than adjacent regions of untransformed quartz (Appendix E). The duration of these thermal gradients is the subject of this appendix. It is desired to estimate

(1) if appreciable decay of the temperature of the stishovite region occurred in the several (less than 10) microseconds duration of peak shock pressures. This will govern the final temperature of the core after it inverts to coesite.

(2) if radiation or conduction from residual hot cryptocrystalline coesite cores heated the surrounding quartz grains in the 20 to 30 milliseconds available before the pressure decayed below the coesite stability field.

The change in temperature due to radiative transfer can be calculated for a simple limiting model. A simplifying assumption which maximizes the radiative transfer between two regions is that both have an emissivity of one. The net initial heat loss rate, H, from a sphere of radius a and temperature T into a surrounding medium of temperature T is then

$$H = 4\pi a^2 \sigma (T^4 - T'^4) \qquad (F1)$$

where σ is the Stefan Boltzmann constant (1.35×10^{-12} cal $cm^{-2} deg^{-4} sec^{-1}$.

This heat loss can be attributed to a uniform temperature drop within the sphere because the thermal photon mean free path in silica for temperatures of interest is on the order of 1 to 3 cm (Aronson, et al., 1970), which is much greater than the mean sphere radius. The cooling rate is then

$$\frac{dT}{dt} = \frac{H}{\rho c \frac{4}{3} \pi a^3} = \frac{\sigma (T^4 - T'^4)}{\rho c \frac{1}{3} a} \qquad \text{(F2)}$$

Using representative physical constants and temperatures calculated in Appendix E for stishovite and quartz at 144 kb (ρ = 4.3 g/c m^3, c = 0.3 cal/g - °C, a = 2 x 10^{-3} cm), one obtains $\frac{dT}{dt}$ = 80 deg sec^{-1} for T = 575°K and T' = 490°K, and $\frac{dT}{dt}$ = 4000 deg sec^{-1} for T = 1270°K and T' = 763°K. Therefore radiative heat transfer was negligible during the several microseconds for which the stishovite existed. The residual temperature of the cryptocrystalline coesite core formed by inversion of the stishovite could be no higher than the initial temperature of the stishovite region (see Chapter IV). Therefore H can be no greater than given by the calculations above, and $\frac{dT}{dt} \approx$ 4000 deg sec^{-1}. It follows that in the 20 to 30 milliseconds before release of pressure below the coesite stability field, radiation will not appreciably alter the temperature of the core. Because no heat transfer from the stishovite core occurs by radiation, it follows that no heat will be added to the surrounding quartz by radiation.

To estimate the transfer of heat by conduction from the locally hot regions, assume that a sphere of radius A and temperature T_o is surrounded

by a medium of initial temperature T'. In order to pose a solvable problem, it must be assumed that the density, thermal conductivity, and specific heat of the sphere and the surrounding medium are equal. The equation of linear heat flow is

$$\nabla^2 v - \frac{1}{\varkappa} \frac{\partial v}{\partial t} = 0 \qquad \text{(F3)}$$

where $v = T - T'$, t is time and $\varkappa$ is $K/\rho c$ where K is the thermal conductivity. A graphical solution to Eq. (F3) for the above initial and boundary conditions has been given by Carslaw and Jaeger, 1952, p. 55, and is shown in Fig. F1. In this figure, the curves are functions of the parameter $\varkappa t/a^2$.

A large uncertainty exists in the assignment of $\varkappa$, since K, on which $\varkappa$ depends, is unknown for coesite and stishovite and is unknown for quartz and glass as a function of pressure. Two cases shall be examined as estimates of limiting values: (a) K is assumed equal to the room temperature value for glass, 0.002 cal/sec cm^3 °C (Handbook of Chemistry and Physics, 1953) and (b) K is assumed equal to the mean room temperature value of quartz, parallel and perpendicular to the c-axis, 0.02 cal/sec cm^2 °C (Handbook of Chemistry and Physics, 1953).

To examine the transfer of heat by conduction from the region of stishovite during the estimated 10 μsec of peak pressures, it is assumed that the material is compressed to density 4.3 g/cm^3, and that the specific heat of the sphere and surrounding region at the temperatures of interest is equal to 0.3 cal/g °C. The parameter $\frac{\varkappa t}{a^2}$ then has the

value 0.003 for glass and 0.03 for quartz. From the graphic solution shown in Fig. F1, it may be seen that in neither case would conduction lower the temperature of the center of the sphere. In the case of a glass-like thermal conductivity, some cooling of the exterior of the sphere ($r/a > 0.9$) and heating of the adjacent material ($1 < r/a < 1.1$) would occur.

Under the same assumptions of material constants, $\frac{\chi t}{a^2}$ for $t = 30$ msec is 10 for material of glass-like thermal conductivity and 100 for material of quartz-like thermal conductivity. In either case, heat conduction would have completely dissipated the hot spot and carried the heat into the surrounding regions before the shock wave released the material below pressures at which coesite could form. These calculations are only estimates of the thermal behavior; and in addition to this local behavior, general cooling of the material occurs as the pressure is released. These calculations suggest, however, that appreciable cooling of the stishovite core will not occur during its lifetime. This means that the transformation of the stishovite region into a cryptocrystalline core may leave the region at a higher temperature than the surrounding quartz grains. This calculation also suggests that the cryptocrystalline core would come into thermal equilibrium with its surroundings before pressures were released below those at which coesite could form.

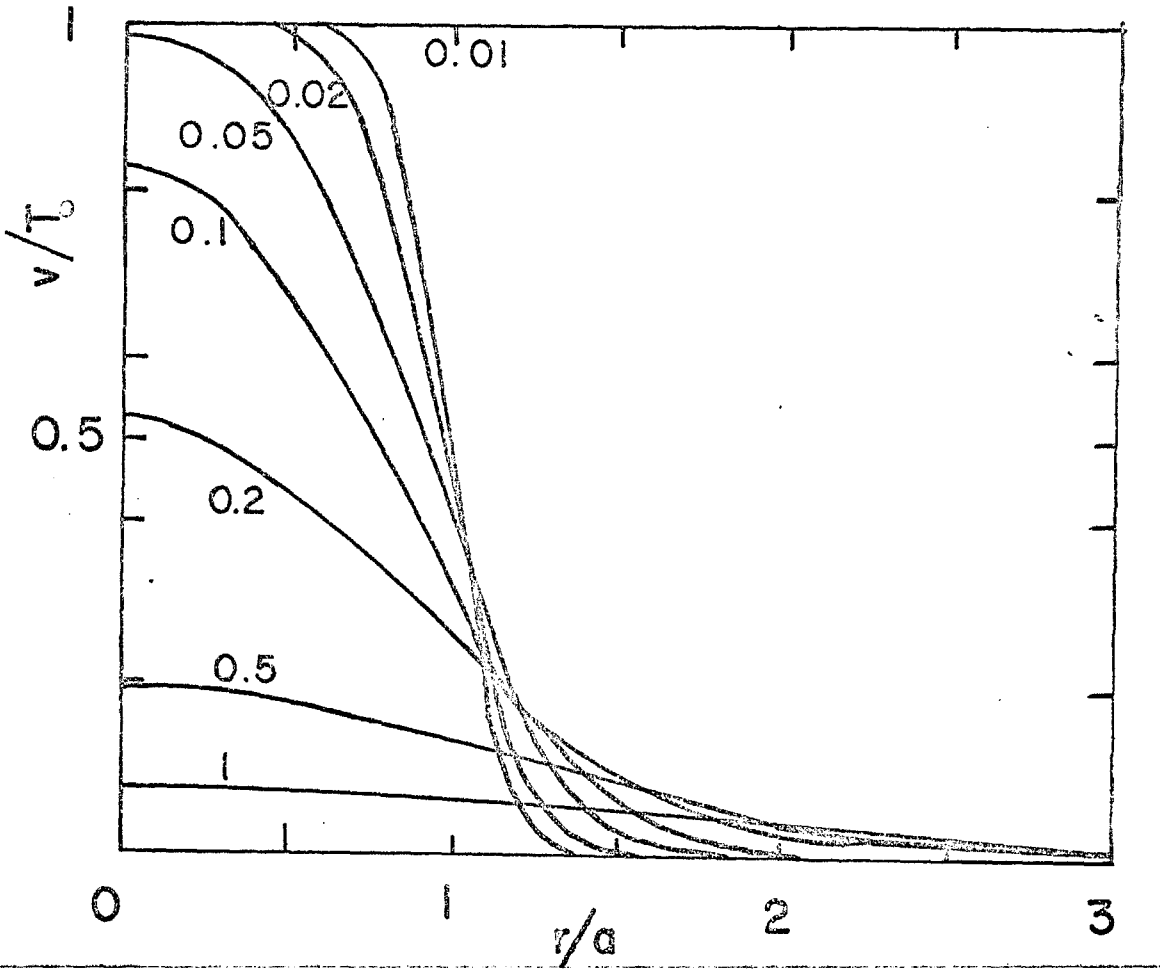

Fig. F1. The temperature ratio $v = T - T'/T_o$ as a function of distance ratio r/a, where a is the radius of the sphere, for a sphere initially at temperature T_o in an infinite medium initially at temperature T'.

REFERENCES

Anderson, O. L., E. Schreiber, R. Liebermann, and N. Soga, Some elastic constant data on minerals relevant to geophysics, Rev. Geophys., 6, 491-524, 1968.

Ahrens, T. J., D. L. Anderson, and A. E. Ringwood, Equations of state and crystal structures of shocked silicates and oxides, Rev. Geophys., 7, 667-707, 1969.

Ahrens, T. J., and V. G. Gregson, Jr., Shock compression of crustal rocks: data for quartz, calcite, and plagioclase rocks, J. Geophys. Res., 69, 4839-4874, 1964.

Ahrens, T. J., and J. T. Rosenberg, Shock metamorphism: Experiments on quartz and plagioclase, in Shock Metamorphism of Natural Minerals, edited by B. French and N. Short, Mono Book Corp., Baltimore, 1968.

Ahrens, T. J., T. Takahashi, and G. F. Davies, A proposed equation of state of stishovite, J. Geophys. Res., 75, 310, 1970.

Akimoto, S., and Y. Syono, Coesite-stishovite transition, J. Geophys. Res., 74, 1653, 1969.

Alexander, L., H. P. Klug, and E. Kummer, Statistical factors affecting the intensity of X-rays diffracted by crystalline powders, J. Appl. Phys., 19, 742, 1948.

Baker, A. A., and J. B. Reeside, Jr., Correlation of the Permian of southern Utah, northern Arizona, northwestern New Mexico and southwestern Colorado, Bull. Amer. Assoc. Petrol. Geol., XIII, 1413-1448, 1929.

Barringer, D. M., Coon Mountain and its crater, Acad. Nat. Sciences Philadelphia Proc., 57, 861-886, 1905.

Barringer, D. M., Meteor Crater (formerly called Coon Mountain or Coon Butte) in northern central Arizona, published by the author, 24 pages, 1909.

Bell, P. M., and F. R. Boyd, Phase equilibrium data bearing on the pressure and temperature of shock metamorphism, in Shock Metamorphism of Natural Minerals, edited by B. French and N. Short, Mono Book Corp., Baltimore, 1968.

Bell, P. M., G. Simmons, and J. F. Hays, Shearing squeezer experiments with quartz and coesite, Carnegie Inst. Wash. Yr. Book, 64, 141-144, 1965.

Bjork, R. L., Analysis of the formation of Meteor Crater, Arizona, J. Geophys. Res., 66, 3379-3387, 1961.

Boyd, F. R., and J. L. England, The quartz-coesite transition, J. Geophys. Res., 65, 749, 1960.

Boyd, F. R., P. M. Bell, J. L. England, and M. C. Gilbert, Pressure measurements in single-stage apparatus, Carnegie Inst. Wash. Yr. Book, 65, 410-414, 1966.

Borg, I., M. Friedman, J. Handen, and D. V. Higgs, Experimental deformation of St. Peter Sand: A study of cataclastic flow, Geol. Soc. America Memoir 79, 133, 1960.

Bridgman, P. W., The compression of 39 substances to 100,000 kb/cm^2, Proc. Am. Acad. Arts Sci., 76, 55, 1948.

Bridgman, P. W., Linear compressions to 30,000 kg/cm^2, including relatively incompressible substances, Proc. Am. Acad. Arts Sci., 77, 189, 1949.

Bunch, T. E., and A. J. Cohen, Shock deformation of quartz from two meteorite craters, Geol. Soc. America Bull., 75, 1263, 1964.

Carslaw, H. S., and J. C, Jaeger, Heat Conduction in Solids, Clarendon Press, Oxford, 1959.

Carter, N. L., Dynamic deformation of quartz, in Shock Metamorphism of Natural Minerals, edited by B. French and N. Short, Mono Book Corp., Baltimore, 1968.

Chao, E. C. T., Impact metamorphism, in Researches in Geochemistry, v. II, John Wiley and Sons, 1967a.

Chao, E. C. T., Shock effects in certain rock-forming minerals, Science, 156, 192, 1967b.

Chao, E. C. T., Pressure and temperature histories of impact metamorphosed rocks--based on petrographic observations, N. Jb. Miner. Abh., 108, 209, 1968a.

Chao, E. C. T., J. J. Fahey, and J. Littler, Stishovite, SiO_2, a very high pressure new mineral from Meteor Crater, Arizona, J. Geophys. Res., 67, 419, 1962.

Chao, E. C. T., J. J. Fahey, J. Littler, and D. J. Milton, Stishovite, Amer. Mineral., 46, 807, 1962.

Chao, E. C. T., E. M. Shoemaker, and B. M. Madsen, First natural occurrence of coesite, Science, 132, 220, 1960.

Coes, L., Jr., A new dense crystalline silica, Science, 118, 131, 1953.

Cohen, L. H., and W. Klement, Jr., High-low quartz inversion: Determination to 35 kb, J. Geophys. Res., 72, 4245, 1967.

Cullity, B. D., Elements of X-Ray Diffraction, Addison-Wesley, Reading, Massachusetts, 1956.

Dachille, F. D., and R. Roy, High pressure region of the silica isotopes, Z. Krist., 111, 451, 1959.

Darton, N. H., A reconnaissance of parts of northwestern New Mexico and northern Arizona, U. S. Geol. Survey Bull., 435, 21, 1910.

DeCarli, R. S., and J. C. Jamieson, Formation of an amorphous form of quartz under shock conditions, J. Chem. Phys., 31, 1675, 1959.

DeCarli, R. S., and D. J. Milton, Stishovite: Synthesis by shock wave, Science, 147, 144-145, 1965.

v. Engelhardt, W., and D. Stöffler, Stages of shock metamorphism in crystalline rocks of the Ries Basin, Germany, in Shock Metamorphism of Natural Minerals, edited by B. French and N. Short, Mono Book Corp., Baltimore, 1968.

Fahey, J. J., Separation of coesite and stishovite, Abstract, Ann. Meeting, Geological Society of America, p. 49, New York, 1962.

Fairchild, H. L., Origin of Meteor Crater (Coon Butte), Arizona, Geol. Soc. America Bull., 18, 493-504, 1907.

Fowles, G. R., Shock wave compression of quartz, Ph.D. thesis, Stanford University, June 1961.

Griggs, D. T., and G. C. Kennedy, A simple apparatus for high pressures and temperatures, Am. J. Sci., 254, 722, 1956.

Handbook of Chemistry and Physics, 35th edition, edited by C. D. Hodgman, R. C. Weast, C. W. Wallace, Chemical Rubber Publ. Co., 1953.

Herrmann, W., P. Holzhauser, and R. J. Thompson, WONDY, A computer program for calculating problems of motion in one-dimension, Sandia Research Report SC-RR-66-601, Albuquerque, New Mexico, 1967.

Hertz, H., On the contact of elastic solids, in Miscellaneous Papers, Chap. V, trans. D.E. Jones and G.H. Schott, Macmillan, London, 1896.

Hoffman, R., D. J. Andrews, and D. E. Maxwell, Computed shock response of porous aluminum, J. Appl. Physics, 39, 4555, 1968.

Holm, J. L., O. L. Kleppa, and E. F. Westrum, Jr., Thermodynamics of polymorphic transformations in silica. Thermal properties from 5 to 1070°K and pressure-temperature stability fields for coesite and stishovite, Geochim. et Cosmochim. Acta, 31, 2289, 1967.

Hörz, F., Statistical measurements of deformation structures and refractive indices in experimentally shock loaded quartz, in Shock Metamorphism of Natural Minerals, edited by B. French and N. Short, Mono Book Corp., Baltimore, 1968.

Janaf Thermochemical Tables, Project Principia of the Advanced Research Projects Agency at the Thermal Research Laboratory, Dow Chemical Company, Midland, Michigan, 1965; also First, Second, and Third Addenda, 1965-67.

Kennedy, G. C., G. J. Wasserburg, H. C. Heard, and R. C. Newton, The upper three-phase region in the system SiO_2- H_2O, Am. J. Sci., 260, 501, 1962.

Kitihara, S., and G. C. Kennedy, The quartz-coesite transition, J. Geophys. Res., 69, 5395, 1964.

Klug, H. P., and L. E. Alexander, X-Ray Diffraction Procedures, John Wiley and Sons, New York, 1954.

Krumbein, W. C., Measurement and geological significance of shape and roundness of sedimentary particles, J. Sediment. Petrol., 11, 64, 1941.

Liu, L. G., T. Takahashi, and W. A. Bassett, Compression of stishovite and magnesian ilmenite at 25°C, Abstract, 50th Ann. Meeting, Amer. Geophys. Union, p. 312, Washington, D.C., 1969.

MacDonald, G. J. F., Quartz-coesite stability relations at high temperatures and pressures, Am. J. Sci., 254, 713, 1956.

McKee, E. D., The Coconino sandstone -- Its history and origin, Carnegie Inst. Wash. Papers Concerning the Palaeontology of California, Arizona and Idaho, p. 79, March 1934.

McQueen, R. G., J. N. Fritz, and S. O. Marsh, On the equation of state of stishovite, J. Geophys. Res., 68, 2319, 1963.

McSkimmin, H.J., P. Andreach, Jr., and R. N. Thurston, Elastic moduli of quartz versus hydrostatic pressure at 25° and -195.8°C, J. Appl. Physics, 36, 1624, 1965.

Merrill, G. P., and W. Tassin, Contributions to the study of the Canyon Diablo Meteorites, Smithsonian Misc. Collections, Quarterly Issue, 50, 1907.

Merrill, G. P., On a peculiar form of metamorphism in siliceous sandstone, U. S. Natl. Museum Proc., 32, 547, 1908.

Noble, L. F., The Shinumo quadrangle, U. S. Geol. Survey Bull., 549, 1-100, 1914.

Opdyke, N. D., and S. K. Runcorn, Wind direction in the western United States in the late Paleozoic, Geol. Soc. America Bull., 71, 959, 1960.

Ostrovsky, I. A., 1. On some sources of errors in phase-equilibria investigations at ultra-high pressure, 2. Phase diagram of silica, Geol. J., 5, 321, 1967.

Ostrovsky, I. A., Experimental fixation of the position of the coesite-stishovite equilibrium curve (in Russian), Izv. Akad. Sci. USSR, Ser. Geol., no. 10, 132-135, 1965.

Read, C. B., Stratigraphy of the outcropping Permian rocks around the San Juan Basin, in New Mexico Geol. Soc. Guidebook of the San Juan Basin, New Mexico and Colorado, p. 62, 1950.

Read, C. B., and A. A. Wanek, Correlation of Permian rocks in northeastern Arizona and adjoining parts of New Mexico and Utah, art. 206, U. S. Geol. Survey Prof. Paper 424C, C156, 1961.

Reichl, P., An analysis of cross-lamination of the Coconino sandstone, J. Geol., XLVI, 905, 1938.

Rogers, A. F., Natural history of the silica minerals, Amer. Mineral., 13, 73-92, 1928.

Ruoff, A. L., Linear shock-velocity-particle-velocity relationship., J. Appl. Physics, 38, 4976, 1967.

Schuchert, C., On the Carboniferous of the Grand Canyon of Arizona, Am. J. Sci., XLV (4th ser.), 347, 1918.

Shipman, F. H., and V. G. Gregson, A shock wave study of Coconino sandstone, Final Report, Part I, Materials and Structures Laboratory, General Motors Corp., Warren, Michigan, 1970.

Shoemaker, E. M., Penetration mechanics of high velocity meteorites, illustrated by Meteor Crater, Arizona, Rept. Intern. Geol. Congr., XXI Session, Norden, 18, 418, 1960.

Shoemaker, E. M., Impact mechanics at Meteor Crater, Arizona, in The Solar System, v. 4, The Moon, Meteorites and Comets, edited by B. M. Middlehurst and G. P. Kuiper, p. 301, University of Chicago Press, Chicago, 1963.

Skinner, B. J., and J. J. Fahey, Observations on the inversion of stishovite to silica glass, J. Geophys. Res., 68, 5595, 1963.

Stishov, S. M., On the equilibrium line between coesite and rutile-like modification of silica (in Russian), Dokl. Akad. Sci. USSR, 148(5), 1186, 1963.

Takahashi, T., Factors influencing pressure in multi-anvil devices, in High Pressure Measurement, edited by A. A. Giardini and E. C. Lloyd, p. 240, Butterworth, London, 1963.

Tilghman, B. C., Coon Butte, Arizona, Proc. Acad. Nat. Sci., Philadelphia, 861, 1905.

Timoshenko, S., and J. N. Goodier, Theory of Elasticity, 3rd edition, McGraw-Hill, New York, 1970.

Wackerle, J., Shock-wave compression of quartz, J. Appl. Physics, 33, 922, 1962.

PART II

THE SPECIFIC HEATS OF SOLIDS OF GEOPHYSICAL INTEREST

The Specific Heats of Solids of Geophysical Interest

1. Introduction

The use of Debye temperatures as parameters for material properties of silicate minerals is becoming common in geophysical studies. Recently it has become common practice to calculate Debye temperatures for this purpose from elastic or acoustic data. For example, Anderson et al. (1968) calculated the molar specific heats of such minerals as spinel, quartz, and forsterite on the assumption that these minerals behave as Debye solids with Debye temperatures computed from the measured elastic constants; from the specific heats calculated on this assumption, temperature derivatives of the bulk modulus were deduced over a temperature range from 298° to about 1000°K. Similarly, specific heats obtained from Debye models were used by Ahrens, Anderson and Ringwood (1969) to reduce shock wave Hugoniots to adiabats for high pressure phases of shocked silicates and oxides. Horai and Simons (1970) introduced an empirical relationship between thermal conductivity and the Debye temperature calculated from elastic data.

The purpose of this paper is to call attention to the fact that the elastic Debye temperature alone is, in general, insufficient to specify properties which depend on lattice vibrations. As an alternative to the Debye model, a somewhat more complicated model is proposed that is nevertheless still reasonably convenient, and that is able to account much better than the Debye model does for the variation of specific heat of complex substances (including silicates of geophysical interest) over a wide range of temperature. The parameters required for this model are

the maximum lattice vibrational frequency, the elastic Debye temperature, and the specific heat at a single (say, room) temperature. Adequate approximations to these parameters are generally available.

To provide a basis for the model introduced, a discussion of the specific heats of simple and complex substances, which brings out the characteristic differences between ideal Debye solids and actual complex substances is given in §2. In §3 the proposed model for calculating the specific heat of complex solids is developed. The results of applying this model to twelve solids of geophysical interest are given in §4.

2. Temperature Dependence of the Specific Heat of Complex Substances

Debye model.— To provide a standard of comparison we consider first the behavior of simple solids as predicted by the Debye model. This model assumes that the density $\underline{g}(\nu)$ of lattice-vibrational frequencies ν is given by

$$\underline{g}(\nu)\ d\nu = \underline{a}\nu^2\ d\nu \tag{1}$$

The coefficient $\underline{a}$ depends fundamentally only on the elastic wave velocity. For simplicity the elastic properties are assumed to be isotropic, but even so, there should in principle be separate spectral contributions, with separate $\underline{a}$'s, for the P and S waves. In the simplest, commonly-used form of the Debye model, these separate contributions are ignored, and are replaced by a single contribution from lattice vibrational waves assumed to propagate with a mean sound velocity. In this case $\underline{a}$ is given by

$$\underline{a} = 4\pi\ \underline{V}\left(\frac{1}{\underline{v}_P^3} + \frac{2}{\underline{v}_S^3}\right) \tag{2}$$

where $\underline{v}_P$ and $\underline{v}_S$ are the P- and S-wave velocities, and $\underline{V}$ is the volume of the crystal, which for definiteness we take to consist of one mole of the substance of interest. Although the lattice-vibrational behavior of a solid in the Debye model is completely specified by the value of the parameter $\underline{a}$ given by (2), it is conventional to characterize this behavior in terms of an alternative parameter, the Debye

temperature θ_D. The definition of θ_D follows from the added assumption that the vibrational spectrum extends from $\nu = 0$ up to an upper cutoff frequency ν_D, where the spectral density $\underline{g}(\nu)$ given by equation (1) is sharply terminated. The requirement that the total number of lattice vibrational modes be $3\underline{N}$, where $\underline{N}$ is the number of atoms in the crystal, leads to the following condition on ν_D:

$$\nu_D = \left(\frac{9\underline{N}}{\underline{a}}\right)^{\frac{1}{3}} = \left(\frac{9\underline{n}\ \underline{N}_A}{\underline{a}}\right)^{\frac{1}{3}} \tag{3}$$

Here $\underline{N}_A$ is Avogadro's number, and $\underline{n}$ is the number of atoms in the chemical formula on the basis of which the molar volume and other molar quantities are specified. θ_D is then defined in terms of ν_D as

$$\theta_D = \frac{\underline{h}\nu_D}{\underline{k}} \tag{4}$$

where $\underline{h}$ and $\underline{k}$ are respectively Planck's and Boltzmann's constants. From (2)-(4) it follows that the Debye temperature can be calculated from

$$\theta_D^3 = \left(\frac{\underline{h}^3}{\underline{k}^3}\right) \frac{9}{4\pi} \frac{\underline{n}\underline{N}_A}{\underline{V}} \left(\frac{1}{\underline{v}_P^3} + \frac{2}{\underline{v}_S^3}\right)^{-1} \tag{5}$$

In order to ignore the elastic anisotropy of crystalline solids, it is conventional to take the velocities in (5) to be "VRH" averages (see Anderson, 1965).

The specific heat of a Debye solid is obtained as follows:

The heat-capacity contribution of an individual lattice-vibrational oscillator (Einstein oscillator) of frequency ν is given by

$$E\left(\frac{h\nu}{kT}\right) = \frac{\partial}{\partial T}\left(\frac{h\nu}{e^{h\nu/kT} - 1}\right) \tag{6}$$

where T is the absolute temperature. Equation (6) contains a definition of the Einstein function $E\left(\frac{h\nu}{kT}\right)$. The molar specific heat is a weighted summation of Einstein functions:

$$c_v = \int_0^{\nu_D} g(\nu)\ E\left(\frac{h\nu}{kT}\right)\ d\nu \tag{7}$$

With the use of (2)-(5), equation (7) reduces to the dimensionless form

$$c_v \Big/ R = 9\ n\left(\frac{T}{\theta_D}\right)^3 \int_0^{\theta_D/T} \frac{x^4\ e^x}{(e^x - 1)^2}\ dx = n\ D\left(\frac{\theta_D}{T}\right) \tag{8}$$

where R is the gas constant, $x = \frac{h\nu}{kT}$, and $D\left(\frac{\theta_D}{T}\right)$ is the Debye function. From the Debye function $D(\theta_D/T)$, which is tabulated in many references, and from a knowledge of the acoustic velocities, the heat capacity as a function of temperature can be predicted.

Actual heat capacities in relation to the Debye model.— Applicability of the Debye model to real substances is governed by the extent to which the actual lattice vibrational spectrum is approximated by the $g(\nu)$ given by (2) and (3) (with the assumed sharp upper cutoff frequency ν_D). Mathematical study of the vibrational modes of crystalline arrays of atoms (Blackman, 1955) shows that for monatomic crystals, in which there is only one atom per unit cell (which allows

the choice $\underline{n} = 1$ in (3), (5), and (8)), the vibrational spectrum is reasonably well represented by the Debye model. The separate spectral contributions from the P and S vibrations cause a definite departure from the simple Debye spectrum at the higher frequencies; however, the form of the dispersion relation (ν vs the wave vector K) for the individual branches (P or S) departs from the linearity assumed in the Debye model in such a way as to tend to compensate the first effect (see Leibfried, 1955, p. 251).

A similar conclusion follows for polyatomic solids ($\underline{n} > 1$) if the different atoms play nearly equivalent mechanical roles in the vibrational process. In general terms, the conditions for this are that (a) the various atoms have nearly equal masses, (b) the coordination environments of the different atoms are nearly identical and (c) are essentially isotropic, and (d) the various near-neighbor interatomic force constants are nearly equal. In this case it is possible to think of the polyatomic crystal as essentially a monatomic crystal as far as the atomic vibrations are concerned; the "vibrational unit" of the crystal can be taken as the individual atom without regard to type.

For more complex substances, the failure of one or more of the conditions (a)-(d) above results in such large changes in the vibrational spectrum that the Debye model no longer provides an adequate approximation to the heat capacity. The extent of departure from Debye-like behavior is shown by the widely-used procedure of representing the observed c_v at each temperature in terms of a so-called "calorimetric Debye temperature," $\theta_{cal}(T)$, which is the value of θ_D in equation (8) that will reproduce the observed $c_v(T)$. Examples of

$\theta_{cal}(T)$ for simple, rather Debye-like solids and solids of geophysical interest, taken from the more extensive compilation in §4, are shown in Fig. 1 and Fig. 2.

For those elements and alkali halides to which the Debye model may be expected to apply, $\theta_{cal}(T)$ should be a constant equal to θ_D. The near constancy of $\theta_{cal}(T)$ for Pb, KCl, and NaCl in Fig. 1, particularly at the higher temperatures, is about as good an approach to ideal Debye behavior as is achieved for any real solids. The $\theta_{cal}(T)$ curves for Ge, gray Sn, and GaSb are examples of about the largest departures from ideal Debye behavior that are found for elements or simple compounds, excluding molecular solids such as I_2. Most simple compounds show significant departures from ideal Debye behavior over a range of temperatures just above 0° K. In this range, $\theta_{cal}(T)$ typically drops by some 10-20% from its value $\theta_{cal}(0)$ at absolute zero. The curve for Ge in Fig. 1 shows a relatively exaggerated example of this type of behavior for a simple solid. For most simple solids, $\theta_{cal}(T)$ becomes essentially constant for $T \geqslant 0.1\ \theta_D$. (A detailed discussion of these points is given by Blackman, 1955.)

The mineral examples in Fig. 2 show a very different behavior. Over most of the plotted temperature range, $\theta_{cal}(T)$ is a strongly increasing function of temperature. $\theta_{cal}(400^\circ K)$ is two or three times $\theta_{cal}(0^\circ K)$. There is a tendency for $\theta_{cal}(T)$ to approach a constant value asymptotically at high temperature, but this behavior sets in only for temperatures $T \geqslant \theta_{cal}(0)/2$, much higher than for the simple compounds. In the low-temperature range, most minerals for which data are available

show the drop in $\theta_{cal}(T)$ from $\theta_{cal}(0)$, similar to that for simple compounds, but for certain examples, notably stishovite and rutile, an extreme behavior of this type occurs. The significance of this is considered in §4.

Elastic Debye temperature.— A more stringent test of the Debye model lies in its quantitative prediction of the heat capacity in terms of the elastic properties: θ_{cal} should be the same as θ_D calculated from the sound velocities via equation (5). To make the distinction explicit, Debye temperatures calculated in this way from elastic data (or the corresponding sound velocities) are often called "elastic Debye temperatures" and are designated with the symbol θ_{el}. Because the elastic constants vary somewhat with temperature, we must consider a temperature dependence for $\theta_{el}(T)$, but the dependence is usually slight enough to be ignored for most purposes. In calculating θ_{el} from (5) for simple compounds satisfying conditions (a)-(d) stated above, it is the practice to take nN_A/V as the particle density (number of atoms per unit volume without regard to type), in accordance with the rationale discussed, in which the "vibrational unit" of the crystal is the single atom without regard to type. This practice has generally been followed also in calculating θ_{el} for minerals of geophysical interest, as in the examples cited above, even though conditions (a)-(d) generally do not hold for these substances.

The θ_{el} values marked in Fig. 2 by the circles have been obtained for the most part from elastic or acoustic measurements at room temperature, but, as noted

above, they can be considered appropriate over a wide temperature range, because the temperature variation of particle density and sound velocity is slight. For elements and simple compounds that are Debye-like in showing a nearly T-independent $\theta_{cal}(T)$, it is found that θ_{el} generally agrees with θ_{cal} to within 10% (Blackman, 1955). Alers (1965) has shown that θ_{el} and θ_{cal} should be in reasonable agreement for $T < \theta_D/50$ in the case of the cubic metals, for $T < \theta_D/100$ in the case of alkali halides, and for $T < \theta_D/150$ in the case of the hexagonal metals.

For complex compounds, the situation is different. Since they do not behave at all like Debye solids — as shown by the extreme temperature variation of $\theta_{cal}(T)$ — one might at first suppose that the quantity θ_{el} has no particular meaning, and does not bear comparison with the highly variable $\theta_{cal}(T)$. In principle, however, θ_{el} should be essentially equal to $\theta_{cal}(0)$, even for solids departing greatly from Debye-type behavior. This follows from the fact that the spectral density function $g(\nu)$ always tends, in principle, to the form (1) as $\nu \to 0$. Thus as $T \to 0$, when only the lowest-frequency lattice oscillations contribute appreciably to the specific heat, a Debye-like, "T^3" behavior ($c_v(T)$ varying as T^3) always can be observed; $\theta_{cal}(0)$ is determined from this limiting T^3 behavior. The lowest-frequency lattice oscillations are in fact just the ordinary acoustic waves, whose velocities can be measured (though not usually at 0° K), and for which the relationship in equation (2) is exactly valid, provided the crystal is elastically isotropic. No assumption is needed of waves propagating with a velocity that is an average of v_P and v_S, because the separate

contributions of the P and S waves to $\underline{g}(\nu)$ simply add in accordance with equation (2). However, any elastic anisotropy requires a detailed summation of the contributions to $\underline{g}(\nu)$ for waves travelling in different directions. There is no reason to expect that this summation would lead exactly to the same result as is obtained by the common practice of substituting into (2) values of $\underline{v}_P$ and $\underline{v}_S$ obtained by making "VRH" averages for elastically anisotropic crystals or by measuring $\underline{v}_P$ and $\underline{v}_S$ for polycrystalline specimens. Because all crystals are elastically anisotropic to some degree, some discrepancy (although perhaps slight) may on this basis be expected between $\theta_{cal}(0)$ and θ_{el} as conventionally calculated from (5).

As shown in Fig. 2, for typical silicate minerals $\theta_{cal}(T)$ drops down at low temperatures to approximately the value of θ_{el}. For most examples, c_v data do not extend to low enough temperatures for the limiting $\theta_{cal}(0)$ to be determined. The trend of $\theta_{cal}(T)$ at the lowest available temperatures is generally such as to carry it below θ_{el} at even lower temperatures. From the preceding discussion we may reasonably assume that as $0^{\circ}K$ is approached, $\theta_{cal}(T)$ will drop to a minimum and then rise again to the value θ_{el}. This assumption can be tested only for rutile and quartz, and for both of these it appears to hold, at least to a fair approximation. The rutile data are considered in §4. For quartz and other forms of SiO_2, the essential equality of θ_{el} and $\theta_{cal}(0)$ was discussed in detail by Anderson (1959). (However, interpretation by Lord and Morrow (1957) of more recent specific heat data of Westrum for quartz below $10^{\circ}K$ suggests that $\theta_{cal}(0^{\circ}K) = 527^{\circ}K$, whereas

$\theta_{el}(300^{\circ}K) = 586^{\circ}K$ (Anderson, 1968). The variation of θ_{el} with temperature from $300^{\circ}K$ to $0^{\circ}K$ is probably not sufficient to account for this discrepancy. Hence it appears at this time that the equality of θ_{cal} and θ_{el} for quartz is not fully established.)

The expected equality of θ_{el} and $\theta_{cal}(0)$ applies also, of course, to the simple, nearly Debye-like compounds. The 2% latitude quoted by Alers (1965) in the agreement between θ_{el} and θ_{cal} may reflect difficulties in obtaining accurate elastic constants, in extrapolating them to 0° K, and in measuring the heat capacity accurately to the very low temperatures required to obtain a reliable value of $\theta_{cal}(0)$. In addition, the effect of elastic anisotropy, noted above, can upset an exact agreement between θ_{el} and $\theta_{cal}(0)$.

Causes of the non-Debye behavior of silicates.— The failure of the simple Debye model to take into account detailed spectral features of complex crystals, such as anisotropy and the separation of acoustic and various optic branches in the dispersion relation is responsible in a general way for the strong departure from Debye-like behavior shown by the silicate minerals in Fig. 2. It is possible, however, to go beyond this generality, and to understand in rather definite terms why the $\theta_{cal}(T)$ behavior shown in Fig. 2 occurs. Spectroscopic study of silicates reveals lattice vibrational frequencies extending up to $\nu \sim 1000$ cm^{-1} (Fig. 3); the highest frequencies represent the Si-O stretching vibrations. In contrast, values of θ_{el} or $\theta_{cal}(T) \sim 500^{\circ}K$ for silicates at low temperatures would correspond, if interpreted in terms of equation (4), to upper cutoff frequencies $\nu_D \sim 350$ cm^{-1} for a Debye-type vibrational

spectrum. It is thus evident that the actual spectrum contains, in addition to the necessary Debye-like portion (equation (1)) at low frequencies, an array of vibrations extending to much higher frequencies than the upper limit that would be anticipated from the form of the Debye-like portion.

This state of affairs can be expected from the structural features of silicates. The strong Si-O bond, with high force constant, binds local portions of the structure together into tight units, the more-or-less localized internal vibrations of which contribute high frequencies to the vibrational spectrum. During a broad-scale compression or deformation of the structure, as occurs in the propagation of acoustic waves, the tightly-bound units tend not to compress or deform internally, but instead to shift relative to one another by the distortion of weaker bonds, with lower force constants, between the tightly-bound units. In orthosilicates, the relatively weak bonds are the cation-oxygen bonds such as Mg - O; in tectosilicates, bending of the Si - O - Si linkages provides the soft mechanism for relative shifts of SiO_4 tetrahedra; for silicates of intermediate polymerization, both mechanisms operate. The soft deformation mechanisms dominate the elastic behavior, so that the acoustic velocities are relatively low, $\underline{a}$ in (1) is large, and the inferred cutoff frequency ν_D from (2) is relatively small. The high frequencies in the actual spectrum are dominated by the hard deformation mechanisms, and are thus shifted to frequencies higher than would occur in the absence of any change of effective force constant with frequency, hence higher than the inferred ν_D.

The discrete-frequency spectroscopic model.— Spectroscopists have frequently accounted for the complex spectra by separating the vibrations into a discrete "intramolecular" spectrum plus an acoustic spectrum. This model is briefly reviewed to provide a basis of comparison and contrast for the model presented in §3.

A detailed compilation of vibrational frequencies and degeneracies for a mineral must be obtained from an assumed lattice model for which the vibrating unit of the crystal is specified (see, for example, Raman, 1961; Saksena, 1940). As such a compilation of infrared and Raman frequencies exists for quartz, it was possible for Lord and Morrow (1957) to calculate the specific heat of quartz by assigning individual Einstein oscillators to the assumed frequencies. The frequency assignment of R. C. Lord and J. B. Wilmont, as reported by Lord and Morrow (1957) is as follows: species A, 207, 356, 466, 1082 cm^{-1}; species B, 365, 520, 780, 1055 cm^{-1}; species E, 128, 264, 397, 452, 695, 800, 1064, 1160 cm^{-1}. Species E is doubly degenerate. Lord and Morrow (1957) assumed that the three SiO_2 groups associated with each α-quartz unit cell were the fundamental vibrating unit. Each unit cell contributes 27 degrees of freedom to the total for the crystal. The above listed frequencies account for twenty-four degrees of freedom, and correspondingly, twenty-four Einstein oscillators; the remaining three degrees of freedom were assumed to be "translational" motions of the unit cell and to obey a Debye frequency distribution law with a Debye temperature of 254° K, appropriate to $\frac{1}{9}$ of the degrees of freedom. This Debye temperature was determined from experimental heat

capacities below 10° K. The choice of a unit cell to represent the fundamental vibrating unit was arbitrary, and this spectroscopic method of assignment of Debye and Einstein oscillators is not a unique assignment. It relies on the assumption that the discrete frequencies can be identified and counted as those of the atoms in one unit cell of the quartz structure, but, in fact, individual unit cells are not mechanically isolated in the crystal, so that in no sense do they constitute "vibrational units" to which a unique mechanical role can be attributed. The difficulty with Lord and Morrow's frequency assignments can be appreciated from the fact that several of the discrete frequencies chosen lie within the range of the Debye spectrum assigned to the acoustic vibrations. In addition to these difficulties, this type of model requires far more information than is available for most solids.

The model developed in §3 provides an approach for dealing with the above difficulty for silicates and other complex minerals, while retaining the basic guiding features discussed in the present section. In addition it brings out significant systematic similarities and differences among the calorimetric properties of different silicates.

3. The Acoustic - Optic Model

A model is developed here that takes into account the essential features of silicate vibration spectra discussed in §2. The low frequency part of the spectrum is assumed to be Debye-like, which must be the behavior as the frequency approaches zero. In addition, a substantial proportion of oscillators is assumed to exist at frequencies higher than the ν_D of a pure Debye spectrum, in order to account for the high-frequency vibrations observed in infrared and Raman spectra.

The introduction of a group of Einstein oscillators at a single high frequency, ν_E, is perhaps the simplest way to introduce high frequency oscillators. Si-O stretching vibrations of the SiO_4 tetrahedra can be identified as the source of the highest vibrational frequencies. Coupling between the vibrations of different tightly-bonded units results, however, in a broad band of frequencies in the spectrum. A single discrete frequency, therefore, is not a realistic model.

As discussed in §2, infrared and Raman spectra demonstrate the presence of vibrational modes with frequencies spanning essentially the full range from 350 cm^{-1} to 1100 cm^{-1}. On this basis a spectrum is here assumed in which the Debye part of the spectrum is truncated at a frequency $\nu_D' < \nu_D$, and a continuum of frequencies is added spanning the range ν_D' to ν_M, where ν_M is the maximum lattice vibrational frequency. For simplicity, it is assumed that $\underline{g}(\nu)$ is constant over the range ν_D' to ν_M, so that $\underline{g}(\nu)$ has the form

$$\underline{g}(\nu) = \begin{cases} \underline{a}\nu^2 & 0 < \nu < \nu_D' \\ \underline{g}_o & \nu_D' < \nu < \nu_M \end{cases} \qquad (9)$$

The Debye part of the spectrum assumed in (9) is generally attributed to acoustic modes of vibration. The high frequency vibrations between ν_D' and ν_M represent, in a general way, high frequency vibrations due to optic modes. For this reason, spectra of the form given in (9) will be referred to as <u>acoustic-optic</u> spectra.

The possible relationships between $\underline{a}$, ν_D', ν_M and $\underline{g}_0$ allow three significantly different forms of $\underline{g}(\nu)$ to be recognized. The first type, shown in Fig. 4a, has a portion of the total oscillators at frequencies higher than the Debye cutoff frequency ν_D. This will be called a "tailed spectrum." From the discussion in §2, it is clear that a tailed spectrum will result in a $\theta_{cal}(T)$ that increases with T. The second type (Fig. 4b), called here a "compressed spectrum," has oscillators below ν_D in excess of the Debye oscillators, and will give a $\theta_{cal}(T)$ that decreases with T. The third type (Fig. 14c) has excess oscillators below ν_D as well as oscillators at frequencies greater than ν_D and will be called a "hybrid spectrum." In this type of spectrum, $\underline{g}_0 > \underline{a}\nu_D'^2$ and $\nu_M > \nu_D$. It will give a $\theta_{cal}(T)$ that decreases with T at low T because of the oscillators in excess of Debye oscillators below ν_D, but $\theta_{cal}(T)$ will increase at higher temperatures because of the presence of oscillators at frequencies greater than ν_D.

temperatures.

The constant $\underline{a}$ must fit the elastic or acoustic behavior at low ν_M is taken to be the maximum observed infrared or Raman frequency. The parameters ν_D' and $\underline{g}_0$ are less clearly constrained <u>a priori</u>, but since they must be related in such a way that the total number of vibrational modes given by (9) is $3\underline{N}$, only one of them is independent.

The total number of degrees of freedom is

$$3\underline{N} = 3\underline{N}' + \underline{g}_0 \ (\nu_M - \nu_D') \tag{10}$$

where

$$3\underline{N}' = \int_0^{\nu_D'} \underline{a}\ \nu^2 \underline{d}\ \nu = \tfrac{1}{3}\ \underline{a}\ \nu_D'^3 \quad . \tag{11}$$

From (11) and (3), it may be seen that

$$\frac{\underline{N}'}{\underline{N}} = \left(\frac{\nu_D'}{\nu_D}\right)^3 \quad . \tag{12}$$

From (10) and (12), $\underline{g}_0$ is given by

$$\underline{g}_0 = \frac{3(\underline{N} - \underline{N}')}{\nu_M - \nu_D'} = \frac{3\underline{N}\left(1 - \dfrac{\nu_D'^3}{\nu_D^3}\right)}{(\nu_M - \nu_D')} \tag{13}$$

in which ν_D' remains to be determined. From (7), the specific heat of a solid having an acoustic-optic spectrum of the type (9) is

$$c_v(T) = \int_0^{\nu_D'} \frac{\underline{a}\nu^2\left(\dfrac{\underline{h}\nu}{\underline{k}T}\right)^2 \underline{k} e^{\underline{h}\nu/\underline{k}T}\ \underline{d}\nu}{(e^{\underline{h}\nu/\underline{k}T} - 1)^2} + \int_{\nu_D'}^{\nu_M} \frac{\underline{g}_0\left(\dfrac{\underline{h}\nu}{\underline{k}T}\right)^2 \underline{k}\, e^{\underline{h}\nu/\underline{k}T}\ \underline{d}\nu}{(e^{\underline{h}\nu/\underline{k}T} - 1)^2} \tag{14}$$

In the application of the acoustic-optic model in this thesis, ν_D' has been determined from the observed value of c_v at one temperature. Asuming c_v known at particular T, equation (14) is easily solved for ν_D' by iteration on a small computer.

Asymptotic behavior.— The asymptotic value of $\theta_{cal}(T)$ can be obtained by expanding equation (14) in powers of θ/T. Changing to the dimensionless variables

$$\begin{aligned} \underline{x} &= \frac{h\underline{\nu}}{\underline{k}T} \\ \underline{x}'_D &= \frac{h\underline{\nu}'_D}{\underline{k}T} = \frac{\underline{\theta}'_D}{T} \\ \underline{x}_M &= \frac{h\underline{\nu}_M}{\underline{k}T} = \frac{\underline{\theta}_M}{T} \\ \underline{x}_D &= \frac{h\underline{\nu}_D}{\underline{k}T} = \frac{\underline{\theta}_D}{T} \end{aligned} \tag{15}$$

equation (14) becomes

$$\frac{\underline{c}_v}{\underline{n}R} = \frac{9}{\underline{x}_D^3} \int_0^{\underline{x}'_D} \frac{\underline{x}^4 \, e^{\underline{x}} \, d\underline{x}}{(e^{\underline{x}} - 1)^2} + \frac{3\left(1 - \frac{\underline{x}_D'^3}{\underline{x}_D^3}\right)}{\underline{x}_M - \underline{x}'_D} \int_{\underline{x}'_D}^{\underline{x}_M} \frac{\underline{x}^2 \, e^{\underline{x}} \, d\underline{x}}{(e^{\underline{x}} - 1)^2} \tag{16}$$

For T greater than θ_M, $\underline{x}$ is everywhere less than 1 and the integrals become

$$\begin{aligned} \int_0^{\underline{x}'_D} \frac{\underline{x}^4 \, e^{\underline{x}} \, d\underline{x}}{(e^{\underline{x}} - 1)^2} &= \frac{\underline{x}'^3_D}{3} - \frac{\underline{x}_D^5}{60} + \cdots \\ \int_{\underline{x}'_D}^{\underline{x}_M} \frac{\underline{x}^2 \, e^{\underline{x}} \, d\underline{x}}{(e^{\underline{x}} - 1)^2} &= (\underline{x}_M - \underline{x}'_D) - \left(\frac{\underline{x}_M^3}{36} - \frac{\underline{x}_D'^3}{36}\right) + \cdots \end{aligned} \tag{17}$$

From (16) and (17), the asymptotic high temperature form for c_v is

$$c_v = 3\underline{n}R\left[1 - \frac{1}{T^2}\left(\frac{\underline{\theta}_D'^5}{20\,\underline{\theta}_D^3} + \frac{\underline{\theta}_M^2 + \underline{\theta}_M\underline{\theta}'_D + \underline{\theta}_D^2}{36}\left(1 - \frac{\underline{\theta}_D'^3}{\underline{\theta}_D^3}\right)\right) + \cdots\right] \tag{18}$$

For a solid in which all degrees of freedom are included in the Debye spectrum, the high temperature series for c_v is

$$c_v(\text{Debye solid}) = 3\underline{n}R\left[1 - \frac{1}{T^2}\left(\frac{\theta_D^2}{20}\right) + \cdots\right] \tag{19}$$

In both the Debye and acoustic-optic models, only even powers of 1/T occur in the high temperature expansion of c_v and, therefore, the solids described by the acoustic-optic model behave as Debye solids at high temperatures, with calorimetric Debye temperatures given by

$$\theta_{cal}(\infty) = \left[\left(\frac{\theta_D'^5}{\theta_D^3} + \frac{5}{9}\left(\theta_M^2 + \theta_M\theta_D' + \theta_D^2\right)\left(1 - \frac{\theta_D'^3}{\theta_D^3}\right)\right)\right]^{\frac{1}{2}} \tag{20}$$

Although equation (18) is strictly valid for $T \gg \theta_M$, it generally is a reasonable approximation for $\theta_{cal}(\infty)/T \geq 2$.

4. Application to minerals of geophysical interest

The acoustic-optic model given in §3 is here applied to the twelve minerals listed in Table 1. Specific heats for the minerals are shown in Fig. 5; the sources of these data are given in Table 1. Specific heat data for minerals at atmospheric pressure are usually measured and tabulated in terms of c_p, the specific heat at constant pressure, rather that in terms of c_v, the quantity calculated by (14). These two are related by

$$c_v = c_p - TV\alpha^2K \tag{21}$$

where $\alpha(T)$ is the volume coefficient of thermal expansion, K(T) is the

bulk modulus, and V(T) is the specific volume. To use (21), α, K and V must be known as functions of temperature, but values of these quantities are generally available only at about 300°K. Values of $c_p - c_v$ at 300°K are given in Table 1. They show that $c_p - c_v$ is generally less than 0.01 c_p at this temperature. An estimate $c_p - c_v \approx 0.04\ c_p$ is available for quartz at 700°K (Lord and Morrow, 1957). It is assumed that deviations of similar magnitude occur for the other minerals that have $\theta_D > 500°K$, and, accordingly, the difference between c_p and c_v is ignored for these minerals. Small discrepancies between measured c_p values and calculated c_v values are to be expected at high temperatures on this account. For NaCl the correction from c_p to c_v is large and cannot be ignored. Values of c_v used here are from Raman (1961) and Janaff (1965). The specific heat values shown in Fig. 5, and labelled simply c there, are c_p for all minerals except halite and quartz, for which the values given are c_v, the $c_p - c_v$ correction for these minerals being available over a range of temperatures.

The results of the calculations with the acoustic-optic model are summarized in figs. 6 and 7. In Figs. 6a and 7a, the measured specific heats of fig. 5 have been reduced to a normalized specific heat, c*, by dividing by the number of atoms, n, on which the gram-formula weight is based. Measured specific heats, c*, shown by data points in Figs. 6a and 7a, are compared with c_v computed from the acoustic-optic model, the heavy solid line. Specific heats computed from the Debye model, $D(\theta_D/T)$ with θ_D equal to the elastic Debye temperature, are shown by the long dashed lines. The short dashed lines are "calorimetric" Debye curves, $D(\theta_{cal}(300°K)/T)$. These are Debye curves fitted to the specific heat

measured at room temperature, and probably represent the best specific heat curves that could be predicted if the Debye temperature θ is used as a parameter to fit the specific heat instead of being given independently by elastic data.

The calorimetric Debye temperature as a function of temperature was calculated for the acoustic-optic model and is compared with measured $\theta_{cal}(T)$ curves in Figs. 6b and 7b. The $\theta_{cal}(T)$ curves are a more sensitive indicator of deviations from the measured values than are the specific heat curves and show well systematic deviations between different models. Values of $\theta_{cal}(\infty)$ calculated from (20) are indicated in Figs. 6b and 7b by arrows pointing to the right and located at the right-hand margin of the graphs.

The parameters ν_M and ν_D', and the experimental value $c_p(T)$ used in obtaining the parameter ν_D', are listed in Table 2, columns 1, 3, and 4. The resultant frequency distribution curves are defined by the parameters ν_D', $\underline{a}/N$, $\underline{a}\nu_D'^2/N$, and $\underline{g}_0/N$ (Table 3, columns 5-8). ν_D' is the Debye cutoff frequency associated with N' oscillators; the fraction of oscillators of frequency lower than ν_D' is N'/N (Table 3, column 9). $\underline{a}\nu_D'^2$ is the density of states at the truncation frequency ν_D'. $\underline{g}_0$ is the level of the "optic" continuum between ν_D' and ν_M. The calculated frequency distribution curves based on these parameters are shown in Figs. 8, 9, and 11.

General features of the results.— The thermal behavior of the minerals studied, as seen both in measured θ_{cal} values and in the $\theta_{cal}(T)$ curves calculated from the acoustic-optic model (Figs. 6b and 7b), shows a systematic relationship to the mineral structure type. The framework silicates (quartz, coesite, albite, microcline) show a large and consistent increase in $\theta_{cal}(T)$, from $\theta_{cal}(0) \sim 500^{\circ}K$ to $\theta_{cal}(\infty) \sim 1100^{\circ}K$. The chain silicates (diopside, jadeite) show a similar but distinctly smaller increase ($\sim$ 700 to $\sim$ 1050°K). For the one orthosilicate studied (forsterite), the increase is slightly smaller than for the chain silicates. Rutile and stishovite show only a small increase, spinel almost none, and periclase and halite show a definite decrease from $\theta_{cal}(0)$ to $\theta_{cal}(\infty)$.

These systematic differences among the various minerals reflect the influence of complex ions on the vibrational spectra. Structures in which no complex ions are recognizable, such as spinel and NaCl, show a nearly Debye-like behavior, and their acoustic-optic spectra as derived here do not have a high-frequency "optic" tail. The high-frequency vibrations of the SiO_4^{4-} complex ion are responsible for the tail in the acoustic-optic spectrum of olivine, and for the corresponding rise from $\theta_{cal}(0)$ to $\theta_{cal}(\infty)$. Polymerization of the SiO_4^{4-} complex ions in chain and framework silicates leads to further increases in the highest vibrational frequencies, but without a proportionate increase in the lower frequencies, so that the tail becomes relatively stronger (measured by $1' - \underline{N}'/\underline{N}$) and the rise from $\theta_{cal}(0)$ to $\theta_{cal}(T)$ becomes correspondingly greater. In comparing the quartz form of SiO_2 with the stishovite form, we compare a structure built of completely polymerized complex ions with a structure in which complex ions are not distinguishable. Consequently the rise from $\theta_{cal}(0)$ to

$\theta_{cal}(\infty)$ for stishovite is much less than for quartz.

Spectra derived by applying the acoustic-optic model to the minerals listed in Table 1 show the three possible forms discussed in §3 (Figs. 4, 8, 9, and 11). In general, silicates give "tailed" spectra (Fig. 4a), without regard to the extent of polymerization of the complex ions, whereas substances without complex ions generally give either "compressed" spectra (Fig. 4b) or else tailed spectra in which the "tail" is weak. Stishovite and rutile give hybrid spectra, whose significance will be considered later.

On the basis of the correlations discussed above, it is believed that the vibrations in the tail represent the high frequency vibrations of tight units within the structure. In applying the name acoustic-optic to the spectra, it should be remembered that these vibrations of the tight units in the crystal may not include all of the vibrational modes which are strictly defined as "optic".

Of the three types of spectra, only the tailed spectra and the hybrid spectra represent combinations of Debye and optic vibrational frequencies in the sense discussed in §2. The compressed spectra, with maximum frequency ν_M depressed below the acoustic Debye frequency ν_D, do not contain the type of optic high frequency vibrations which are necessary to explain the θ_{cal} behavior of silicates. Nevertheless, the form of these compressed spectra can be interpreted in terms of known properties of lattice vibrations. In the following discussion of the specific heats and acoustic-optic spectra of the minerals, it will be demonstrated that the tailed spectra characteristic of the silicates and the compressed spectra characteristic of the other substances studied represent entirely different

lattice properties. Furthermore, it will be shown that the hybrid spectrum is an inadequate combination of the features associated with the tailed and compressed spectra and that a simple model such as the acoustic-optic model cannot be satisfactorily used in such a situation.

Minerals with tailed spectra.— The tailed spectra of Figs. 4a and 8 give $\theta_{cal}(T)$ curves that rise with increasing temperature. No initial decrease in $\theta_{cal}(T)$ occurs. The occurrence of $\theta_{cal}(T) > \theta_D$ requires the presence of oscillators at frequencies greater than ν_D. Therefore tailed spectra are obtained whenever ν_M exceeds ν_D and $\theta_{cal}(T)$ exceeds θ_D at the temperature at which the model was fit to c_v. The degree to which $\theta_{cal}(T)$ exceeds θ_D at high temperatures is controlled by the position of ν_M and by the fraction of oscillators N'/N in the tail relative to the fraction of oscillators in the Debye part of the spectrum.

Quartz.— The excellent agreement between the calculated and measured values of the specific heat for quartz over the whole range of temperatures is due to two factors: (1) a, and hence θ_D, were determined from actual measurements of specific heat of quartz below 10°K instead of from elastic constants at room temperatures, (2) the frequencies in the quartz vibrational spectrum appear to be nearly randomly distributed between 350 cm^{-1} and 1172 cm^{-1}, except for a clustering of vibrational states at the highest frequencies (see Fig. 8a, in which the frequencies and degeneracies of the discrete vibrational states assumed by Lord and Morrow (1957) are shown and also Fig. 3, which shows a deep absorption band centered at 1100 cm^{-1}). This amount of clustering does not affect the heat capacity or $\theta_{cal}(T)$ to any marked extent, as shown by the agreement between observed values and values calculated from the acoustic-optic

model. A suggestion of some influence is seen in the fact that the observed values of $\theta_{cal}(T)$ are slightly higher than the calculated curve for $T > 350^{\circ}K$ (Fig. 6b). A comparison between calculated and measured specific heat values (Table 3) shows less than 10% deviation above $70^{\circ}K$, less than 3% deviation above $100^{\circ}K$ and less than 1% above $280^{\circ}K$. The Debye part of the spectrum (Fig. 8a) includes 28% of the oscillators and extends to 239 cm^{-1}. Lord and Morrow (1957), by comparison, assign 11.2% of the oscillators to a Debye spectrum having a cutoff frequency of 176 cm^{-1}, but also have two Einstein oscillators at the low frequency of 128 cm^{-1}. The Einstein oscillator at 128 cm^{-1} contributes to the low temperature heat capacities in excess of the Debye spectrum, and enables Lord and Morrow to calculate c_v more accurately in the temperature region 50° - $150^{\circ}K$. Debye and acoustic-optic solids both show up to 50% deviations in the temperature range 20° - $40^{\circ}K$.

Coesite.— The specific heat of coesite is similar to that of quartz, Fig. 5a. As the Debye temperatures of quartz ($528^{\circ}K$) and coesite ($645^{\circ}K$) are not equal, and as the upper cutoff of vibrational frequency of coesite is 1218 cm^{-1}, exceeding the quartz cutoff, 1172 cm^{-1}, the striking similarity of specific heat values is somewhat unexpected. The predicted vibrational spectrum of coesite is more Debye-like than that of quartz; 48% of the oscillators are included in the Debye part of the spectrum and the Debye cutoff ν_D' frequency, 350 cm^{-1}, is higher than ν_D' for quartz 239 cm^{-1}. The $\theta_{cal}(T)$ curve for coesite agrees with experimental values at temperatures greater than $100^{\circ}K$. Because θ_D used in this model was obtained from a bulk modulus calculated from the mean density method of Anderson (1965), some improvement may be made when accurate elastic

constants are available. The calorimetric data of Holm, et al. (1967) below 10°K may be indicative of a somewhat lower value of θ_D than used in the acoustic-optic model. (See Fig. 6b, $\theta_{cal}(T)$ at low temperatures.)

Microcline, Albite.— Microcline and albite are structurally similar *frameworks of linked (Si, Al)-O tetrahedra with interstices filled by* sodium or potassium ions. Infrared spectra of the two minerals are nearly identical in the region 400-1200 cm^{-1} and the Debye temperatures θ_D are nearly equal. It is therefore to be expected, if the acoustic-optic model is realistic, that the specific heats at 300°K would be nearly equal and that the resulting calculated spectra would be nearly identical. This indeed is the case: the Debye part of the spectrum (Fig. 8b) extends respectively to ν_D' = 282 and 289 cm^{-1} and consists of 43% of the oscillators. Below 300°K, the calculated c_v for microcline is compared in Fig. 6 with measured c_p for adularia. This comparison is probably justified because the structures and chemical compositions are very similar; for example, measurements on the isostructural pair adularia and ferriferous orthoclase (with slightly greater iron content than adularia) by Kelly et al. (1953) showed virtually no difference in specific heat behavior.

Jadeite, Diopside.— The two chain silicates, jadeite and diopside, have similar infrared spectra in the region 400 - 1100 cm^{-1}. The Debye temperature θ_D of jadeite is higher than for diopside. The Debye cutoff frequency ν_D' *according to the acoustic-optic model for jadeite is slightly* beyond the 383 cm^{-1} cutoff frequency for diopside (Fig. 8c). There is, however, only a small difference in the fraction of Debye oscillators, N'/N = 0.55 for jadeite, 0.58 for diopside. From the examples of albite and microcline, and jadeite and diopside, it may be seen that overall

similarities of spectral behavior, as indicated ν_M, and elastic behavior, as indicated by θ_D, lead to similarities in the heat capacities.

Forsterite.— The agreement between calculated and measured values of specific heat for forsterite is nearly as good as was obtained for quartz, as is best demonstrated by the $\theta_{cal}(T)$ curve in Fig. 7b. At 100°K, the deviation is only 6%. Debye oscillators comprise 55% of the spectrum, and lie below 368 cm^{-1} (Fig. 8c).

Spinel.— For spinel, in contrast to the minerals above, θ_{cal} (300°K) is very nearly equal to the elastic Debye temperature, θ_D = 874°K. Hence, although the highest observed frequency is 1080 cm^{-1}, only 7% of the oscillators in the acoustic-optic model are calculated to be in the continuum between 607 and 1080 cm^{-1}. The infrared spectrum in this region contains only one strong band, centered at 685 cm^{-1}, several weaker features at higher frequencies (765, 1080 cm^{-1}) and a moderately strong band at 1020 cm^{-1}. Although the absence of Raman data and the constraints of the selection rules make a definitive statement impossible, the lack of very many observable frequencies in this region is compatible with the calculated model. However, the calculated $\theta_{cal}(T)$ curve does not fit well the observed data (Fig. 7b).

Summary: Tailed Spectra.— If the behavior of the specific heat or $\theta_{cal}(T)$ below 100°K is ignored, the specific heats of the silicates are well described by "tailed" spectra of the type shown in Fig. 4a, in which the high frequency modes are added as a tail to the Debye part of the spectrum. Good agreement is obtained between $\theta_{cal}(\infty)$ as calculated from (20) and $\theta_{cal}(T)$ at high temperatures from specific heat measurements.

Although the tailed spectra appear to account correctly for the high frequency vibrations, they cannot account for the low temperature decrease $\theta_{cal}(T)$ below $\theta_{cal}(0)$. In the following section, the cause of this low-temperature decrease in $\theta_{cal}(T)$ is examined in terms of the specta computed for NaCl and MgO.

Minerals with compressed spectra.— The compressed spectra of Figs. 4b and 9 give $\theta_{cal}(T)$ curves that initially decrease with temperature and remain depressed below θ_D at higher temperatures. Compressed spectra are obtained whenever ν_M is less than ν_D, which is the case for the substances NaCl and MgO, whose structures have no features indicative of complex ions.

Halite.— Halite is a mineral of primary interest for this study because vibration spectra have been calculated from theory (Neuberger and Hatcher, 1961; Kellerman, 1940) and provide a basis of comparison with the spectrum calculated by the acoustic-optic model.

Some uncertainty exists in the choice of ν_M for NaCl. The maximum observed fundamental frequency ν_M (as interpreted by Raman, 1961) is at 190 cm^{-1}. In contrast, the computed spectrum of Neuberger and Hatcher has a lengthy tail, attributed to the longitudinal optic mode, extending to approximately 330 cm^{-1} (Fig. 9a). The oscillators in this tail may not contribute significantly to the infrared absorption. On the other hand, the fundamental absorption by these modes may be masked by overtones of the fundamental frequencies at 150, 157 and 170 cm^{-1}. Calculations by Raman (1961) do not predict any first order frequencies above 190 cm^{-1}. Raman's computed spectrum is shown in Fig. 9a as discrete frequencies; it is in essential agreement with the calculated spectrum of Neuberger and Hatcher in predicting a double maximum, but it does not have the

high-frequency tail. In order to be consistent with the way in which ν_M was chosen for all other minerals of this study, ν_M for NaCl was chosen to be the maximum fundamental absorption at 190 cm^{-1}, and the "tail" in Neuberger and Hatcher's spectrum has been ignored.

The computed acoustic-optic spectrum for NaCl (fitted to c_v at 50.7° K) has a Debye cutoff frequency at $\nu_D' = 111$ cm^{-1} and a compressed continuum ($g_o > a\nu_D'^2$), i.e., there are oscillators at frequencies less than ν_D in excess of the oscillators associated with the Debye part of the spectrum. The computed spectrum is shown in Fig. 9a, where it is compared to the spectral density function computed by Neuberger and Hatcher (1961) from lattice dynamics. The compressed spectrum obtained from the acoustic-optic model, contains most of the two maxima at 100 and 170 cm^{-1} in the high level part of the continuum. The computed acoustic-optic spectrum is at least in as good agreement with the Neuberger-Hatcher spectrum as a Debye spectrum based on θ_D (Fig. 9a). Clearly, any spectrum which is to predict accurately the low temperature specific heat must include excess oscillators near 100 cm^{-1}. Because the compressed spectrum does this, $\theta_{cal}(T)$ at low temperatures shows a decrease with increasing temperature. $\theta_{cal}(T)$ curves showing this behavior are Liebfried's (1955, p. 249) Type II, in which the initial decrease in $\theta_{cal}(T)$ is preserved at higher temperatures.

Periclase.— The specific heat of MgO and the acoustic-optic spectrum (Fig. 9b) of this solid are similar to NaCl. In the case of MgO, the high θ_D (Barron, et al., 1959) causes a low value of a; hence, although the Debye cutoff, ν_D', is much greater than for NaCl (343 cm^{-1} in MgO, 111 cm^{-1} in NaCl), a comparable number of oscillators, 14% are in the Debye spectrum.

86% are in the compressed part of the continuum which extends only from 343 to 490 cm^{-1}. The vibrational frequencies calculated by Raman (1961) (Fig. 9b, shown as discrete frequencies as in the case of NaCl) are clustered in the same way as upper frequencies of the compressed spectrum calculated from the acoustic-optic model. According to Raman, 75% of the principal modes are in the frequency interval 365 - 490 cm^{-1}. This is roughly in agreement with the 86% obtained by the acoustic-optic model. The acoustic-optic spectrum for MgO predicts a decrease of $\theta_{cal}(T)$ with increasing temperature, but is not in exact agreement with $\theta_{cal}(T)$ from measured c_v values.

Cause of the low-temperature thermal behavior.— The "squashing" of high frequencies to low frequencies below the elastic Debye cutoff frequency (i.e., $\nu_M < \nu_D$) is a consequence of the relation between frequency ν and the wave vector $\vec{K}$ for simple lattices. In the Debye model, it is assumed that the solid is a continuum and that the frequency is a linear function of the wave vector amplitude $|\vec{K}|$. To understand the effect of a lattice of mass points on the dispersion relation (ν vs $\vec{K}$), consider the vibrations of a monatomic lattice (Kittel, 1968, p. 142). If only elastic waves which propagate in directions such that the wave polarizations are purely transverse or purely longitudinal are considered, the wave vector $\vec{K}$ for these special modes of propagation may be written as the scalar K. Solving the equation of motion for $\overset{(harmonic)}{\Lambda}$ interactions only among nearest neighbor planes gives the dispersion relation

$$\nu = \text{constant} \cdot \sin \tfrac{1}{2} Kb \qquad (22)$$

where b is the interplanar spacing,

Thus, in a monatomic, linear lattice, ν is a $\overset{\text{sinusoidal}}{\wedge}$ function of K with period $2\pi/\underline{b}$, where $\underline{b}$ is the interplanar spacing. In contrast to the Debye model of a continuum which assumes ν to be a linear function of K, a lattice of discrete mass points gives this $\overset{\text{sinusoidal}}{\wedge}$ dependence of ν on K (Fig. 10). Relative to a continuum, ν is lowered at the boundaries of the Brillouin zone, $K = \pm \pi/b$. The shape of the dispersion relation affects the spectral function $\underline{g}(\nu)$ given by the simple Debye theory by introducing positive terms of higher order than ν^2; this is necessarily accompanied by a lowering of the cutoff frequency from ν_D to a lower value.

It is known that in the very low frequency limit ($\nu \to 0$) the density of vibrational states approaches zero. In general, the density function $\underline{g}(\nu)$ is of the form (Barron and Morrison, 1957)

$$\underline{g}(\nu) = \underline{a}_2\nu^2 + \underline{a}_4\nu^4 + \underline{a}_6\nu^6 + \ldots\ldots \qquad (23)$$

The first term of this expansion is the term which gives the low temperature Debye behavior and is equivalent to the assumption that ν is a linear function of K. The higher order term in ν^4 causes a variation in the calorimetric Debye temperature with increasing temperature (Bhatia and Horton, 1955) because oscillators in excess of the Debye spectrum exist at low frequencies if $\underline{a}_4 > 0$. Force models, taking into account as many as sixth-neighbor interactions, have been successful in predicting the dispersion laws and thus the low temperature behavior of $\theta_{cal}(T)$ for some substances. For face-centered cubic metals, the typical behavior is a 10% decrease from $\theta_{cal}(0)$ to $\theta_{cal}(T)$ at $T \sim \theta_{cal}(0)/12$

(Horton and Schiff, 1956). This behavior is even more pronounced in substances of lower symmetry. Raubenheimer and Gilat (1967) show that the observed 40% decrease in $\theta_{cal}(T)$ of zinc (hcp) between 0 and 15°K is predictable from a force-constant model. An effect of similar magnitude was calculated for white tin (tetragonal) by Kam and Gilat (1968) from a Born-von Karman force model.

It is evident that quartz and the silicates, showing similar behavior of $\theta_{cal}(T)$ at low temperatures, must have similar low-frequency complexities in $g(\nu)$, and that the simple Debye spectrum assumed at low frequencies in the acoustic-optic model is an oversimplification. The use of the Debye approximation to $g(\nu)$ at low frequencies is adequate for prediction of specific heats when the low temperature behavior can be ignored, as is possible for all of the silicates studied at temperatures above 100 to 200°K. For NaCl and MgO, the appearance of a "compressed" type of acoustic-optic spectrum, which is due to the fact that $\nu_M < \nu_D$ for these substances, makes it possible for the acoustic-optic model to account moderately well for the low-temperature thermal behavior, but this is in some sense an accident, not contemplated in the formulation of the acoustic-optic model in §2.

Minerals with hybrid spectra.— Low temperature heat capacity measurements on stishovite and rutile reveal an unusually large initial decrease in $\theta_{cal}(T)$, with subsequent recovery to values which exceed the θ_D value. To account for the initial decrease in $\theta_{cal}(T)$, excess oscillators (in addition to those given by a Debye spectrum) must be present at low frequencies. The presence of these oscillators will be reflected in a ν^4 term in the Taylor expansion of $g(\nu)$, even though the

actual distribution of the additional oscillators at low frequencies does not necessarily closely resemble a ν^4 distribution. The fact that $\nu_M > \nu_D$ accounts for the rise of $\theta_{cal}(T)$ at high temperatures because oscillators are present at frequencies greater than ν_D. In an attempt to fit the acoustic-optic model to rutile or stishovite, therefore, the model is required both to place oscillators in excess of the Debye oscillators at low frequencies, to account for the drop in $\theta_{cal}(T)$ at low T, and also to place some oscillators between ν_D and ν_M. This results in a hybrid spectrum (Fig. 11). If the parameters of the model are chosen so as to fit c_v at a temperature at which $\theta_{cal}(T)$ exceeds θ_D, thus ignoring the low-T behavior, then a more or less normal "tailed" spectrum is obtained.

Hybrid spectra, although they are capable of qualitatively predicting both the low temperature decrease in $\theta_{cal}(T)$ and the subsequent rise at high temperatures, are not physically reasonable because of the use of the single parameter g_o to relate these two very different effects, when there is no physical reason to believe that the two effects should be related in such a simple way.

The appearance of hybrid spectra for rutile and stishovite is discussed below, to demonstrate the inadequacy of the acoustic-optic model for explaining the combined effects of the dispersion relation and the high frequency vibrations.

Rutile.— Accurate heat capacity measurements have been made on rutile at temperatures of 10°K to 300°K (Keesom and Pearlman, 1958; Dugdale, et al., 1954; Shomate, 1947). The measured values of heat capacity, when reduced to a $\theta_{cal}(T)$ curve, reveal a decrease in $\theta_{cal}(T)$

to 43% of its initial value between 10°K and 25°K, with a subsequent recovery to the $\theta_{cal}(0)$ - value (758°K) by 300°K (Fig. 6b).

When the acoustic-optic model is applied to rutile with a fit to c_v at temperatures at which $\theta_{cal}(T) < \theta_D$, the hybrid spectrum which results has ν_D' at 64 cm^{-1}, with a large high-level continuum portion containing over 99% of the oscillators (Fig. 11b, in which the hybrid spectrum was obtained by fitting at 30°K). This hybrid spectrum gives a low temperature decrease in $\theta_{cal}(T)$ with a subsequent recovery at higher temperatures (dash-dot line in Fig. 6), but is seen to be a very poor fit to the observed values of $\overset{\wedge}{\theta}_{cal}(T)$. When the model is applied to rutile with a fit to the specific heat at 300°K, at which $\theta_{cal}(T) > \theta_D$, the calculated tailed spectrum is nearly that of a Debye solid ($\nu_D' = 517$ cm^{-1} as compared to $\nu_D = 525$ cm^{-1}). Only 6% of the oscillators are in the (short) tail from 517 to 825 cm^{-1}. The tailed spectrum gives a very poor fit to the measured specific heat data at temperatures higher or lower than the temperature at which it was fitted.

Stishovite.— The data of Holm, et al. (1967) imply that with decreasing temperature, $\theta_{cal}(T)$ of stishovite decreases from over 1000°K to 488°K at 5°K. In view of the extremely high bulk modulus of stishovite†, it seems likely that a low temperature T^3-region may be

† Measured values of bulk modulus for stishovite range from 3.0 ± 0.3 Mb (Bassett and Barnett, 1970) to 4.3 Mb (McQueen, Fritz and Marsh, 1963). Recent shock wave data reductions, under the assumption that stishovite is formed give values of 3.6 - 3.7 Mb (Ahrens, Anderson and Ringwood, 1969; Ahrens, Davies and Anderson, 1969). A value of 3.44 ± 0.20 Mb was measured by X-ray methods (Liu, Takahashi and Bassett, 1969).

expected to be evident by 5°K. On the basis of the high bulk modulus, $\theta_{cal}(T)$ would be expected to approach $\theta_D \approx 800 - 1100$°K. The calorimetric data points below 50°K seem incompatible with the high bulk modulus and are shown in Fig. 6 as open circles because of this inconsistency.

If the acoustic-optic model is fit to the stishovite specific heat data at temperatures at which $\theta_{cal}(T) < \theta_D$, a hybrid spectrum is obtained. The hybrid spectrum is also obtained as one of two possible solutions to (14) when the model is fit to c_p at 300 or 350°K, because at those temperatures, the calorimetric and elastic Debye temperatures are approximately equal. When this condition holds, two solutions for the Debye cutoff frequency ν_D' result from (14). The second solution is a nearly Debye-like tailed spectrum in which $\nu_D' = 711\ cm^{-1}$, very close to the elastic Debye cutoff $\nu_D = 729\ cm^{-1}$. Neither of these solutions predicts well the measured specific heat of stishovite.

The existence of two solutions to (14) when the acoustic-optic model is fit to c_v at temperatures at which $\theta_{cal}(T)$ approximately equals θ_D was found for quartz, stishovite, jadeite, diopside and forsterite. For coesite, spinel, and rutile two solutions were not found when the model was fitted at the temperature at which $\theta_{cal}(T) = \theta_D$. For albite and microcline, there is no solution to (14) when $\theta_{cal}(T) < \theta_D$, i.e., when the model is fit at temperatures below 80°K. This implies that there are more oscillators at low frequencies than can be placed there by extending the tail of the spectrum down to low frequencies, i.e., it is not possible to account for the low temperature behavior of albite and microcline with a hybrid spectrum.

5. Summary

The calorimetric Debye temperature $\theta_{cal}(T)$ is the value of Debye temperature that will reproduce the observed $c_v(T)$, the specific heat at constant volume. Although $\theta_{cal}(T)$ has been studied extensively for simple substances, the $\theta_{cal}(T)$ behavior of silicates and oxides of geophysical interest has never been examined. The deviations of $\theta_{cal}(T)$ of silicates are larger than any observed in the simpler substances. These deviations reveal a systematic behavior of the lattice vibrational spectra with the extent of complex-ion development and polymerization of the structures. $\theta_{cal}(T)$ for silicates decreases initially with increasing temperature and then rises to values of $\theta_{cal}(T)$ which greatly exceed the elastic Debye temperature θ_D. The rise in $\theta_{cal}(T)$ is due to the presence of oscillators between ν_D (the elastic Debye frequency) and ν_M (the maximum vibrational frequency). $\theta_{cal}(T)$ of NaCl and MgO decreases initially with temperature and remains lower than θ_D. This decrease in $\theta_{cal}(T)$ is due to the presence of oscillators below ν_D in excess of the Debye oscillators, and spectra in which the maximum frequency ν_M is depressed below ν_D. Rutile and stishovite are substances in which both low and high frequency deviations from the Debye model are important.

The acoustic-optic vibrational model is designed to account in a simple way for the presence of oscillators at frequencies $\nu > \nu_D$. A simple Debye part of the spectrum is assumed at low frequencies; a simple constant-valued continuum is assumed to represent the oscillators present at high frequencies. The acoustic-optic spectra for silicates and spinel are tailed spectra, that is, the spectra rise to peaks associated with the Debye oscillators and then drop off to continuum levels associated

with the high frequency optic modes. The fraction of oscillators in the tail varies from 0.72 (quartz) to 0.07 (spinel). It is suggested that this may be roughly the fraction of oscillators associated with the more tightly bound units of the structures.

The acoustic-optic model is also capable of predicting the specific heat of MgO and NaCl. The capability of the model for predicting these specific heats must be considered somewhat fortuitous since the model was not originally designed to deal with solids for which $\nu_M < \nu_D$. However, the requirement that $\nu_M < \nu_D$ forces a compressed spectrum which qualitatively describes the spectrum that results from the dispersion relation for simple lattices.

The nonlinearity of the dispersion relation, which dominates the specific heat behavior of NaCl and MgO, also influences the low temperature behavior of all silicates with varying degrees of severity. The effect of the dispersion relation can be ignored for some silicates if specific heats only at high temperatures ($T > 100^{\circ}K$) are considered. The effect of excess oscillators at low frequencies cannot be ignored in the case of rutile or stishovite and the hybrid spectra that result for t[illegible] minerals when the acoustic-optic model is applied must be cons[illegible] physically dubious.

Table 1.

List of minerals considered and sources of data. Also given is $(c_p - c_v)$ at 300°K from eqn. 21 , data for which are from Birch (1966) and Skinner (1966).

Mineral	Sources of specific heat data	$c_p - c_v$ (cal/mole-°K)	$(c_p - c_v)/c_p$
Quartz	Lord and Morrow, 1957 (quoting unpublished data of E.F. Westrum)	0.08	0.008
Coesite	Holm, Kleppa and Westrum, 1967 (to 350°K)	- -	- -
Stishovite	Holm, Kleppa and Westrum, 1967 (to 350°K)	0.08	0.008
Rutile	Keesom and Pearlman, 1958 (10-20°K); Dugdale, Morrison and Patterson, 1954 (20-50°K); Shomate, 1947 (50 - 298°K)	0.15	0.011
Albite	Kelley, Todd, Orr, King and Bonnickson, 1953 (to 297°K)	0.11	0.002
Microcline	Kelley, 1960 (above 300°). Data below 300° is for adularia; Kelley, Todd, Orr, King and Bonnickson, 1953	0.10	0.002
Jadeite	Kelley, Todd, Orr, King and Bonnickson, 1953 (to 297°K)	0.17	0.004
Diopside	King, 1957 (to 298.15°K)	0.16	0.004
Forsterite	Kelley, 1943 (53-295°K) Orr, R.L., 1953 (300-700°K)	0.24	0.009
Spinel	King, 1955 (to 298.16°K) Bonnickson, 1955 (to 1805°K)	0.34	0.012
Periclase	Barron, Berg and Morrison, 1959 (to 270°K) Janaff Thermochemical Tables, First Addendum (above 300°K)	0.10	0.012
Halite	Raman, 1961	~ 0.8	0.07

Table 2

Model parameters for minerals of geophysical interest.

Mineral	(1) $c_p(T)$ cal/mole-°K)	(1) (T) (°K)	(2) θ_D (°K)	(3) ν_D (cm^{-1})	(4) ν_M (cm^{-1})	(5) ν_D' (cm^{-1})	(6) a/N_T $\times 10^8$ ($1/cm^{-3}$)	(7) $a\nu_D'^2/N$ $\times 10^4$ ($1/cm^{-1}$)	(8) g_0/N $\times 10^4$ ($1/cm^{-1}$)	(9) N'/N
uartz SiO_2	10.63	300°	528	365	1172	239	6.08	34.8	7.74	0.28
oesite SiO_2	10.90	300°	(645)†	449	1218	350	3.34	40.9	6.02	0.48
tishovite SiO_2	10.33	300°	1050*	728	949	186 711	0.77 0.77	2.68 39.11	12.88 3.06	0.02 0.93
utile TiO_2	13.16	298.16°	758	525	825	517	2.06	54.97	1.71	0.94
	0.43	30°	758	525	825	64	2.06	0.84	13.12	0.002
lbite $NaAlSi_3O_8$	48.78	296.42	521	360	1165	282	5.69	45.2	6.50	0.43
icrocline $KAlSi_3O_8$	58.33	400°	551	382	1140	289	5.35	44.7	6.69	0.43

Table 2 (continued)

Mineral	(1) $c_p(T)$ (Cal/mole-^oK)	(1) T (^oK)	(2) θ_D (^oK)	(3) ν_D (cm^{-1})	(4) ν_M (cm^{-1})	(5) ν_D' (cm^{-1})	(6) a/N_T $\times 10^8$ ($1/cm^{-3}$)	(7) $a\nu_D'^3/N$ $\times 10^4$ ($1/cm^{-1}$)	(8) g_0/N_T $\times 10^4$ ($1/cm^{-1}$)	(9) N'/N
Jadeite $NaAl(Si_2O_6)$	38.13	296.42	719	500	1065	410	2.40	40.3	6.84	0.55
Diopside $CaMg(SiO_3)_2$	39.80	298.15	662	460	1080	383	3.08	45.3	6.05	0.58
Forsterite Mg_2SiO_4	28.46	300°	647	449	995	368	3.31	44.8	7.19	0.55
Spinel $MgAl_2O_4$	27.85	300°	887	616	1080	593	1.34	47.0	1.39	0.93
MgO	8.94	300°	949	659	490	343	1.05	12.33	58.00	0.14
NaCl	3.82	50.70	332	223	190	111	27.05	33.33	111.00	0.12

(†) Estimated by O. L. Anderson from density relation. * Calculated using bulk modulus = 3.4 Mbar, Poisson's ratio assumed equal to rutile, 0.28. The remaining θ_{el} values are from the following references: spinel, forsterite: Anderson, et al., 1968; rutile: Keesom and Pearlman, 1958; jadeite, diopside, microcline, albite: Horai and Simmons, 1970; quartz (calorimetric value): Lord and Morrow, 1957; NaCl: Leibfried, 1955.

Table 3

Comparison of measured and calculated specific heats for quartz.

T	c_p*(Exp)	c_p*(calc)	Δ c*(Exp - calc)	% difference
(°K)	(cal/mole-°K)	(cal/mole-°K)	(cal/mole-°K)	
10	.0033	.003	.0003	3
20	.054	.0254	.0286	53
30	.169	.0849	.0841	50
40	.313	.190	.123	39
50	.463	.3294	.1336	29
60	.62	.510	.11	18
70	.769	.689	.08	10
80	.934	.866	.068	7
100	1.246	1.200	.046	4
120	1.551	1.504	.047	3
140	1.841	1.784	.057	3
180	2.34	2.290	.05	2
200	2.58	2.524	.06	2
240	3.01	2.955	.05	2
280	3.376	3.340	.036	1
300	3.544	3.514	.03	.8
400	4.197	4.219	-.02	-.5
500	4.666	4.695	-.03	-.6
600	5.001	5.017	-.006	-.1
700	5.223	5.239	-.006	-.1

Figure Captions

Fig. 1. Debye temperature ($\theta_{cal}(T)$) as a function of temperature (T) for substances commonly assumed to be nearly Debye-like in behavior. Elastic Debye temperatures θ_D at 0^oK are shown by circles. The values of $\theta_{cal}(T)$ were obtained from the following references: Hill and Parkinson, 1952 (Ge, Sn); Blackman, 1955 (NaCl, Pb, KCl); Cetas, et al., 1968 (GaSB).

Fig. 2. Debye temperature ($\theta_{cal}(T)$) as a function of temperature (T) for typical substances of geophysical interest. Additional data are shown in Figs. 6b and 7b. Room temperature elastic values of θ_D are shown by circles; they are assumed to apply at low temperatures as well.

Fig. 3. Infrared spectra for quartz, stishovite, jadeite, albite, showing the presence of lattice vibrations at frequencies exceeding ν_D. Data for quartz, jadeite, albite after H. Moenke (1962); stishovite after Lyon (1962).

Fig. 4. Three possible forms for the density distribution of vibrational states $g(\nu)$ according to the acoustic-optic model: (a) a tailed spectrum, (b) a compressed spectrum, and (c) a hybrid spectrum.

Fig. 5. Molar specific heat (c) as a function of temperature (T) for minerals of geophysical interest. c_p is given for all minerals except

quartz and NaCl, for which c_v is shown. Data compiled from references in Table 1.

Fig. 6. (a) Normalized specific heat (c*) as a function of temperature (T); c_p is plotted for all minerals except quartz and halite, for which c_v is plotted. The long-dashed line is the Debye function, $D(\theta_{el}/T)\theta_{el}$. The short-dashed line is the Debye function, $D(\theta_{cal}(300^o)K)$. The heavy solid line is the specific heat predicted by the acoustic-optic model. Data points are shown as circles. Open circles are shown for stishovite below 50°K because of the incompatibility of the low temperature specific heat data with the high bulk modulus (see text). Open circles are shown for microcline below 300°K because specific heat data for adularia was used. For stishovite, both Debye curves coincide with the dotted line. Two solutions are obtained when $c_p(300^oK)$ is used to determine ν_D'. One solution coincides with the dotted line; the other solution, the hybrid solution, is shown as the solid line. For rutile, both Debye curves coincide with the solid line, which is also the solution to the acoustic-optic model, when $c_p(298.16^o)$ is used to determine ν_D'. A hybrid solution is obtained from the model if $c_p(30^oK)$ is used to determine ν_D'; this solution is shown by the dash-dot line. (b) Calorimetric Debye temperature ($\theta_{cal}(T)$) as a function of temperature (T). Solid, dash-dot and dotted curves correspond to the notation in (a). Arrows pointing to the left show the room temperature elastic value of θ_D, assumed to be applicable to the low temperature behavior (see text). Arrows pointing to the right are the computed high-temperature asymptotic values of $\theta_{cal}(\infty)$.

Fig. 7. (a) Normalized specific heat (c*) as a function of temperature (T). Notation is same as Fig. 6. Open circles at high temperatures indicate values of c* which are uncertain because no reduction has been made from c_p to c_v. The solution for NaCl is for $\nu_M = 190$ cm^{-1}; the data points for NaCl are c_v from Clusius, Goldmann and Perlick (1949). (b) Debye temperature ($\theta_{cal}(T)$) as a function of temperature (T). Notation is same as Fig. 6.

Fig. 8. Calculated vibrational spectra of minerals which are best characterized by a tailed spectrum which represents the existence of high-frequency (optic) modes. The discrete frequencies and degeneracies assumed by Lord and Morrow (1957) for quartz are shown as a histogram on the absciasa. In this representation, the shortest symbols (↑) represent 1/27 of the total degrees of freedom available to the crystal; other symbols are scaled proportionally. The left facing arrow indicates that 1/9 of the total degrees of freedom are assumed to be in a continuous Debye spectrum below 176 cm^{-1}.

Fig. 9. Acoustic-optic compressed spectra for NaCl and MgO. (a) NaCl spectrum. The lighter line is the spectrum of Neuberger and Hatcher (1961), obtained from theoretical calculations. The heavy solid line for NaCl is the acoustic-optic spectrum obtained for $\nu_M = 190$ cm^{-1} when the model is fit to c_v at 50.7°K. (b) MgO spectrum. For both NaCl

and MgO, the discrete frequency spectrum computed by Raman (1961) is shown.

In this representation the degeneracies of these modes are indicated by the length of the symbol (🡐). The shortest symbol represents a threefold degeneracy; the others are proportionally longer. The left facing arrow at 277 cm^{-1} for MgO and at 92 cm^{-1} for NaCl indicate that 3 of the 48 possible degrees of freedom are assumed to be in a continuous spectrum below this frequency.

Fig. 10. Phonon dispersion relation for a monatomic linear lattice and for a Debye solid.

Fig. 11. Calculated vibrational spectra of (a) stishovite, with the two solutions obtained when the model is fit at 300°K, (b) rutile. The solid line represents the solution for rutile obtained by fitting the model at room temperature. The dotted line represents the solution for rutile obtained by fitting the model at 30°K and is typical of solutions obtained by fitting at temperatures at which $\theta_{cal}(T) < \theta_D$.

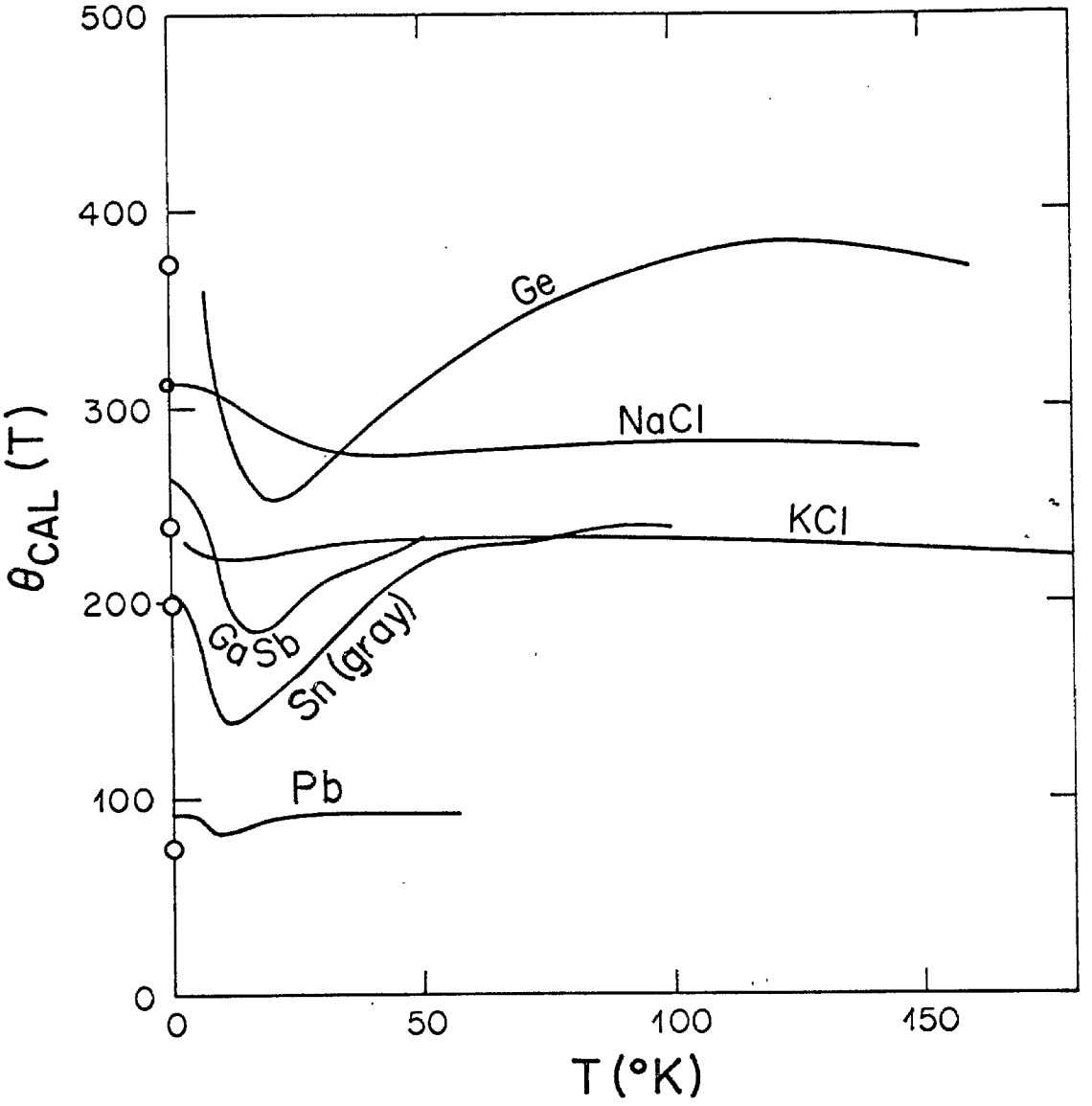
500
400
300
200
100
0
0
50
100
150
θ_{CAL} (T)
T (°K)
Ge
NaCl
KCl
GaSb
Sn (gray)
Pb

Figure 1.

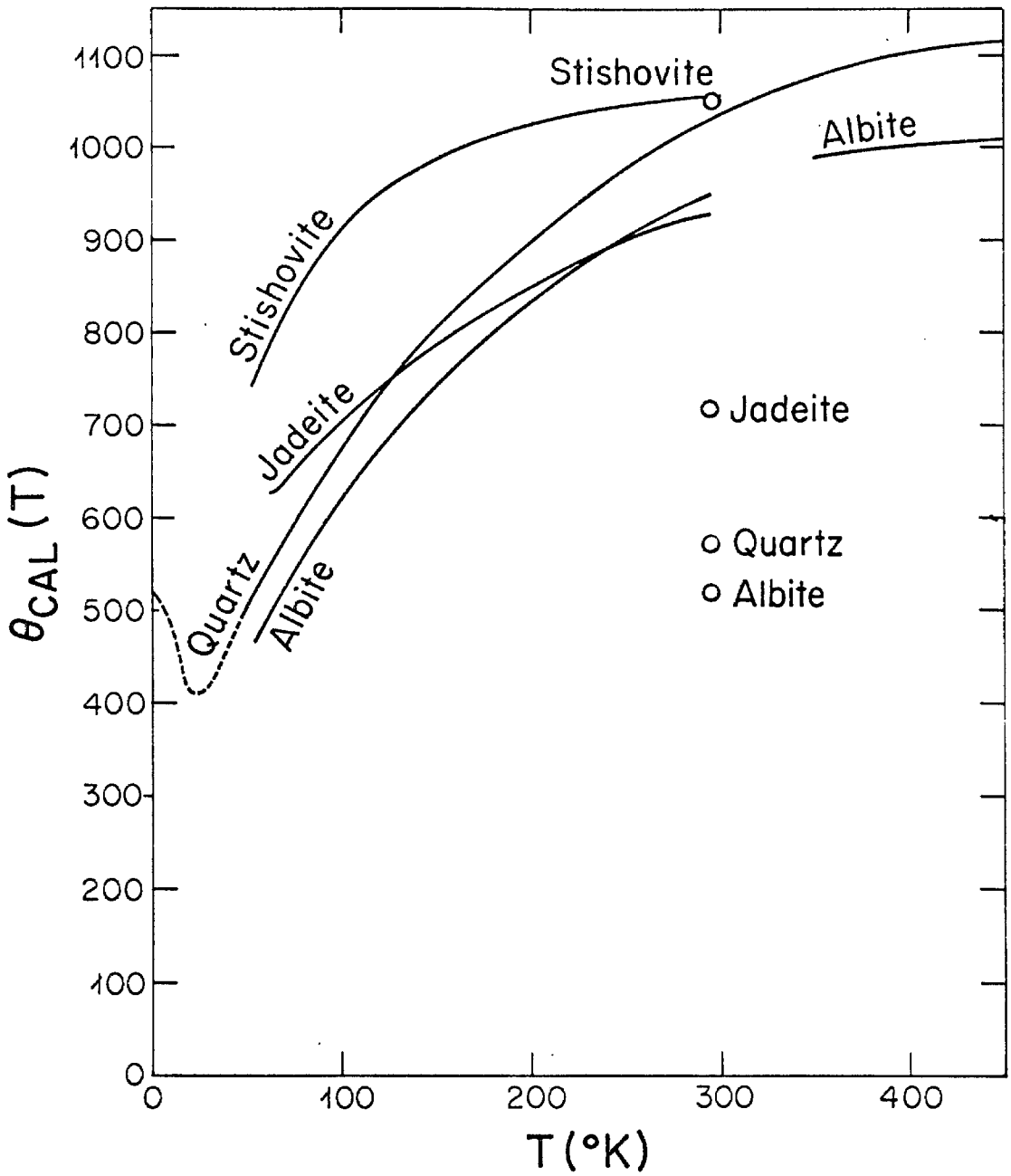
1100
1000
900
800
700
600
500
400
300
200
100
0
0
100
200
300
400
θCAL (T)
T (°K)
Stishovite
Albite
Stishovite
Jadeite
Quartz
Albite
o Jadeite
o Quartz
o Albite

Figure 2.

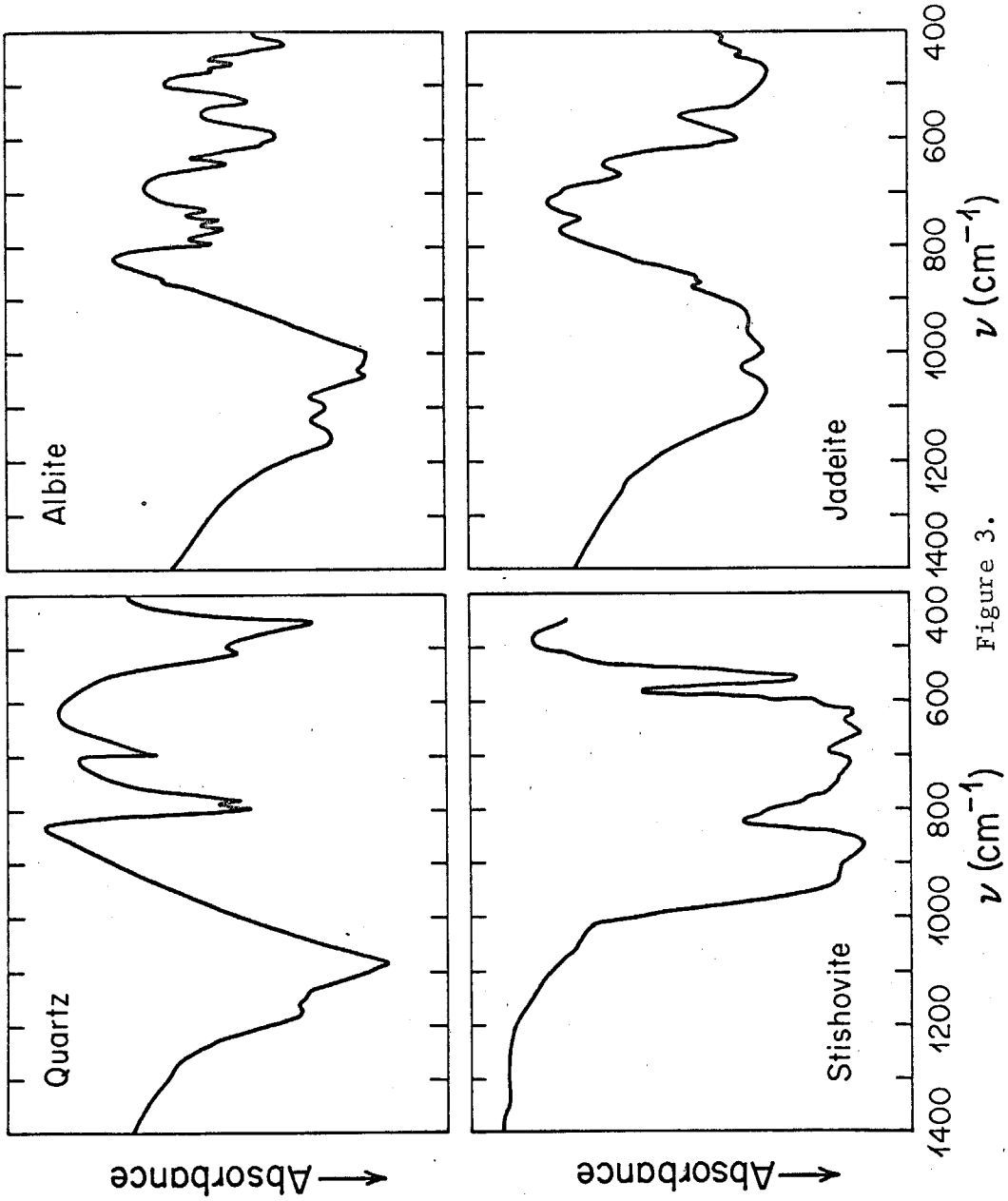
Albite
Quartz
Jadeite
Stishovite
Absorbance
Absorbance
1400 1200 1000 800 600 400
1400 1200 1000 800 600 400
ν (cm⁻¹)
ν (cm⁻¹)

Figure 3.

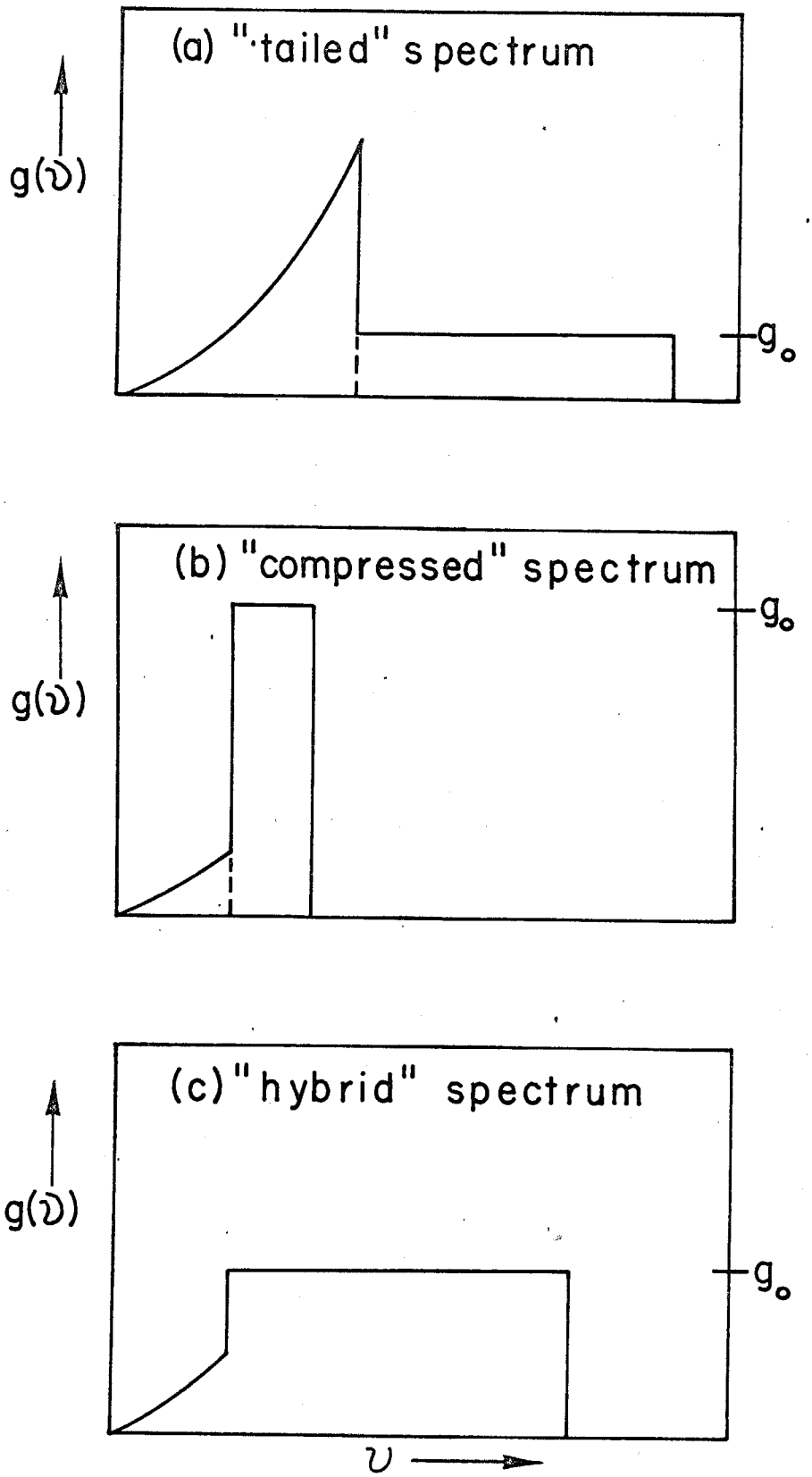
(a) "tailed" spectrum
g(ν)
g_o
(b) "compressed" spectrum
g(ν)
g_o
(c) "hybrid" spectrum
g(ν)
g_o
υ

Figure 4

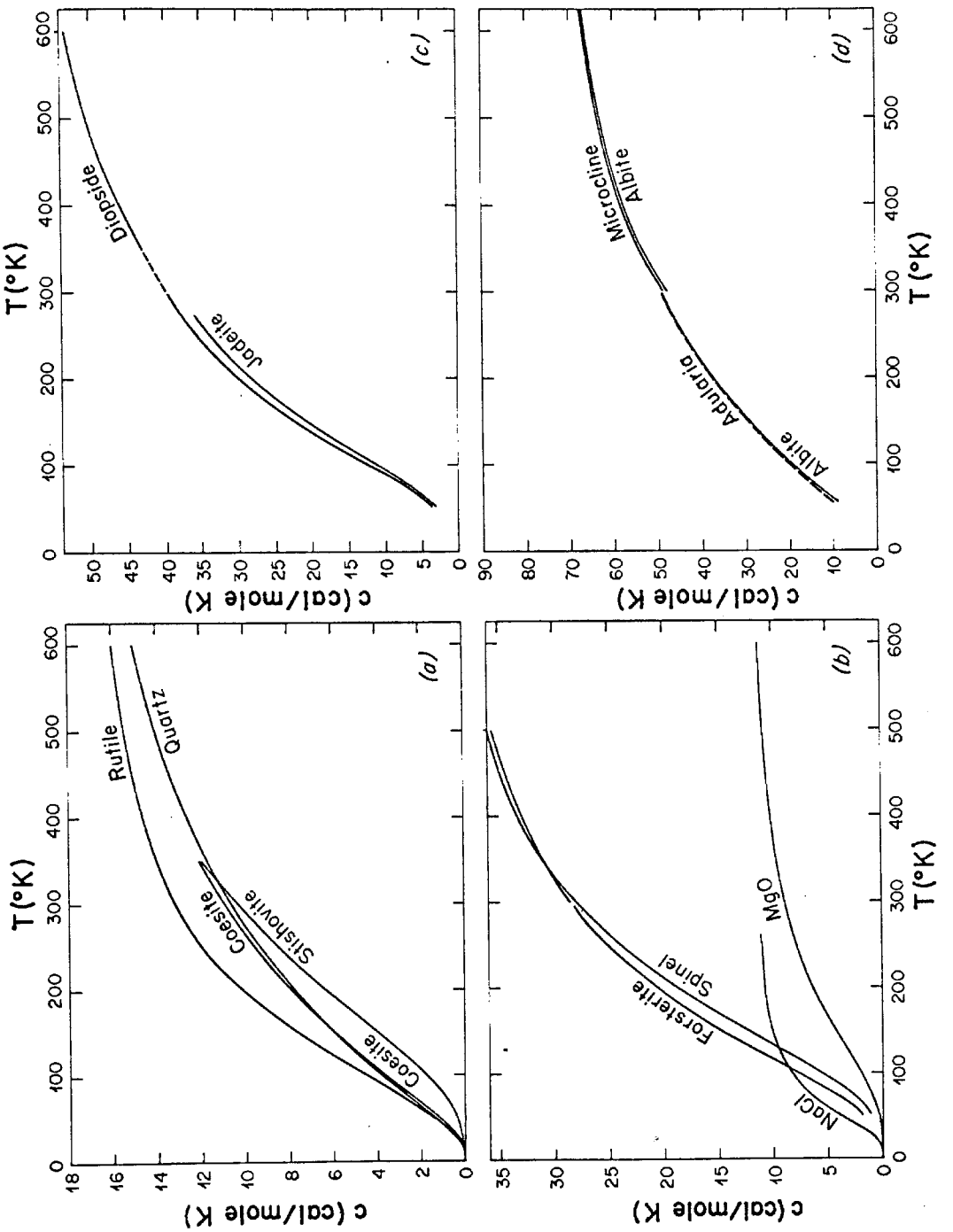
(a)
Rutile
Quartz
Coesite
Stishovite
Coesite
(b)
Forsterite
Spinel
MgO
NaCl
(c)
Diopside
Jadeite
(d)
Microcline
Albite
Albite
Adularia
T(°K)
c (cal/mole K)

Figure 5

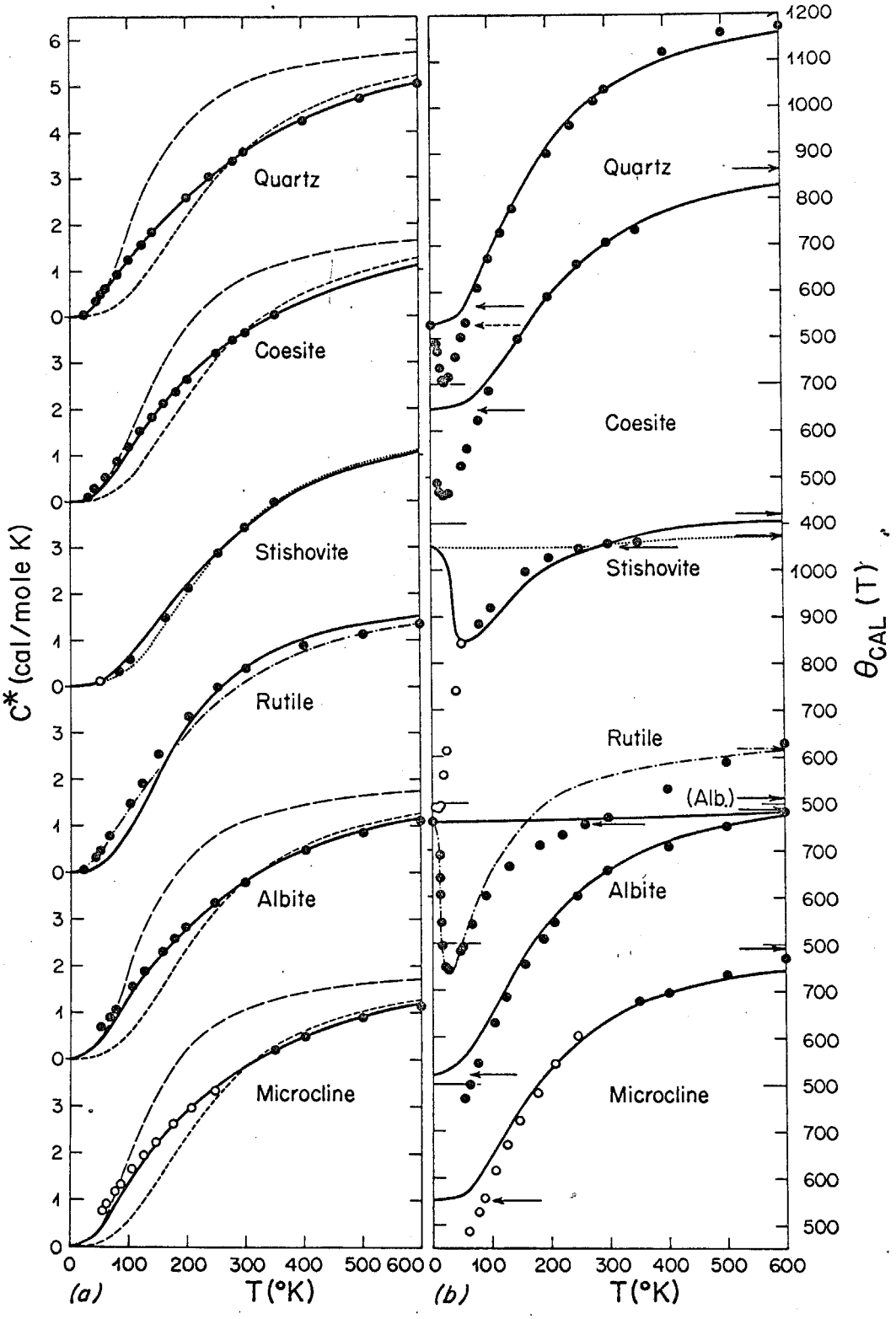
C* (cal/mole K)
Quartz
Coesite
Stishovite
Rutile
Albite
Microcline
(a)
T(°K)
(b)
T(°K)
θCAL (T)
(Alb.)

Figure 6.

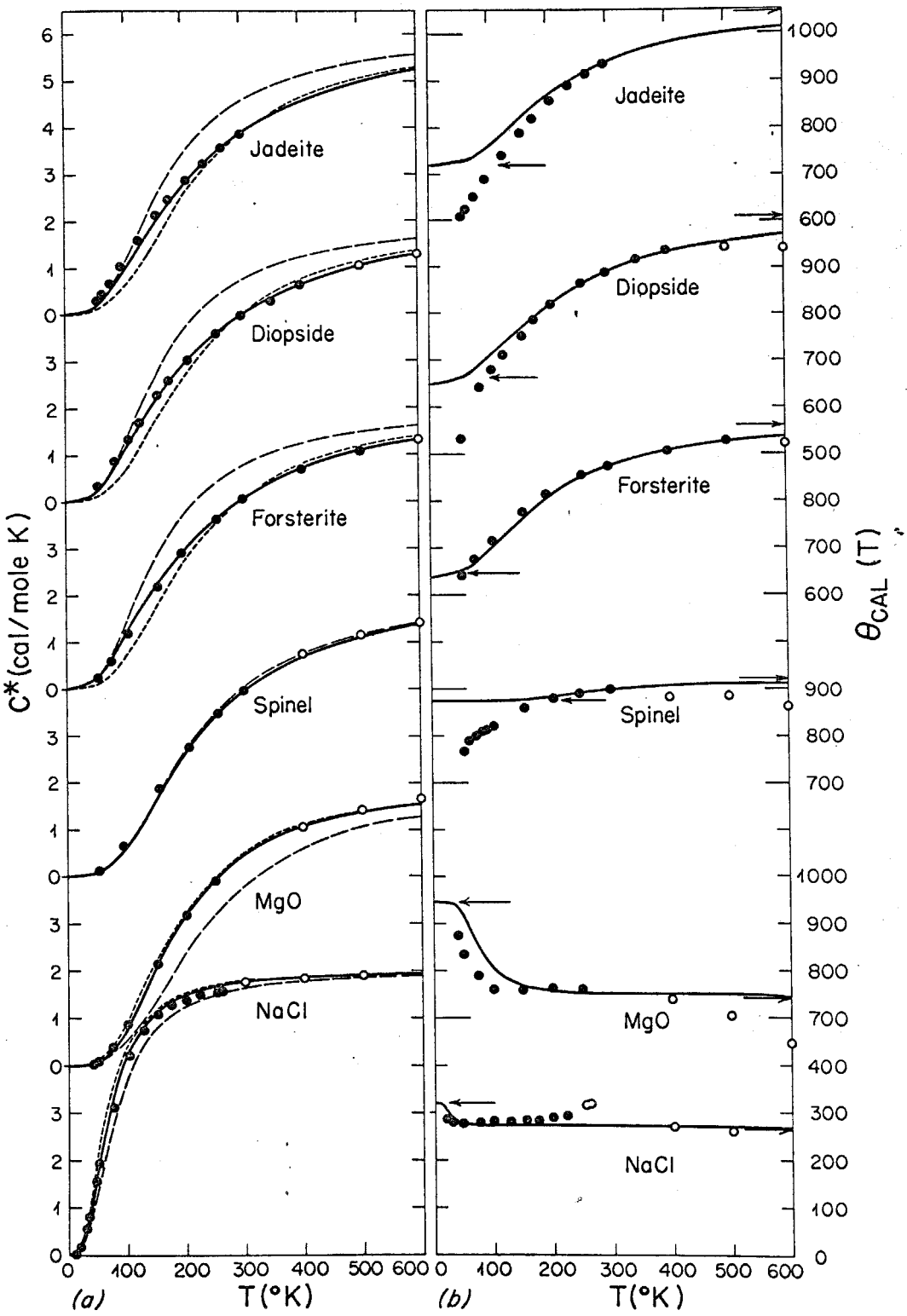
C*(cal/mole K)
Jadeite
Diopside
Forsterite
Spinel
MgO
NaCl
(a)
T(°K)
(b)
T(°K)
θCAL (T)

Figure 7.

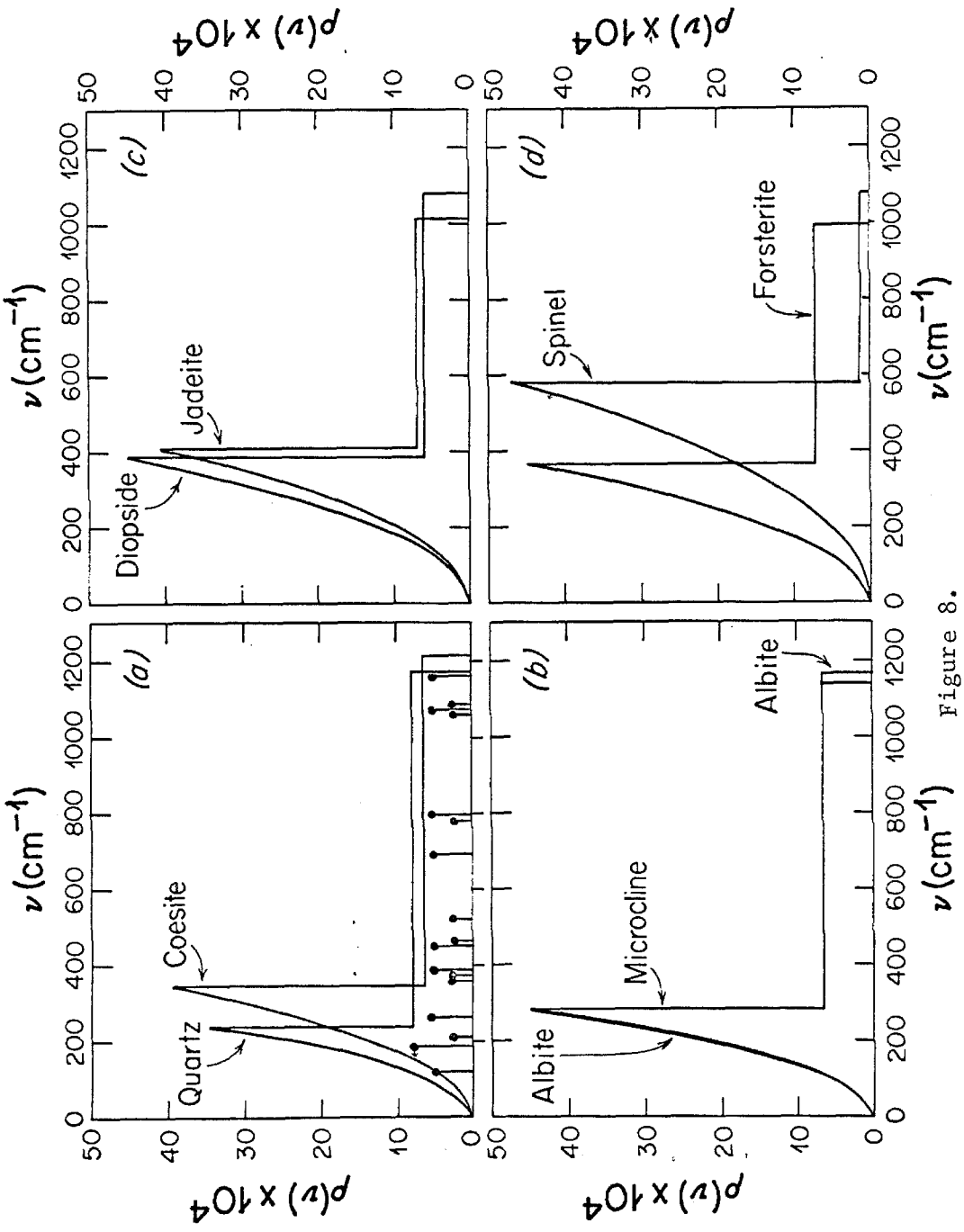
(a)
Quartz
Coesite
(b)
Albite
Microcline
Albite
(c)
Diopside
Jadeite
(d)
Spinel
Forsterite
ν (cm⁻¹)
ρ(ν) x 10⁴
0
200
400
600
800
1000
1200
10
20
30
40
50

Figure 8.

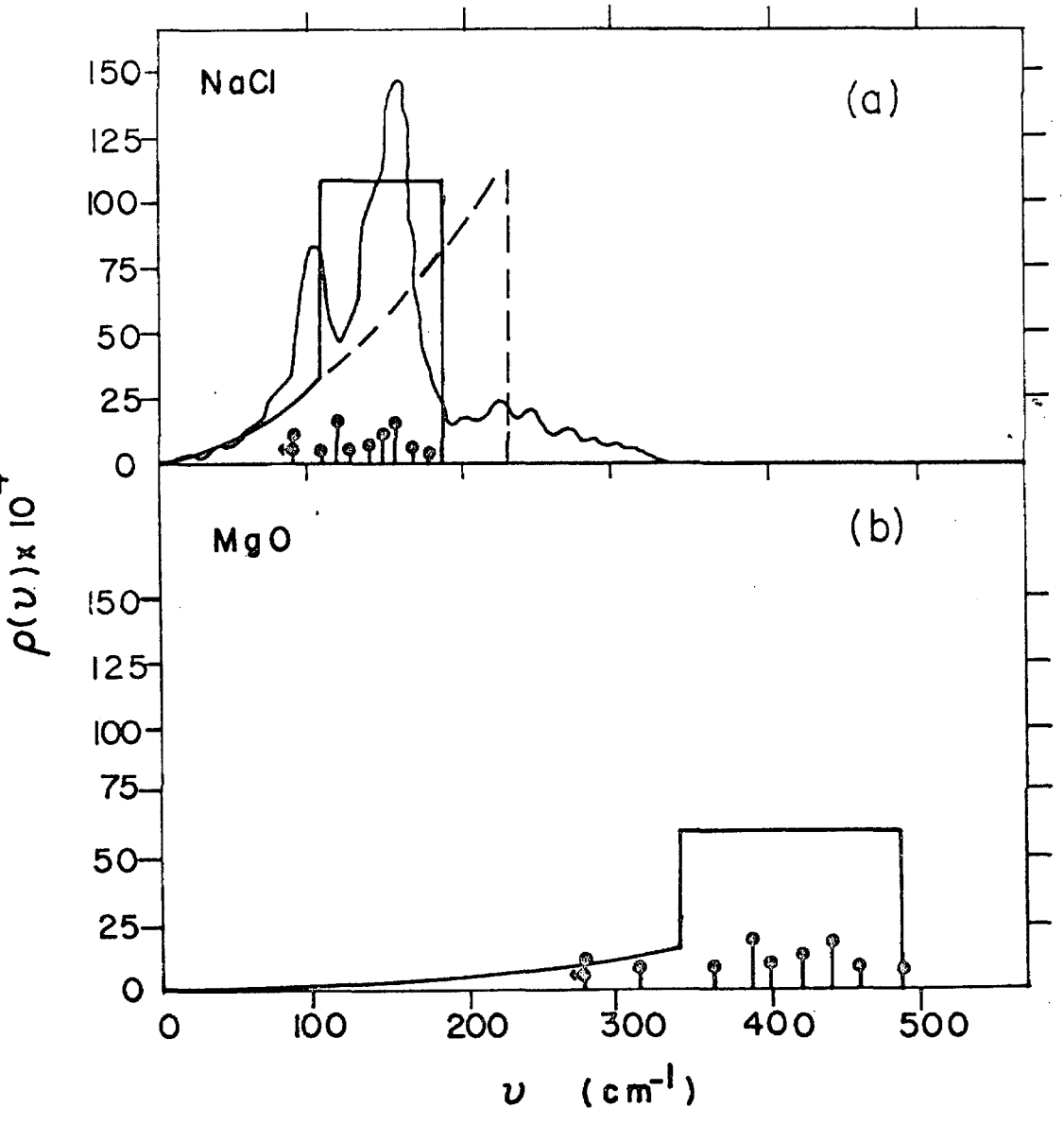
NaCl
(a)
MgO
(b)
150
125
100
75
50
25
0
0
100
200
300
400
500
ρ(υ) x 10^4
υ (cm^-1)

Figure 9

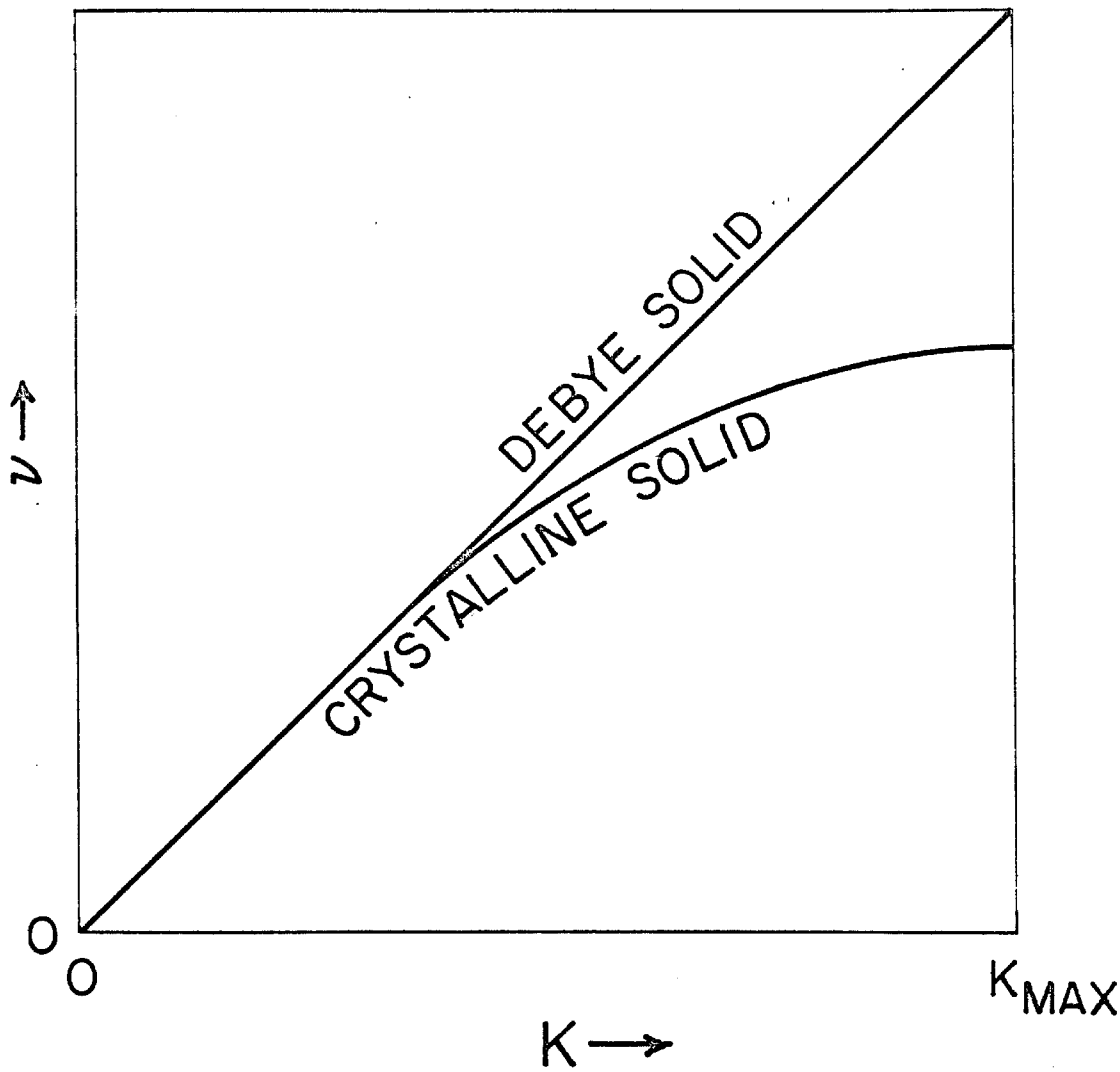

Figure 10

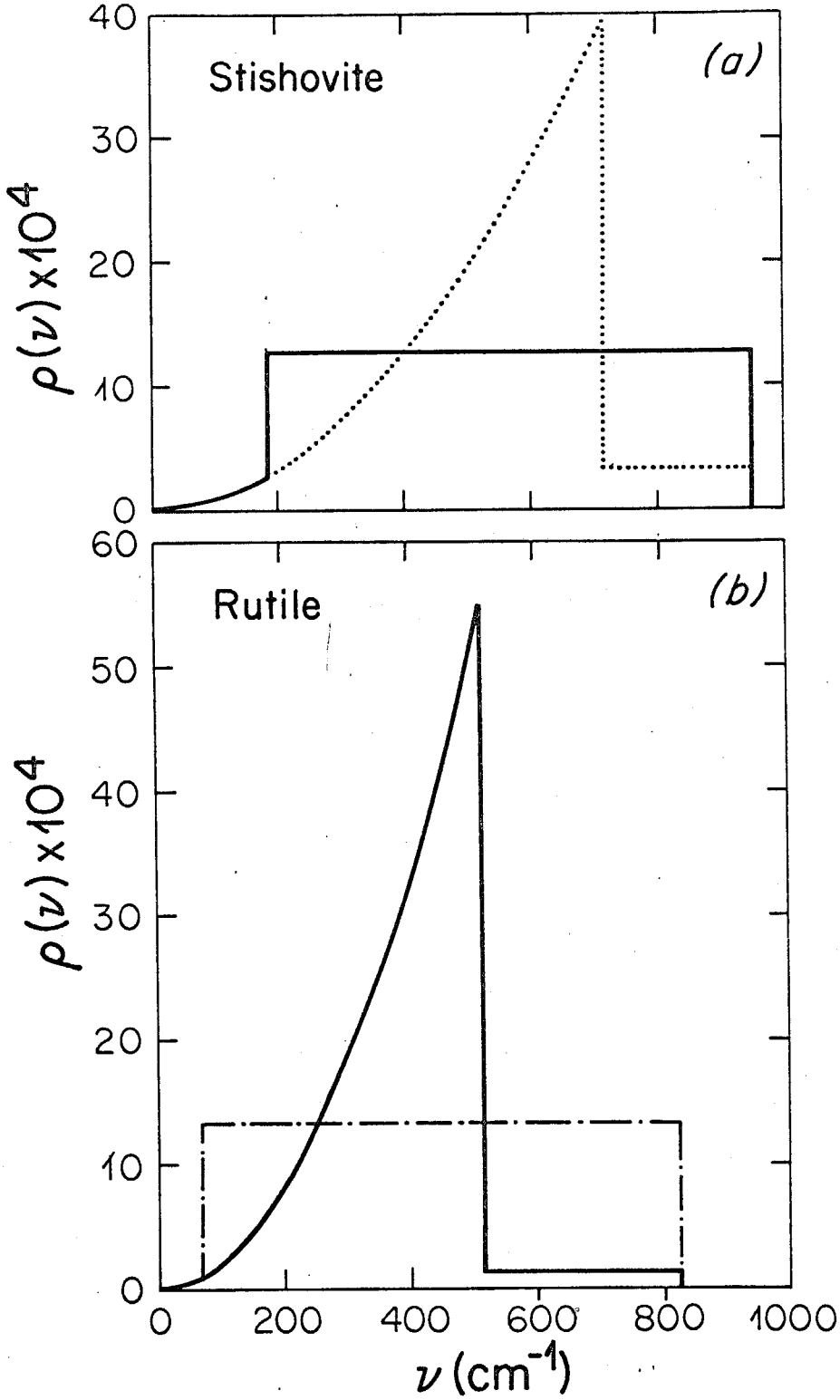
Stishovite
(a)
Rutile
(b)
ρ(ν) x10^4
ν (cm^-1)
0
10
20
30
40
50
60
200
400
600
800
1000

Figure 11

References

Alers, G. A., Use of sound velocity measurements in determining the Debye temperature of solids, in Physical Acoustics, edited by W. P. Mason, pp. 1-42, 1965.

Ahrens, T. J., D. L. Anderson and A. E. Ringwood, Equations of state and and crystal structures of high-pressure phases of shocked silicates and oxides, Rev. Geophys., 7, pp. 667-707, 1969.

Ahrens, T. J., G. Davies, and D. L. Anderson, High pressure equations of state at high temperatures for mantle minerals, Transactions, Amer. Geophys. Union, 50, p. 311, 1969.

Anderson, O. L., Determination and some uses of isotropic elastic constants of polycrystalline aggregates using single crystal data, in Physical Acoustics, edited by W. P. Mason, pp. 43-96, 1965.

Anderson, O. L., The Debye temperature of vitreous silica, Phys. Chem. Solids, 12, 41-52, 1959.

Anderson, O. L., E. Schreiber, R. C. Leibermann, and N. Soga, Some elastic constant data on minerals relevant to geophysics, Rev. Geophys., 6, pp. 491-524.

Barron, T. H. K., W. T. Berg, and J. A. Morrison, On the heat capacity of crystalline magnesium oxide, Proc. Roy. Soc. (London), A250, p. 70, 1959.

Barron, T. H. K. and J. A. Morrison, The specific heat of solids at low temperatures, 35, pp. 799-810, 1957.

Bassett, W. A. and J. D. Barnett, Isothermal compression of stishovite and coesite to 85 kilobars at room temperature by X-ray diffraction,

Phys. Earth and Plan. Int., 3, pp. 54-60, 1970.

Bhatia, A. B. and G. K. Horton, Vibration spectra and specific heats of cubic metals. II. Application to silver, Phys. Rev., 98, pp. 1715-1721, 1955.

Birch, F., Compressibility; elastic constants in Handbook of Physical Constants, edited by Sydney P. Clark, Jr., GSA Memoir 97, 1966.

Blackman, M., The specific heat of solids, in Handbuch der Physik, v. VII, part 1, pp. 325-382, 1955.

Bonnickson, K. R., High temperature heat contents of aluminates of calcium and magnesium, J. Phys. Chem., 59, p. 220, 1955.

Cetas, T. C., C. R. Tilford, and C. A. Swenson, Specific heats of Cu, GaAs, GaSb, InAs, and InSb from 1 to 30°K, Phys. Rev., 174, pp. 835-844, 1968.

Clusius, K., J. Goldmann, and A. Perlick, Ergebnisse der Tieftemperaturforschung. VII. Die Molwärmen der Alkalihalsgenide LiF, NaCl, KCl, KBr, KJ, RbBr, and RbJ von 10° bis 273° abs., Z, Naturforschg., 4A, pp. 424-432, 1949.

Dugdale, J. S., J. A. Morrison, and D. Patterson, The effect of particle size on the heat capacity of titanium dioxide, Proc. Roy. Soc. (London), A224, p. 228, 1954.

Hill, R. W. and D. H. Parkinson, The specific heats of germanium and grey tin at low temperatures, Phil. Mag., 43, p. 309, 1952.

Holm, J. L., O. L. Kleppa, and E. F. Westrum, Jr., Thermodynamics of polymorphic transformations in silica. Thermal properties from 5 to 1070°K and pressure-temperature stability fields for coesite and

stishovite, Geochim, et Cosmochim. Acta, 31, pp. 2289-2307, 1967.

Horai, Ki-iti and Gene Simmons, An empirical relationship between thermal conductivity and Debye temperature for silicates, JGR, 75, pp. 978-982, 1970.

Horton, G. K. and H. Schiff, Low temperature behavior and dispersion relations of face-centered cubic metals, Phys. Rev. 104, pp. 32-36, 1956.

Janaf Thermochemical Tables, Project Principia of the Advanced Research Projects Agency at the Thermal Research Laboratory, Dow Chemical Company, Midland, Michigan, 1965; also, First, Second and Third Addenda, 1965-1967.

Kam, Z. and G. Gilat, Accurate Numerical method for calculating frequency distribution functions in solids. III. Extension to tetragonal crystals, Phys. Rev., 175, p. 1156, 1968.

Keesom, P. H. and N. Pearlman, Low temperature heat capacity of pure and reduced rutile, Phys. Rev., 112, p. 800, 1958.

Kellerman, E. W., The vibrational spectrum of rocksalt, Phil. trans. Roy. Soc., Lond., A238, p. 513 (1940).

Kelley, K. K., Specific heats at low temperatures of magnesium orthosilicate and magnesium metasilicate, J. Am. Chem. Soc., 65, pp. 339-342, 1943.

Kelley, K. K., Contributions to the data on theoretical metallurgy XIII. High-temperature heat-content, heat-capacity, and entropy data for the elements and inorganic compounds, U.S.B.M. Bull. 584, 1960.

Kelley, K. K., S. S. Todd, R. L. Orr, E. G. King, and K. R. Bonnickson,

Thermodynamic properties of sodium-aluminum and potassium-aluminum silicates, U.S.B.M. Rept. Invest. 4955, 1953.

King, E. G., Heat capacities at low temperatures and entropies at 298.16°K of crystalline calcium and magnesium aluminates, J. Phys. Chem., 59, p. 218,, 1955.

King, E. G., Low temperature heat capacities and entropies at 298.15°K of some crystalline silicates containing calcium, J. Am. Chem. Soc., 79, p. 5437, 1957.

Leibfried, G., Gittertheorie der mechanischen und thermischen Ergenschaften der Kristalle, in Handbuch der Physik, v. VII, part 1, pp. 104-324, 1955.

Liu, L. G., T. Takahashi, and W. A. Bassett, Compression of stishovite and magnesian ilmenite at 25°C, Abstract, 50th Annual Meeting, AGU, 312, 1969.

Lord, R. C. and J. C. Morrow, Calculation of the heat capacity of α - quartz and vitreous silica from spectroscopic data, J. Chem. Phys., 26, p. 230, 1957.

Lyon, R. J. P., Infrared confirmation of 6-fold coordination of silica in stishovite, Nature, 194, pp. 266-267, 1962.

Moenke, H., Mineral Spectra, Akademie Verlag-Berlin, 1962.

Neuberger, J. and R. D. Hatcher, Infrared optical constants of NaCl, J. Chem. Phys., 34, p. 1733, 1961.

Orr, R. L., High-temperature heat contents of magnesium orthosilicate and ferrous ortho-silicate, J. Am. Chem. Soc., 75, p. 528, 1953.

Pearlman, N. and P. H. Keesom, The atomic heat of silicon below 100°K,

Phys. Rev., 88, p. 397, 1952.

Raman, C. V., Spectroscopic properties and specific heats of MgO and NaCl, Proc. Ind. Acad. Sci., 54A, pp. 205-304, 1961.

Raubenheimer, L. J. and G. Gilat, Accurate numerical method of calculating frequency distribution functions in solids. II. Extension to hcp crystals, Phys. Rev., 157, p. 586, 1967.

Saksena, B. D., Analysis of the Raman and infrared spectra of α - quartz, Proc. Ind. Acad. Sci., 12A, p. 93, 1940.

Shomate, C. H., Heat capacities at low temperatures of titanium dioxide, J. Am. Chem. Soc., 69, p. 218, 1947.

Skinner, B. J., Thermal expansion, in Handbook of Physical Constants, edited by Sydney P. Clark, Jr., GSA Memoir 97, 1966.

Westrum, E. F., Jr., The low temperature heat capacity of neutron irradiated quartz, in Proceedings of the IVIenne Congres International du Verre, pp. 396-399, Chaix, 1956.